DESIGN OF FUNCTIONAL FULLERENES: INVESTIGATION OF THEIR PHOTOPHYSICAL AND DNA SELF-ASSEMBLY PROPERTIES FOR OPTOELECTRONIC APPLICATIONS

THESIS SUBMITTED TO ACADEMY OF SCIENTIFIC AND INNOVATIVE RESEARCH (AcSIR) FOR THE AWARD OF THE DEGREE OF

DOCTOR OF PHILOSOPHY IN CHEMISTRY

UNDER THE FACULTY OF SCIENCE

By

SANDEEPA K. V.

Enrollment No: 10CC12A39010

Under the Supervision of

Dr. JOSHY JOSEPH

PHOTOSCIENCES AND PHOTONICS SECTION

CHEMICAL SCIENCES AND TECHNOLOGY DIVISION

CSIR-NATIONAL INSTITUTE FOR INTERDISCIPLINARY SCIENCE AND TECHNOLOGY (CSIR-NIIST)

THIRUVANANTHAPURAM - 695019, KERALA

APRIL 2018

Dedicated to

My Amma and Daddy...

DECLARATION

I hereby declare that the matter embodied in the Ph. D. thesis entitled: "**Design of Functional Fullerenes: Investigation of their Photophysical and DNA Self-Assembly Properties for Optoelectronic Applications**" is the result of an independent work carried out by me at the Photosciences and Photonics Section, Chemical Sciences and Technology Division of the CSIR-National Institute for Interdisciplinary Science and Technology (CSIR-NIIST), Thiruvananthapuram, under the supervision of Dr. Joshy Joseph and the same has not been submitted elsewhere for any other degree or diploma.

In keeping with the general practice of reporting scientific observations, research materials obtained from other investigations has been duly cited and acknowledged in the thesis.

Sandeepa K. V.

Thiruvananthapuram
April 26, 2018

National Institute for Interdisciplinary Science and Technology (CSIR-NIIST)

Council of Scientific & Industrial Research (CSIR)
Industrial Estate P. O., Trivandrum - 695 019
Kerala, INDIA

Dr. Joshy Joseph
Scientist
Chemical Sciences and Technology Division

Tel: +91-471-2515 476
Fax: +91-471-2491 712
E-mail: joshyja@gmail.com, joshy@niist.res.in

April 26, 2018

CERTIFICATE

This is to certify that the work embodied in the thesis entitled: "**Design of Functional Fullerenes: Investigation of their Photophysical and Self-Assembly Properties for Optoelectronic Applications**" has been carried out by Mr. Sandeepa K. V. under my supervision and guidance at the Photosciences and Photonics Section, Chemical Sciences and Technology Division of the CSIR-National Institute for Interdisciplinary Science and Technology (CSIR-NIIST), Thiruvananthapuram and the same has not been submitted elsewhere for a degree.

(Joshy Joseph)
Thesis Supervisor

ACKNOWLEDGEMENTS

I have a great pleasure in placing on record my deep sense of gratitude to Dr. Joshy Joseph, my thesis supervisor, for suggesting the research problem and for his constant guidance, endless support, unconditional care and encouragement that led to the successful completion of this work. He not only introduced me on various research programme like functional fullerenes, DNA self-assembly, photophysics, photovoltaics but also empowered my presentation/communication skills and capability to pursue independent research.

I would like to express my sincere thanks to Professor M. V. George for his constant motivation and fruitful advice during my stay at CSIR-NIIST.

I thank Dr. A. Ajayaghosh, Dr. Suresh Das and Dr. Gangan Pratap, present and former Directors of the CSIR-National Institute for Interdisciplinary Science and Technology (CSIR-NIIST), Thiruvananthapuram, for providing me the necessary facilities for carrying out this work.

I sincerely acknowledge Dr. Mangalam S. Nair and Dr. R. Luxmi Varma, former and present AcSIR coordinators for their help in successful completion of the AcSIR course work.

I would like to specially mention Dr. K. R. Gopidas, Dr. K. Yoosaf and Dr. Saju Pillai, Doctoral Advisory Committee members for their valuable advices and comments to improve the quality of doctoral work at various stages. I extend my thanks to Dr. D. Ramaiah, Dr. Biswapriya Deb, Dr. K. N. Narayanan Unni, Dr. C. Vijayakumar, Dr. K. Venugopal, and all other scientists of the Photosciences and Photonics Section, Chemical Sciences and Technology Division, for the help and support.

I would like to thank Dr. Bhoje Gowd, MSTD for helping with XRD and morphological analysis. Also Dr. Reji Varghese, IISER-TVM is greatly acknowledged for helping with HR-TEM analysis.

I am indebted to all group members, especially Mr. Sreejith M., Mr. Mathews K. Manayani., Ms. Sajena K. S for their help and support in synthesis of DNA, understanding photophysics and instrumentation, love in all ups and downs, active and constructive discussions throughout the PhD work. I am also thankful to other group members, Mrs. Silja Abraham, Ms. Anjali B. R., Ms. Shibna, B., Dr. Shanthi Krishna and Ms. Nishna N. for their

valuable inputs and cherishable moments during the end stage of the thesis work. The M.Sc. project students Mrs. Majisha, Mrs. Ashwariya J., Ms. Ashwariya P. are greatly acknowledged for their sincere effort and help in synthesis of few molecules.

I would like to thank the seniors especially Dr. Hari shankar, Dr. Sanju K. S., Dr. Suneesh C. K., Mr. Shanmughasundaram M., for their help and support in understanding instrumentation, photophysics and DNA synthesis at the initial stages. All other former labmates and seniors Dr. Adarsh N., Dr. Nandajan P. C., Dr. T. J. Dhanya, Dr. Albish K. Paul, Dr. M. Viji, Dr. Nidhi Tyagi, Dr. Tony Thomas, Dr. Vinayak, are acknowledged for their advice, care and cordial support.

I would like to thank Dr. Biswapriya Deb and Mrs. Remya R. for their help in BHJ-polymer solar cell fabrication, Mr. Mehesh chandran, RGCB for MALDI analysis, Dr. Baku Nagendra, Mr. Amal Raj, MSTD for their help, discussion in DSC, TGA and XRD measurements, Dr. Samrat Ghosh, Dr. Rahul D. M. for teaching 3D max and artworks. I also thank Mrs. Saumini Mathew, Mr. Saran and Mr. Gokul for NMR analysis and Mrs. Viji, and Ms. Athira for HRMS data, Mr. R. Aswin, Mr. Vishnu and Mr. Vibhu Darshan for AFM analysis and Mr. Robert Philip and Mr. Kiran for general help.

I have very much cherished the true friendship of Dr. Arun Gopi, Mr. Alex Kuriakose, Dr. Ajesh Vijayan, Mr. Shameel T., Mr. Naeem K. C., Mr. Mohammed Yoosuf, Mr. K. V. Sudhish, Dr. Sumesh K. B., Mr. Gourab Das and all the present and former members of the Photosciences and Photonics section and other Divisions of CSIR-NIIST. Special mention to Dr. Nagaraj Nayak for his unconditional friendship, beautiful moments, funny conversations and advices at all walks of my life.

Words are inadequate to express my gratitude to my family members who constantly stood as a source of encouragement and confidence. Especially, my brother Mr. Santhosh, Sister Mrs. Sangeetha, Bhava Mr. Raghavendra, Athige Mrs. Pavithra for their trust, love the moral support. I take this opportunity to pay respect to all my teachers who guided and blessed me.

Finally, I sincerely thank Council of Scientific and Industrial Research (CSIR), UGC, and DST, Government of India for financial assistance.

Sandeepa K. V.

CONTENTS

PREFACE

The functional, monomeric fullerene derivatives are synthetically accessible and exhibit comparable optoelectronic properties to that of the parental [6,6]-phenyl-C_{61}-butyricmethyl ester (**PCBM**), which can be polymerized via covalent or supramolecular techniques. Developing covalently modified polyfullerenes and non-covalently functionalized supramolecular fullerene polymers are promising strategies to create dimension-controlled nanomaterials. The programmed fullerene architectures constructed by intermolecular fullerene cross-linking might be useful in optoelectronic applications where routine self-assembly approach fails. Moreover, the ordered self-assembly of fullerene and their analogous into regular DNA nanostructures may prove to be an effective DNA based template for the selective localization of organic chromophores, inorganic ions, nanoparticles and nanoclusters etc. Therefore, the fullerene-DNA interactions and structural design presented here could be applied to the development of mutual assisted supramolecular nanodevices and nano-machines which can solve the next, most challenging problems of supramolecular chemistry and nanotechnology. The collaboration between these rapidly growing fields - fullerene chemistry and DNA nanotechnology- will open up new avenues in the field of supramolecular architectures and their applications.

In this regard, the present thesis has been divided into four chapters. In the **Chapter 1**, general fullerene functionalization strategies by using aromatic, aliphatic and core substituted moieties towards various applications such as bulk heterojunction polymer solar cells (PSCs), organic field effect transistor, charge separation/stabilization and the construction of various supramolecular nanostructures were discussed. Also various covalent approaches for the construction of fullerene polymers such as main-chain, side-chain and polymer grafted fullerene with relevant applications were discussed. Special emphasis was given to non-covalent approaches used for developing supramolecular fullerene polymers such as polymer assisted, host-guest induced and DNA-templated self-

assembly techniques. Furthermore, the objectives of the thesis are also briefly presented in this chapter.

In the C**hapter 2**, the rational design and synthesis of a novel cross-linkable fullerene derivative, [6,6]-phenyl-C_{61}-butyricbenzoxazine ester (**PCBB**) functionalised with benzoxazine moiety were described which exhibited dual stimuli responsiveness towards temperature and visible light. The heat triggered ring opening polymerisation of benzoxazine moiety in **PCBB** was investigated through differential scanning calorimetry and infrared spectroscopy which resulted in the formation of cross-linked solvent resistive adhesive films upon heating at 200 ^{o}C for 15 min. An inverted bulk hetero junction solar cell device using cross-linked, C-PCBB as electron transport layer based on the configuration ITO/ZnO/C-PCBB/**P3HT**:**PCBM**/V_2O_5/Ag achieved 4.27% PCE compared to the reference device ITO/ZnO/**P3HT**:**PCBM**/V_2O_5/Ag (PCE=3.28%). Moreover, under visible light **PCBB** showed time dependent morphology transformation from core-shell nanoparticle into nanonetwork structure in THF/H_2O (9/1, v/v) solvent mixture. This transformation of self-assembled nanostructure is believed to involve the [2+2] cycloaddition reaction of fullerene as evident from NMR and mass spectral analysis.

The aniline appended covalent modification of fullerene derivative, 3-aminobenzyl-phenyl-C_{61}-butyrate (**PCBAn**), its polymer (**P-PCBAn**) obtained through $FeCl_3$ induced oxidative polymerisation and their photophysical studies towards application in PSCs were discussed in **Chapter 3**. The morphology of **PCBAn**, **P-PCBAn** alone and the polymer blend with Poly (3-hexylthiophene), **P3HT** donor was investigated using AFM and TEM analysis. Also, the square wave voltammetry revealed the upshifted LUMO levels of **PCBAn** and **P-PCBAn** (0.1 eV and 0.12 eV respectively) compared to the parental **PCBM**. Moreover, the fluorescence quenching experiments, life-time studies and Stern-Volmer plots indicated the efficient electron transfer from **P3HT** to **P-PCBAn** compared to **PCBAn**. The fabrication of inverted BHJ-PSC device using **PCBAn** and **P-PCBAn** as acceptors, in combination with **P3HT** showed 0.9% and 1.1% PCE, respectively.

Three monosubstituted fullerene derivatives having pyridinium, aniline or phenothiazine end groups (**F-Py**, **F-An** and **F-PTz**, respectively) were synthesized and their differential interaction with calf thymus DNA (CT-DNA) was probed via spectroscopic and imaging techniques, the details of which are presented in **Chapter 4: Part A**. The pyridinium derivative, **F-Py** gets molecularly dissolved in 10% DMSO-PBS and interacts with CT-DNA via groove binding and electrostatic interactions leading to initial condensation of CT-DNA into micrometer sized aggregates as evidenced through DLS, Zeta potential and microscopic studies. On the other hand, the aniline derivative **F-An,** which form nanoclusters of 3-5 nm size, interact with DNA through ordered, chiral assemblies on CT-DNA template perturbing the highly networked structure of CT-DNA to form nanonetworks, which eventually transform to condensed aggregates. In contrast, the phenothiazine derivative, **F-PTz**, which forms larger nanoclusters of ~70 nm in 10% DMSO-PBS showed only weak interactions with CT-DNA without affecting its network structure.

Programmable, hierarchical assembly of DNA nanostructures with precise organisation of functional components have been demonstrated previously with tiled assembly and DNA origami. However, building organised nanostructures with random oligonucleotide strands remains as an elusive problem. In **Chapter 4: Part B**, we describe a simple and general strategy in which unique nanoclusters of a fullerene derivative act as stapler motifs in bringing ordered nanoscale assembly of short oligonucleotide duplexes and DNA three way junctions into micrometer-sized nanofibres, nanosheets and nanonetwork respectively. Moreover, the horizontal conductivity measurements using c-AFM confirmed the charge transport properties of these nanowires. Furthermore, the silver nanoclusters (AgNCs) templated over 3WJ-overhang/**F-An** nano-construct exhibited 40% fluorescence enhancement compared to that of 3WJ-OH. We demonstrate that the optimum cluster size, availability of DNA anchoring motifs and the nature of the DNA strands control the structure of these nanomaterials.

***Note**: The abbreviations of various compounds used here correspond to those given under the respective chapters.*

LIST OF ABBREVIATIONS

1. A° - Angstrom
2. Ag – Silver
3. Al – Aluminum
4. AFM- Atomic force microscopy
5. APS- Ammonium persulphate
6. BHJ – Bulk heterojunction
7. ^{o}C – Degree Celsius
8. CC - Charge collection
9. CF - Chlroform
10. CS - Charge separation
11. cm – Centimeter
12. *ca.* – *circa*
13. Ca – Calcium
14. CV – Cyclic voltammetry
15. $CDCl_3$ – Deuterated chloroform
16. CH_3CN – Acetonitrile
17. Calcd. – Calculated
18. D/A – Donor/ Acceptor
19. Da - Dalton
20. DCM – Dichloromethane
21. DIO – 1,8-diiododoctane
22. DNA – Deoxy-ribonucleic acid

23. DLS – Dynamic Light Scattering
24. DSC - Differential scanning calorimetry
25. e^- - Electron
26. ED – Exciton diffusion
27. *et al.* – *Et allii/alia*
28. ε – Molar extinction coefficient
29. E_{gap} – Energy gap (bandgap)
30. E_{HOMO} – Energy of HOMO
31. E_{LUMO} – Energy of LUMO
32. E_{ox} – Oxidation potential
33. E_{red} – Reduction potential
34. ESI-MS – Electrospray ionization mass spectrometry
35. ETL – Electron transporting layer
36. eV – Electron volt
37. EQE - External quantum efficiency
38. FAB-MS – Fast atom bombardment mass spectrometry
39. $FeCl_3$ – Ferric chloride
40. FF - Fill factor
41. FT-IR – Fourier transform infrared
42. g - Gram
43. ^1H - Proton
44. h – Hour
45. h^+ - Hole

46. Hz - Hertz
47. H_2O - Water
48. HOMO – Highest occupied molecular orbital
49. HCl – Hydrochloric acid
50. HTL – Hole transporting layer
51. I_h - Icosahedron
52. IR – Infrared
53. ITO – Indium tin oxide
54. *J* – Current density
55. J_{sc} - Short-circuit current density
56. K – Kelvin
57. k - Kilo
58. KBr – Potassium bromide
59. LED- Light Emitting Diode
60. LUMO – Lowest unoccupied molecular orbital
61. λ_{max} – Wavelength maximum
62. % - Percentage
63. β - Beta
64. γ - Gamma
65. M – Molar
66. mg – Milligram
67. mL – Millilitre
68. min - minutes
69. µL - Microlitre

70. μM – Micromolar

71. μs – Microseconds

72. μm – Micrometer

73. mM – Millimolar

74. mmol – Millimole

75. mp – Melting point

76. MALDI-TOF-MS – Matrix-assisted laser desorption ionization-time of flight- mass spectrometry

77. nm – Nanometer

78. NMR – Nuclear magnetic resonance

79. ns – Nanosecond

80. *o* - Ortho

81. ODCB – 1,2-dichlrobenzene

82. OFET – Organic Field effect transistor

83. OPV – Organic Photovoltaic

84. *p*- Para

85. PCE – Power Conversion efficiency

86. P_{in} - Power density of the incident light

87. PV - Photovoltaic

88. PSC – Polymer solar cell

89. P3HT- Poly(3-hexylthiophene)

90. ppm – Parts per million

91. RT – Room emperature

92. RMS – Root mean square

93. R_f - Retention factor

94. S - Siemen

95. s – Seconds

96. SEM – Scanning electron microscope

97. st - Syndiotactic

98. TEM – Transmission electron microscope

99. TiO_2 - Titanium dioxide

100. TLC – Thin layer chromatography

101. TGA – Thermogravimetric analysis

102. THF – Tetrahydrofuran

103. TMS – Tetramethylsilane

104. UV – Ultraviolet

105. V_2O_5 - Vanadium Pentoxide

106. Vis – Visible

107. V_{oc} - Open-circuit voltage

108. vs – Versus

109. 3WJ – Three-way junction

110. ZnO - Zinc Oxide

CHAPTER 1

AN OVERVIEW ON FUNCTIONAL FULLERENES AND THEIR APPLICATIONS

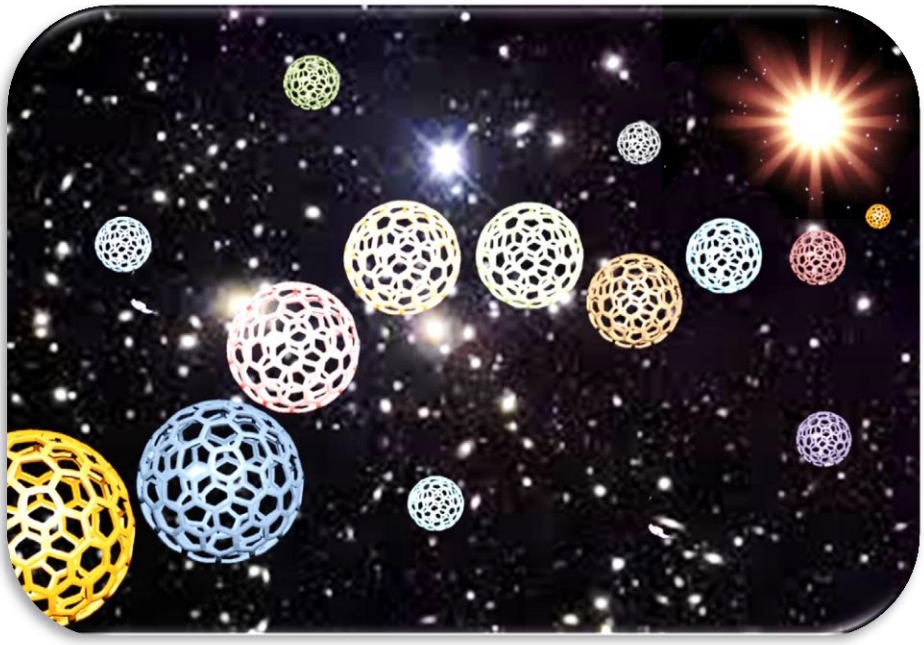

1.1. ABSTRACT

*Unique photophysical, electrochemical and self-assembling properties of fullerene derivatives render them as an attractive class of materials with wide range of applications in nanotechnology and material science. Many research groups approached smart modification of well-studied acceptor, [6,6]-phenyl-C_{61}-butyric acid methyl ester (**PCBM**) using visible absorbing moieties, self-assembling units and altering Lowest Unoccupied Molecular Orbitals (LUMO) to enhance the electron acceptor properties of fullerene derivatives. However, the rational design of fullerene materials which can organize in one or two dimensional fashion is challenging due to their higher aggregation/crystallization tendency in the solid state leading to changes in electronic and charge transport*

*properties. Developing covalently modified polyfullerenes and non-covalently functionalized supramolecular fullerene polymers are promising strategies to create dimension controlled nanomaterials. The functional, monomeric fullerene derivatives are synthetically accessible and exhibit comparable optoelectronic properties to that of the parental **PCBM** which can be polymerized via covalent or supramolecular techniques.*

1.2. INTRODUCTION

Fullerenes are a family of molecules composed entirely of carbon atoms that form a 3-dimensional shape including spheres, ellipsoids, and tubes.[1,2] Although the term fullerene is most often associated with buckyballs, carbon nanotubes and nano-onions are also fundamentally included in the fullerene family. C_{60} and C_{70}, are the two most stable buckyballs and the structure of these fullerenes, along with widely used

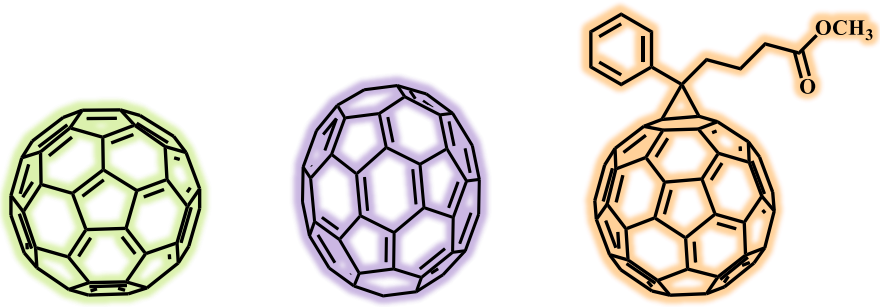

Figure 1.1. Chemical structures of fullerene, (from left) C_{60}, C_{70} and [6, 6]-Phenyl-C_{61}-butyricacidmethyl ester, commonly abbreviated as **PCBM**.

PCBM derivative, are shown in Figure 1.1.[3] The number in the subscript refers to the number of carbons atoms contained in the spherical molecule. Fullerene (C_{60}), a truncated icosahedron (I_h) having a diameter of 7.1 Å, has 20 hexagons and 12 pentagons consisting of sp^2-hybridized carbon atoms.[4] Experimentally, it was first discovered by Curl, Kroto, and Smalley in 1985, who shared the Nobel Prize (chemistry)

in 1996.[5] But it was the synthesis of a macroscopic quantity of fullerenes by Kratschmer and Huffman in 1990 fuelled the interest of experimentalists in fullerenes.[6] Fullerenes are one of the most extensively studied carbon nanomaterials in recent years, with a variety of interesting properties such as ability to accept and release electrons,[7] photo activity,[8] physiological activity and biocompatibility.[9] These pristine C_{60} carbon nano-materials and their derivatives hold great promise in many applications such as liquid crystals,[10] organic LEDs,[11,12] photocurrent generation devices[13] and organic photovoltaics.[14,15] Despite having these fascinating properties, poor solubility in common organic solvents limit practical applications of pristine C_{60}. Some of the most commonly used solvents in fullerene chemistry include toluene, 1,2-dichlorobeznene, and 1-chloronapthalene. However, fullerenes are the only known allotrope of carbon that can be dissolved and processed in such solvents at room temperature. In 1995, Fred Wudl's group synthesized the first modified fullerene derivative, **PCBM** (Figure 1.1).[16] Ever since the introduction of **PCBM**, the synthesis of functional fullerenes and their structure, properties have been heavily investigated.

1.3. FUNCTIONAL FULLERENES FOR OPTOELECTRONIC APPLICATIONS

Functional fullerenes are electron acceptor material with aliphatic, aromatic or core substituted fullerene unit and are most widely used for various optoelectronic applications.[17,18] For instance, by rational functionalization of fullerenes, one can tune their solubility, energy levels, molecular interactions, morphology of the resultant nanostructure in the solution and film state.[19] Functional fullerenes are more practical choice as interfacial or active layer component in bulk heterojunction (BHJ) PSCs due to

their high electron affinity, small reorganization energy and excellent electron transport properties.[20] Moreover, they can give desirable solubility in aromatic solvents, superior processability and matching energy levels with electron donor materials.[21] These merits render functional fullerenes as one of the excellent electronic component in material science and organic photovoltaics. Out of several applications of functionalized fullerenes few important ones are discussed in this chapter.

1.3.1. BULK HETEROJUNCTION POLYMER SOLAR CELLS (BHJ-PSCs)

One of the most promising ways to tackle today's energy issues is harnessing solar energy.[22] Although at present inorganic photovoltaic (PV) technology is dominant in its performance, high material and manufacturing costs limit its wide acceptance. Out of many research conducted, organic photovoltaic (OPV) devices are one of the promising approach towards the development of low-cost renewable energy sources. The working principle of both conventional and inverted can be explained as follows (figure 1.2).[23] Upon absorption of light the donor molecules generate the electrostatically coupled electron-hole pairs (η_A). These photo generated excitons undergo hoping towards the donor-acceptor BHJ interface (η_{ED}). These exciton diffusion lengths are limited to ~10 nm which plays crucial role in the design of donor-acceptor molecules in PSCs. The exciton at the donor-acceptor BHJ undergoes electron-hole dissociation into free charge carriers. For efficient dissociation, the difference between LUMO of donor and acceptor energy levels should be greater than that of exciton binding energy which is typically around 0.2-0.3 eV.[24] Further, the free charge

carriers move through respective transporting materials (η_{CT}) and get collected at specific electrode (η_{CC}).

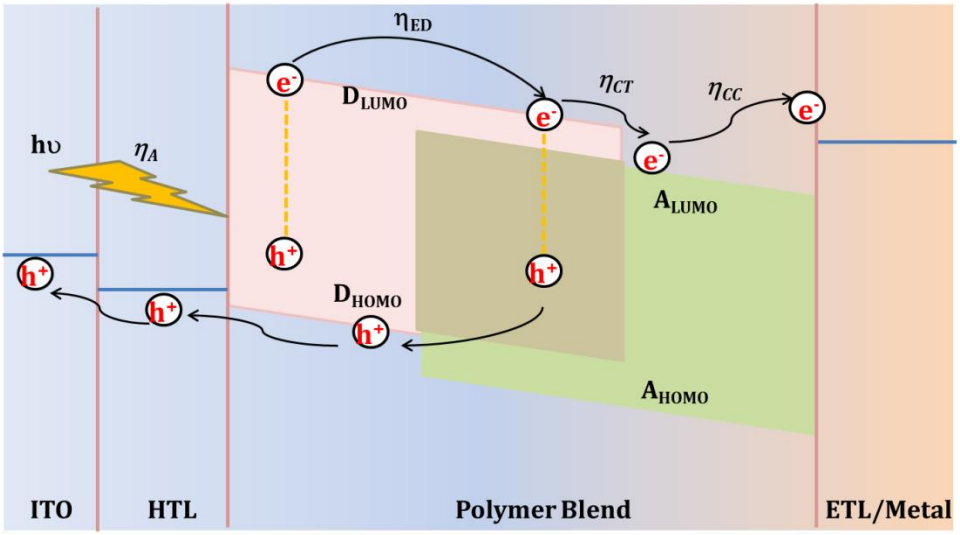

Figure 1.2. Pictorial illustration of polymer solar cell operating mechanism.

The external quantum efficiency (EQE) as a function of wavelength (λ) is the ratio between the collected photo generated charges and the number of incident photons, ultimately being the product of four efficiencies (η): absorption (A), exciton diffusion (ED), charge separation (CS) and charge collection (CC), giving EQE = $\eta_A \times \eta_{ED} \times \eta_{CS} \times \eta_{CC}$. More than inherent properties of donor and acceptor, device related parameters such as open-circuit voltage (V_{oc}), short-circuit current density (J_{sc}), and fill factor (FF) are critical in determining the **PCE** which depends on the electrical contact between the **BHJ** layer and the electrodes. The power conversion efficiency (η) of a solar cell is defined by the ratio of V_{oc} x J_{sc} x FF and the power density of the incident light (P_{in}). Figure 1.3a describes the state-of-the-art configuration of conventional **BHJ-PSCs** composed of an active layer sandwiched between metal oxide i.e. ITO (Indium Tin

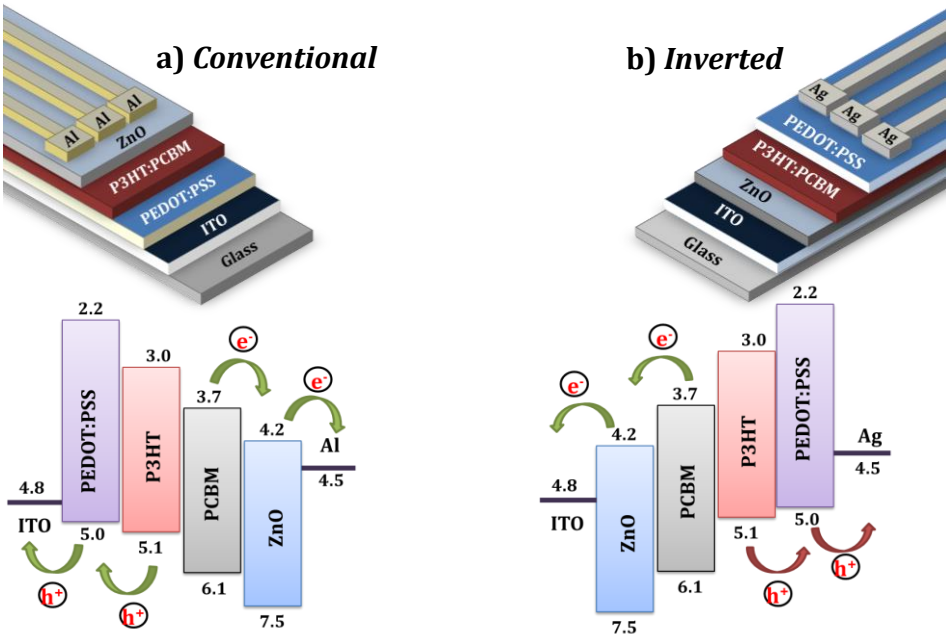

Figure 1.3. Schematic representation of a) conventional and b) inverted BHJ device architecture and (c-d) their corresponding energy level diagrams (energies are given in eV below vacuum level).

Oxide) and metal electrode (Aluminium, Al). The conventional **PSC** have limitations over device stability due to the oxidation of low work function aluminum electrode. For this purpose, inverted **PSCs** with opposite polarity have been introduced (Figure 1.3b).[25] The ideal energy level diagram and electron (e^-)/hole (h^+) transport pathways in the conventional and inverted device are shown in figure 3c and 3d respectively.

Typically the active layer of **BHJ-PSC** consists of a small molecule/polymer electron donor and an acceptor being **PCBM**, the favorite choice of many researchers due to its high electron accepting abilities. As previously reviewed by Li *et al*., a large number of methanofullerene and **PCBM** derivatives have been studied by varying the substitution moieties to further improve the properties of **PSCs** (Figure 1.4).[26] For

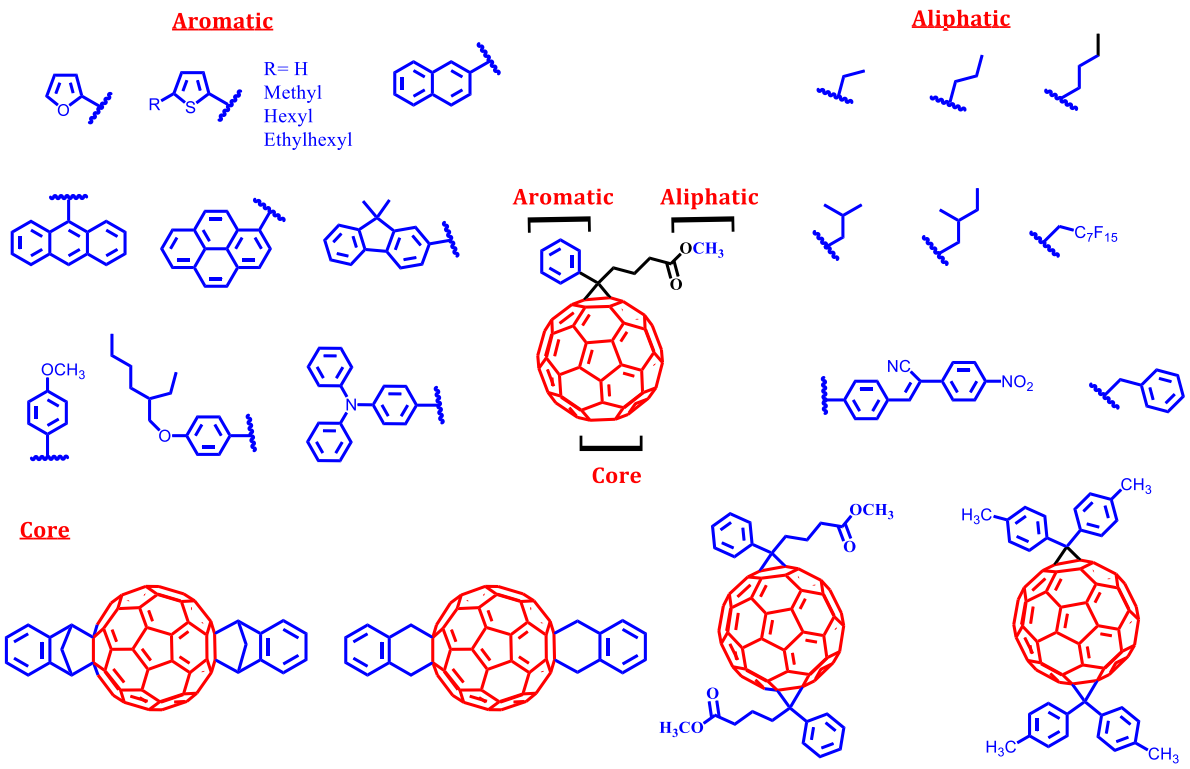

Figure 1.4. Few representative molecular structure and analogous of fullerene derivative with various aromatic, aliphatic and core substitution.

instance, aromatic phenyl ring of **PCBM** have been substituted with other aromatic/heteroaromatic groups such as naphthalene, pyrene, anthracene, fluorene, triphenylamine, furan, thiophene and substituted phenyl group with methyl, 2-ethylhexanyl moieties.[27-29] Moreover, aliphatic ester linkage were also modified with other groups such as ethyl, propyl, butyl, isopropyl, isobutyl, benzyl, perfluoroalkyl and light absorbing 4-nitro-4'-hydroxy-α-cyanostilbene units.[26,30] On the other hand, core substituted fullerene derivative were also introduced to upshift the energy levels by decreasing the number of electrons. For example, the LUMO of **PCBM** can be easily upshifted by converting it from 58 to 56 π electrons system. Hence, many bisadduct of fullerene such as **bis-PCBM**,[31] Indene-C_{60}-bisadduct (**ICBA**),[32] fullerene-di(4-methyl-

phenyl)methano-C_{60} (**DMPCBA**)[33] and bis-*o*-quino-dimethane C_{60} (***o*-QDMC$_{60}$**)[34] have superior performance than their monomer counterpart.

1.3.2. ORGANIC THIN FILM TRANSISTORS

The n-type semiconducting property of fullerene has also been explored in the fabrication of organic thin film transistor.[35] Though n-type transistors are required for the assembly of ambipolar transistors and complementary circuits, their research is still in developing stage compared to p-type materials. This is mainly because of low charge carrier mobilities of n-type materials (10^{-2} $cm^2V^{-1}s^{-1}$ or less) compared to p-type one.[36] For the first time, Sang Yun Lee *et al.* demonstrated all solution processed n-type transistor using [5,6] and [6,6] **PCBM** derivative achieving high electron mobilities of 0.021-0.1 $cm^2V^{-1}s^{-1}$, depending on the source and drain electrode metal work function.[37] Alex K. Y. Jen *et al.* have demonstrated the construction of solution processed **OFET** device using highly conductive doped amphiphilic fullerene derivative, fulleropyrollidinium iodide (**FPI-1**, Figure 1.5a).[38] *I-V* plot the device showed straight line with negligible dependence of gate voltage on current. This suggests the metallic like conductivity of **FPI-1** thin film. The iodide doping in **FPI-1** causes effective electron transfer from iodide to fullerene resulting in conductivity as high as 2 S/m. While blending **PCBM** with **FPI-1**, even higher conductivity of 3.2 S/m was observed. The conductivity reported in this report is the highest among solution processed and doped fullerenes. Recently, the same group reported the formation of crystalline co-assemblies of **FPI-1** in the presence of 20 mol% of other fullerenes revealing the tight packing through increased pi-pi interaction.[39] The **FPI-1** with **FPI-2**, **FPI-3**, C_{60} and $Sc_3N@C_{80}$

(Figure 1.5b) showed higher conductivities of 0.46 ± 0.07, 0.54 ± 0.14, 0.63 ± 0.09, and 0.68 ± 0.12 S/cm respectively. This metallic like conductivity can be useful in future molecular design and functional material developments.

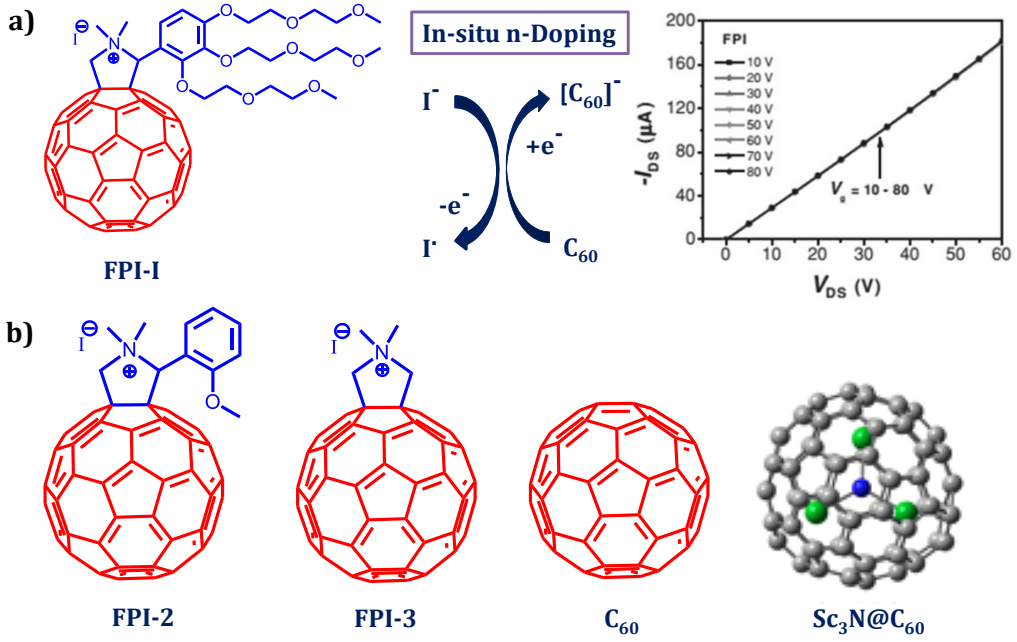

Figure 1.5. a) Chemical structures of FPI-1, *in situ* n-doping mechanism and FET electrical output characteristics (Adapted from reference 38). b) Chemical structures of fullerene derivatives used for the doping namely, FPI-2, FPI-3, C_{60} and $Sc_3N@C_{80}$ (Adapted from reference 39).

1.3.3. CHARGE SEPARATION AND STABILIZATION

The electron accepting ability of fullerene has been utilized in creating artificial photosynthetic systems.[40] But stabilizing the charge separated state is as important as creating radical cation-anion pair. So, covalently modified fullerene-donor-based dyad systems attracted great deal of interest to understand the photophysical and photochemical properties. Several fullerene-based donor-acceptor systems containing porphyrins, phtholocyanines, ruthenium complexes, ferrocenes, and anilines as donors

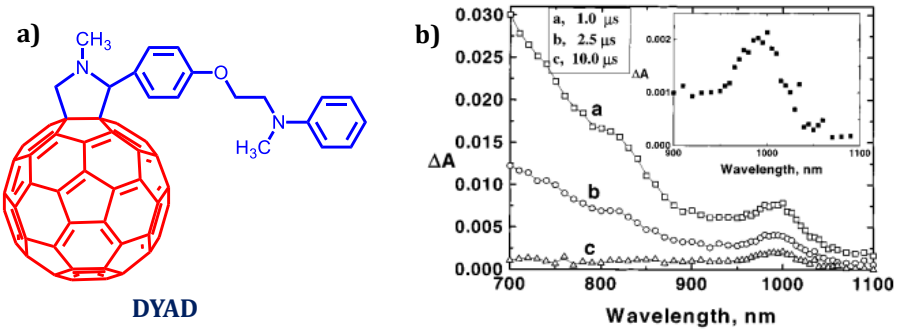

Figure 1.6. a) Structure of Fullerene-aniline dyad; b) Difference absorption spectra (NIR region) recorded after 337 nm laser pulse excitation of dyad (30 μM) in a deoxygenated toluene-acetonitrile (1:3) mixture. The inset shows the enlarged spectra recorded 10 μs after excitation (Adapted from reference 44).

have been synthesized for achieving efficient photoinduced charge separation in these dyads.[41-43] K. George Thomas *et.al* reported fullerene-bridge-aniline dyad compound (figure 1.6a) which form stable, optically transparent clusters in acetonitrile and toluene mixtures (3:1).[44] The formation of fullerene radical anion (absorption maximum at 1010 nm) with a lifetime of several hundreds of microseconds was further confirmed using nanosecond laser (337 nm) flash photolysis experiments (Figure 1.6b). This dyad did not yield any detectable charge-transfer intermediates following laser pulse excitation even in polar solvents such as benzonitrile or nitromethane, suggesting that fast back-electron transfer process must be operative in the monomeric dyad system.[45] Francis D'Souza and co-workers developed new palladium-porphyrin-fullerene donor-acceptor systems and studied donor-acceptor distance dependent electron transfer processes (Figure 1.7a).[41] Out of several derivatives, palladium-porphyrin substituted with three electron rich triphenylamine entities exhibited electron transfer from the triplet excited state of palladium porphyrin with high

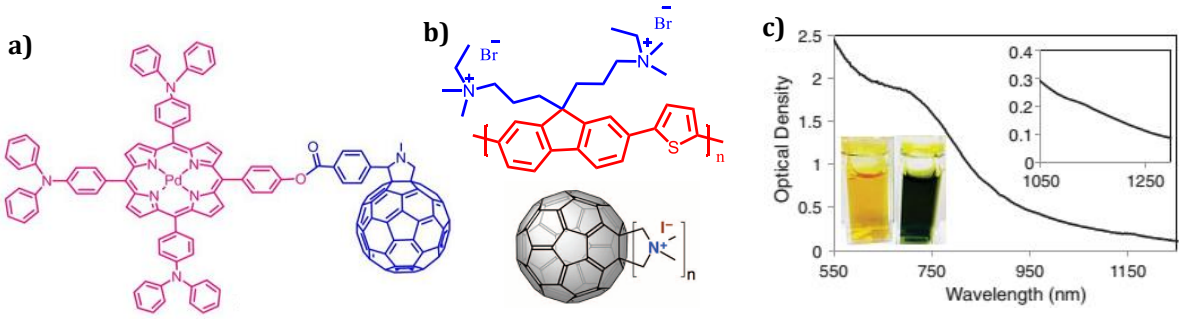

Figure 1.7. The chemical structures of a) palladium(II)-porphyrin-fullerene donor-acceptor conjugate (Adapted from reference 41), b) poly(fluorene-*alt*-thiophene), PFT and isomers of fulleropyrollidinium iodide used for the generation of long lived charge transfer state. c) Absorption from a green concentrated PFT/fullerene solution showing both P^{+} and N polaron aqueous medium (Adapted from reference 46).

quantum yield. The life time of charge separated state observed was around 10-14 μs. Though the high lifetime of charge separated state observed for these systems are in organic solvents, for the actual practical application it should be carried out in aqueous medium. Sarah H. Tolbert *et al.* recently described long lived polaron in different isomers of functionalized fulleropyrollidinium iodide encapsulated in the polyelectrolyte **PFT**, poly (fluorene-*alt*-thiophene) matrix (Figure 1.7b).[46] The steady-state absorption studies upon photoirradiation and the color change from yellow to green confirm the appearance of the **PFT** radical cation (550 nm) with concomitant formation of fullerene radical anion at 1180 nm (Figure 1.7c). The self-assembled system in aqueous medium showed photoinduced charge separated state which is stable for several weeks. The long-lived charge separated state is mainly due to the well-ordered polymer-fullerene coassemblies facilitating cascade photoinduced electron transfer. These examples represent the unique electron acceptor property of fullerene derivative making it an ideal candidate for artificial photosynthetic systems.

1.3.4. FUNCTIONAL SUPRAMOLECULAR NANOMATERIALS

The amphiphilic assembly approach through hydrophilic functionalization on a hydrophobic pi-conjugated core is the most common strategy to improve the molecular arrangements in the supramolecular organization of building blocks.[10] Infact, the amphiphilic approach is not only limited to planar pi-conjugated systems, but also for spherical fullerene-C_{60} molecule. Fulleropyrrolidine functionalized with solvophilic derivatization such as 3,4,5, 3,4 or 4-alkyloxyphenyl group (**1-7**, Figure 1.8a) are reported to be excellent molecular building block for the construction of supramolecular nanostructures.[15] Interstingly, 2, 4, 6-alkyloxyphenyl group substituted fulleropyrrolidine derivative with varying alkyl chains have shown unusual room-temperature fluid behaviour (**8-10**, Figure 1.8b).[47] Supramolecular assemblies in nano/micro/bulk length scales were constructed by utilizing the unique hydrophobic

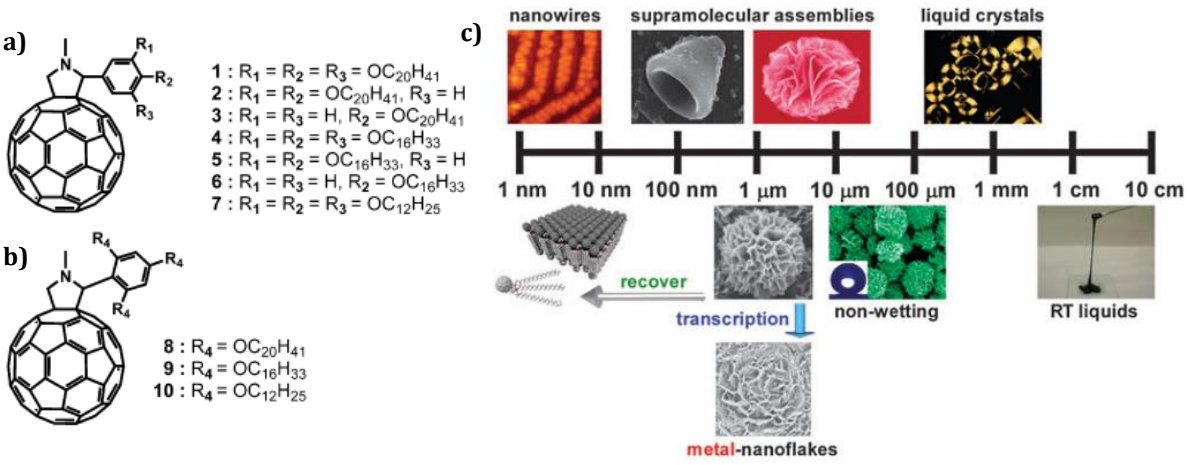

Figure 1.8. Chemical structures of (a) Fulleropyrrolidine functionalized with a) 3, 4, 5, 3, 4 or 4-alkyloxyphenyl group (Adapted from reference 15). (b) 2, 4, 6-alkyloxyphenyl group and c) various supramolecular nanostructures developed with controlled dimensionality (Adapted from reference 47).

conjugates consisting of fullerene (C_{60}) bearing long alkyl tails (Figure 1.8c). The globular nanoflowers exhibits superhydrophoic behaviour due to the presence of wrinkled, flakelike structure with increased nano and microscopic roughness.[48] The morphology can endure transcription to nanoflake metals or photo-polymerized in order to freeze the nanostructured morphology. In solventless environment, some fullerene derivatives undergo long-range ordered self-assembly into thermotropic liquid crystals with excellent electron transport characteristics.[49] Moreover, Takashi Nakanishi and co-workers reported supramolecular assembly of functional fullerene derivatives through careful selection of solvophobic/solvophilic segments and *n*-alkane solvents. By varying the concentration they could control the assembled structures from micellar to nanofibrillar to lamellar mesophases which exhibit comparably high photo-conductivities.[50] Hence the strategy of C_{60} functionalization is novel and attractive and can be used for the design of well-ordered efficient organic/polymeric materials.

1.4. FUNCTIONAL FULLERENE POLYMERS

Although functionalized fullerenes have been widely used, they still require optimization in order to replace standard fullerene acceptors. Inspired from polymer chemistry, fullerene polymers were developed by substituting fullerene in polymer backbone in which fullerene can be part of main chain or as a pendent unit.[51] Moreover, fullerene polymers are best counterparts compared to monomeric fullerenes to address the limitations of stability and macrophase separation in the **BHJ** or interfacial layer.[52] For example, polymer blend formed along with fullerene polymers can result in large

interfacial area, efficient exciton dissociation and well separated pathways for the free charge carrier transport across the electrodes. Although, polyfullerene have several advantages such as inbuilt to form 1D nanofibres, easy processability and excellent stability, their synthesis without affecting the structural properties of core fullerene part remained as a scientific challenge.[53] In this regard, we have listed some of the recent developments in covalent and non-covalently functionalized fullerene polymers used for various applications.

1.4.1. COVALENTLY FUNCTIONALIZED FULLERENE POLYMERS

The process of connecting each individual molecule with neighboring ones by covalent bond upon various stimuli such as temperature, UV light, photoinitiator etc. is termed as 'cross-linking' and is widely used in the solid-state **BHJ** devices during device fabrication to generate stable film morphology.[54] During the last decade, one of the major breakthrough in realizing long-term stability of active film morphology of **PSCs** for practical applications is the strategy of "freezing" the nanostructures of self-assembled fullerene molecules.[19] There have been numerous investigations on use of cross-linkable materials in **OPV** cells. Cross-linkable fullerenes originated after the development of significant number of cross-linkable polymers.[55] Nazario Martin and co-workers beautifully summarized the different types of C_{60} containing polymers using main chain, side chain, star shaped, double cable, end capped, cross-linked and supramolecular fullerene derivatives (Figure 1.9).[54] Few of the important type of fullerene polymers were discussed below in detail.

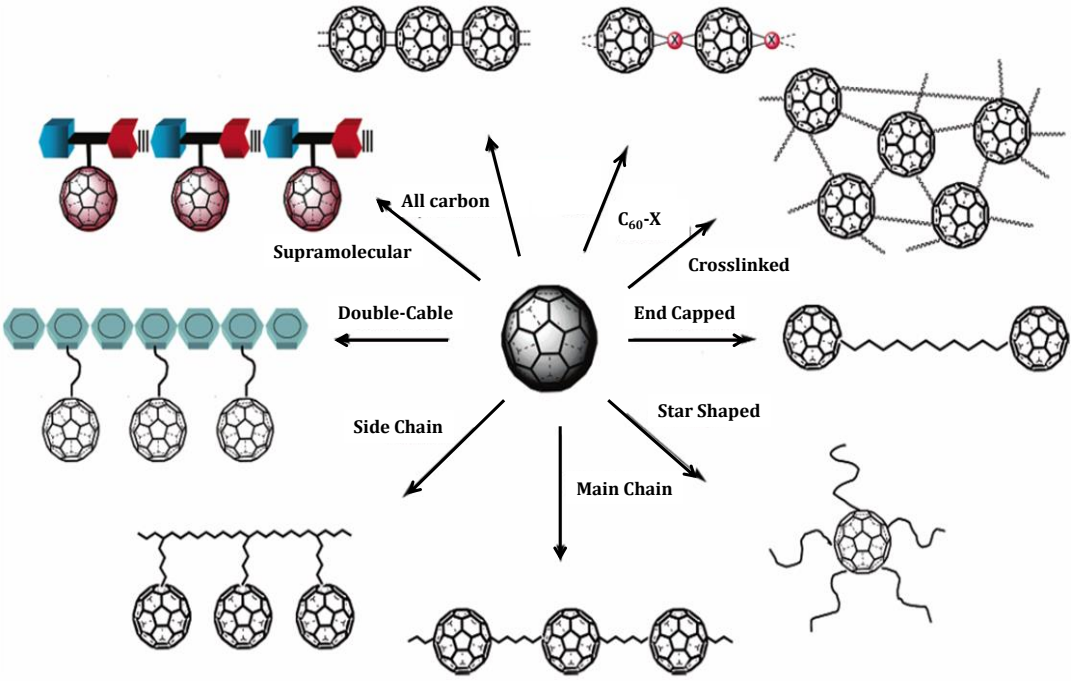

Figure 1.9. Schematic representation of C_{60}-containing polymers (Adapted from reference 54).

1.4.1.1. SIDE-CHAIN FUNCTIONALIZED FULLERENE POLYMERS

These are another class of functionalized fullerene polymers in which cross-linking unit is attached at the side chain of fullerene unit. From the synthetic viewpoint side-chain fullerene polymers can be easily prepared without affecting core structure of the fullerene. Using available cross-linkable groups from the polymer chemistry, one can construct fullerene polymers under known curing conditions. The fullerene polymers synthesized in this manner not only find application in organic photovoltaics as an active layer acceptor component but also be used *in situ* as cross-linkable electron transport layer. One of the earliest demonstrations of an efficient cross-linking of functionalized **PCBM** is by Martin Drees *et al.* They have reported mono-functionalization of PCBG with epoxy moiety which could be cross-linked upon thermal annealing at 120 ^{o}C for 5 min in solid state (Figure 1.10a).[56] While the **PCBM** has phase

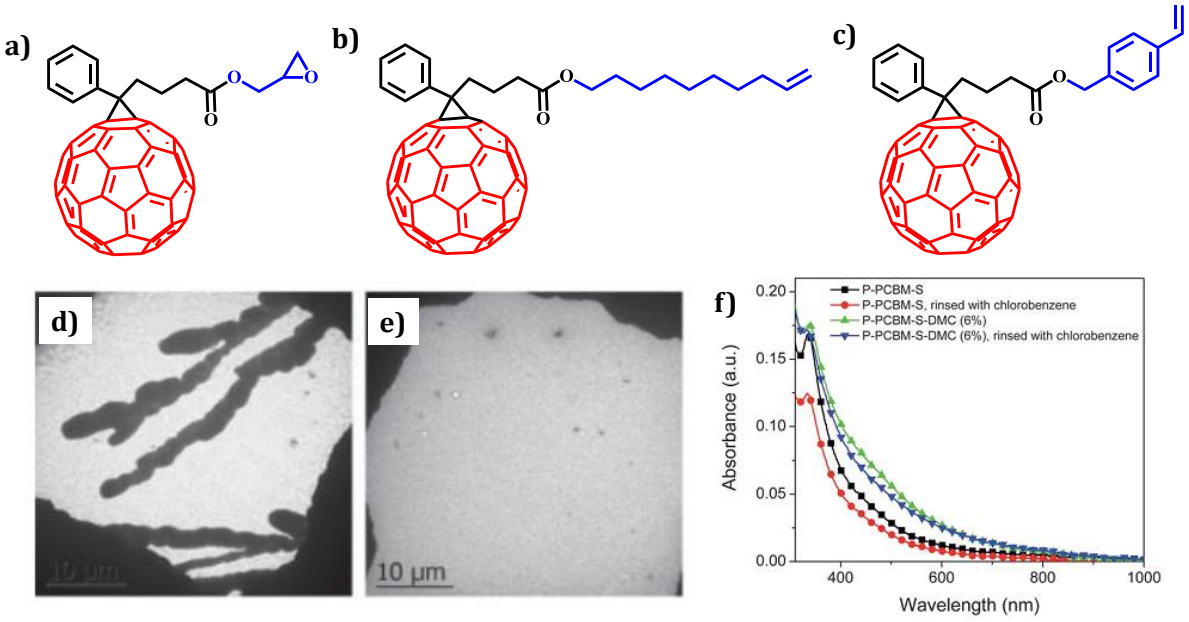

Figure 1.10. a) Crosslinkable fullerene derivatives bearing a) epoxy, b) alkene and c) styrene functionalities; TEM images of d) **P3HT**: **PCBM** and e) **P3HT**: PCBG film both annealed at 140 °C for 1 h (Adapted from reference 56); f) Absorption spectra of the undoped and DMC doped P-**PCBM**-S polymer films on glass substrate before and after washing with chorobenzene (Adapted from reference 58).

separated into large crystals, the **PCBG** does not show any large scale phase separation (Figure 1.10d). It can also be cross linked under similar thermal conditions in solution using Lewis acid tris(pentafluorophenyl)borane. Even though the polymerisation was incomplete, partial polymerisation was enough to form robust network structures so as to stop the diffusion of unreacted molecules. But, incomplete polymerisation was resulted in degradation of the device performance upon thermal treatment. Yiwang Chen *et al.* recently reported alkenyl functionalized fullerenes (**PCBD**, Figure 1.10b), which cross-link with unsaturated bonds of the polymer used (**PBDTTT**) at a temperature of 150°C for 2h.[57] It was successfully applied in **BHJ-PSCs** and demonstrated the stability of the morphology in comparison with the standard

PBDTTT: **PCBM**. Alex K. Y. Jen *et al.* developed styrene modified fullerene derivative (**PCBM**-S, Figure 1.10c), which can be cross linkable upon thermal treatment at 200°C for 30 min.[58] After the deposition of **PCBM**-S film from solution, the styryl groups of **PCBM**-S were polymerized by post-thermal treatment to form a robust film which is resistive to common organic solvents (Figure 1.10f). Additionally, the **PCBM**-S was n-doped with decamethylcobaltocene (**DMC**) to increase the conductivity of the film, which resulted in a significant improvement of the efficiency from 1.24% to 2.33%. Therefore, this approach opens up a viable strategy by substituting possible polymerizable units to **PCBM** for improved stabilities and solar cell performance.

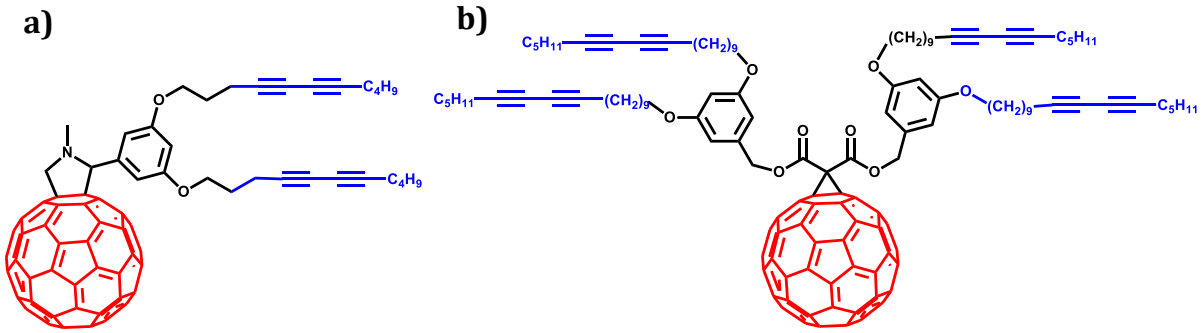

Figure 1.11. Chemical structure of a) diacetylene and b) tetraactylene functionalized fullerene derivatives.

Inorder to attain complete cross-linking and reduce the thermal cross-linking temperature, side-chain fullerene polymers with multiple cross-linkable moieties have been developed. Denis E. Markov *et al.* first demonstrated the utilization of diacetylenic moieties in cross-linking.[59] Fulleropyrrolidine derivative containing two diacetylenic moieties (Figure 1.11a) was reported which could be cross-linked by heating at 175°C for 2-3 h.[60] They have employed these molecules in studying exciton diffusion and photoluminescence quenching in *p*-phenylenevinylene (**PPV**) based conjugated

polymer heterostructures. Substitution of four diacetylenic units (Figure 1.11b) resulted in dramatic reduction in cross-linking temperature to 100 ^{o}C for 2 hours. Chain-Shu Hsu *et al.* reported easily polymerizable fullerene derivative, bis(2-(trichlorosilyl)propyl)malonate C_{60} (**TSMC**) by attaching two trichlorosilane groups via platinum catalyzed olefin hydrosilylation (Figure 1.12a).[61] Cross-linking was performed by hydrolysis of silyl groups without the aid of photoirradiation or post-thermal treatments. The rapid formation of self-assembled and cross-linked TSMC (**SA-C-TSMC**) effectively passivates the residual hydroxyl groups on the TiO_2 surface. The spin coating deposition of **TSMC** led to the cross-linking reaction of trichlorosilane group with hydroxyl group of TiO_2 surface (Figure 1.12b). The moisture exposure after the deposition experienced intermolecular cross-linking creating multilayered **SA-C-TSMC** (Figure 1.12c). The inverted device prepared using this TSMC interfacial layer outperformed (PCE = 3.9%, **P3HT**:$PC_{61}BM$) in comparison to the one without the interfacial layer (PCE = 3.2%, **P3HT**:$PC_{61}BM$).

Cross-linkable fullerenes were also used for other applications. Eiichi Nakamura *et al.* extended the idea of UV cross-linking approach to stabilize the resultant nanostructures formed through fullerene self-assembly.[62] The bilayer vesicle made of pentasubstituted C_{60}-fullerene anions was photocross-linked under aerobic conditions.[63] The cross-linked bilayer became water-tight due to the suppression in the phase transition of the bilayer which reduced the speed of water permeation through the bilayer. These cross-linked fullerenes can be used in creating stable water repellent materials. Self-assembled microparticles of three diacetylenic moieties substituted

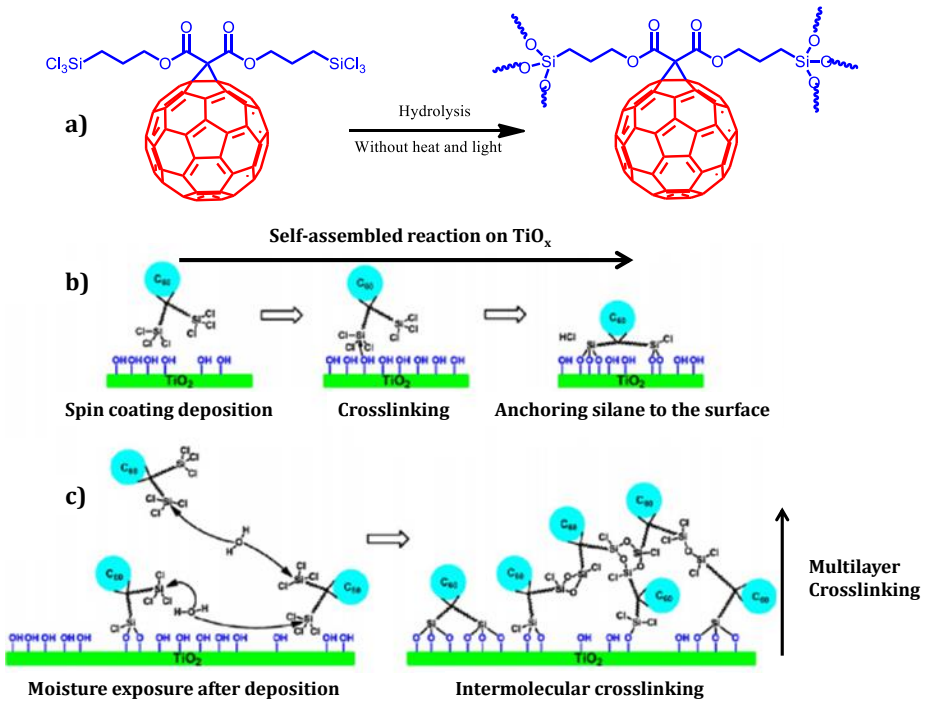

Figure 1.12. a) Chemical structure of TSMC and hydrolysis reaction. Possible mechanism of b) self-assembled monolayer formation and c) multilayer cross-linking through hydrolysis of disilyl moieties above TiO_2 surface (Adapted from reference 61).

fulleropyrrolidine can be stabilized by UV treatment upon heating at 200 ^{o}C for 12 h.[62] Along with remarkable resistivity to various organic solvents, aqueous, acidic or basic media, the structures also exhibited water repellent properties. These examples demonstrate the application of cross-linkable fullerenes in material science other than constructing the stable BHJ active layer nanostructures.

1.4.1.2. MAIN-CHAIN FUNCTIONALIZED FULLERENE POLYMERS

Main chain polyfullerenes are fullerene polymers in which fullerene itself is included in the backbone of the polymer.[64] Since, almost all available polymerizable groups have been successfully attached to fullerene or fulleropyrrolidine, there is a need to change the strategy to develop new C_{60} polymeric material. The only available

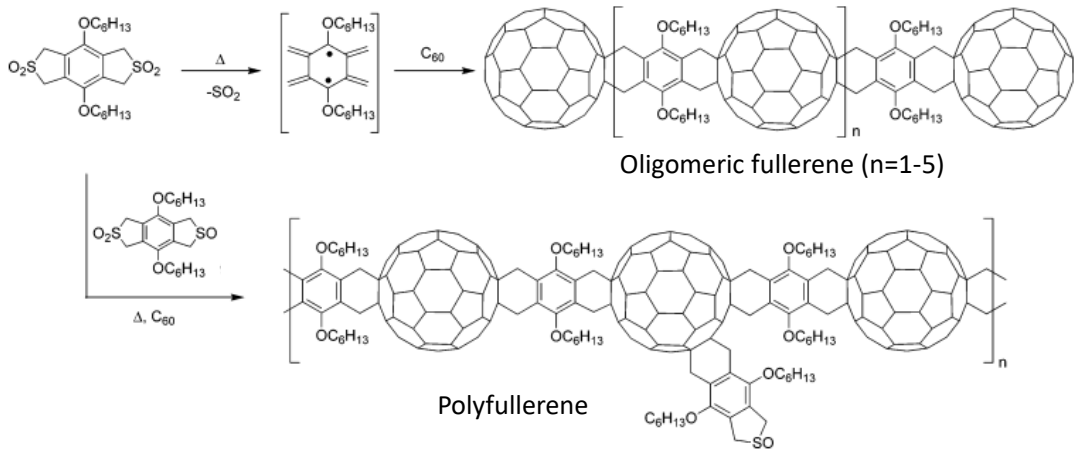

Figure 1.13: Schematic representation of main chain oligomeric fullerenes and polyfullerenes constructed from bis-sulfone reaction (Adapted from reference 65).

chemistry other than covalent functionalization is externally adding polymerization inducing groups. Two possible synthetic strategies to prepare main-chain polymers are: (i) direct reaction between bis-functionalized monomer and the fullerene unit and (ii) Condensation reaction between fullerene bisadduct and bis-functionalized monomer. Taki *et al.* in 1997 prepared first main-chain fullerene polymers in which the mixture of C_{60} bisphenol and 1:1 equivalent of dibasic acid dichloride at room temperature were reacted (figure 1.13).[65] To obtain linear polyfullerenes, sebacoyl chloride or a 1:1 mixture of isophthaloyl chloride/terephthaloyl chloride was used. Although, the oligomeric fullerenes had good solubility in DMF, their low molecular weight (4000-6000 Da) limits further applications. Bis-sulfone with C_{60} were also attempted to obtain oligomeric mixture. Further reaction to increase the molecular weight of the oligomer by additional bis-sulfones failed due to undesired cross-linking. So, the mixture of bis-sulfone/monosulfone was used to afford linear polyfullerene with enhanced solubility. Jang J. *et al.* used chemistry of acrylate polymerisation to improve the performance of

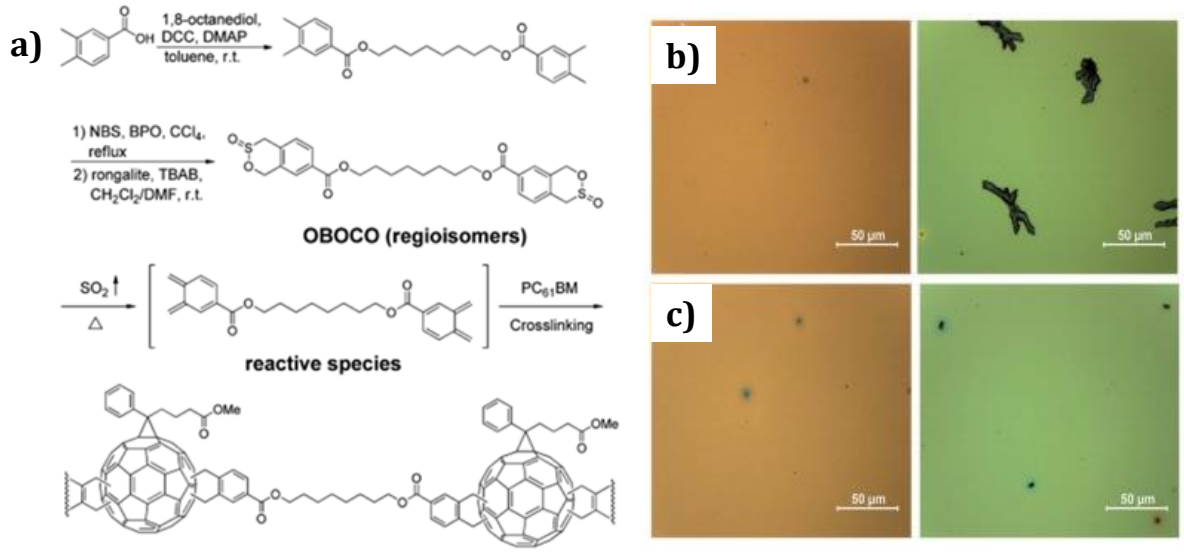

Figure 1.14. a) Synthesis of octane-1,8-diyl bis(1,4-dihydrobenzo[d][1,2]oxathiine-6-carboxylate 3-oxide) (OBOCO) and the scheme for the crosslinking reaction; Optical microscopy images of the active layer **P3HT**/$PC_{61}BM$ b) without and with c) 5% OBOCO before (left) and after (right) heating at 150 ^{o}C aged for 100 h (Adapted from reference 66).

PSC through the self-organisation of the **P3HT** and $PC_{71}BM$ using photocurable cross-linker along with photoinitiator.[66] The photo-curable cross-linker at different ratio from 1% to 5% was added in the active layer to change the surface morphology of the BHJ organic solar cell. Cross linking produced 11% improvement in the performance compared to the control device. Liming Ding *et al.* reported a cross-linker, octane-1,8-diyl-bis(1,4-dihydrobenzo[d] [1,2]oxathiine-6-carboxylate-3-oxide) (**OBOCO**) which can cure **PCBM** through a heat-triggered Diels–Alder reaction and suppress the aggregation tendency of fullerene molecules (Figure 1.14).[67] These examples provide rational strategy used in the construction of main-chain polymers to achieve stable nanostructures. However, the polyfullerene prepared through main-chain polymerisation methods led to structural distortions of fullerene core, and hence alter

the basic fullerene charge transport properties. Therefore, a clever design involves the post functionalization of polymer backbone keeping fullerene structure and properties intact.

1.4.1.3. POLYMER GRAFTED PENDANT FULLERENES

This is an extended form of side-chain functionalized fullerene polymers in which the presynthesized polymer was specifically functionalized with fullerene units. The resultant polyfullerene contains pendant fullerene with large polymer backbone. Steven Holdcroft *et al.* reported first covalent functionalization of **PCBM** with polymer. In this work, a series of postfunctionalized **P3HT** copolymers bearing azide moiety with low graft-chain density (1%) was studied (figure 1.15a).[68] These polymers were blended with **PCBM** and the resultant heat triggered cycloaddition reaction between the azide and **PCBM** was used to stabilize the bicontinuous D-A network. The optical

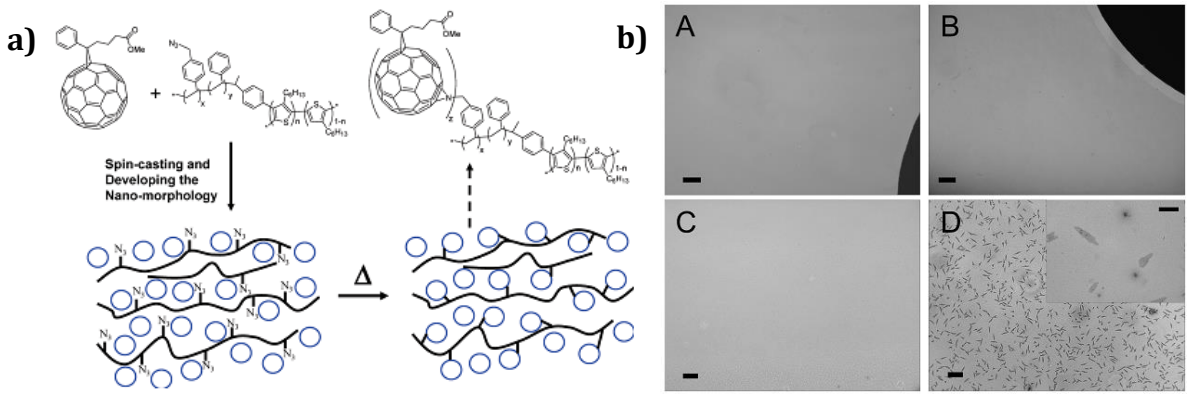

Figure 1.15. a) Solid state reaction of **PCBM** with azide-functionalized conjugated polymer and schematic representation of mechanism involved. b) Optical micrographs of (A, B) polyfullerene/**PCBM** blend (50:50) and (C, D) **P3HT**/**PCBM** (50:50) blend before (left) and after (right) thermal treatment (1 h at 150 °C). Scale bar = 100 μm. The inset in D shows an expanded view (scale bar, 8μm) (Adapted from reference 68).

microscopy studies clearly indicate micrometer scale crystallites of fullerene for **P3HT**:**PCBM** blends (Figure 1.15A and 1.15B) whereas polyfullerene/**PCBM** blend prevented such crystallite formation (Figure 1.15C and 1.15D). However, this strategy did not suppress degradation completely which indicates the presence of other degradation pathways.

Well-defined, controlled fullerene attached poly(3-alkylthiophene) based copolymers was also achieved using the radical polymerization (Figure 1.16a)[69] and azide–alkyne click chemistry (Figure 1.16b).[70] These diblock copolymers have crystalline structures similar to **P3HT** and self-assemble into nanopatterned structure as shown in Figure 1.16c and 1.16d, respectively. As a result, the photovoltaic

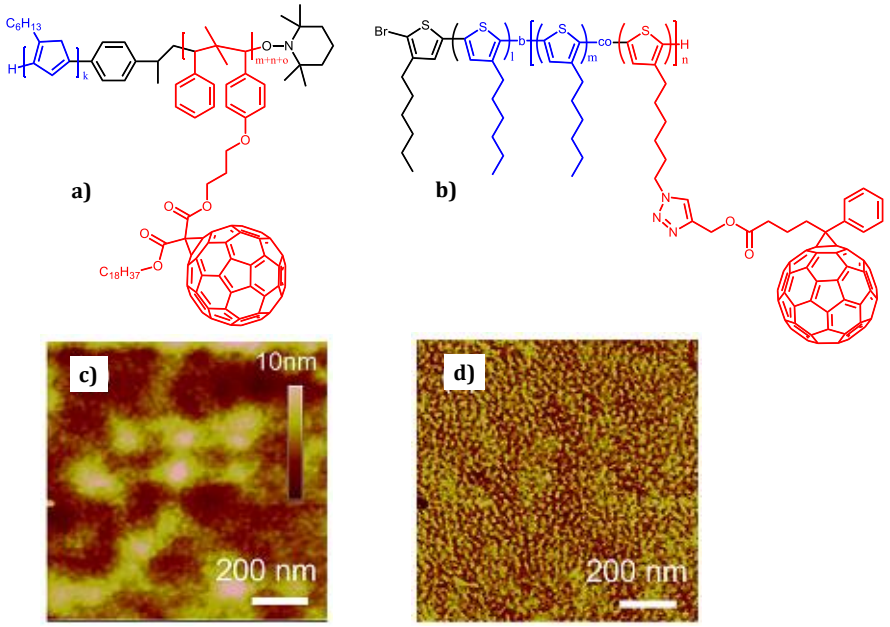

Figure 1.16. Chemical structure of **P3HT** linked C_{60} block copolymer obtained through a) radical polymerization (Adapted from reference 69) and b) azide–alkyne click chemistry (Adapted from reference 70); (c-d) The respective AFM images.

performance of diblock copolymer showed 2.5% **PCE**, higher than the control device. These examples demonstrate that single-component donor–acceptor block polymer design is better rational approach for the active layer BHJ devices than physically mixed polymer blend approach. Later, Bumjoon J. Kim *et al.* developed a simple but powerful approach to achieve solvent-resistant and thermally stable organic electronic devices by introducing a polythiophene with azide groups attached to end of the alkyl chain (**P3HT**-azide, Figure 1.17a).[71] Photo-cross-linking of **P3HT**-azide copolymers

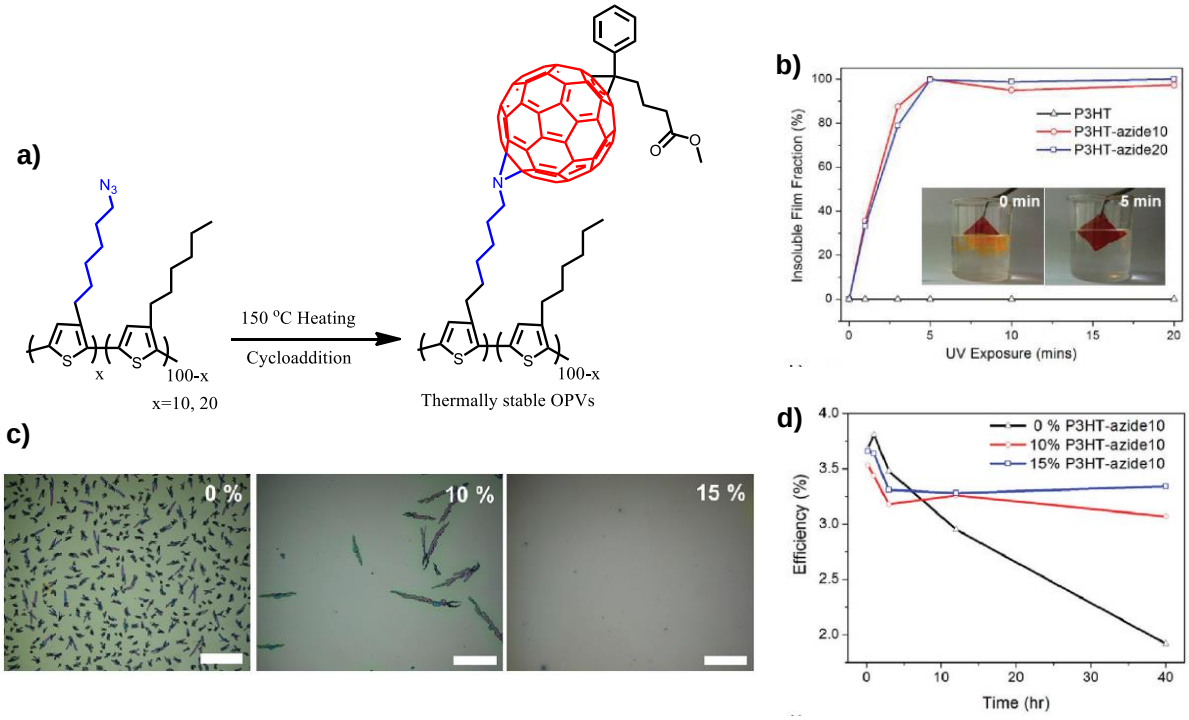

Figure 1.17. a) **P3HT**-azide copolymer forming cycloaddition reaction with **PCBM**; b) Photo-cross-linking behavior of **P3HT**-azide copolymers. The insoluble fraction was measured as a function of UV exposure time. c) Optical microscopy images of the **P3HT/PCBM** films containing 0, 10, or 15% **P3HT**-azide copolymer after annealing at 150°C for 24 h. Scale bar = 100μm; d) Efficiencies of **P3HT/PCBM** devices containing 0, 10, or 15% of **P3HT**-azide10 copolymer during thermal annealing at 150°C with **PCBM** as the electron acceptor (Adapted from reference 71).

dramatically improved the solvent resistance of the active layer without disrupting the molecular ordering and charge transport (Figure 1.17b). This is the first demonstration of solvent-resistant organic transistors using modified polymer-C_{60} derivative. Optical microscopy images of the thermally annealed **P3HT**/**PCBM** films containing 0, 10, or 15% **P3HT**-azide copolymer shows the decrease in the formation of aggregates (Figure 1.17c). Furthermore, the BHJ organic photovoltaics (OPVs) containing **P3HT**-azide copolymers show an average efficiency more than 3.3% after 40 h annealing at an elevated temperature of 150 °C (Figure 1.17d), which represents one of the most thermally stable OPV devices reported so far.

1.4.2. SUPRAMOLECULARLY FUNCTIONALISED FULLERENE POLYMERS

In recent years, the supramolecular chemistry of fullerenes has gathered much attention in developing various dimension-controlled functional nanostructures with tailored properties.[72] Non-covalent interactions play a leading role in determining the secondary and tertiary structure of many natural macromolecules. Out of several publications coming up related to the development of supramolecular architectures one dimensional self-assembly of C_{60} and its derivatives such as nanofibres/nanowires and nanonetworks find significance in optoelectronic applications.[18] Therefore, it is necessary to design and develop new functional C_{60} derivatives in combination with other electronic polymers that would provide efficient polymer blend structures in a cost effective way. In this context, we have listed an overview on some of the efforts to organize the fullerenes in 1D fashion using polymer template, host-guest chemistry and DNA templated assembly for various applications.

1.4.2.1. POLYMER ASSISTED SELF-ASSEMBLY

Although self-assembly of wide variety of polymeric systems have been explored, supramolecular assemblies of fullerene and polymer conjugates are rarely studied. Therefore, it is important to study the self-assembly behaviour of new functional C_{60} derivatives with polymers that would give controlled supramolecular assemblies for optoelectronic applications.[73] Many functional polymer templates have been developed to organize C_{60} through various non-covalent interactions. James J. Watkins *et al.* achieved well-defined nanostructures and improved morphological stability through cooperative self-assembly of conjugated diblock co-polythiophene (**P3HT-b-P3TODT**) and carboxylic acid functionalized fullerenes (**bis-PCBA**).[74] The strong interactions between bis-PCBA and the oligo(ethylene oxide) side chain result in a preferential distribution of the fullerenes within the **P3TODT** domains and lead to nanostructured D/A interpenetrated networks (Figure 1.18a).[75] AFM, TEM and GISAXS studies indicate the lamellar morphology of the blend system (40 wt % loading of **bis-PCBA**) with domain size of 10–20 nm. Moreover, the **P3HT-b-P3TODT/bis-PCBA** blend was stable for extended periods of time at elevated annealing temperatures (150 °C) with no sign of fullerene aggregation.

An interesting amphiphilic assembly approach has been demonstrated by Charvet, Ariga and co-workers in which photoconductive films of domain-segregated nanowires with tailorable dimensions were formed by block copolymer coupled with a hydrophilic porphyrin donor and a hydrophobic C_{60} acceptor as side chains (Figure 1.18b).[76] In this case, irrespective of the substrate used (silicon, mica, glass, or **HOPG**

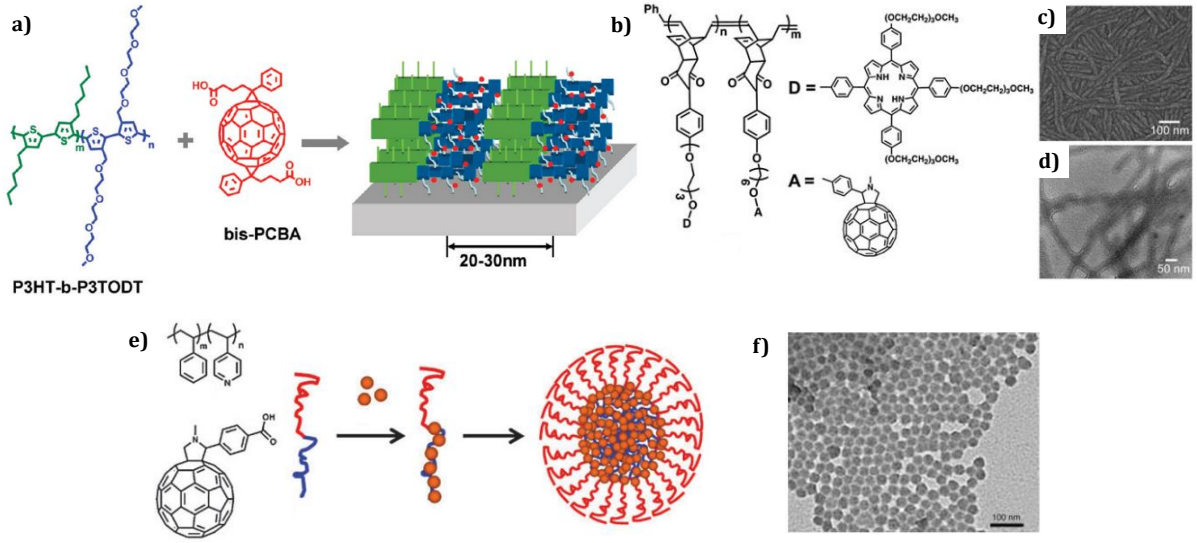

Figure 1.18. a) Chemical structures of **P3HT**-b-P3TODT and bis-PCBA and schematic of the ordered, self-assembled blend that serves as the active layer in the OPV device (Adapted from reference 75). b) The nanowires formed by the polymer containing adjacent porphyrin and fullerene unit with corresponding TEM images upon c) spin-coating or d) drop-casting (Adapted from reference 76). e) Formation of supramolecular rod-coil polymers leading to the generation of **C_{60}** encapsulated micelles and f) corresponding TEM images of micelles (Adapted from reference 77).

surfaces), spin-coating (Figure 1.18c) or drop-casting (Figure 1.18d) of the chloroform solutions resulted in the formation of nanowire-like 1D nanostructure. Seiji Shinkai *et al.* utilized the selective interaction of carboxylic acid to organize C_{60} derivative on polyvinylpyridine (**P4VP**) backbone as shown schematically in Figure 1.18e.[77] These rod–coil diblock copolymers under appropriate conditions led to the construction of self-assembled C_{60}-fullerene nanoparticles with narrow distributions (Figure 1.18f).

Rachel C. Huber *et al*., reported conjugated polyelectrolyte, poly(fluorene-alt-thiophene) (**PFT**) which forms a wedge-shaped monomer facilitating the charged polymer into rod-like micelles (Figure 1.19a).[46] The mixed bis-adduct of C_{60}-*N*,*N*-dimethylpyrrolidinium iodide formed co-assemblies with the **PFT** polyelectrolyte as

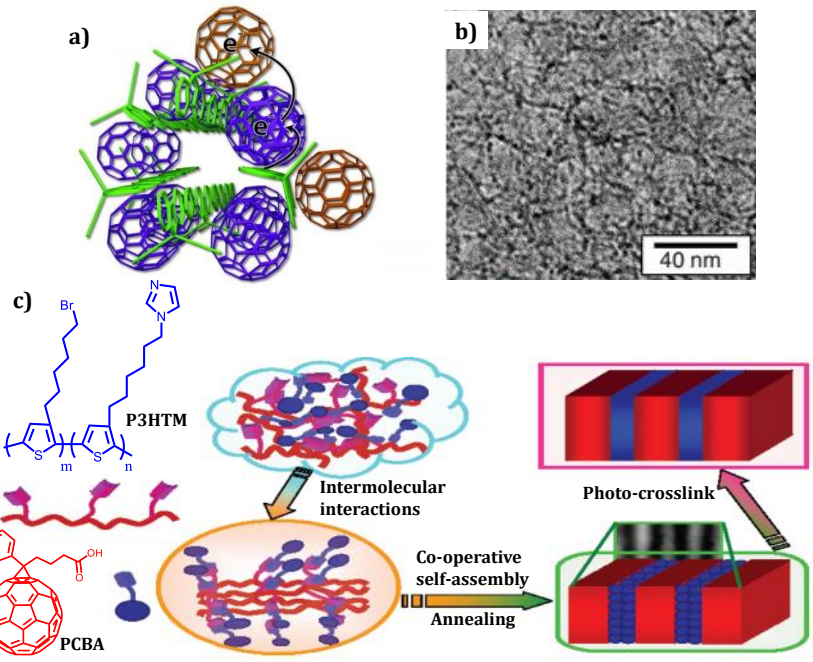

Figure 1.19. a) Schematic representation of mutual self-assembly between poly(fluorene-alt-thiophene) (PFT) and charged fullerene and b) TEM image of PFT: fullerene adduct (Adapted from reference 46). c) Cooperative assembly donor-acceptor system induced by intermolecular hydrogen bonds leading to oriented nanomorphology (Adapted from reference 74).

confirmed by cryogenic electron microscopy studies (Figure 1.19b). Yiwang Chen *et al.* synthesized a new **P3HT** derivative (**P3HTM**) and have demonstrated a simple approach to control the molecular interaction via the intermolecular hydrogen bonds (Figure 1.19c).[74] In the film state, **P3HTM** forms intermolecular O–H···N hydrogen bonds with **PCBA**. The effective organization of semiconductor nanoparticles into ordered nanoarrays was confirmed from TEM analyses. The co-assembled nanostructures of **P3HTM: PCBA** donor/acceptor could be cross-linked by photoirradiation which provides more effective charge-transfer pathways (Scheme and Figure 1.19c).

1.4.2.2 HOST GUEST INDUCED SELF-ASSEMBLY

It is well known that cyclodextrin (CD) and C_{60} has strong affinity to each other which forms strong host-guest induced self-assembly. Guowang Diao and coworkers used physical mixing of γ-cyclodextrin polymer (Figure 1.20a) and C_{60}-fullerene (Figure 1.20b) to achieve inclusion complex of C_{60} with γ-CDP (C_{60}–γ-CDP, Figure 1.20c).[78] The fullerene alone is highly insoluble in water (Figure 1.20d) while inclusion complex showed high solubility (Figure 1.20e). Kurt E. Geckeler *et al.* first demonstrated the possibility of constructing the water soluble polyfullerene based on CD and C_{60}.[79] The synthesis has been achieved by nucleophilic reaction of a *p*-phenylenediamine supramolecularly shielded in a cyclodextrin cavity with fullerene, leading to a versatile new main-chain fullerene polymer (Figure 1.20f). Janarthanan J. and co-workers reported the formation of water-soluble unidirectional C_{60}–porphyrin nanorods using β-cyclodextrin (β-CD) functionalized octadentate tetraphenylporphyrin and pristine C_{60} in a DMF–toluene mixture, utilizing the ability of the β-CD cavity to encapsulate

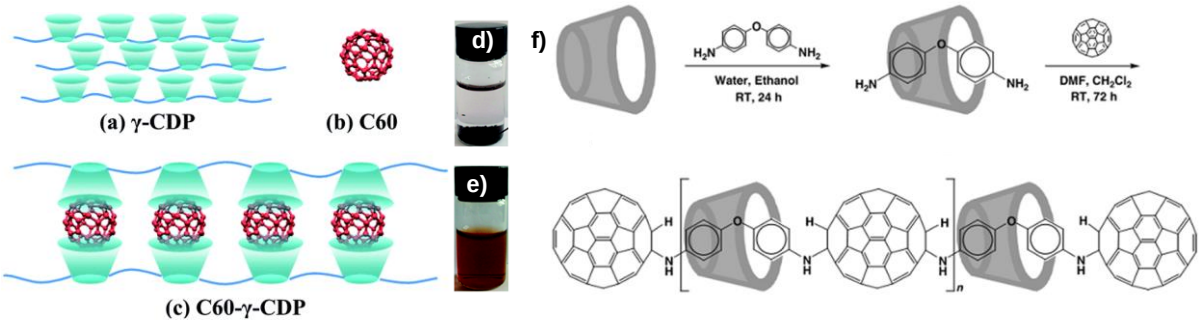

Figure 1.20. Schematic illustration of (a) γ-cyclodextrin polymer (γ-CDP), (b) C_{60}, and (c) C_{60}–γ-CDP inclusion complex; Photograph of d) C_{60} and e) C_{60}–γ-CDP in water (Adapted from reference 78); f) Reaction scheme for the synthesis of water-soluble CD based polyfullerene (Adapted from reference 79).

one C_{60} molecule (Figure 1.21a).[80] The TEM and STM image of the aqueous assembly revealed the presence of several unidirectional structures with 300 nm to 500 nm length and the long axes of the resulting nanorods are formed by the inclusion complexation of approximately 150–250 units of the porphyrin–C_{60} co-assembly (Figure 1.21b and 121c). Eiji Yashima *et al.* reported a thermally reversible physical gel in aromatic solvents such as toluene based on *st*-PMMA chains and C_{60} in which the PMMA adopt a helix of 74 units per 4 turns (74/4 helix) with a sufficiently large cavity of about 1 nm (Figure 1.21d).[81] Hence, fullerenes of specific sizes might be encapsulated in the helical cavity of the *st*-PMMA to form ordered 1D fullerene arrays (Figure 1.21e). This *st*-PMMA can encapsulate fullerenes to mimic the behaviour of CNTs to some extent. Unlike the latter, the fullerene encapsulated *st*-PMMA is easy to prepare, inexpensive and processable. In another approach, Nazario Martin and coworkers explored the host-guest self-assembly using fullerene derivative conjugated with extended tetrathiofulvalene, **ex-TTF** (Figure 1.21f).[82] They have described a donor–acceptor supramolecular polymer based on the guest association of a C_{60} derivative by an **ex-TTF** macrocyclic receptor (Figure 1.21g).[83] By introducing pre-organization in the **ex-TTF** host part of the monomer, they could obtain a very remarkable degree of polymerization reaching estimated MW>150 kDa in solution with upto 90 kDa measured experimentally in the gas phase. This degree of polymerization is well above any other fullerene-based supramolecular polymer reported to date. Mihaiela C. Stuparu reported a new class of fullerene C_{60} hosts based on corranulene polymers by careful design of the molecular structure of the repeat unit through host-guest

interaction between the polymer unit and the C_{60} molecule (Figure 1.21h).[82] These hosts were synthesized by free-radical polymerization. They constructed hosts with various chemical compositions and architectures by appropriate design of the monomer receptor (Figure 1.21i). Eventhough, host-guest self-assembly is highly beneficial to self-organize the C_{60} derivative in controlled fashion, their applications were not much explored.

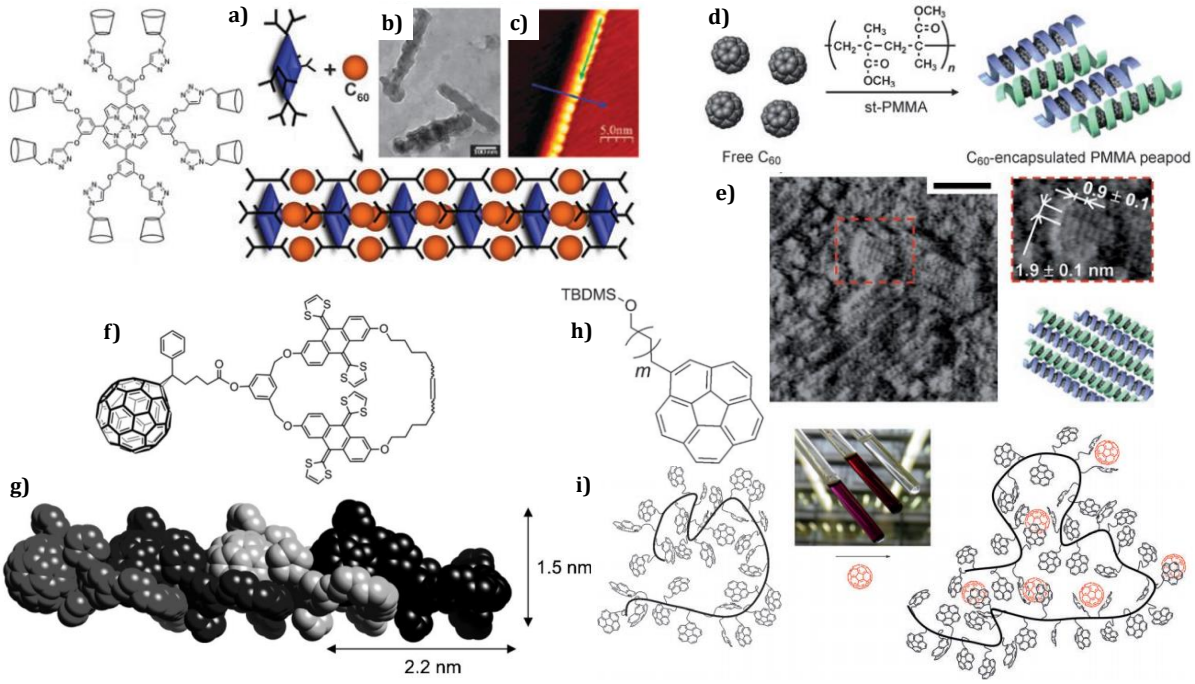

Figure 1.21. a) The mode of complexation of pristine C_{60} by β-CD carrying porphyrin (Inset shows b) TEM and c) STM micrographs of the assembly (Adapted from reference 80); d) C_{60} encapsulated helical PMMA polymer, e) corresponding TEM images (Adapted from reference 81); f) Chemical structure of fullerene conjugated exTTF, g) Supramolecular polymer formed between C_{60} and exTTF units (Adapted from reference 83); h) Chemical structure of the corranulene precursor used, i) Host-guest complexation between corranulene polymer and C_{60} (Adapted from reference 82).

1.4.2.3. DNA TEMPLATED SELF-ASSEMBLY

Construction of predefined unnatural molecular architectures beyond 25 nm length is challenging.[84] The double helical DNA is particularly well-suited for molecular scaffold purpose due to its programmable self-assembly with various molecules through non-covalent interactions.[85] The primary structure of DNA has a string of nucleosides each joined to its two neighbours through phosphodiester linkages as shown in Figure 1.22A. DNA secondary structure consists of two chains which run in anti-parallel directions and are coiled around each other to form a double helix. These two chains are linked together by a large number of weak hydrogen bonds between the complementary bases (Figure 1.22B). The double helical structure of DNA is stabilized by hydrogen bonding between the complementary base pairs (adenine-thymine and guanine-cytosine) and also by hydrophobic interactions between the stacked bases.

DNA (B-form) secondary structure possesses a variety of sites for the ligands to interact including the sugar-phosphate backbone, the central base core and the major/minor grooves which is schematically represented in Figure 1.22C. Ligands bind with DNA through number of modes of interactions such as electrostatic, groove binding and intercalative interactions. For example, alkali metal ions and surfactants are electrostatically attracted to the phosphate backbone of DNA and prefer electrostatic binding,[86] whereas planar aromatic heterocyclic compounds prefer intercalative binding interactions with DNA due to the hydrophobic interior of the double helix.[87]

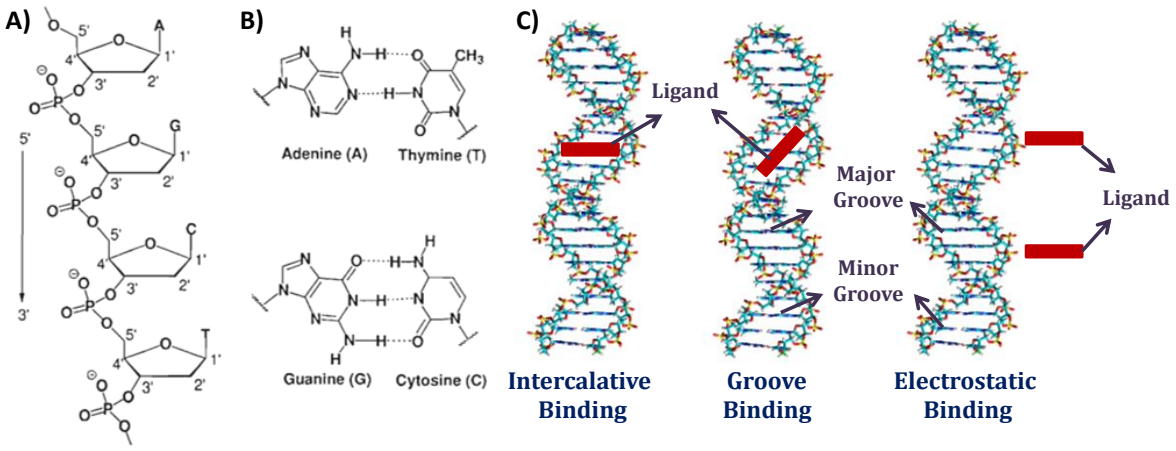

Figure 1.22. A) Schematic representation of the primary structure of DNA and B) Watson-Crick base pairing of adenine-thymine (A-T) and guanine-cytosine (G-C); C) Illustration of electrostatic, intercalative and groove binding of small molecules to the DNA double helix.

Most of the studies involving DNA self-assembly have focused on the complementary oligonucleotide interactions, covalent or noncovalent functionalization of specific nucleotides with desired chromophore. Various small organic moleucles such as naphthalene, aniline, pyrenes, Nile red and porphyrins were assembled with DNA thorough various noncovalent interactions.[88] Moreover, DNA has been successfully used as a template for organizing metal ions, clusters, nanoparticles and polymers into controlled supramolecular nanostructures.[89-91] Assembly of molecules which bind grooves of DNA and interact with the backbone through electrostatic, weak hydrogen bonding and Van der Waals interactions are less explored. Alan M. Cassell *et al.* has studied the assembly of a cationic fullerene derivative, C_{60}–*N,N*-dimethylpyrrolidinium iodide (Figure 1.23a) on DNA through electrostatic interactions by TEM analysis.[92]

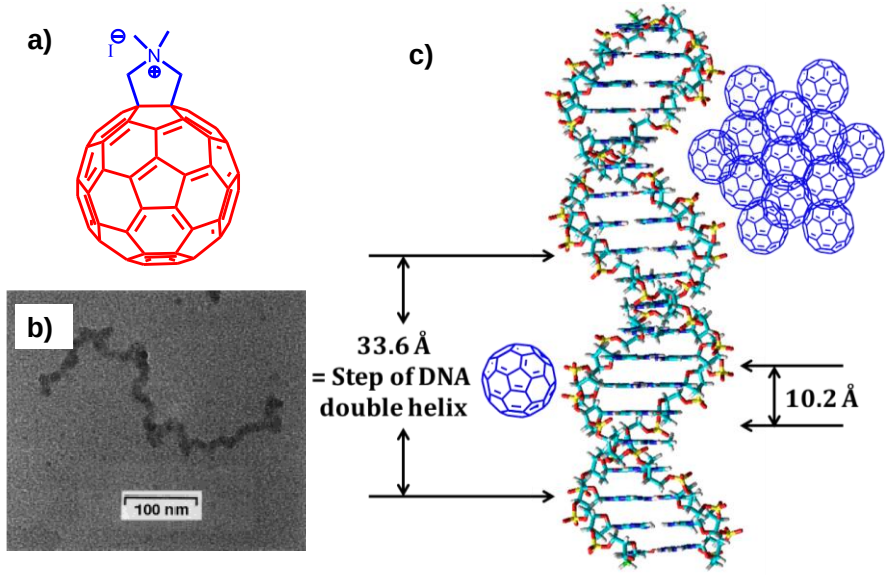

Figure 1.23. a) The structure of the fullerene derivative used in the assembly of DNA/Fullerene hybrid materials and b) the TEM image of DNA templated fullerenes (Adapted from reference 92) and c) Schematic representation showing the size of fullerene matching with the height of DNA stack consisting of three nucleobases.

They studied effective interaction between DNA and fullerene leading to DNA supercoiling which can be relieved by adding a non-ionic surfactant (Figure 1.23b). The diameter of fullerene is ~1 nm, which is equal to the length span of three base pairs on DNA and one helical pitch of DNA (3.4 nm) can accommodate almost three fullerene units, or a cluster of fullerene containing 12-14 fullerenes as shown in Figure 1.23c. Recently, the groove binding nature of triazine functionalised cationic fullerene and pentaamino-C_{60}-fullerene were also reported.[93] Later, Cheng Song *et al.* demonstrated the templated assembly of fullerene derivative using DNA Scaffolds as shown schematically in Figure 1.24a.[94] For this purpose, the periodic distance (64 nm) of the parallel strips in DNA lattices were used for the selective docking of water dispersed fullerene vesicles. The resultant nanostructures were compared using AFM images. By

incubating the fullerene vesicle and a 2D DNA lattice bearing a phosphate-labelled protruded strand together (Figure 1.24b), pearl-like arrays of fullerene domains were obtained on the DNA template (Figure 1.24c). Therefore, phosphated oligonucleotide plays a role in the alignment of fullerene vesicles. These results show the possibility of constructing one dimensional array of fullerene by using suitable DNA. Also, the nanostructure formed can be stabilized by using 2+2 cycloaddition reaction of fullerene.[95] Therefore, in future DNA might find crucial role in developing stable morphology required for various material science and nanotechnology applications.

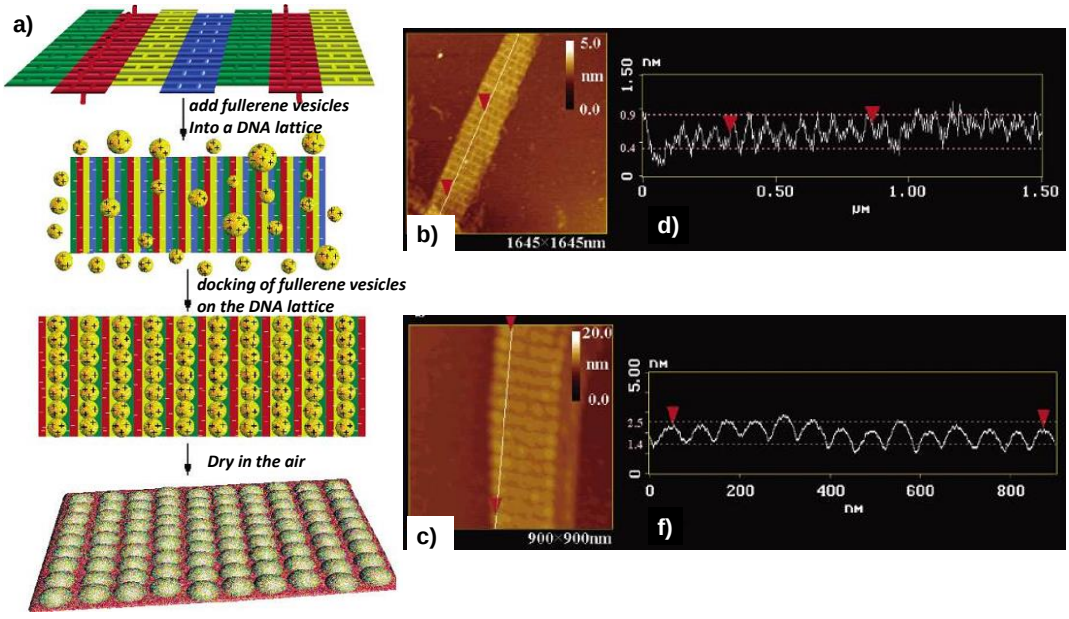

Figure 1.24. a) Sketch of the self-assembly procedure of fullerene vesicles on the 2D DNA scaffolding. Topographical AFM images of the b) DNA scaffolding and c) fullerene arrays in the DNA lattice (Adapted from reference 94).

1.5. OBJECTIVES OF THE PRESENT INVESTIGATION

Implementing the chemistry of fullerenes into macromolecular chemistry has allowed the preparation of new polymer materials exhibiting outstanding structural, electrochemical and photophysical properties that might find application in various fields. The so-called "cross-linkable" approach is an elegant and realistic concept for the preparation of *in situ* fullerene polymers for photovoltaic applications. In the present work our objective was to investigate the different strategies to develop novel fullerene containing polymers, either covalently or supramolecularly and study their photophysical, morphological behaviour towards optoelectronic applications. For this purpose, our strategy was to functionalize the parental **PCBM** derivative with cross-linkable groups in such a way that the core electrochemical and photophysical properties of the resultant derivative will not be perturbed. Cross-linking groups namely Benzoxazine and aniline were chosen so that they can be polymerised under the stimuli such as heat and oxidative conditions, respectively. The benzoxazine moiety was chosen mainly because it causes the resultant polymer resistive towards various fullerene solvents used in device fabrication. This property is very much necessary in order to be used in inverted PSCs as electron transport layers. It prevents the structural imperfections due to solvent penetration during the degradation of subsequent layers. Secondly, ever since the discovery of **PCBM** and the architecture of **BHJ PSC**, the most favorable choice for the acceptor part in the active layer remained to be the monomeric fullerene. It is reported that the polymeric donor tend to self-assemble into one dimensional nanofibre and fullerene in the active layer aggregate into microcrystals

with time. In this context, our design strategy was to synthesize polymeric fullerene which can organize in one dimensional fashion and study their photophysical, and morphological behaviour with polymer donor, **P3HT**. The aniline appended fullerene derivative was synthesized through $FeCl_3$ mediated oxidative polymerization. The polymeric fullerene has a better tendency to form one dimensional nanostructure which intern can give rise to interpenetrating network structure with polymer donor. This strategy of using polymer donor-polymer acceptor could be one of the better architectures than the conventional one.

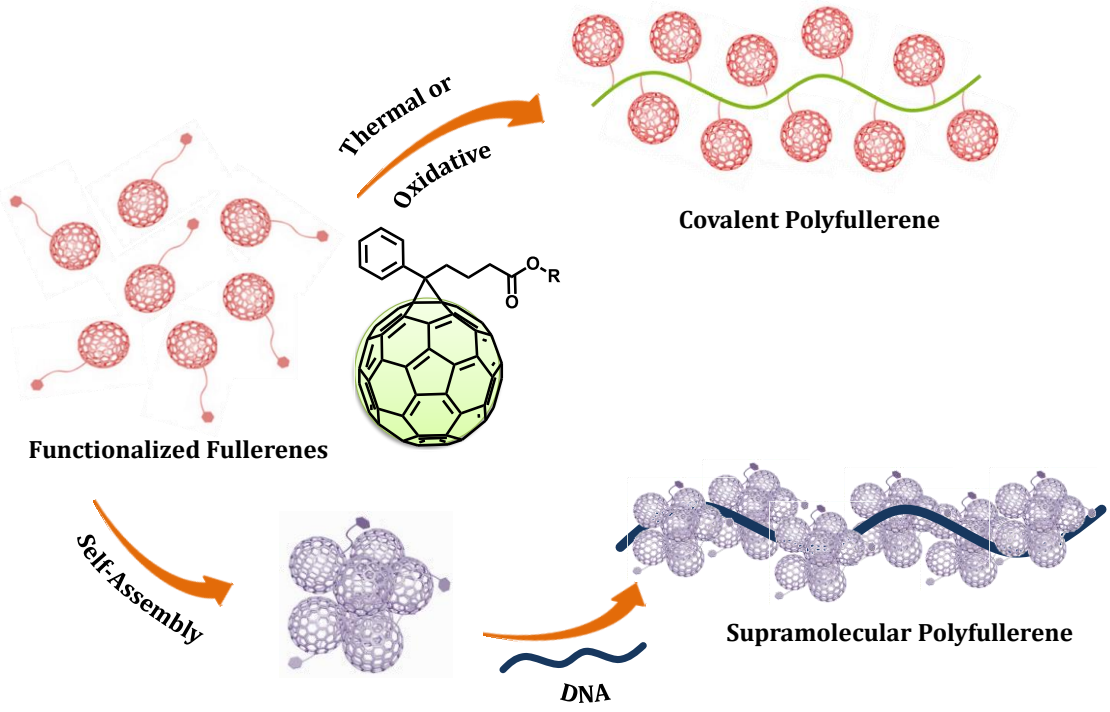

Figure 1.25. Schematic representation of functionalized fullerenes and the strategy used for the polymerisation.

Programmable, hierarchical assembly of DNA nanostructures with precise organisation of functional components have been demonstrated previously with tiled assembly and DNA origami. However, building organised nanostructures with random

oligonucleotide strands remains as an elusive problem. In this context, three monosubstituted fullerene derivatives having pyridinium, aniline or phenothiazine end groups were synthesized and their differential interaction with calf thymus DNA (CT-DNA) was probed via spectroscopic and imaging techniques. Further, we describe a simple and general strategy in which unique nanoclusters of a fullerene derivative act as stapler motifs in bringing ordered nanoscale assembly of short oligonucleotide duplexes and DNA three way junctions into micrometer-sized nanofibres, nanosheets and nanonetwork respectively. Moreover, the horizontal conductivity measurements using c-AFM confirmed the charge transport properties of these nanowires. The silver nanoclusters (AgNCs) templated over 3WJ-overhang/**F-An** nano-construct exhibited 40% fluorescence enhancement compared to that of 3WJ-OH. We also demonstrate that the optimum cluster size, availability of DNA anchoring motifs and the nature of the DNA strands control the structure of these nanomaterials. Thus the present thesis discusses the rational design of functionalized fullerenes and investigation of various polymerisation methods. The self-assembly aspects, application as electron transport layer and active layer component in **BHJ-PSC** was studied in detail. Finally, the self-assembly properties of functional fullerene derivative with CT-DNA templates, short DNA strands such as dsDNA, 3WJ-DNA and 3WJ-OH into various dimension controlled nanostructures were described.

1.6. REFERENCES

1) Hirsch, A., The era of carbon allotropes. *Nat. Mater.* **2010**, *9*, 868-871.

2) Dobrowolski, J. C.; Mazurek, A. P., C(60) topological isomers: Other carbon allotropes. *J. Phys. Chem. A* **1998**, *102*, 5260-5262.

3) Howard, J. B.; McKinnon, J. T.; Makarovsky, Y.; Lafleur, A. L.; Johnson, M. E., Fullerenes C60 and C70 in flames. *Nature* **1991**, *352*, 139-41.

4) Hsieh, C.-H. H.; Cheng, Y.-J. J.; Li, P.-J. J.; Chen, C.-H. H.; Dubosc, M.; Liang, R.-M. M.; Hsu, C.-S. S., Highly efficient and stable inverted polymer solar cells integrated with a cross-linked fullerene material as an interlayer. *J. Am. Chem. Soc.* **2010**, *132*, 4887-4893.

5) C60: Buckminsterfullerene. *Nature* **1985**, *318*, 162-163.

6) Kratschmer, W.; Lamb, L. D.; Fostiropoulos, K.; Huffman, D. R., Solid C-60 - a New Form of Carbon. *Nature* **1990**, *347*, 354-358.

7) Brenton, A. G. H.; Felicia, A. B.; Ryan, C. H.; Todd, E., Cross-Linked Conjugated Polymer Fibrils: Robust Nanowires from Functional Polythiophene Diblock Copolymers. *Chem. Mater.* **2011**, *23*, 4550-4556.

8) Nierengarten, J.-F.; Setayesh, S., Towards polymerizable fullerene derivatives to stabilize the initially formed phases in bulk-heterojunction solar cells. *New J. Chem.* **2006**, *30*, 313.

9) Nakamura, E.; Isobe, H., Functionalized fullerenes in water. The first 10 years of their chemistry, biology, and nanoscience. *Acc. Chem. Res.* **2003**, *36*, 807-815.

10) Li, W.-S. S.; Yamamoto, Y.; Fukushima, T.; Saeki, A.; Seki, S.; Tagawa, S.; Masunaga, H.; Sasaki, S.; Takata, M.; Aida, T., Amphiphilic molecular design as a rational strategy for tailoring bicontinuous electron donor and acceptor arrays: photoconductive liquid crystalline oligothiophene--C60 dyads. *J. Am. Chem. Soc.* **2008**, *130*, 8886-8887.

11) Matsuo, Y., Tahara, K.., Sawamura, M. and Nakamura, E., Creation of Hoop- and Bowl-Shaped Benzenoid Systems by Selective Detraction of [60]Fullerene Conjugation. [10]Cyclophenacene and Fused Corannulene Derivatives. *J. Am. Chem. Soc.* **2004**, *126*, 87258734.

12) Matsuo, Y., Tahara, K., Morita, K., Matsuo, K. and Nakamura, E., Regioselective Eightfold and Tenfold Additions of a Pyridine-Modified Organocopper Reagent to [60]Fullerene. *Angew. Chem. Int. Ed.* **2007**, *46*, 2844-2847.

13) Matsuo, Y., Kanaizuka, K., Matsuo, K., Zhong, Y-W., Nakae, T., and Nakamura, E., Photocurrent-generating properties of organometallic fullerene molecules on an electrode. *J. Am. Chem. Soc.* **2008**, *130*, 5016-5017.

14) Brabec, C. J., Gowrisanker S., Halls J. J., Laird, D., Jia, S., and Williams, S. P., Polymer-Fullerene Bulk-Heterojunction Solar Cells. *Adv. Mater.* **2009**, *21*, 13231338.

15) Babu, S.; Möhwald, H.; Nakanishi, T., Recent progress in morphology control of supramolecular fullerene assemblies and its applications. *Chem. Soc. Rev.* **2010**, *39*, 4021-4035.

16) Sein, L. T.; Wei, Y.; Duong, T.; Kemmerer, M. D.; Jansen, S. A., Anomalous failure of configuration interaction - Singles (CIS) method in the computation of the electronic states of N,N '-bis(4 '-aminophenyl)-1,4-quinonenediimine. *Int. J. Quantum Chem.* **1999**, *75*, 623-629.

17) He, Y.; Li, Y., Fullerene derivative acceptors for high performance polymer solar cells. *Phys. Chem. Chem. Phys.* **2011**, *13*, 1970-83.

18) Dirk, M. G.; Beatriz, M. I.; Carmen M, A.; Mateusz, W.; Nazario, M., Fullerene for organic electronics. *Chem. Soc. Rev.* **2009**, 1587-1597.

19) Wantz, G., Derue, L., Dautel, O., Rivaton, A., Hudhommed, P., and Dagron-Lartigau, C., Stabilizing polymer-based bulk heterojunction solar cells via crosslinking. *Polym. Int.* **2014**, *63*, 1346-1361.

20) Lai, Y. Y.; Cheng, Y. J.; Hsu, C. S., Applications of functional fullerene materials in polymer solar cells. *Energ. Environ. Sci.* **2014**, *7*, 1866-1883.

21) Heremans, P.; Cheyns, D.; Rand, B. P., Strategies for increasing the efficiency of heterojunction organic solar cells: material selection and device architecture. *Acc. Chem. Res.* **2009**, *42*, 1740-1747.

22) Clarke, T. M.; Durrant, J. R., Charge photogeneration in organic solar cells. *Chem. Rev.* **2010**, *110*, 6736-67.

23) Li, G., Zhu, R., and Yang, Y., Polymer solar cells. *Nat. Photonics* **2012**, *6*, 153-161.

24) Blom, P. W. M.; Mihailetchi, V. D.; Koster, L. J. A.; Markov, D. E., Device Physics of Polymer:Fullerene Bulk Heterojunction Solar Cells. *Adv. Mater.* **2007**, *19*, 1551-1566.

25) Li, Y., Molecular design of photovoltaic materials for polymer solar cells: toward suitable electronic energy levels and broad absorption. *Acc. Chem. Res.* **2012**, *45*, 723-33.

26) Li, C.-Z.; Yip, H.-L.; Jen, A. K. Y., Functional fullerenes for organic photovoltaics. *J. Mater. Chem.* **2012**, *22*, 4161-4177.

27) Kim, H. U.; Kim, J. H.; Kang, H.; Grimsdale, A. C.; Kim, B. J.; Yoon, S. C.; Hwang, D. H., Naphthalene-, anthracene-, and pyrene-substituted fullerene derivatives as electron acceptors in polymer-based solar cells. *ACS Appl. Mater. Interfaces* **2014**, *6*, 20776-85.

28) Zhang, Y.; Yip, H.-L.; Acton, O.; Hau, S. K.; Huang, F.; Jen, A. K. Y., A Simple and Effective Way of Achieving Highly Efficient and Thermally Stable Bulk-Heterojunction Polymer Solar Cells Using Amorphous Fullerene Derivatives as Electron Acceptor. *Chem. Mater.* **2009**, *21*, 2598-2600.

29) Choi, J. H.; Son, K.-I.; Kim, T.; Kim, K.; Ohkubo, K.; Fukuzumi, S., Thienyl-substituted methanofullerene derivatives for organic photovoltaic cells. *J. Mater. Chem.* **2010**, *20*, 475-482.

30) Mikroyannidis, J. A.; Kabanakis, A. N.; Sharma, S. S.; Sharma, G. D., A Simple and Effective Modification of **PCBM** for Use as an Electron Acceptor in Efficient Bulk Heterojunction Solar Cells. *Adv. Funct. Mater.* **2011**, *21*, 746-755.

31) Lenes, M.; Wetzelaer, G.-J. A. H.; Kooistra, F. B.; Veenstra, S. C.; Hummelen, J. C.; Blom, P. W. M., Fullerene Bisadducts for Enhanced Open-Circuit Voltages and Efficiencies in Polymer Solar Cells. *Adv. Mater.* **2008**, *20*, 2116-2119.

32) He, Y.; Chen, H.-Y. Y.; Hou, J.; Li, Y., Indene-C(60) bisadduct: a new acceptor for high-performance polymer solar cells. *J. Am. Chem. Soc.* **2010**, *132*, 1377-1382.

33) Cheng, Y.-J.; Liao, M.-H.; Chang, C.-Y.; Kao, W.-S.; Wu, C.-E.; Hsu, C.-S., Di(4-methylphenyl)methano-C60Bis-Adduct for Efficient and Stable Organic Photovoltaics with Enhanced Open-Circuit Voltage. *Chem. Mater.* **2011**, *23*, 4056-4062.

34) Voroshazi, E.; Vasseur, K.; Aernouts, T.; Heremans, P.; Baumann, A.; Deibel, C.; Xue, X.; Herring, A. J.; Athans, A. J.; Lada, T. A.; Richter, H.; Rand, B. P., Novel bis-C60 derivative compared to other fullerene bis-adducts in high efficiency polymer photovoltaic cells. *J. Mater. Chem.* **2011**, *21*, 17345-17352.

35) Anthony, J. E.; Facchetti, A.; Heeney, M.; Marder, S. R.; Zhan, X., n-Type organic semiconductors in organic electronics. *Adv. Mater.* **2010**, *22*, 3876-92.

36) Mas-Torrent, M.; Rovira, C., Novel small molecules for organic field-effect transistors: towards processability and high performance. *Chem. Soc. Rev.* **2008**, *37*, 827-38.

37) Lee, T. W.; Byun, Y.; Koo, B. W.; Kang, I. N.; Lyu, Y. Y.; Lee, C. H.; Pu, L.; Lee, S. Y., All-Solution-Processed n-Type Organic Transistors Using a Spinning Metal Process. *Adv. Mater.* **2005**, *17*, 2180-2184.

38) Li, C. Z.; Chueh, C. C.; Yip, H. L.; Ding, F.; Li, X.; Jen, A. K., Solution-processible highly conducting fullerenes. *Adv. Mater.* **2013**, *25*, 2457-61.

39) Zhang, J.; Li, C. Z.; Williams, S. T.; Liu, S.; Zhao, T.; Jen, A. K., Crystalline co-assemblies of functional fullerenes in methanol with enhanced charge transport. *J. Am. Chem. Soc.* **2015**, *137*, 2167-70.

40) Tkachenko, N. V.; Lemmetyinen, H.; Sonoda, J.; Ohkubo, K.; Sato, T.; Imahori, H.; Fukuzumi, S., Ultrafast photodynamics of exciplex formation and photoinduced electron transfer in porphyrin-fullerene dyads linked at close proximity. *J. Phys. Chem. A* **2003**, *107*, 8834-8844.

41) D'Souza, F.; Chitta, R.; Gadde, S.; Shafiqul Islam, D. M.; Schumacher, A. L.; Zandler, M. E.; Araki, Y.; Ito, O., Design and Studies on Supramolecular Ferrocene−Porphyrin−Fullerene Constructs for Generating Long-Lived Charge Separated States. *J. Phys. Chem. B* **2006**, *110*, 25240-25250.

42) Ito, O.; D'Souza, F.: *Recent Advances in Photoinduced Electron Transfer Processes of Fullerene-Based Molecular Assemblies and Nanocomposites*, 2012; Vol. 17.

43) Sariciftci, N. S.; Wudl, F.; Heeger, A. J.; Maggini, M.; Scorrano, G.; Prato, M.; Bourassa, J.; Ford, P. C., Photoinduced electron transfer and long lived charge separation in a donor-bridge-acceptor supramolecular 'diad' consisting of ruthenium(II) tris(bipyridine) functionalized C-60. *Chem. Phys. Lett.* **1995**, *247*, 510-514.

44) Thomas, K. G.; Biju, V.; Kamat, P. V.; George, M. V.; Guldi, D. M., Dynamics of photoinduced electron-transfer processes in fullerene-based dyads: effects of varying the donor strength. *ChemPhysChem* **2003**, *4*, 1299-307.

45) Thomas, K. G., Biju, V., Guldi, D. M., Kamat, P. V., and George, M. V., Photoinduced Charge Separation and Stabilization in Clusters of a Fullerene-Aniline Dyad. *J. Phys. Chem. B* **1999**, *103*, 8864-8869.

46) Huber, R. C.; Ferreira, A. S.; Thompson, R.; Kilbride, D.; Knutson, N. S.; Devi, L. S.; Toso, D. B.; Challa, J. R.; Zhou, Z. H.; Rubin, Y.; Schwartz, B. J.; Tolbert, S. H., Long-lived photoinduced polaron formation in conjugated polyelectrolyte-fullerene assemblies. *Science* **2015**, *348*, 1340-1343.

47) Nakanishi, T., Supramolecular soft and hard materials based on self-assembly algorithms of alkyl-conjugated fullerenes. *Chem. Commun.* **2010**, *46*, 3425-36.

48) Nakanishi, T.; Michinobu, T.; Yoshida, K.; Shirahata, N.; Ariga, K.; Möhwald, H.; Kurth, D. G., Nanocarbon Superhydrophobic Surfaces created from Fullerene-Based Hierarchical Supramolecular Assemblies. *Adv. Mater.* **2008**, *20*, 443-446.

49) Nakanishi, T.; Shen, Y.; Wang, J.; Yagai, S.; Funahashi, M.; Kato, T.; Fernandes, P.; Mohwald, H.; Kurth, D. G., Electron transport and electrochemistry of mesomorphic fullerenes with long-range ordered lamellae. *J. Am. Chem. Soc.* **2008**, *130*, 9236-7.

50) Edwardson, T. G. W.; Carneiro, K. M. M.; McLaughlin, C. K.; Serpell, C. J.; Sleiman, H. F., Site-specific positioning of dendritic alkyl chains on DNA cages enables their geometry-dependent self-assembly. *Nat. Chem.* **2013**, *5*, 868-875.

51) Giacalone, F.; Martín, N.; Wudl, F., Fullerene-Containing Polymers: An Overview. *Fullerene Polymers* **2009**.

52) Lara, P.; Ali, N.; Emilie, P.; Christian, C.; Nicole, A.; Lionel, F., Fullerene-based processable polymers as plausible acceptors in photovoltaic applications. *J. Polym. Sci. Pol. Phys.* **2013**, *51*, 291-302.

53) Maeyoshi, Y.; Saeki, A.; Suwa, S.; Omichi, M.; Marui, H.; Asano, A.; Tsukuda, S.; Sugimoto, M.; Kishimura, A.; Kataoka, K.; Seki, S., Fullerene nanowires as a versatile platform for organic electronics. *Sci. Rep.* **2012**, *2*, 1-6.

54) Francesco, G.; Nazario, M., Fullerene Polymers: Synthesis and Properties. *Chem. Rev.* **2006**, *106*, 5136-5190.

55) Carlos, A. Z.; Stephen, B.; Seth, R. M., Approaches to Solution-Processed Multilayer Organic Light-Emitting Diodes Based on Cross-Linking. *Chem. Mater.* **2011**, *23*, 658-681.

56) Martin, D.; Harald, H.; Christoph, W.; Helmut, N.; Niyazi, S. S.; Wolfgang, S.; Friedrich, S.; Christoph, T.; Markus, C. S.; Zhengguo, Z.; Russell, G., Stabilization of the nanomorphology of polymer–fullerene "bulk heterojunction" blends using a novel polymerizable fullerene derivative. *J. Mater. Chem.* **2005**, *15*, 5158-5163.

57) Chen, L., Lia, X., and Chen, Y., Inter-crosslinking through both donor and acceptor with unsaturated bonds for highly efficient and stable organic solar cells. *Poly. Chem.* **2013**, *4*, 5637.

58) Namchul, C.; Hin-Lap, Y.; Steven, K. H.; Kung-Shih, C.; Tae-Wook, K.; Joshua, A. D.; David, F. Z.; Alex, K. Y. J., n-Doping of thermally polymerizable fullerenes as an electron transporting layer for inverted polymer solar cells. *J. Mater. Chem.* **2011**, *21*, 6956-6961.

59) Markov, D. E.; Amsterdam, E.; Blom, P. W.; Sieval, A. B.; Hummelen, J. C., Accurate measurement of the exciton diffusion length in a conjugated polymer using a heterostructure with a side-chain cross-linked fullerene layer. *J. Phys. Chem. A* **2005**, *109*, 5266-74.

60) Towards polymerizable fullerene derivatives to stabilize the initially formed phases in bulk-heterojunction solar cells. *New J. Chem.* **2006**, *30*, 313.

61) Liang, W.-W., Chang, C-U., Lai, Y-Y., Cheng, S-W., Chang, H-H., Lai, Y-Y., Cheng, Y-J., Wang, C-L., and Hsu, C-S., Formation of Nanostructured Fullerene Interlayer through Accelerated Self-Assembly and Cross-Linking of Trichlorosilane Moieties Leading to Enhanced Efficiency of Photovoltaic Cells. *Macromolecules* **2013**, *46*, 4781-4789.

62) Wang, J.; Shen, Y.; Kessel, S.; Fernandes, P.; Yoshida, K.; Yagai, S.; Kurth, D. G.; Möhwald, H.; Nakanishi, T., Self-assembly made durable: water-repellent materials formed by cross-linking fullerene derivatives. *Angew. Chem. Int. Ed.* **2009**, *48*, 2166-2170.

63) Koji, H.; Akimitsu, N.; Eiichi, N., Photocrosslinking of Fullerene Vesicles that Prevents Phase Transition and Decreases Water Permeation. *Chem. Lett.* **2013**, *42*, 1176-1178.

64) Ramanitra, H. H.; Santos Silva, H.; Bregadiolli, B. A.; Khoukh, A.; Combe, C. M. S.; Dowland, S. A.; Bégué, D.; Graeff, C. F. O.; Dagron-Lartigau, C.; Distler, A.; Morse, G.; Hiorns, R. C., Synthesis of Main-Chain Poly(fullerene)s from a Sterically Controlled Azomethine Ylide Cycloaddition Polymerization. *Macromolecules* **2016**, *49*, 1681-1691.

65) Gügel, A.; Belik, P.; Walter, M.; Kraus, A.; Harth, E.; Wagner, M.; Spickermann, J.; Müllen, K., The repetitive Diels-Alder reaction: A new approach to [60]fullerene maindashchain polymers. *Tetrahedron* **1996**, *52*, 5007-5014.

66) Ryu, M. S.; Jang, J., Improvement of conversion efficiency of bulk heterojunction organic solar cells using photo-curable crosslinker. *Sol. Energy Mater. Sol. Cells* **2010**, *94*, 1384-1388.

67) Dan, H.; Xiaoyan, D.; Wei, Z.; Zuo, X.; Liming, D., Improving the stability of **P3HT**/PC61BM solar cells by a thermal crosslinker. *J. Mater. Chem. A* **2013**, *1*, 4589-4594

68) Bobak, G.; Steven, H., Toward Stabilization of Domains in Polymer Bulk Heterojunction Films. *Chem. Mater.* **2010**, *22*, 5371-5376

69) Maria, H.; Hartmut, K.; Tim, E.; Volodymyr, S.; Anton, K.; Brigitte, V., Fullerene-Functionalized Donor–Acceptor Block Copolymers through Etherification as Stabilizers for Bulk Heterojunction Solar Cells. *Macromolecules* **2012**, *45*, 4101-4114

70) Shoji, M.; Yue, Z.; Kazuhito, H.; Keisuke, T., Controlled Synthesis of Fullerene-Attached Poly(3-alkylthiophene)-Based Copolymers for Rational Morphological Design in Polymer Photovoltaic Devices. *Macromolecules* **2012**, *45*, 6424-6437.

71) Hyeong Jun, K.; Han, A. R.; Chul-Hee, C.; Hyunbum, K.; Han-Hee, C.; Moo Yeol, L.; Jean, M. J. F.; Joon Hak, O.; Bumjoon, J. K., Solvent-Resistant Organic Transistors and Thermally Stable Organic Photovoltaics Based on Cross-linkable Conjugated Polymers. *Chem. Mater.* **2012**, *24*, 215-221.

72) Shrestha, L. K.; Ji, Q.; Mori, T.; Miyazawa, K. i.; Yamauchi, Y.; Hill, J. P.; Ariga, K., Fullerene nanoarchitectonics: from zero to higher dimensions. *Chem. Asian J.* **2013**, *8*, 1662-1679.

73) Brady, M. A.; Su, G. M.; Chabinyc, M. L., Recent progress in the morphology of bulk heterojunction photovoltaics. *Soft Matt.* **2011**, *7*, 11065-11077.

74) Kai, Y.; Lie, C.; Fan, L.; Peishan, W.; Yiwang, C., Cooperative Assembly Donor–Acceptor System Induced by Intermolecular Hydrogen Bonds Leading to Oriented Nanomorphology for Optimized Photovoltaic Performance. *J. Phys. Chem. C* **2012**, *116*, 714-721.

75) Ying, L.; Jung Ah, L.; Qingshuo, W.; Stefan, C. B. M.; Alejandro, L. B.; James, J. W., Cooperative Assembly of Hydrogen-Bonded Diblock Copolythiophene/Fullerene Blends for Photovoltaic Devices with Well-Defined Morphologies and Enhanced Stability. *Chem. Mater.* **2012**, *24*, 622-632.

76) Richard, C.; Somobrata, A.; Jonathan, P. H.; Misaho, A.; Meiyong, L.; Shu, S.; Yoshihito, H.; Akinori, S.; Katsuhiko, A., Block-Copolymer-Nanowires with Nanosized Domain Segregation and High Charge Mobilities as Stacked p/n Heterojunction Arrays for Repeatable Photocurrent Switching. *J. Am. Chem. Soc.* **2009**, *131*, 18030-18031.

77) Fujita, N.; Yamashita, T.; Asai, M.; Shinkai, S., Formation of [60]fullerene nanoclusters with controlled size and morphology through the aid of supramolecular rod-coil diblock copolymers. *Angew. Chem. Int. Ed.* **2005**, *44*, 1257-1261.

78) Zhang, W.; Gong, X. D.; Liu, C.; Piao, Y. Z.; Sun, Y.; Diao, G. W., Water-soluble inclusion complex of fullerene with gamma-cyclodextrin polymer for photodynamic therapy. *J. Mat. Chem. B* **2014**, *2*, 5107-5115.

79) Samal, S.; Choi, B. J.; Geckeler, K. E., The first water-soluble main-chain polyfullerene. *Chem. Commun.* **2000**, 1373-1374.

80) Maher, F.; Shao-Chun, L.; Ulrike, D.; Alina, A.; Janarthanan, J., Water-soluble nanorods self-assembled via pristine C60 and porphyrin moieties. *Chem. Commun.* **2009**, 4209-4211.

81) Kawauchi, T.; Kumaki, J.; Kitaura, A.; Okoshi, K.; Kusanagi, H.; Kobayashi, K.; Sugai, T.; Shinohara, H.; Yashima, E., Encapsulation of fullerenes in a helical PMMA cavity leading to a robust processable complex with a macromolecular helicity memory. *Angew. Chem. Int. Ed.* **2008**, *47*, 515-519.

82) Stuparu, M. C., Rationally designed polymer hosts of fullerene. *Angew. Chem. Int. Ed.* **2013**, *52*, 7786-7790.

83) Isla, H.; Perez, E. M.; Martin, N., High degree of polymerization in a fullerene-containing supramolecular polymer. *Angew. Chem. Int. Ed.* **2014**, *53*, 5629-33.

84) Aldaye, F. A.; Palmer, A. L.; Sleiman, H. F., Assembling materials with DNA as the guide. *Science* **2008**, *321*, 1795-1799.

85) Gothelf, K. V.; Brown, R. S., A Modular Approach to DNA-Programmed Self-Assembly of Macromolecular Nanostructures. *Chem. Eur. J.* **2005**, *11*, 1062-1069.

86) Liu, K.; Zheng, L.; Ma, C.; Gostl, R.; Herrmann, A., DNA-surfactant complexes: self-assembly properties and applications. *Chem. Soc. Rev.* **2017**, *46*, 5147-5172.

87) Hannah, K. C.; Armitage, B. A., DNA-templated assembly of helical cyanine dye aggregates: a supramolecular chain polymerization. *Acc. Chem. Res.* **2004**, *37*, 845-853.

88) Malinovskii, V.; Wenger, D.; Häner, R., Nucleic acid-guided assembly of aromatic chromophores. *Chem. Soc. Rev.* **2010**, *39*, 410-422.

89) Buceta, D.; Busto, N.; Barone, G.; Leal, J. M.; Domínguez, F.; Giovanetti, L. J.; Requejo, F. G.; García, B.; López-Quintela, A. M., Ag2 and Ag3 Clusters: Synthesis, Characterization, and Interaction with DNA. *Angew. Chem. Int. Ed.* **2015**, *54*, 7612-7616.

90) Kankia, B. I.; Buckin, V.; Bloomfield, V. A., Hexamminecobalt(III)-induced condensation of calf thymus DNA: circular dichroism and hydration measurements. *Nucleic Acids Res.* **2001**, *29*, 2795-2801.

91) Song, Q.; Shi, Y.; He, D.; Xu, S.; Ouyang, J., Sequence-Dependent dsDNA-Templated Formation of Fluorescent Copper Nanoparticles. *Chem. Eur. J.* **2015**, *21*, 2417-2422.

92) Cassell, A. M.; Scrivens, W. A.; Tour, J. M., Assembly of DNA/fullerene hybrid materials. *Angew. Chem. Int. Ed.* **1998**, *37*, 1528-1531.

93) Manishkumar, B. P.; Uma, H.; Nikunj, N. V.; Deval, S. M.; Kuldeep, V. J.; Sivakumar Prasanth, K.; Kishor, H. C.; Linz Buoy, G.; Yogesh, T. J.; Shobhana, K. M., Novel cationic fullerene derivatized s-triazine scaffolds as photoinduced DNA cleavage agents: design, synthesis, biological evaluation and computational investigation. *Rsc Adv* **2013**, *3*, 8734-8746.

94) Song, C.; Chen, Y. Q.; Xiao, S. J.; Ba, L.; Gu, Z. Z.; Pan, Y.; You, X. Z., Assembly of fullerene arrays templated by DNA scaffolds. *Chem. Mater.* **2005**, *17*, 6521-6524.

95) Sun, Y.-P.; Ma, B.; Bunker, C. E.; Liu, B., All-Carbon Polymers (Polyfullerenes) from Photochemical Reactions of Fullerene Clusters in Room-Temperature Solvent Mixtures. *J. Am. Chem. Soc.* **1995**, *117*, 12705-12711.

CHAPTER 2

A STIMULI RESPONSIVE CROSS-LINKABLE FULLERENE DERIVATIVE: STUDY OF PHOTOPHYSICAL, MORPHOLOGICAL AND PHOTOVOLTAIC PROPERTIES

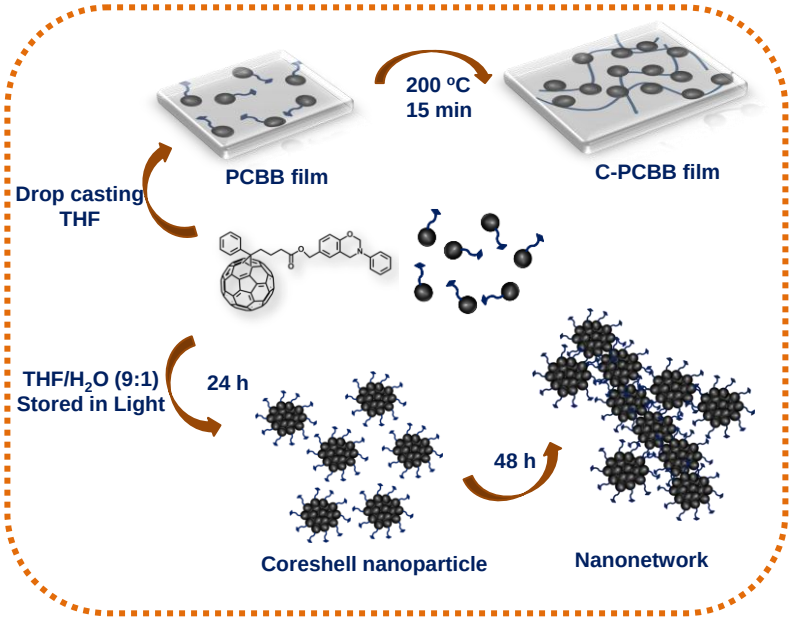

2.1. Abstract

A crosslinkable fullerene derivative, [6,6]-phenyl-C_{61}-butyric benzoxazine ester, ***PCBB*** *having pendant benzoxazine moiety was synthesized, which showed stimuli responsiveness towards light and temperature. The* ***PCBB*** *inherits all the basic photophyscial and electrochemical properties of parental [6, 6]-phenyl-C_{61}-butyric methyl ester (****PCBM****) as evidenced from UV-Visible absorption, square wave voltametry, thermogravimetry and poly(3-hexylthiophene) (****P3HT****) based fluorescence quenching experiments. The heat triggered ring opening polymerisation of benzoxazine moiety in* ***PCBB****, investigated through Differential Scanning Calorimetry (DSC) and Infra-Red*

Sectroscopy (IR) revealed the formation of crosslinked solvent resistive adhesive films upon heating at 200 °C for 15 min. Moreover, Atomic Force Microscopy (AFM) and optical microscopic studies revealed the dramatic reduction in the roughness and aggregation behaviour of ***P3HT***:***PCBM*** *polymer blend film upon incorporation of cross-linked* ***PCBB*** *(****C-PCBB****) interfacial layer. The* ***C-PCBB*** *film as electron transport layer (ETL) enabled the successful deposition of other layers, realizing the all solution processed inverted device. An inverted bulk hetero junction solar cell device based on the configuration ITO/ZnO/****C-PCBB/P3HT****:* ***PCBM****/* V_2O_5*/Ag achieved 4.27% power conversion efficiency (PCE) compared to the reference device ITO/ZnO/****P3HT****:* ***PCBM****/*V_2O_5*/Ag (PCE=3.28%), indicating a 25% enhancement in PCE value. Moreover, under visible light* ***PCBB*** *showed time dependent morphology transformation from core-shell nanoparticle into nanonetwork structure in THF/*H_2O *(9/1, v/v) solvent mixture. This transformation of self-assembled nanostructure is believed to involve the cycloaddition reaction of fullerene as evident from NMR and mass spectral analysis.*

2.2. Introduction

In the recent decades, polymer solar cells (PSCs) received widespread interest in the scientific community due to their potential of fabrication on light weight and flexible material by low cost solution processing techniques.[1-3] Inorder to increase the donor-acceptor interfacial area in the polymer blend for efficient exciton dissociation and charge transport, the concept of bulk heterojunction (BHJ) composing bicontinuous interpenetrating nanonetwork of polymer blend containing p-type donor and n-type acceptor architecture have been adopted.[4] The poly(3-hexylthiophene) (**P3HT**) and

[6,6]-phenyl-C_{61}-butyric acid methyl ester (**PCBM**) donor-acceptor combination was used as standard to understand the role of active layer morphology towards efficient BHJ-Polymer Solar Cell (BHJ-PSC) device which reached power conversion efficiency (PCE) of >5% and is being used as a reference system till today.[5] Previously, many groups have shown improved efficiency by introducing innovative polymer donors,[6] fullerene acceptors[7] and incorporating new interfacial electron/hole transport layers.[8] Also, the inverted PSC configuration is most suited to realize stable and long lasting device than conventional architecture.[9] The detailed descriptions of both conventional and inverted device architectures are discussed in chapter 1 (Figure 1.3). Yang Yang *et al.* have developed a low bandgap polymer poly[2,7-(5,5-bis-(3,7-dimethyloctyl)-5H-dithieno[3,2-b:2',3'-d]pyran)-alt-4,7-(5,6-difluoro-2,1,3-benzothia diazole)] (PDTP-DFBT) with a PCE of 8.1% in combination with $PC_{71}BM$ as an acceptor with inverted configuration and a high PCE of 10.2% with tandem device architecture.[10] Modified fullerene derivative such as indene C_{60}-bisadduct,[11] fullerene-di(4-methyl-phenyl)methano-C_{60} (DMPCBA),[12] bis-o-quino-dimethane C_{60} (Bis-QDMC)[13] etc. along with **P3HT** donor showed improved PCE also compared to reference **PCBM** acceptor.

It has been demonstrated that the nanoscale morphology of BHJ active layer tend to grow into micro-scale domains due to the high aggregation/crystallization tendency of fullerene molecules.[4] When solar cells are working under natural conditions, such an aggregation will enhance with time due to the continuous heat-cool cycle, which will hamper the device performance.[14] Therefore, to create stable and high life time PSCs for practical applications, it is essential to stabilize their BHJ film

morphology.[15-17] One of the strategies is to "freeze" the active layer nano-structure obtained after spin coating.[18] In this line, researchers have developed methods of cross-linking active layer using cross-linkable groups such as epoxide,[19] halide,[20] azide,[21] oxetane,[22] and styrene.[23,24] These moieties were successfully installed into the side chains of the polymer or fullerene and have shown promising results in terms of stable nanostructures and devices. Also, many reactions for cross-linking namely, click chemistry,[25,26] disulfide bond formation,[25] olefin metathesis,[25,27] etc. have been introduced to retain the initial supramolecular nanostructure.

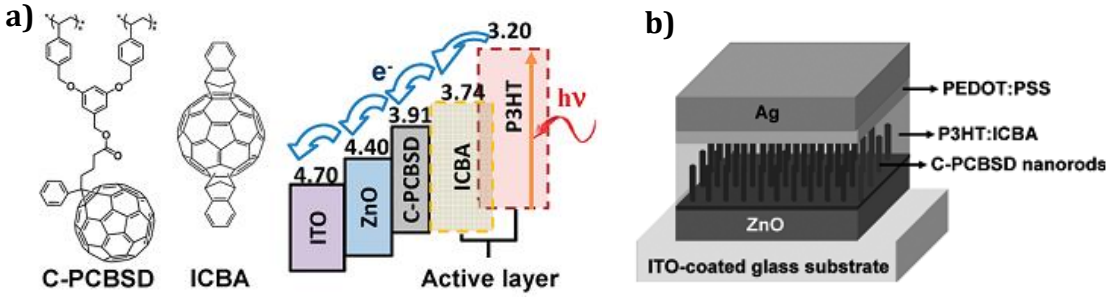

Figure 2.1. a) Molecular structure of C-PCBSD and ICBA, and the multilayer structure with LUMO energy levels (Adapted from reference 28); b) corresponding to the device configuration ITO/ZnO/C-PCBSD/**P3HT**: ICBA/PEDOT: PSS/Ag for favorable electron collection (Adapted from reference 29).

Yongfang Li *et al.* reported incorporation of an electron extracting C-PCBSD interlayer into the **P3HT**: ICBA based inverted device which modulates the electronic and orbital interactions at the interface, boosting the PCE to a remarkable 6.2% (Figure 2.1a).[28] Later the same group fabricated vertically aligned C-PCBSD fullerene derivative as ETL instead of cross-linked film using the same **P3HT**: ICBA polymer blend system and achieved record high PCE of 7.4% due to the high charge transport across the

vertical nanorods of ETL (Figure 2.1b).[29] Similarly, Yen-Ju Cheng and coworkers constructed cross-linkable [6, 6]-phenyl-C_{61}-butyric oxetane dendron ester (PCBOD) fullerene derivative which showed cationic ring-opening reaction under thermal and UV treatment (Figure 2.2).[22] The oxetane functionality with neutral nature can anchor onto the TiO_x surface leading to adhesive monolayer with intimate contact. The cross-linking further passivates and forms multiple layers above the monolayer. Application of C-PCBOD as electron acceptor layer in the inverted configuration achieved PCE of 4.5% compared to reference device without C-PCBOD (PCE=3.57%). These highest efficiencies achieved using modified fullerene derivatives in the presence of **P3HT** electron donor shows the requirement and role of fullerene functionalization towards simple and stable PSC device with improved efficiencies.

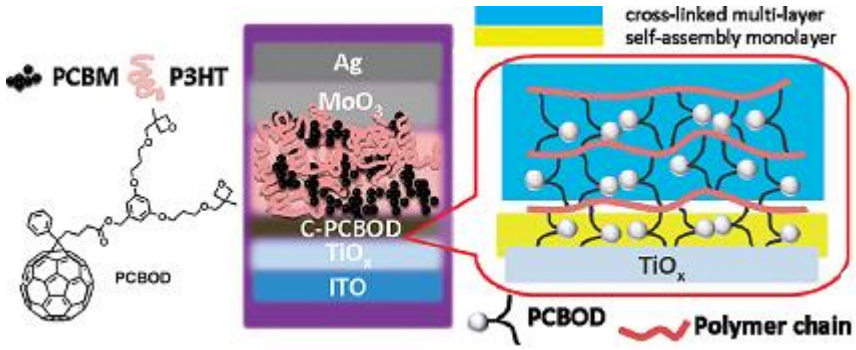

Figure 2.2. Molecular structure of PCBOD and the corresponding multilayer device configuration ITO/ZnO/C-PCBOD/**P3HT**: **PCBM**/PEDOT: PSS/Ag showing crosslinked multilayer formation above self-assembled monolayer (Adapted from reference 22).

The functionalization of cross linkable fullerenes can be done, either covalently attaching cross-linkable units to fullerene monomer or by adding reactive moieties externally during solution processing where it can undergo reaction upon thermal annealing.[30] The first method maintains the organization of fullerenes along the

polymerizable groups which facilitate a possible stable nanostructure formation guided by self-assembly through non-covalent interactions.[31] On the other hand, the second approach sometimes fails in controlling the desired nano-morphology.[32] Recently, cross-likable benzoxazine derivatives gather tremendous attention due to their excellent properties including, low water absorption, low coefficient of thermal expansion, near-zero volumic shrinkage during curing.[33,34] Moreover, they can be easily synthesized from conventional cheap precursors and polymerizable under heat triggered reaction, without the aid of external initiators or catalysts.[35] In the present work, we have designed covalent functionalization of fullerene with benzoxazine crosslinkable group and demonstrated their potential application as electron transport layers in BHJ PSCs.

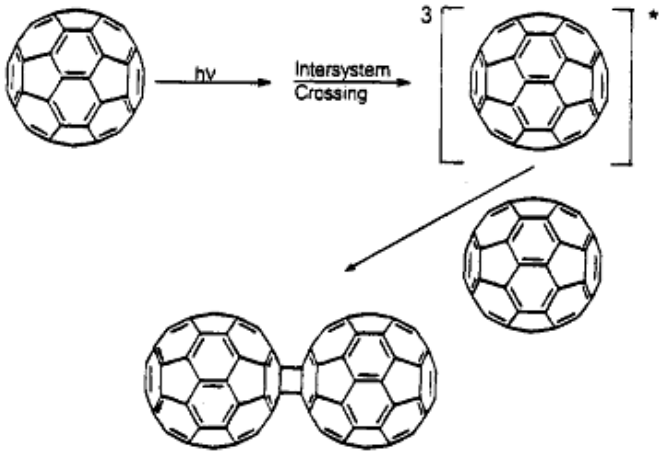

Figure 2.3. Light induced excited state reaction pathways of fullerene in aggregated solutions (Adapted from reference 39).

Furthermore, development of stable functional supramolecular architectures from fullerenes by tuning the molecular interaction such as π-π and van der Waals interactions and their self-assembling behaviour is an important scientific

challenge.[36,37] Many self-assembled structures which are organized by weak non-covalent interactions suffer from morphological changes when exposed to air, temperature and organic solvents.[38] Self-assembled fullerenes were known to undergo cycloaddition through excited state reactions as shown in Figure 2.3.[39] Recently, Eiichi Nakamura *et al.* used the phenomenon of photocross-linking of fullerenes to stabilize the resulting morphology.[40] Also, Takashi Nakanishi *et al.* showed photocross-linking of diacetylene based fullerene derivative which can stabilize the self-assembled nanostructure.[41] Nicolas Giuseppone and coworkers showed the light-controlled differential self-assembly behaviour of triarylamine functionalized fullerene conjugates.[42] Under visible light it self-assembled into micrometer sized nanofibres whereas sunlight exposure induced the formation of spherical particles as shown in Figure 2.4. These results demonstrate the feasibility of constructing the desired stable supramolecular materials from fullerenes through the combination of appropriate molecular design, self-assembly and cross-linking techniques.

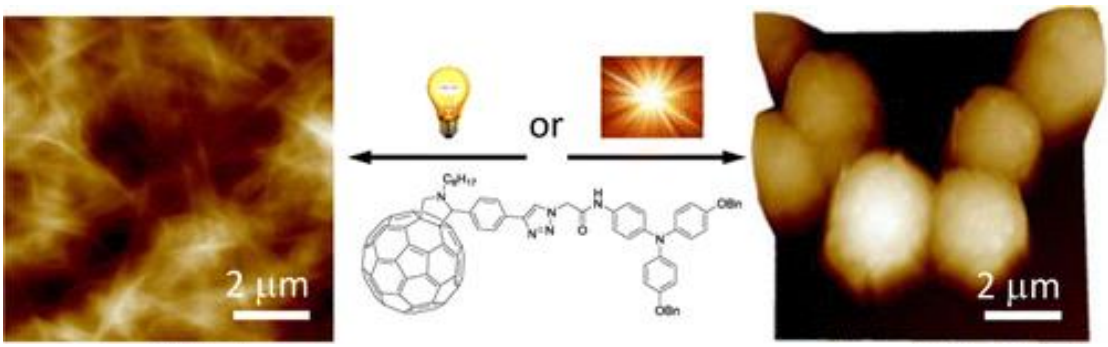

Figure 2.4. The triarylamine–fullerene conjugate showing differential self-assembly under white light (micrometric fibres) and sunlight (monodisperse spherical objects) (Adapted from reference 42).

In this chapter, we have designed a cross-linkable fullerene-benzoxazine derivative (**PCBB**, Scheme 2.2) and investigated its cross-linking, morphological and photophysical properties in comparison with the parent **PCBM** derivative. The *para*-position of the phenolic ring in benzoxazine was blocked specifically, to prevent network formation and facilitate the formation of linear polybenzoxazine. This derivative showed the expected heat triggered cross linking reaction at 200 °C, well below the known methylol benzoxazine cross-linking temperature of ~230 °C. The designed cross-linking strategy provides a fullerene nanomaterial with enhanced morphological stability towards organic solvents and temperature. Furthermore, **PCBB** showed light triggered morphology transformations from core shell particle into nanonetwork structure in THF/H_2O (9:1) solvent mixture. The morphology evolution is believed to involve radical initiated polyfullerene formation through cycloaddition reactions of fullerenes. The strategy used here provides way to arrest the nanostructure formed by self-assembly which are stable towards air, organic solvents and temperature. Moreover, we have demonstrated the application of this cross-linked **PCBB** as electron transport material in PSCs.

2.3. RESULTS AND DISCUSSION

2.3.1. SYNTHESIS AND PHOTOPHYSICAL PROPERTIES OF PCBB

The [6,6]-phenyl-C_{61}-butyricmethyl ester (**PCBM**) was synthesized using a reported procedures, as shown in Scheme 2.1.[43] The synthesis started with the esterification of 4-Benzoylbutyric acid (**1**) using methanol and sulphuric acid under reflux conditions, which gave 4-Benzoylbutyric methyl ester (**2**) in 80%

yield. The compound **2** upon further reaction with *p*-tosylhydrazide in methanol under reflux conditions gave the corresponding hydrazone (3, 72%). Finally, the *in situ* generated carbene by heating hydrazone with sodium methoxide and pyridine was heated with the solution of C_{60} in 1,2-dichlorobenzene (ODCB) at 75 °C, to obtain **PCBM** in 16% yield.

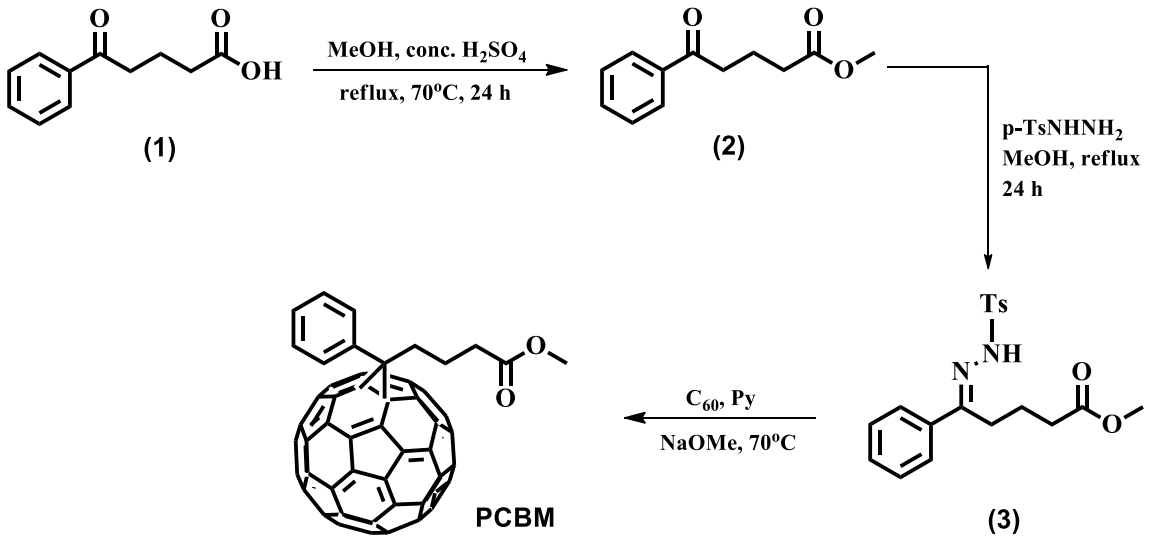

Scheme 2.1. Synthetic scheme for **PCBM**. MeOH: Methanol, conc. H_2SO_4: concentrated sulphuric acid, p-$TsNHNH_2$: p-tosylhydrazide, NaOMe: sodium methoxide.

The synthesis of [6,6]-Phenyl-C_{61}-butyricbenzoxazine ester, **PCBB** with benzoxazine cross-linkable group was carried out as shown in Scheme 2.2. The starting materials [6,6]-phenyl C_{61}-butyric acid (PCBA), obtained by the ester hydrolysis of **PCBM** and methylol benzoxazine (MB) were synthesized following reported literature procedures.[44] Subsequently, PCBA was reacted with MB using 1-ethyl-3-(3-(dimethylamino)propyl)carbodiimide (EDC) and 4-(dimethylamino) pyridine (DMAP) mediated ester coupling in ODCB to obtain the desired final

product **PCBB**. **PCBB** was characterized by ^{1}H NMR, ^{13}C NMR, FT-IR and UV-visible absorption, as well as MALDI-TOF mass spectral analysis. For

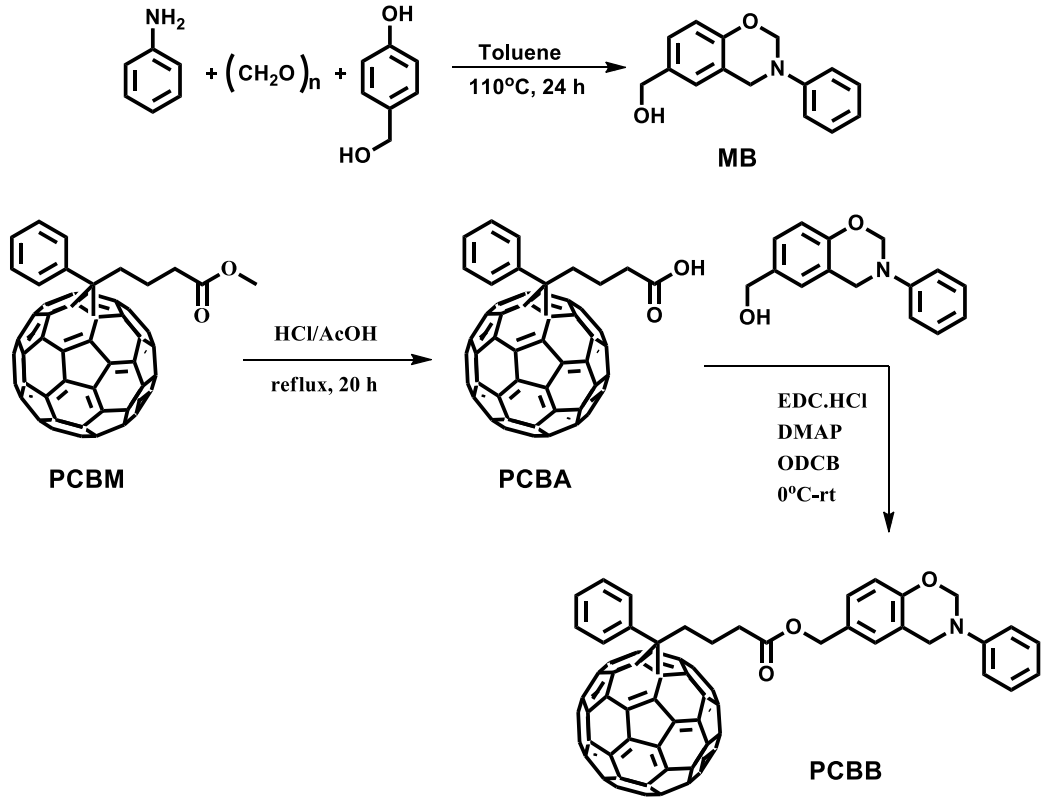

Scheme 2.2. Synthetic scheme for **PCBB**. EDC: 1-ethyl-3-(3-(dimethylamino)propyl) carbodiimide, DMAP: 4-(dimethylamino)pyridine, ODCB: *1,2*-dichlorobenzene.

example, ^{1}H NMR spectra of **PCBB** showed characteristic proton signals corresponding to the methyl protons of the benzoxazine moiety at 5.35 ppm and 4.94 ppm and the alkyl protons in the range of 2.19-2.9 ppm. In the ^{13}C NMR, we have observed chemically distinct carbon signals which can be assigned as per the structure of **PCBB**. FT-IR spectrum of **PCBB** showed characteristic carbonyl stretching (1738 cm^{-1}) and the out of plane bending vibration of benzene –C-H to which oxazine ring was attached (948 cm^{-1}). Also, UV-Visible absorption spectrum revealed characteristic absorption of

functionalized fullerene at 328 nm. The MALDI analysis showed the exact mass of **PCBB** at 1120.41 (M+H). These spectral and analytical techniques confirm the successful coupling of the PCBA and benzoxazine moieties.

Since, the core structure of **PCBB** resembles to its parental derivative **PCBM**, we have studied the physical and optoelectronic properties of **PCBB** in comparison with **PCBM** using UV-Visible absorption spectroscopy, square wave voltammetry, thermogravimetric analysis and **P3HT** fluorescence quenching experiments. Typical UV-Visible absorption spectra of **PCBB** in chloroform showed the characteristic peak at 328 nm, which is almost similar to that of **PCBM** (Figure 2.5a).[45] The electrochemical properties of **PCBB** and **PCBM** were compared by using square wave voltammetry (Figure 2.5b). Measurements were carried out using thin films of **PCBB** and **PCBM** coated glassy carbon as working electrode in the presence of 0.1 M tetrabutylammonium hexafluorophosphate ($TBAPF_6$) as supporting electrolyte, Ag/AgCl electrode as reference electrode and

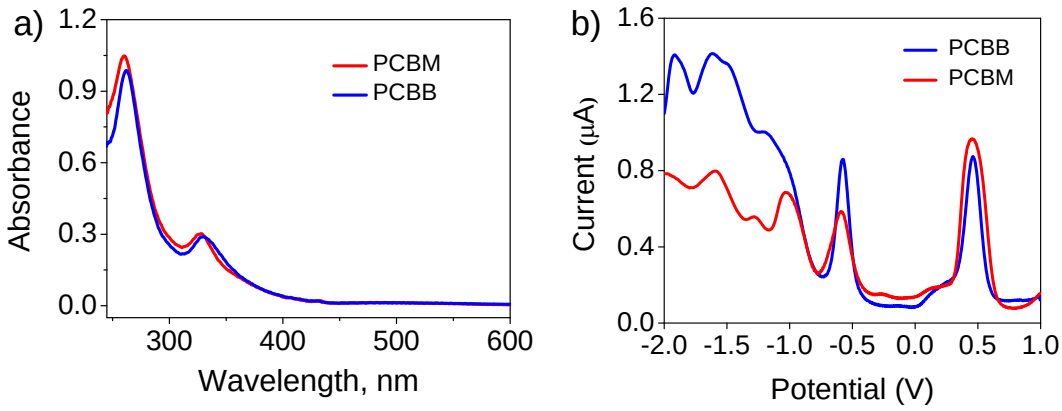

Figure 2.5. (a) Absorption spectra (10 μM) of **PCBB** and **PCBM** in chloroform. (b) Square wave voltamogram of **PCBB** and **PCBM** vs Ag/AgCl at a scan rate of 100 mV s^{-1}.

platinum wire as counter electrode in acetonitrile, calibrated by ferrocene ($E_{1/2(ferrocene)}$ = 0.45 V vs Ag/AgCl). Both compounds exhibited similar first reduction potential of -0.57 V vs Ag/Ag^{+}. The LUMO energy levels were calculated relative to the reference energy level of ferrocene (4.8 eV below the vacuum level) using the equation: $E_{HOMO/LUMO} = -e\,[4.8 + E_{ox/red} - 0.45]$ eV.[46] HOMO energy values were calculated using the LUMO values and optical band gap calculated from the onset of absorption band of **PCBB/PCBM** (E_{gap}= 1.72 eV). The HOMO and LUMO energy levels of both compounds were found to be -5.5 eV and -3.78

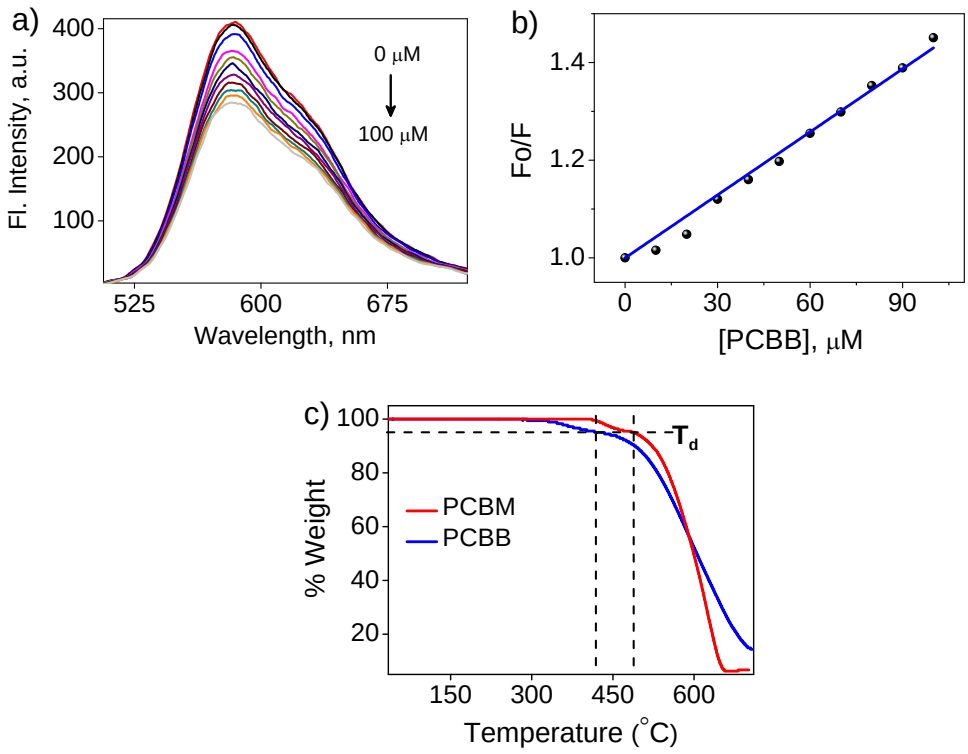

Figure 2.6. (a) Changes in the fluorescence of **P3HT** in the presence of varying [**PCBB**] from 0 to 100 μM. (b) Stern-Volmer plot of **PCBB** and **PCBM** obtained from fluorescence quenching studies. (c) TGA profiles of **PCBB** and **PCBM**; the black lines in thermogram indicate the T_d value.100 mV s^{-1}.

eV respectively. The similar HOMO and LUMO energy values of **PCBB** and **PCBM** indicates that benzoxazine substitution does not perturb the electronic properties of the **PCBB**.

The fluorescence of **P3HT** in presence of varying concentrations of **PCBB** showed efficient quenching (Figure 2.6a) and the corresponding linear Stern-Volmer plots revealed presence of dynamic quenching behaviour between **P3HT-PCBB** molecules (Figure 2.6b).[47] The Stern-Volmer constant was found to be K_{sv}= 4.3 x 10^3 M^{-1} indicating efficient electron transfer process between **P3HT-PCBB** donor-acceptor pairs. The linear Stern-Volmer plot obtained from the emission profile revealed that the Stern-Volmer constant is quite similar to that reported for **P3HT-PCBM** donor-acceptor pairs which further confirm that **PCBB** exhibits similar electronic properties of **PCBM**.[48] The thermal stability of **PCBB** was measured and compared with **PCBM** through thermogravimetric analysis before carrying out thermal cross-linking experiments. The TGA profile of both **PCBB** and **PCBM** showed almost no weight loss up to a temperature of 400 $^{\circ}$C and exhibited 5% weight loss (T_d) at 416 $^{\circ}$C and 488 $^{\circ}$C, respectively (Figure 2.6c). The relative lower T_d value of **PCBB** is attributed to the bulkier benzoxazine moiety at the ester linkage compared to methoxy group of **PCBM**. The thermal characterization studies indicate that the benzoxazine derivative, **PCBB** is thermally stable under the experimental condition and can be used for thermal curing studies.

2.3.2. CROSS-LINKING AND SOLVENT RESISTIVE PROPERTIES

The thermal transition properties of **PCBB** monomer were investigated through Differential Scanning Calorimetry (DSC) analysis (Figure 2.7a). It showed a broad exothermic peak with a T_{max} value around 210 °C, indicating the thermal cross-linking of benzoxazine groups.[34] The functional group transformation before and after heat cross-linking of the sample at 200 °C for 15 min were monitored using FT-IR spectroscopy (Figure 2.7b). The FTIR spectrum of **PCBB** after heating showed the disappearance of peak characteristic to the out of plane bending vibrational mode of benzene –C-H to which oxazine ring was attached at 948 cm^{-1}.[49] Moreover, heat cross-linking results in the appearance of a new peak

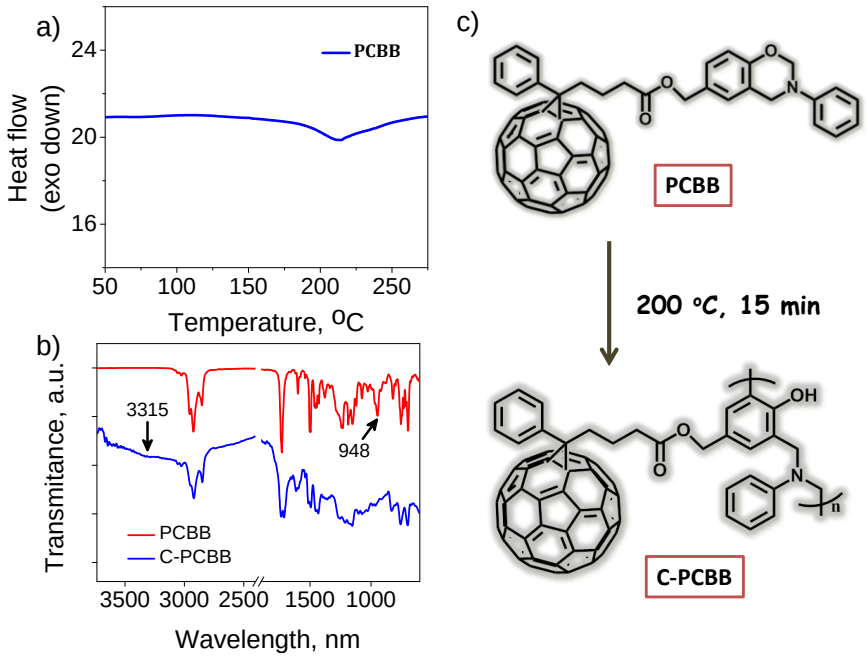

Figure 2.7. (a) DSC thermogram of the **PCBB** with a heating rate of 10 °C min^{-1}. (b) Solid state FT-IR spectra of the **PCBB** and thermally cross-linked **PCBB** (**C-PCBB**). (c) Chemical structures of **PCBB** and **C-PCBB** indicating the functional group transformation upon thermally triggered crosslinking.

at 3315 cm^{-1}, which is attributed to the phenolic –OH stretching frequency. This confirms thermal cross linking of **PCBB** molecule. Based on the reported mechanism of benzoxazine cross linking in the literature, we propose the heat - triggered ring opening polymerisation of benzoxazine group in **PCBB**, as shown schematically in Figure 2.7c.[33] From these photophysical and crosslinking experiments, we can consider **PCBB** as a cross linkable **PCBM** derivative with similar optoelectronic properties.

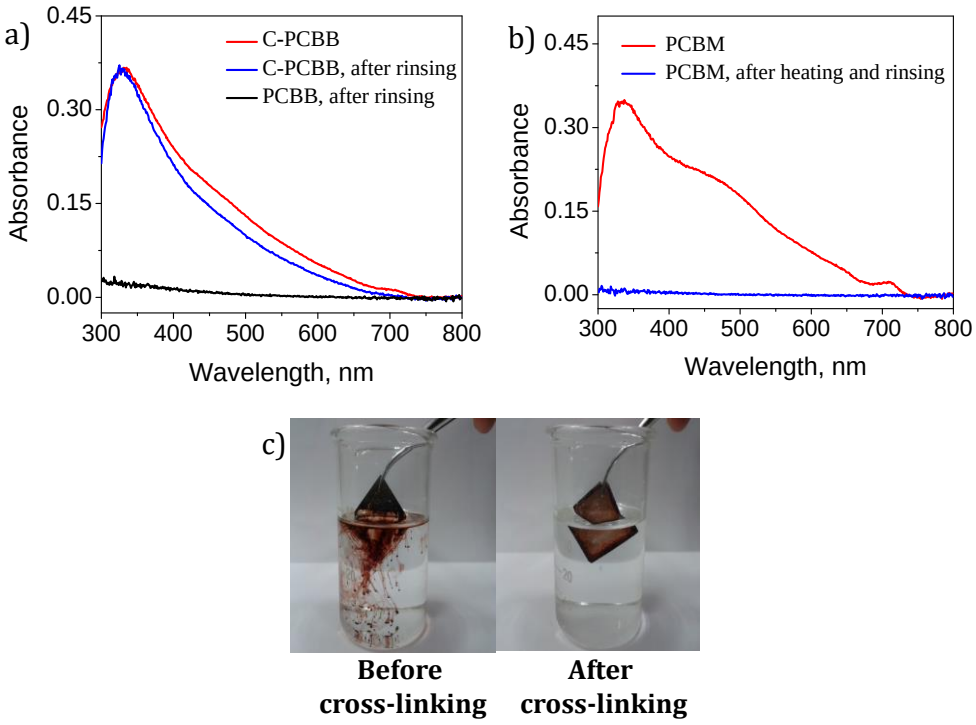

Figure 2.8. (a) Solid state absorption spectra of the **C-PCBB** film before (red), after (blue) rinsing with chloroform and non-crosslinked **PCBB** layer after rinsing with chloroform (black). (b) Solid state absorption spectra of **PCBM** film (red), after heating and rinsing with chloroform (blue). (c) Photograph of glass coated **PCBB** film (thickness *ca.* 150 nm) dipped in chloroform, before and after crosslinking at 200 °C for 15 min.

To get further insight into the cross-linking behaviour, solid state absorption spectra of **PCBB** film cured at 200 °C for 15 min coated on a glass plate was measured before and after rinsing with chloroform (Figure 2.8a). For comparison, we also used **PCBM** coated film processed under similar conditions (Figure 2.8b). More interestingly, the crosslinked **PCBB** (**C-PCBB**) film showed almost unchanged absorption properties before and after rinsing, whereas **PCBM** film completely washed away during rinsing irrespective of temperature and heating time. As expected, the absorbance of the non-cross-linked **PCBB** film also has completely disappeared after rinsing with solvent indicating the importance of curing, without which the material can get washed out by the solvent. This confirms that **PCBB** forms adhesive films exhibiting excellent solvent resistive property after heat cross-linking. The photograph in Figure 2.8c represents the glass plate with **C-PCBB** and **PCBB** films immersed in beaker containing chloroform which indicates the insoluble nature of **C-PCBB** film and dissolution of non-cross-linked **PCBB** film. These results ascertain that when the temperature is about 200 °C benzoxazine groups of **PCBB** molecule provide adequate flexibility to react in solid state and forms insoluble cross-linked films as proposed in Figure 2.7c.

2.3.3. VISIBLE LIGHT INDUCED MORPHOLOGY TRANSFORMATIONS

2.3.3.1. UV-VISIBLE ABSORPTION AND DLS STUDIES

Due to the solvophobic characteristics, C_{60}-based amphiphilic derivatives and polymers are known to form self-assembled nano-clusters.[50] Also, the time dependent

construction of supramolecular nano-network and photocross-linking of C_{60} clusters were reported previously.[51] With a view to combine both of these properties, we investigated the visible light stimuli induced self-assembly of **PCBB** and its propensity to endure morphological transformations. The time dependent absorption changes of **PCBB** (1 mM) in THF/H_2O (9:1) solvent mixture upon ageing for 0 h, 24 h and 48 h

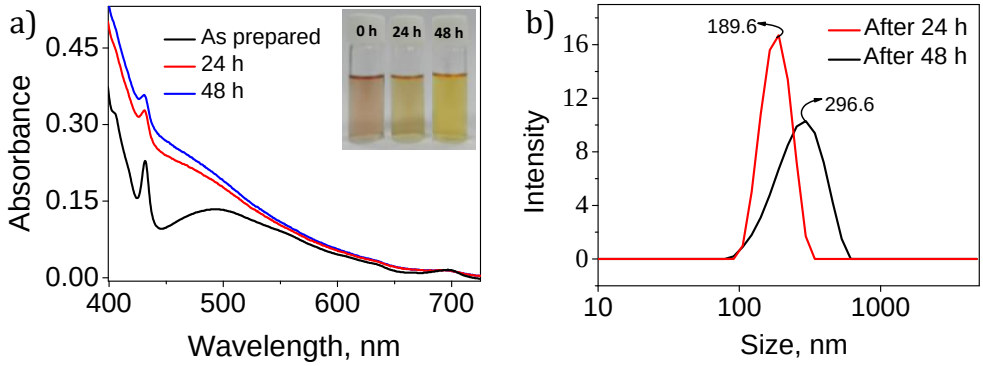

Figure 2.9. (a) Time dependent absorption spectra of **PCBB** in THF/H_2O (9:1). Inset shows the corresponding photograph. (b) DLS measurements of the same solution after 24 h and 48h.

under visible light exposure showed considerable hyperchromicity with a colour change of the solution from brown to yellow (Figure 2.9a and inset). This might be due to the fact that increasing solvent polarity induces aggregation of fullerene molecules through solvophobic effect. The size of the supramolecular aggregates of respective solutions was further evaluated by DLS analysis (Figure 2.9b). Though as-prepared solution did not produce in any scattering, after 24 h and 48 h, the aggregated nanostructure with average hydrodynamic diameter of *ca.* 190 nm and 296 nm were observed. Similar observation was reported earlier in the case of self-assembled fullerene clusters and polyfullerenes.

2.3.3.2. TIME DEPENDENT MORPHOLOGICAL STUDIES

To investigate the visible light induced morphological features of **PCBB**, solutions aged for different time intervals were analyzed under Transmission Electron Microscope (TEM) (Figure 2.10). For these studies, 1 mM solution of **PCBB** in THF/H_2O (9:1) aged for 0, 24 h and 48 h were drop cast on TEM grid. DLS analysis was conducted

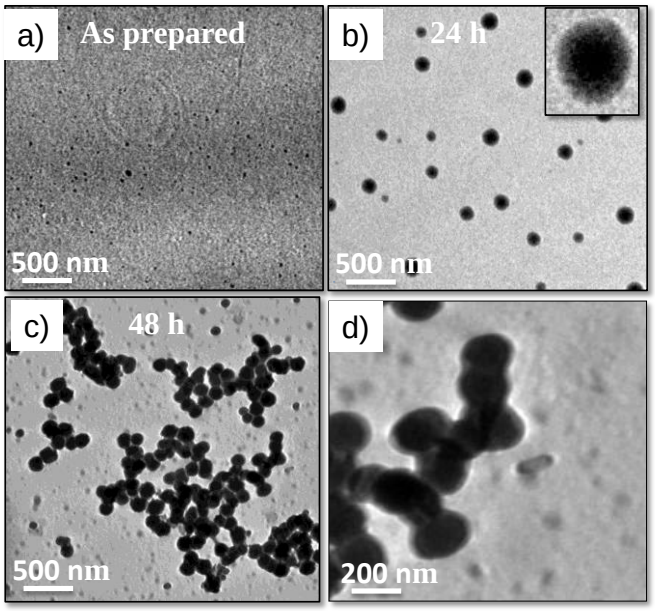

Figure 2.10. TEM images of **PCBB** in THF/H_2O (9:1) mixture at different time intervals, (a) as prepared, (b) after 24 h, (c) after 48 h and (d) zoomed portion of c showing joining of nanoparticles.

in these solutions to understand the size changes and aggregation which may be causing the observed colour changes (Figure 2.9b). Since, as-prepared solution contains **PCBB** in its monomeric form it does not result in any noticeable nanostructures (Figure 2.10a). After 24 h, TEM image of **PCBB** aged for 24 h, revealed the formation of coreshell nanoparticles with an average size of 150 nm (Figure 2.10b). Figure 2.10b

inset shows the zoomed image of one nanoparticle which showed clear contrast difference between inner and outer surface. This suggests the self-organization of **PCBB** molecules into large clusters with C_{60} as the core and the alkyl chain bearing benzoxazine as the shell. Interestingly, after 48 h the TEM image revealed the fusion of coreshell nanoparticle into nanonetwork structures without much change in the shape of the particles (Figure 2.10c). The zoomed TEM image in Figure 2.10d clearly indicates the fusion of adjacent coreshell nanoparticles.

2.3.3.3. ^{1}H NMR AND MASS SPECTRAL ANALYSIS

Our attempts to reverse the colour change of the visible light exposed solutions by sonication, addition of THF and heating were not successful and the solution remained stable under experimental conditions. This motivated us to carry out the time

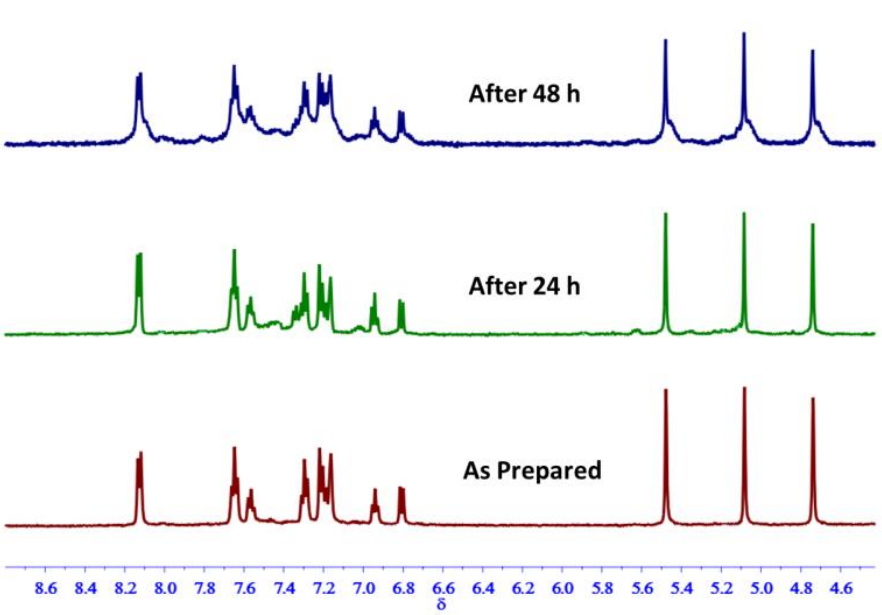

Figure 2.11. ^{1}H NMR spectrum of **PCBB** in THF-d_8/D_2O (9:1) solvent mixture at different time intervals under the visible light exposure.

dependent structural analysis of **PCBB** using ^{1}H NMR studies in THF-d_8/D_2O (9:1) revealed broadening of the peaks with time corresponding to **PCBB** protons without change in the respective chemical shifts (Figure 2.11).

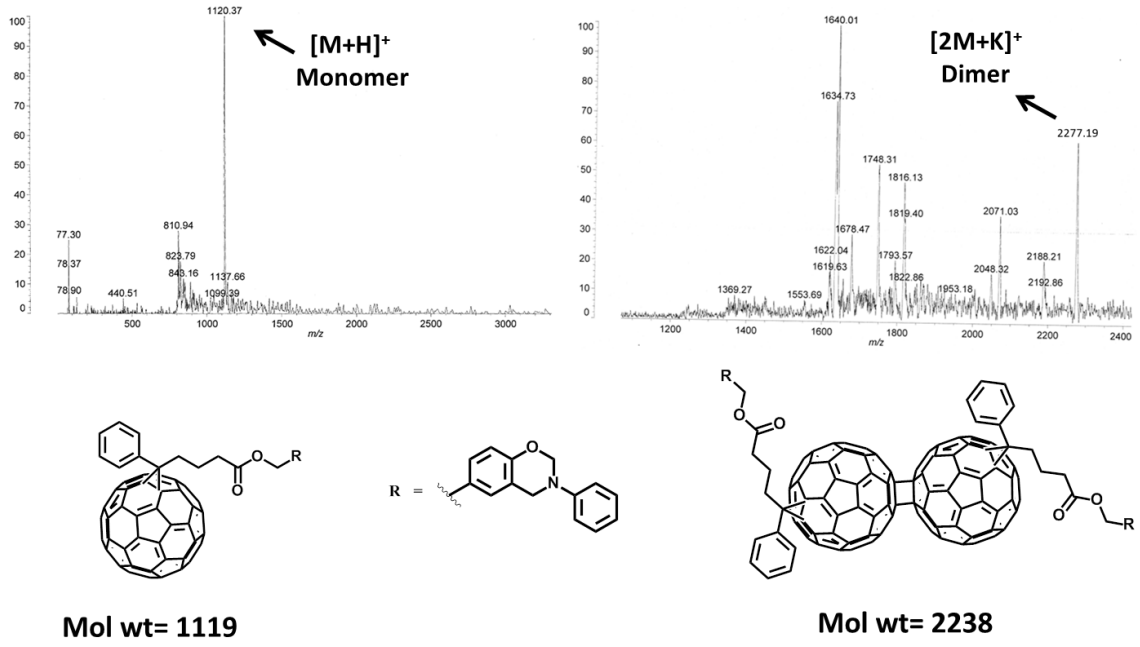

Figure 2.12. MALDI-TOF spectrum of as prepared **PCBB**, after exposure to visible light for 48 h in THF/H_2O (9:1) solvent mixture and possible chemical structure of the dimer.

Also, under identical conditions, MALDI-TOF analysis generated the base peak equivalent to the dimer mass of **PCBB** (Figure 2.12). Based on these results and earlier reports on UV light mediated polyfullerene formation in self-assembled clusters, we propose the possibility of fullerene being reacted via light assisted [2+2] cycloaddition reactions within the self-assembled cluster. Although, aging of the solution under visible light resulted in the polyfullerene formation, it was unable to observe in MALDI-TOF analysis. This might be due to the difficulty in desorption and ionization of polyfullerene without being decomposed under experimental conditions.[37] The

polymerisation is believed to involve visible light assisted [2+2] cycloaddition of self-assembled fullerene leading to polyfullerene structures as revealed by morphological analysis.

2.3.4. PROPOSED MECHANISM OF MORPHOLOGICAL TRANSFORMATIONS

The overall dual stimuli responsive behaviour of **PCBB** monomer under temperature and visible light can be schematically represented as shown in Figure 2.13. The drop cast solutions of **PCBB** on glass showed efficient heat assisted cross-linking at 200 °C for 15 min to form solvent resistive films. Here, individual benzoxazine act as thermal crosslinking units which undergo ring opening polymerisation. On the other hand, under the stimuli of visible light **PCBB** in THF/H_2O (9:1) exhibited time

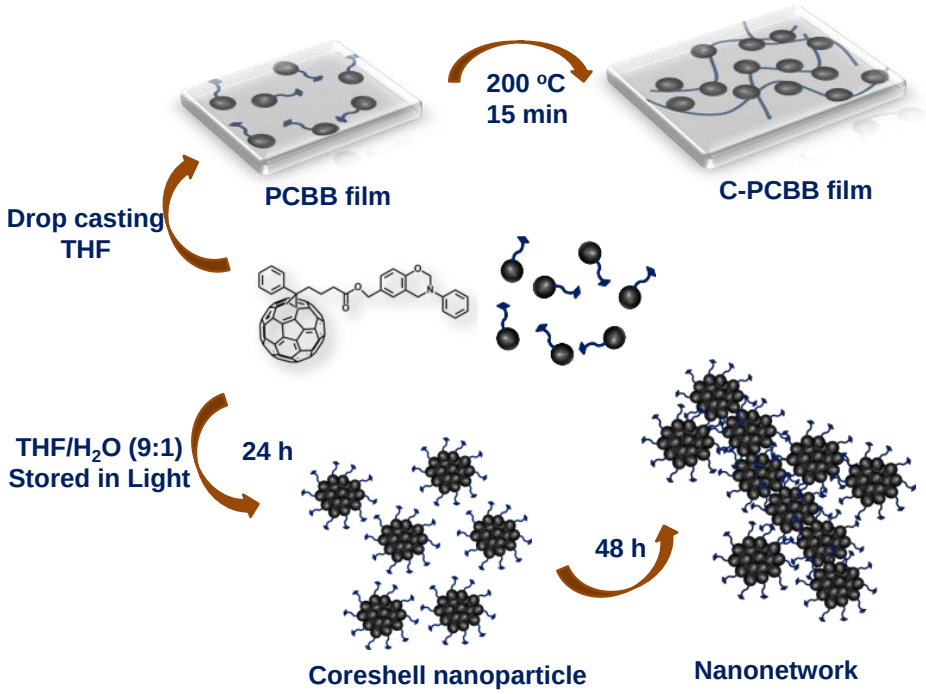

Figure 2.13. Schematic illustration of **PCBB** forming thermally triggered crosslinking and visible light induced time dependent morphological transformations.

dependent morphology transformation into nanonetwork structure mediated by coreshell nanoparticle formation.

Initially, the monomers in THF/H_2O (9:1) solvent mixture were self-assembled into coreshell nanoparticle due to the solvophobic effect induced by the polar solvent. Further, light induced [2+2] cycloaddition reactions drive the joining of adjucent cluster leading to a nanonetwork of clusters. Both self-assembly assisted by non-covalent interactions between initially formed core-shell nanostructures and visible light driven cycloaddition reactions are responsible for the formation of observed nanonetwork structures.

2.3.5. OPTICAL MICROSCOPE STUDIES

A major issue affecting the long term stability and performance of the **P3HT-PCBM** polymer blend films is their tendency to undergo macrophase separation as a result of crystallisation/aggregation of **PCBM** over the time.[14] This has adverse effect on performance of organic photovoltaics. The direct contact with the usual hydrophilic electron transport layer, Zinc oxide (ZnO) and interfacial erosion is the primary concern. Therefore, the aggregate growth of **P3HT-PCBM** polymer blend with and without a **C-PCBB** layer was studied using optical microscope. For these studies, the samples of **P3HT**, **P3HT-PCBM** (1:1, w/w) and **C-PCBB/P3HT-PCBM** were prepared on glass plate and analysed after ageing for 48 h. Both **P3HT** and **P3HT-PCBM** film after 48 hours of ageing showed aggregated crystal like structure indicating macroscopic phase separation of nanomorphology (Figure 2.14A and 14B).

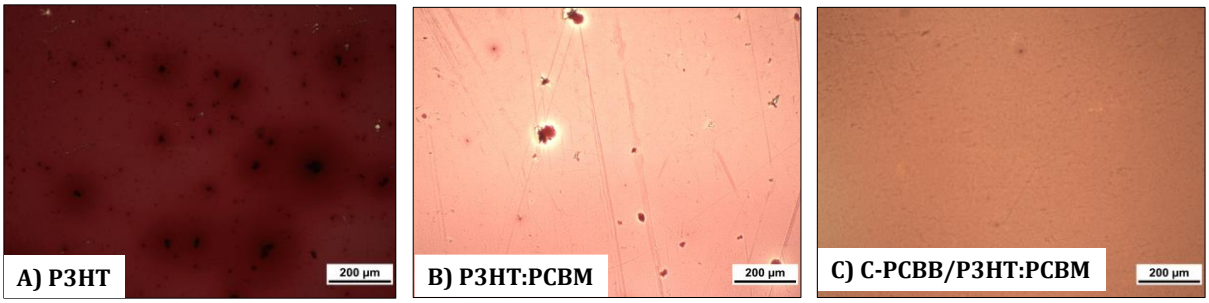

Figure 2.14. Optical microscope images of (A) **P3HT**, (B) **P3HT**:**PCBM** and (C) **C-PCBB/P3HT**:**PCBM** film after 48 h.

On the other hand, **P3HT-PCBM** in the presence of **C-PCBB** interfacial layer exhibited smooth and homogeneous film under similar experimental conditions (Figure 2.14C). The **C-PCBB** layer provide a smooth hydrophobic contact to the polymer blend retarding the crystallization which otherwise in contact with the hydrophilic ZnO promotes faster phase separation. This further indicates that *in situ* cross linking of **PCBB** has an indirect effect on the morphological stabilization of polymer blends and therefore help in inhibiting the possible macrophase separation over time.

2.3.6. SOLID STATE ABSORPTION AND EMISSION WITH P3HT DONOR

The solid state absorption and emission spectra of **P3HT**, **P3HT-PCBM** and **C-PCBB/P3HT-PCBM** were investigated using drop cast films on glass and the results were summarized in Figure 2.15. In general, the absorption spectra were additive and showed no sign of any ground state charge-transfer complexes. For example, in the presence of **PCBM**, the absorption spectrum of **P3HT** remain

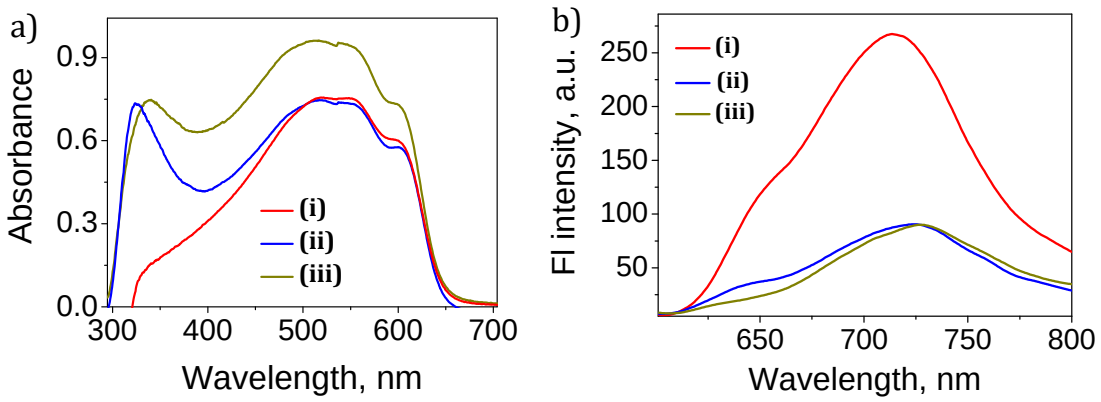

Figure 2.15. Solid state absorption and emission spectrum of (i) **P3HT** alone, (ii) **P3HT-PCBM** blends and (iii) **C-PCBB/P3HT-PCBM**. λ_{exc} = 600 nm.

unchanged in the region of 400-600 nm while there was an increase in the intensity from 300-400 nm due to added absorption of **PCBM** (Figure 2.15a). In the presence of **C-PCBB** interfacial layer, the polymer blend displayed slight increase in the absorption due to the presence of extra layer of **PCBB**. The shoulder bands at 603 nm in the absorption spectrum of **P3HT** and the blends indicate the crystallinity of **P3HT** which remain intact even after blending with **PCBM** and in the presence of **C-PCBB** layer. Moreover, the emission maximum of **P3HT** at 715 nm was quenched efficiently (67%) in the **P3HT-PCBM** blends (Figure 2.15b). Similar trend was observed in the case of polymer blend with **C-PCBB** as the interfacial layer. This experiment revealed that incorporation of **C-PCBB** interfacial layer increases the absorption of the polymer blend in the visible region without compromising crystallinity of the polymer.

2.3.7. FILM ROUGHNESS STUDIES THROUGH AFM

We have studied a photovoltaic device with an inverted configuration of ITO/ZnO/**C-PCBB**/**P3HT**-**PCBM**/V_2O_5/Ag for investigation of PV properties. The propensity of **C-PCBB** layer on the polymer blend morphology was studied before carrying out device fabrication (Figure 2.16). Initially ZnO nanoparticle solution prepared using sol-gel process was coated on ITO. The surface of ITO/ZnO showed root mean square (RMS) roughness of 4.68 nm (Figure 2.16a). Upon coating of **C-PCBB** layer, the ITO/ZnO/**C-PCBB** surface exhibited relatively lower roughness of 0.31 nm (Figure 2.16b). The polymer blend was coated with and without **C-PCBB** layer on

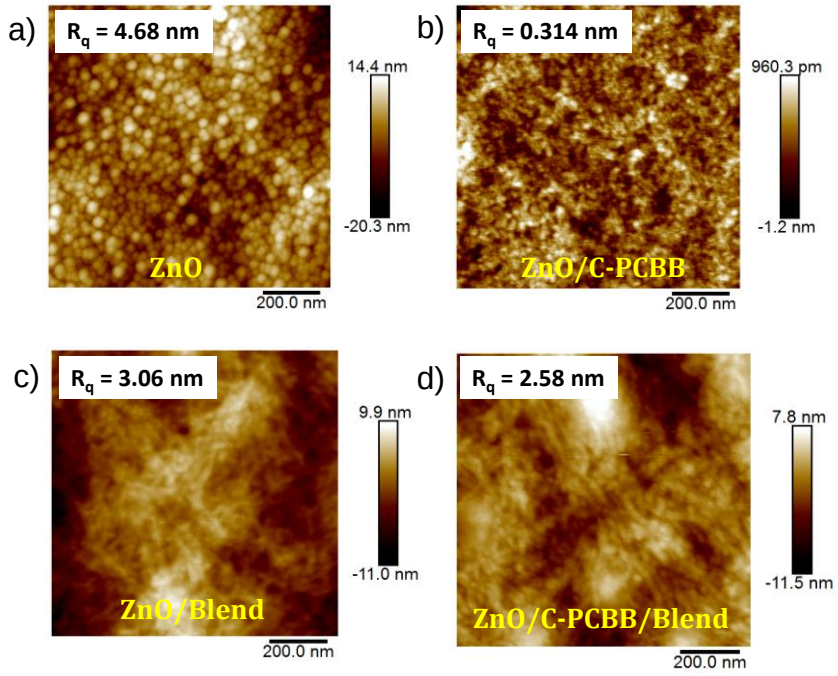

Figure 2.16. AFM tapping mode height images of (a) the bare ZnO surface and (b) **C-PCBB** thin film on top of the ZnO. **P3HT**:**PCBM** polymer blend films (c) without and (d) with **C-PCBB** interfacial layer after thermal annealing at 130 °C for 10 min, (1.0 ×1.0μm). The root mean square roughness (R_q) was indicated in the insets.

ITO/ZnO (Figure 2.16c and 16d). The surface of polymer blend with an interfacial **C-PCBB** film was found to be 2.58 nm whereas a roughness value of 3.06 nm was observed for polymer blends without the **C-PCBB** layer. The decreased roughness in the presence of **C-PCBB** is due to the reduction in the voids of unevenly distributed ZnO by **PCBB** rendering smoother and more hydrophobic surface.

2.3.8. PHOTOVOLTAIC PROPERTIES

BHJ-PSC devices were fabricated with inverted configuration without and with **C-PCBB** layer to understand the propensity of **C-PCBB** as electron transport layer. Device A and B were prepared by spin-coating a mixture of **P3HT/PCBM** (1:1, w/w) from ODCB to form a ~130 nm thin film on ZnO coated ITO substrates without

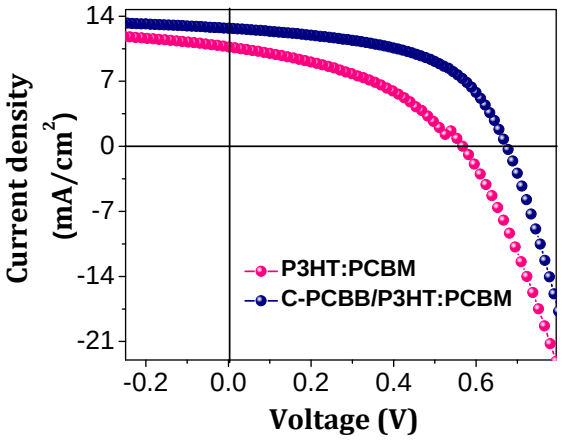

Figure 2.17. J-V curves of devices A and B under AM 1.5 G illumination at 100 mV/cm^2.

and with **C-PCBB** interlayer, respectively. Figure 2.17 and Table 2.1 represent the J-V characteristics and summary of photovoltaic performance of the devices A and B, respectively. Under identical fabrication conditions reference device A showed a PCE of 3.28% which is in agreement with literature reported values for **P3HT/PCBM** system.[28]

With an additional interfacial layer of **C-PCBB**, the PCE in device B was improved to 4.27%. This value represents a ~25% improvement over device A recording an enhancement in the short-circuit current (Jsc), and fill factor (FF) relative to device A. In

Table 2.1: Summary of photovoltaic performance of different devices.

Device	V_{oc} (V)	J_{sc} (mA/cm^2)	FF (%)	η (%)
A	0.56	11.68	50.20	3.28
B	0.64	12.75	52.41	4.27

Definitions: open-circuit voltage, V_{oc}; short-circuit current, J_{sc}; fill factor, FF; PCE, η; Configurations: device A, ITO/ZnO/**P3HT**: **PCBM** (1:1, w/w)/V_2O_5/Ag; device B, ITO/ZnO/**C-PCBB**/**P3HT**: **PCBM** (1:1, w/w)/ V_2O_5/Ag.

BHJ active layer both **P3HT** donor and **PCBM** acceptor domains at the interface are expected to make contact with the ZnO bottom layer to form two types of localized heterojunction at nanoscale level (Figure 2.18). Hence, device A contains **P3HT**/ZnO and **PCBM**/ZnO localized heterojunctions at the interface, whereas device B has **P3HT**/**C-PCBB** and **PCBM**/**C-PCBB** contact at the interface.

Careful analysis of the **P3HT** domain in the interface we can have following advantages in the case of device B by employing extra **C-PCBB** layer. In device B, the **C-PCBB** interfacial layer provides an extra **P3HT**/**C-PCBB** interface area for exciton dissociation, which is more efficient than the **P3HT**/ZnO interface in device A. Also, the LUMO energy level of **C-PCBB** (3.8 eV) is located between the LUMO of **P3HT** (3.3 eV) and the conduction band of ZnO (4.4 eV). Therefore, the C- **PCBB** can function as an intermediate energy gradient where electrons can be efficiently transported to the ZnO layer through cascade

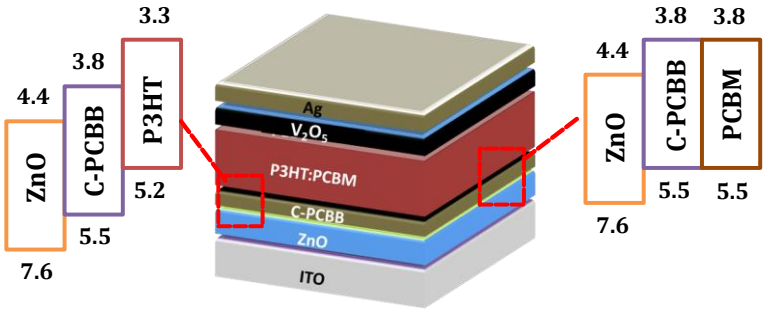

Figure 2.18. Schematic configuration of inverted device architecture, ITO/ZnO/**C-PCBB**/**P3HT**:**PCBM** (1:1, w/w)/V_2O_5/Ag (Device B) showing energy diagrams of the two localized heterojunctions at the interface.

pathway. These advantages might be associated with the improvement of J_{sc}, from 11.68 $mAcm^{-2}$ (device A) to 12.75 mA/cm^2 (device B). Further, the energy offset between the conduction band of ZnO and the HOMO energy of **P3HT** (5.2 eV) is only 0.8 eV, which may give rise to easy charge recombination at the **P3HT**/ZnO interface in device A. The n-type **C-PCBB** acting as a hole-blocking layer in device B with energy offset of 1.4 eV at this interface, compared to 0.8 eV at **P3HT**/ZnO is still beneficial for reducing its probability. Hence, in device B the electron transport can occur very efficiently in both heterojunctions of **P3HT**/**C-PCBB** and **PCBM**/**C-PCBB** while in device A it can happen only at **PCBM**/ZnO heterojunction. The overall 25% increase in the PCE of the reference device using **C-PCBB** interfacial layer confirms that the **PCBB** act as an efficient cross-linkable electron transport layer in inverted PSCs with efficient exciton dissociation reduced charge recombination and decreased interface contact resistance compared to the reference device.

2.4. CONCLUSIONS

We have successfully synthesized a new cross-linkable fullerene derivative, **PCBB** and showed its dual stimuli responsive behaviour and application as electron transport layer in **P3HT/PCBM** based inverted polymer solar cells. **PCBB** act as 'cross-linkable **PCBM**' inheriting all the photophysical and electrochemical properties of **PCBM**. Thermally cross-linking of **PCBB** at 200 $^{\circ}$C for 15 min led to the formation of solvent resistive films, which otherwise will get washed away during solution processing. Ageing a solution of **PCBB** in THF/H_2O (9:1) under visible light yielded an initial coreshell nanoparticle morphology which eventually transform into nanonetwork structures. From NMR and Mass analysis, these morphological transformations are assigned to visible light assisted [2+2] cycloaddition of C_{60}. Additionally, incorporation of **C-PCBB** interfacial layer reduced both roughness and aggregate growth in the active layer morphology. The performance of device fabricated with inverted configuration of ITO/ZnO/**P3HT**:**PCBM**/V_2O_5/Ag with **C-PCBB** interfacial layer showed ~25% improvement in PCE (4.27%) compared to the reference device (PCE = 3.28%). Our results confirm that incorporation of **PCBB** electron transport layer facilitates cascade electron transport towards effective charge collection in PSCs. The strategies adopted in this work could be used in device fabrication for the construction of stable and efficient solar cells.

2.5. EXPERIMENTAL SECTION

2.5.1. Materials and Methods

The materials and reagents for synthesis were purchased from Sigma-Aldrich, Merck, and Spectrochem chemical suppliers. Regioregular **P3HT** (55 kDa) was purchased from Rieke Metal Inc. and **PCBM** (>99.5%) was obtained from Nano-C. These chemicals were used as received without further purification. Vanadium Pentoxide (V_2O_5) (Baytron P VP AI 4083) was purchased from H. C. Stark and passed through a 0.45 μm syringe filter before spin-coating. Patterned ITO was obtained from Ossila Ltd. All other reagents were purchased from Sigma-Aldrich and used as received. PCBA and methylol benzoxazine (MB) were synthesized according to the reported procedures.

^{1}H (500 MHz) and ^{13}C NMR (125 MHz) spectra were measured on a Bruker Avance DPX spectrometer. Chemical shifts are reported in parts per million (ppm) using tetramethylsilane (TMS) (δ_H = 0 ppm) or the solvent residual signal ($CDCl_3$: δ_C = 77.00 ppm) as an internal reference. The resonance multiplicity is described as s (singlet), d (doublet), t (triplet) and m (multiplet). High resolution mass spectral (HRMS) analysis was performed on a Thermo Scientific Q Exactive Hybrid Quadrupole-Orbitrap electrospray ionization mass spectrometer (ESI-MS) instrument. Infrared spectra were recorded in the diffused reflectance mode in the solid state (KBr) using Shimadzu IR Prestige-21 Fourier Transform Infrared Spectrophotometer. All experiments were carried out using

spectroscopic grade solvents at room temperature (25± 1 °C) unless otherwise mentioned.

The UV/Vis absorption spectra were recorded on a Shimadzu UV-2600 Spectrophotometer. Fluorescence spectra were collected using a SPEX-Fluorolog F112X Spectrofluorimeter equipped with a 450 W Xenon arc lamp. Thermogravimetric analyses were carried using TG/DTA-6200 instrument (SII Nano Technology Inc.) by heating the sample from room temperature to 700 °C at a heating rate of 10 °C min^{-1} under nitrogen atmosphere. Curing temperature was measured using differential scanning calorimeter (Perkin-Elmer Pyris 6 DSC instrument) in sealed aluminium pans by heating the sample from 20 °C to 250 °C at a rate of 10 °C min^{-1}. The square wave voltammetry was done on CV, BASI CV-50W instrument using thin film coated glassy carbon as working electrode at room temperature in the presence of 0.1 M tetrabutylammonium hexafluorophosphate ($TBAPF_6$) as supporting electrolyte, Ag/AgCl electrode as reference electrode and platinum wire as counter electrode in acetonitrile under argon atmosphere with a scan rate of 50 mV/s. A BRUKER MULTIMODE AFM operating with a tapping mode regime was used to record AFM images under ambient conditions. Micro-fabricated TiN cantilever tips (NSG10) with a resonance frequency of 299 kHz and a spring constant of 20–80 Nm^{-1} were used. AFM section analysis was done offline. Samples for the imaging and roughness measurements were prepared as explained in device fabrication section under ambient conditions. The thickness of various films was measured using Bruker

profilometer. The current density-voltage (J–V) characteristics were measured with a Keithley 2400 source-meter under AM 1.5G (100 $mWcm^{-2}$) solar simulator.

2.5.2. Synthesis of 5-oxo-5-phenylpentanoate (2)

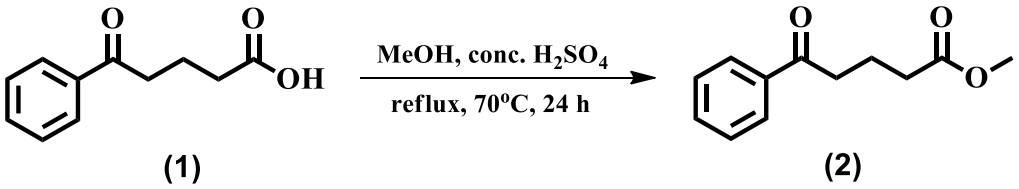

(1) (2)

To mixture of 4-benzoylbutyric acid, **1** (10 g, 52.6 mmol) and methanol (30 mL), concentrated sulphuric acid (1 mL) was added dropwise through the sides of the R.B. flask. The resultant solution was refluxed at 70 °C for 18 h. Reaction mixture was allowed to cool to room temperature; the solvent was evaporated under reduced pressure and extracted with ethyl acetate (3 x 50 mL). Organic layer was evaporated and the crude product was purified through column chromatography using silica gel (100-200 mesh) with ethyl acetate-hexane as the eluent (R_f : 0.5, eluent: 20% ethyl acetate-hexane). Yield = 80% (9.2 g) as colourless oil.

^{1}H NMR ($CDCl_3$, 500 MHz), δ (ppm): 7.97 (t, J = 7 Hz, 2H), 7.58 (t, J = 12 Hz, 1H), 7.48 (t, J = 12.25 Hz, 2H), 3.67 (s, 3H), 3.07 (t, J = 12 Hz, 2H), 2.47 (t, J = 12 Hz, 2H), 2.12 (m, J = 12 Hz, 2H).

^{13}C NMR ($CDCl_3$, 125 MHz), δ (ppm): 199.34, 173.66, 136.75, 133.04, 128.75, 127.97, 51.50, 37.38, 33.05, 19.42.

Mass (HRMS): Calculated for $C_{12}H_{14}O_3$: 206.09 (M); found: 207.19 (M+H).

2.5.3. Synthesis of 5-oxo-5-phenylpentanoate p-tosylhydrazone (3)

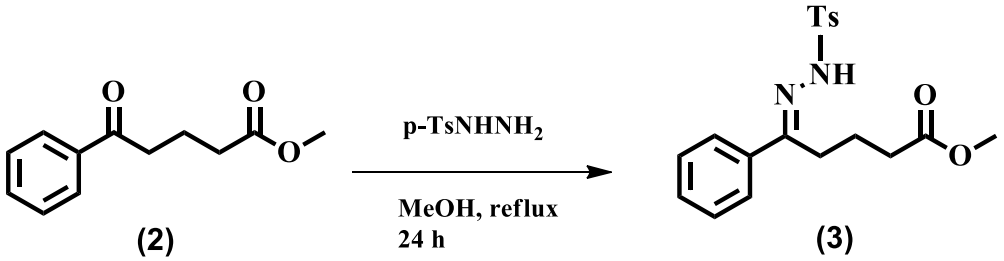

A mixture of 5-oxo-5-phenylpentanoate, **2** (9 g, 44.1 mmol), p-toluenesulfonyl hydrazide (12.33 g, 66.15 mmol) and methanol (30 mL) was stirred and refluxed for 6 h. The mixture was stirred at room temperature for 24 h and then cooled to -10 °C. The precipitated product was collected by filtration, washed with cold methanol and dried in a desiccator to yield 12 g (72%) tosylhydrazone as white crystals.

^{1}H NMR ($CDCl_3$, 500 MHz), δ (ppm): 7.92 (d, J = 8 Hz, 1H), 7.65 (t, J = 6 Hz, 2H), 7.34 (t, J = 3.25 Hz, 3H), 7.30 (t, J = 11.5 Hz, 2H), 3.81 (s, 3H), 2.64 (t, J = 8.25 Hz, 2H), 2.40 (s, 3H), 2.34 (t, J = 6 Hz, 2H), 1.71 (m, J = 5.6 Hz, 2H).

^{13}C NMR ($CDCl_3$, 125 MHz), δ (ppm): 174.74, 153.85, 143.79, 136.18, 135.98, 129.50, 128.44, 127.93, 126.23, 52.31, 32.15, 25.88, 21.59, 20.93.

Mass (HRMS): Calculated for $C_{19}H_{22}N_2O_4S$: 374.13 (M); found: 375.90 (M+2H).

2.5.4. Synthesis of methyl [6, 6]-Phenyl-C_{61}-butyrate, PCBM

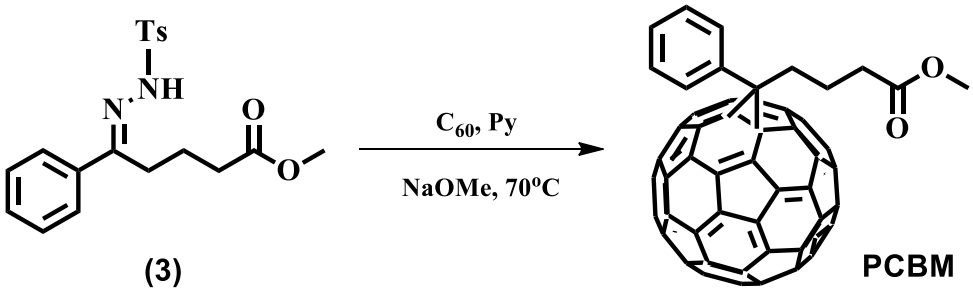

5-oxo-5-phenylpentanoate p-tosylhydrazone, **3** (50 mg, 0.134 mmol) was dissolved in 5 mL of anhydrous pyridine in a dried two-neck R.B. flask provided with N_2 inlet. Then sodium methoxide (10 mg, 0.185 mmol) was added and the mixture was stirred for 15 min. A solution of C_{60} (48 mg, 0.067 mmol) in 15 mL of HPLC grade 1,2-dichlorobenzene was added and the homogeneous reaction mixture was stirred at 75 $^{\circ}$C for 12 h. The course of the reaction was followed by TLC (SiO_2/toluene). The desired compound was separated by column chromatography using silica gel (100-200 mesh) with toluene as the eluent (R_f : 0.7, eluent: toluene). The resulting solution was concentrated to 15 mL and refluxed for 24 hours for isomerization. 1,2-dichlorobenzene was removed by micro distillation and the product was precipitated by methanol and dried to obtain brown solid in 16% yield (20 mg).

^{1}H NMR ($CDCl_3$, 500 MHz), δ (ppm): 7.98, (t, J = 4.25 Hz, 2H), 7.58 (t, J = 7.75 Hz, 2H), 7.45 (m, J = 2.3 Hz, 3H), 3.61 (s, 1H), 2.17(m, J = 8 Hz, 2H), 1.66 (m, J = 4.125 Hz, 2H), 1.48 (m, J = 4.125 Hz, 2H).

^{13}C NMR ($CDCl_3$, 125 MHz), δ (ppm): 173.52, 148.81, 147.81, 145.16, 145.09, 145.04, 144.80, 144.68, 144.52, 144.44, 144.02, 143.77, 143.04, 143.00, 142.94, 142.24, 142.19, 142.14, 142.12, 141.00, 140.76, 138.04, 137.58, 136.74, 132.10, 128.45, 128.26, 51.86, 51.71, 33.89, 33.68, 22.38.

MALDI (m/z): Calculated for $C_{71}H_{14}O_2$: 912.09 (M); found: 913.19 (M+H).

2.5.5. Synthesis of [6, 6]-Phenyl-C_{61}-butyric acid, PCBA

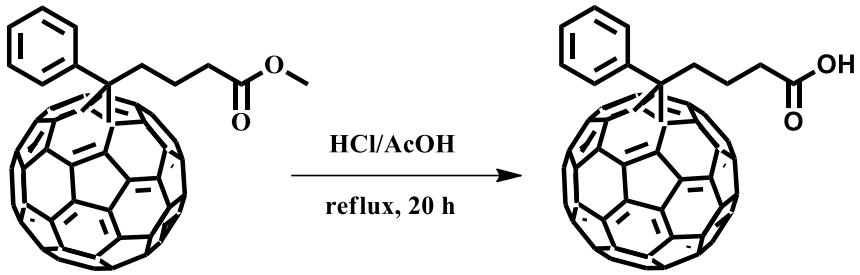

PCBM **PCBA**

To a solution of **PCBM** (200 mg) in toluene (75 mL) was added glacial acetic acid (30 mL) and concentrated hydrochloric acid (15 mL). The mixture was stirred and refluxed for 20 h. The course of the reaction was followed by TLC. All volatile components were removed under reduced pressure. The solid residue was washed with methanol and dried to obtain black coloured product with quantitative yield. The PCBA was highly insoluble in common NMR solvents to record a spectrum.

MALDI (m/z): Calculated for $C_{71}H_{14}O_2$: 898.10 (M); found: 898 (M).

2.5.6. Synthesis of (3-Phenyl-3,4-dihydro-2H-benzo[e]-[1,3] oxazin-6-yl)methanol , MB

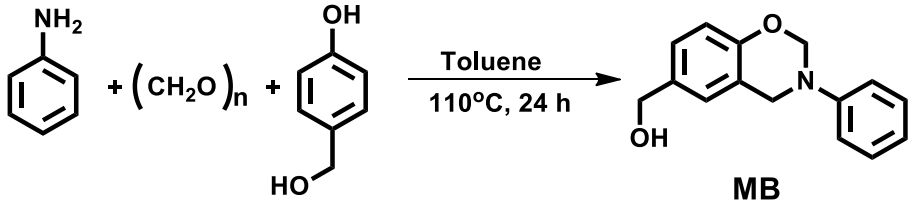

MB

To a solution of aniline (1 g, 80.6 mmol) in toluene (40 ml) 4-hydroxybenzyl alcohol (0.75 g, 80.6 mmol) and paraformaldehyde (484 mg, 161.2 mmol) were added and stirred at 110 ^oC for 8 h. The solution was allowed to cool to room temperature and

the solid residue was collected by filtration and recrystallized using toluene to afford pale yellow crystals in 38% (0.75 g) yield.

^{1}H NMR (500 MHz, $CDCl_3$), δ (ppm): 7.25 (t, 2H), 7.11 (m, 3H), 7.44 (m, 1H), 7.03 (s, 1H), 6.92 (t, 1H), 6.77 (d, 1H), 5.35 (s, 2H), 4.62 (s, 2H), 4.56 (s, 2H).

^{13}C NMR (125 MHz, $CDCl_3$), δ (ppm): 153.98, 148.33, 133.23, 129.29, 127.03, 125.83, 121.58, 120.89, 118.38, 117.04, 79.61, 65.06, 50.53.

HRMS (m/z): Calculated for $C_{15}H_{15}NO_2$: 240.28 (M); Found: 240.28 (M).

2.5.7. Synthesis of [6, 6]-phenyl-C_{61}-butyricbenzoxazine ester, PCBB

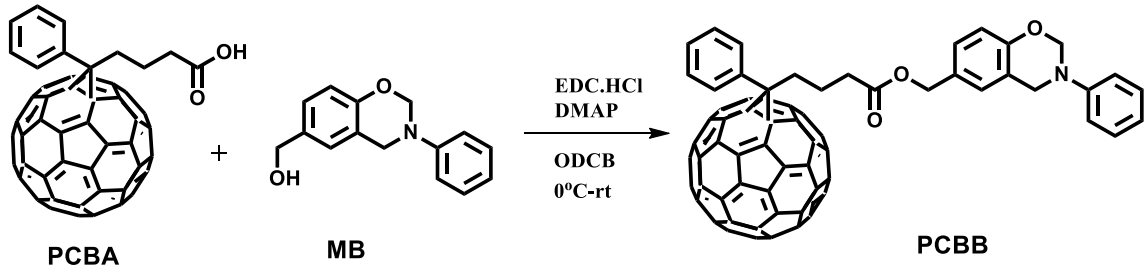

To a solution of [6, 6]-Phenyl-C_{61}-butyric acid (50 mg, 0.056 mmol) in 1,2-dichlorobenzene (5 mL) was added 4-dimethylaminopyridine (7 mg, 0.056 mmol), (16 mg, 0.084 mmol) and stirred for 10 min at 0 °C. Methylol benzoxazine (17 mg, 0.067 mmol) was added directly to the reaction mixture and stirred overnight at room temperature. The crude mixture was purified by column chromatography using toluene (R_f = 0.6) afforded brown colour solid in 24% yield (15 mg).

^{1}H NMR (500 MHz, $CDCl_3$), δ (ppm): 7.91 (t, 2H), 7.52 (m, 3H), 7.43(m, 3H), 7.09(t, 2H), 6.97(m, 2H), 6.91(t, 1H), 5.35 (s, 2H), 4.94 (s, 2H), 4.61(s, 2H), 2.90(t, 2H), 2.54(t, 2H), 2.19(m, 2H).

^{13}C NMR (125 MHz, $CDCl_3$), δ (ppm): 172.96, 154.50, 150.69, 148.80, 148.26, 147.78, 145.84, 145.20, 145.15, 145.07, 145.04, 144.79, 144.67, 144.51, 144.40, 144.01, 143.76, 143.10, 143.00, 142.94, 142.91, 142.21, 142.18, 142.13, 142.11, 140.98, 140.75, 138.03, 137.57, 136.72, 132.11, 129.05, 128.45, 128.26, 128.14, 127.30, 121.62, 120.92, 118.99, 118.31, 79.86, 66.21, 51.84, 34.11, 33.62, 22.37.

MALDI (m/z): calculated for $C_{86}H_{25}NO_3^+$, 1119.48 (M); found, 1120.41 (M+H).

2.5.8. BHJ Device Fabrication

The ZnO sol was prepared using a sol-gel procedure by dissolving zinc acetate dihydrate ($C_4H_6O_4Zn.2(H_2O)$, 99.9%, 1.6 g) and monoethanolamine ($HOCH_2CH_2NH_2$, 99%, 0.045 g) in anhydrous 2-methoxyethanol (> 99.8%, 0.96 mL) under vigorous stirring for hydrolysis reaction and aging for 3 h. The solar cell devices were fabricated under optimized conditions according to the modified reported procedure.[28] The patterned indium tin oxide (ITO)-coated glass substrate was first cleaned with detergent, ultrasonicated in DI-water, chloroform and isopropyl alcohol for 10 min, respectively and subsequently dried in an oven overnight. After UV-ozone treatment for 15 min, nanosized ZnO thin films with a thickness of ca. 50 nm were spin-coated using the sol-gel precursor solution at 3000 rpm on top of the ITO substrate. The films were sintered at 200 °C for 30 min in air. During this process the precursor converts to ZnO gel and forms a transparent thin film of ZnO nanoparticle. For device fabricated with **C-PCBB** interfacial layer (device B), an *o*-DCB solution containing **PCBB** (5 mg/mL) was spin-cast on the ZnO film to form a thin film with a

thickness of ca. 10 nm. Subsequently, the drop-cast film were heated at 200 °C for 15 min in the glove box for thermal cross-linking. For devices A and B, a ODCB solution containing a mixture of **P3HT**/$PC_{61}BM$ (1:1, w/w) was then spin-cast to form a 130 nm thin film on top of the ZnO (Device A) and **C-PCBB** (Device B) thin films, respectively. Both the devices were thermally annealed at 120 °C for 10 min in the glove box followed by spin-coating vanadium pentoxide with a thickness of ca. 40 nm and then heated at 120 °C in the glove box. Finally, the top electrode of Ag film (100 nm-thick), was evaporated thermally at a pressure below 10^{-6} torr. Devices without encapsulation were characterized in ambient condition. The active area used for the measurement was 0.1 cm^2 and were optimized by testing approximately 10-12 cells.

2.6. REFERENCES

1) Li, G., Zhu, R., and Yang, Y., Polymer solar cells. *Nat. Photonics* **2012**, *6*, 153-161.
2) Kippelen, B.; Brédas, J.-L., Organic photovoltaics. *Energ. Environ. Sci.* **2009**, *2*, 251-261.
3) Peet, J.; Heeger, A. J.; Bazan, G. C., "Plastic" solar cells: self-assembly of bulk heterojunction nanomaterials by spontaneous phase separation. *Acc. Chem. Res.* **2009**, *42*, 1700-1708.
4) Brady, M. A.; Su, G. M.; Chabinyc, M. L., Recent progress in the morphology of bulk heterojunction photovoltaics. *Soft Matt.* **2011**, *7*, 11065-11077.
5) Dang, M. T.; Hirsch, L.; Wantz, G.; Wuest, J. D., Controlling the morphology and performance of bulk heterojunctions in solar cells. Lessons learned from the benchmark poly(3-hexylthiophene):[6,6]-phenyl-C61-butyric acid methyl ester system. *Chem. Rev.* **2013**, *113*, 3734-3765.
6) Cheng, Y. J.; Yang, S. H.; Hsu, C. S., Synthesis of conjugated polymers for organic solar cell applications. *Chem. Rev.* **2009**, *109*, 5868-5923.
7) Li, C.-Z.; Yip, H.-L.; Jen, A. K. Y., Functional fullerenes for organic photovoltaics. *J. Mater. Chem.* **2012**, *22*, 4161-4177.

8) Yip, H.-L.; Jen, A. K. Y., Recent advances in solution-processed interfacial materials for efficient and stable polymer solar cells. *Energ. Environ. Sci.* **2012**, *5*, 5994-6011.

9) Heremans, P.; Cheyns, D.; Rand, B. P., Strategies for increasing the efficiency of heterojunction organic solar cells: material selection and device architecture. *Acc. Chem. Res.* **2009**, *42*, 1740-1747.

10) Letian, D.; Jingbi, Y.; Jun, Y.; Chun-Chao, C.; Youjun, H.; Seiichiro, M.; Tom, M.; Keith, E.; Gang, L.; Yang, Y., Tandem polymer solar cells featuring a spectrally matched low-bandgap polymer. *Nat. Photonics* **2012**, *6*, 180–185.

11) He, Y.; Chen, H.-Y. Y.; Hou, J.; Li, Y., Indene-C(60) bisadduct: a new acceptor for high-performance polymer solar cells. *J. Am. Chem. Soc.* **2010**, *132*, 1377-1382.

12) Cheng, Y.-J.; Liao, M.-H.; Chang, C.-Y.; Kao, W.-S.; Wu, C.-E.; Hsu, C.-S., Di(4-methylphenyl)methano-C60Bis-Adduct for Efficient and Stable Organic Photovoltaics with Enhanced Open-Circuit Voltage. *Chem. Mater.* **2011**, *23*, 4056-4062.

13) Voroshazi, E.; Vasseur, K.; Aernouts, T.; Heremans, P.; Baumann, A.; Deibel, C.; Xue, X.; Herring, A. J.; Athans, A. J.; Lada, T. A.; Richter, H.; Rand, B. P., Novel bis-C60 derivative compared to other fullerene bis-adducts in high efficiency polymer photovoltaic cells. *J. Mater. Chem.* **2011**, *21*, 17345-17352.

14) Lee, J. U.; Jung, J. W.; Jo, J. W.; Jo, W. H., Degradation and stability of polymer-based solar cells. *J. Mater. Chem.* **2012**, *22*, 24265.

15) Stabilizing polymer-based bulk heterojunction solar cells via crosslinking. *Polym. Int.* **2014**, *63*, 1346-1361.

16) Xiaoniu, Y.; Joachim, L., Toward High-Performance Polymer Solar Cells: The Importance of Morphology Control. *Macromolecules* **2007**, *40*, 1353-1362.

17) Ye, L.; Zhang, S.; Ma, W.; Fan, B.; Guo, X.; Huang, Y.; Ade, H.; Hou, J., From Binary to Ternary Solvent: Morphology Fine-tuning of D/A Blends in PDPP3T-based Polymer Solar Cells. *Adv. Mater.* **2012**, *24*, 6335-6341.

18) Liao, M. H.; Tsai, C. E.; Lai, Y. Y.; Cao, F. Y.; Wu, J. S.; Wang, C. L.; Hsu, C. S.; Liau, I.; Cheng, Y. J., Morphological Stabilization by Supramolecular Perfl uorophenyl-C-60 Interactions Leading to Effi cient and Thermally Stable Organic Photovoltaics. *Adv. Funct. Mater.* **2014**, *24*, 1418-1429.

19) Martin, D.; Harald, H.; Christoph, W.; Helmut, N.; Niyazi, S. S.; Wolfgang, S.; Friedrich, S.; Christoph, T.; Markus, C. S.; Zhengguo, Z.; Russell, G., Stabilization of the nanomorphology

of polymer–fullerene "bulk heterojunction" blends using a novel polymerizable fullerene derivative. *J. Mater. Chem.* **2005**, *15*, 5158-5163.

20) Bumjoon, J. K.; Yoshikazu, M.; Biwu, M.; Jean, M. J. F., Photocrosslinkable Polythiophenes for Efficient, Thermally Stable, Organic Photovoltaics. *Adv. Funct. Mater.* **2009**, *19*.

21) Chang-Yong, N.; Yang, Q.; Young, S. P.; Htay, H.; Xinhui, L.; Benjamin, M. O.; Charles, T. B.; Robert, B. G., Photo-Cross-Linkable Azide-Functionalized Polythiophene for Thermally Stable Bulk Heterojunction Solar Cells. *Macromolecules* **2012**, *45*, 2338-2347.

22) Yen-Ju, C.; Fong-Yi, C.; Wei-Cheng, L.; Chiu-Hsiang, C.; Chao-Hsiang, H., Self-Assembled and Cross-Linked Fullerene Interlayer on Titanium Oxide for Highly Efficient Inverted Polymer Solar Cells. *Chem. Mater.* **2011**, *23*, 1512-1518.

23) Namchul, C.; Hin-Lap, Y.; Steven, K. H.; Kung-Shih, C.; Tae-Wook, K.; Joshua, A. D.; David, F. Z.; Alex, K. Y. J., n-Doping of thermally polymerizable fullerenes as an electron transporting layer for inverted polymer solar cells. *J. Mater. Chem.* **2011**, *21*, 6956-6961.

24) Cheng, Y. J.; Hsieh, C. H.; He, Y.; Hsu, C. S.; Li, Y., Combination of indene-C60 bis-adduct and cross-linked fullerene interlayer leading to highly efficient inverted polymer solar cells. *J. Am. Chem. Soc.* **2010**, *132*, 17381-17383.

25) Iskin, B.; Yilmaz, G.; Yagci, Y., Mono-addition synthesis of polystyrene-fullerene (C60) conjugates by thiol-ene chemistry. *Chem. Eur. J.* **2012**, *18*, 10254-10257.

26) Shoji, M.; Yue, Z.; Kazuhito, H.; Keisuke, T., Controlled Synthesis of Fullerene-Attached Poly(3-alkylthiophene)-Based Copolymers for Rational Morphological Design in Polymer Photovoltaic Devices. *Macromolecules* **2012**, *45*, 6424-6437.

27) Dan, H.; Xiaoyan, D.; Wei, Z.; Zuo, X.; Liming, D., Improving the stability of **P3HT**/PC61BM solar cells by a thermal crosslinker. *J. Mater. Chem. A* **2013**, *1*, 4589-4594

28) Hsieh, C.-H. H.; Cheng, Y.-J. J.; Li, P.-J. J.; Chen, C.-H. H.; Dubosc, M.; Liang, R.-M. M.; Hsu, C.-S. S., Highly efficient and stable inverted polymer solar cells integrated with a cross-linked fullerene material as an interlayer. *J. Am. Chem. Soc.* **2010**, *132*, 4887-4893.

29) Chang, C.-Y. Y.; Wu, C.-E. E.; Chen, S.-Y. Y.; Cui, C.; Cheng, Y.-J. J.; Hsu, C.-S. S.; Wang, Y.-L. L.; Li, Y., Enhanced performance and stability of a polymer solar cell by incorporation of vertically aligned, cross-linked fullerene nanorods. *Angew. Chem. Int. Ed.* **2011**, *50*, 9386-9390.

30) Francesco, G.; Nazario, M., Fullerene Polymers: Synthesis and Properties. *Chem. Rev.* **2006**, *106*, 5136-5190.

31) Isla, H.; Perez, E. M.; Martin, N., High Degree of Polymerization in a Fullerene-Containing Supramolecular Polymer. *Angew. Chem. Int. Ed.* **2014**, *53*, 5629-5633.

32) Haruk, A. M.; Mativetsky, J. M., Supramolecular Approaches to Nanoscale Morphological Control in Organic Solar Cells. *Int J Mol Sci* **2015**, *16*, 13381-13406.

33) Chutayothin, P.; Ishida, H., Cationic Ring-Opening Polymerization of 1,3-Benzoxazines: Mechanistic Study Using Model Compounds. *Macromolecules* **2010**, *43*, 4562-4572.

34) Sawaryn, C.; Landfester, K.; Taden, A., Cationic Polybenzoxazines. A Novel Polyelectrolyte Class with Adjustable Solubility and Unique Hydrogen-Bonding Capabilities. *Macromolecules* **2011**, *44*, 7668-7674.

35) Carlos, A. Z.; Stephen, B.; Seth, R. M., Approaches to Solution-Processed Multilayer Organic Light-Emitting Diodes Based on Cross-Linking. *Chem. Mater.* **2011**, *23*, 658-681.

36) Babu, S. S.; Mohwald, H.; Nakanishi, T., Recent progress in morphology control of supramolecular fullerene assemblies and its applications. *Chem. Soc. Rev.* **2010**, *39*, 4021-4035.

37) McClenaghan, N. D.; Absalon, C.; Bassani, D. M., Facile Synthesis of a Fullerene-Barbituric Acid Derivative and Supramolecular Catalysis of Its Photoinduced Dimerization. *J. Am. Chem. Soc.* **2003**, *125*, 13004-13005.

38) Buchaca-Domingo, E.; Ferguson, A. J.; Jamieson, F. C.; McCarthy-Ward, T.; Shoaee, S.; Tumbleston, J. R.; Reid, O. G.; Yu, L.; Madec, M. B.; Pfannmoller, M.; Hermerschmidt, F.; Schroder, R. R.; Watkins, S. E.; Kopidakis, N.; Portale, G.; Amassian, A.; Heeney, M.; Ade, H.; Rumbles, G.; Durrant, J. R.; Stingelin, N., Additive-assisted supramolecular manipulation of polymer:fullerene blend phase morphologies and its influence on photophysical processes. *Mater. Horizons* **2014**, *1*, 270-279.

39) Sun, Y.-P.; Ma, B.; Bunker, C. E.; Liu, B., All-Carbon Polymers (Polyfullerenes) from Photochemical Reactions of Fullerene Clusters in Room-Temperature Solvent Mixtures. *J. Am. Chem. Soc.* **1995**, *117*, 12705-12711.

40) Koji, H.; Akimitsu, N.; Eiichi, N., Photocrosslinking of Fullerene Vesicles that Prevents Phase Transition and Decreases Water Permeation. *Chem. Lett.* **2013**, *42*, 1176-1178.

41) Wang, J.; Shen, Y.; Kessel, S.; Fernandes, P.; Yoshida, K.; Yagai, S.; Kurth, D. G.; Möhwald, H.; Nakanishi, T., Self-assembly made durable: water-repellent materials formed by cross-linking fullerene derivatives. *Angew. Chem. Int. Ed.* **2009**, *48*, 2166-2170.

42) Busseron, E.; Cid, J. J.; Wolf, A.; Du, G.; Moulin, E.; Fuks, G.; Maaloum, M.; Polavarapu, P.; Ruff, A.; Saur, A. K.; Ludwigs, S.; Giuseppone, N., Light-controlled morphologies of self-assembled triarylamine-fullerene conjugates. *ACS Nano* **2015**, *9*, 2760-72.

43) Hummelen, J. C.; Knight, B. W.; LePeq, F.; Wudl, F.; Yao, J.; Wilkins, C. L., Preparation and Characterization of Fulleroid and Methanofullerene Derivatives. *J. Org. Chem.* **1995**, *60*, 532-538.

44) Chacun-Lefevre, L.; Buon, C.; Bouyssou, P.; Coudert, G., Synthesis of 3-substituted-4H-1,4-benzoxazines. *Tetrahedron Lett.* **1998**, *39*, 5763-5764.

45) He, Y.; Zhao, G.; Peng, B.; Li, Y., High-Yield Synthesis and Electrochemical and Photovoltaic Properties of Indene-C70 Bisadduct. *Adv. Funct. Mater.* **2010**, *20*, 3383-3389.

46) Zhang, Y.; Matsuo, Y.; Li, C.-Z.; Tanaka, H.; Nakamura, E., A Scalable Synthesis of Methano[60]fullerene and Congeners by the Oxidative Cyclopropanation Reaction of Silylmethylfullerene. *J. Am. Chem. Soc.* **2011**, *133*, 8086-8089.

47) Wang, Y.; Benten, H.; Ohara, S.; Kawamura, D.; Ohkita, H.; Ito, S., Measurement of Exciton Diffusion in a Well-Defined Donor/Acceptor Heterojunction based on a Conjugated Polymer and Cross-Linked Fullerene Derivative. *ACS Appl. Mater. Interfaces* **2014**, *6*, 14108-14115.

48) Kim, H. U.; Kim, J. H.; Kang, H.; Grimsdale, A. C.; Kim, B. J.; Yoon, S. C.; Hwang, D. H., Naphthalene-, anthracene-, and pyrene-substituted fullerene derivatives as electron acceptors in polymer-based solar cells. *ACS Appl. Mater. Interfaces* **2014**, *6*, 20776-85.

49) Liang, Z.; Ni, X.; Li, X.; Shen, Z., Synthesis and characterization of benzoxazine-functionalized amine bridged bis(phenolate) lanthanide complexes and their application in the ring-opening polymerization of cyclic esters. *Dalton Trans.* **2012**, *41*, 2812-9.

50) Fujita, N.; Yamashita, T.; Asai, M.; Shinkai, S., Formation of [60]fullerene nanoclusters with controlled size and morphology through the aid of supramolecular rod-coil diblock copolymers. *Angew. Chem. Int. Ed.* **2005**, *44*, 1257-1261.

51) Kawauchi, T.; Kumaki, J.; Yashima, E., Nanosphere and nanonetwork formations of [60]fullerene-end-capped stereoregular poly(methyl methacrylate)s through stereocomplex formation combined with self-assembly of the fullerenes. *J. Am. Chem. Soc.* **2006**, *128*, 10560-10567.

CHAPTER 3

RATIONAL SYNTHESIS OF A POLYMERIZABLE FULLERENE-ANILINE DERIVATIVE: STUDY OF PHOTOPHYSICAL, MORPHOLOGICAL AND PHOTOVOLTAIC PROPERTIES

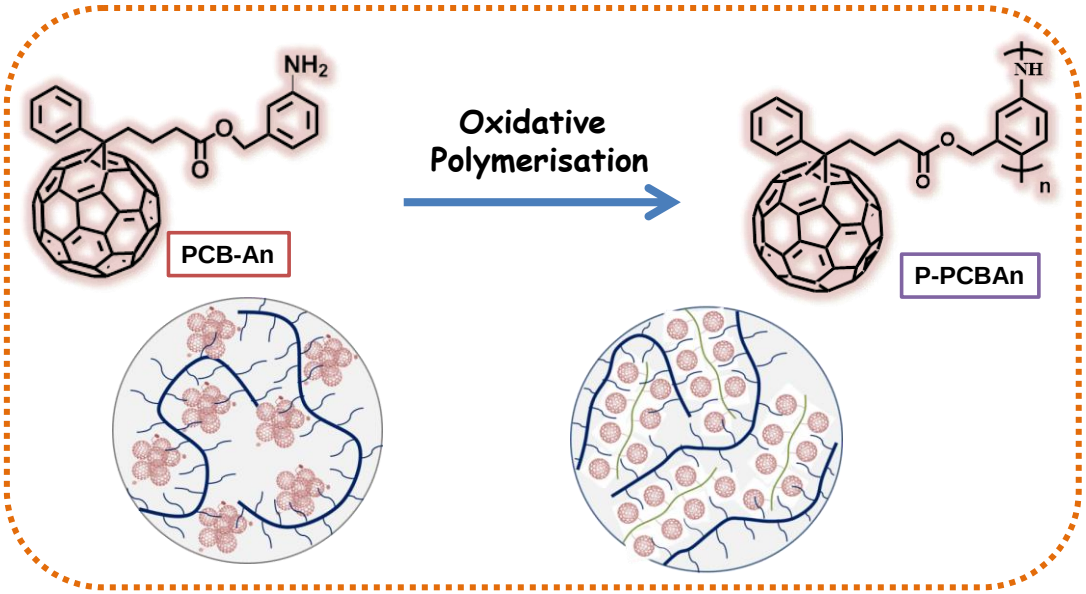

3.1. ABSTRACT

*This chapter report the synthesis of a polymerizable, aniline appended fullerene derivative, 3-aminobenzyl-phenyl-C_{61}-butyrate (**PCBAn**) and its corresponding polymer, and detailed photophysical and morphological analysis towards application as acceptors in polymer solar cells (BHJ-PSCs). The synthesis of **PCBAn** was accomplished via the coupling of [6,6]-Phenyl-C_{61}-butyric acid (**PCBA**) with tert-butyl-3-(hydroxymethyl)phenyl)carbamate and subsequent deprotection of the BOC group. The poly-3-aminobenzyl-phenyl-C_{61}-butyrate (**P-PCBAn**), having a substituted polyaniline (PANI) skeletal structure, was synthesized via $FeCl_3$ oxidative polymerisation of **PCBA** in*

its non-conducting leucoemaraldine state. Both the derivatives were characterized using various spectroscopic techniques such as UV-Vis, FT-IR, ^{1}H NMR and Mass Spectroscopy. HOMO and LUMO energies estimated using optical and electrochemical techniques revealed upshifted LUMO levels for ***PCBAn*** *(-3.68 eV, ∆E = 0.1 eV) and* ***P-PCBAn*** *(-3.66 eV, ∆E = 0.12 eV) compared to the parental fullerene derivative,* ***PCBM*** *(-3.78 eV). The morphologies of* ***PCBAn*** *and* ***P-PCBAn*** *individualy and in polymer blends with* ***P3HT*** *were investigated using AFM and TEM analysis, which showed nanoflake like aggregates for* ***PCBAn*** *and a favourable interconnected nanonetwork structure for* ***P-PCBAn****. Similarly, the wide angle X-ray scattering (WAXS) studies of* ***PCBAn*** *films from THF/water (3:7) mixture and* ***P-PCBAn*** *films from 1,2-dichlorobenzene exhibited plane reflections of lamellar mesophases with d-spacing of 3.4 nm and 3 nm for PCBAn and P-PCBAn, repsectively. The fluorescence quenching experiments with* ***P3HT*** *indicated efficient electron transfer from* ***P3HT*** *to* ***P-PCBAn*** *and* ***PCBAn*** *fullerene acceptors with* ***P-PCBAn*** *being more efficient. This is attributed to the combined effect of bicontinuous interpenetrating network and better charge transport properties of* ***P3HT****:****P-PCBAn*** *polymer blend compared to* ***P3HT****:****PCBAn****. The fabrication of inverted BHJ-PSC device using* ***PCBAn*** *and* ***P-PCBAn*** *as acceptor in combination with* ***P3HT*** *showed PCE of 0.9% and 1.1%, respectively. The observed lower PCE of both devices in comparison to reported* ***P3HT: PCBM*** *device might be due to the presence of nitrogen groups of aniline in* ***PCBAn*** *and nonconducting* ***PANI*** *in* ***P-PCBAn*** *which might induce charge imbalance in the BHJ active layer. The polymeric acceptor and rational design strategy used here could open up new opportunities in the PSC device fabrication.*

3.2. INTRODUCTION

Tremendous research has been commenced in the last two decades in the area of bulk heterojunction (BHJ) polymer solar cells (PSCs) because of its potential future application as an easy processable, flexible, lightweight, inexpensive and transportable energy source.[1,2] During this period, Poly(3-hexylthiophene) (**P3HT**) donor and the phenyl-C_{61}-butyric acid methyl ester (**PCBM**), acceptor polymer blends were came out to be one of the most well studied systems and widely used as standard for comparing the power conversion efficiency (PCE) of PSCs.[3] Along with device architecture, processability and annealing with different solvent composition lead the **P3HT-PCBM** system to reach PCE of greater than 5%.[4] Also, the development of various polymeric donor systems led to the record high PSC efficiency of >10%.[5]

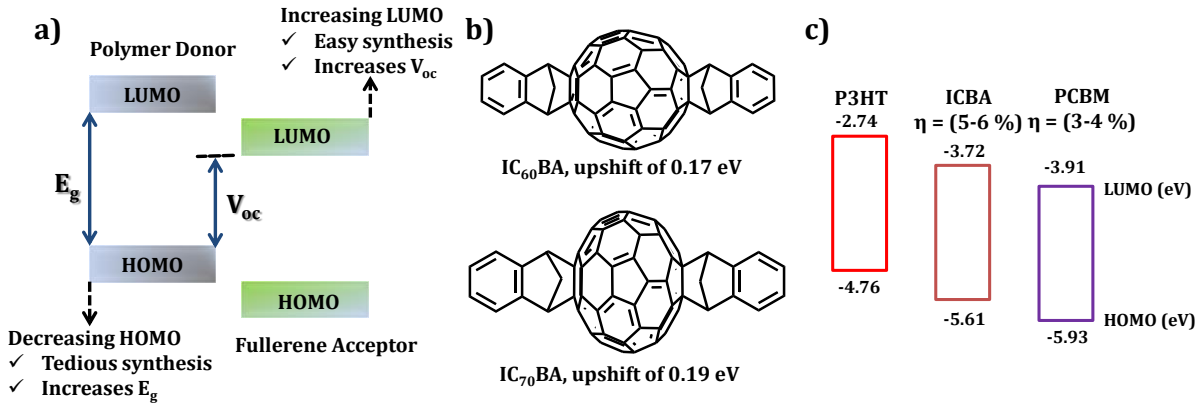

Figure 3.1. a) Energy diagram indicating puzzle of upshifting the LUMO of acceptor is more convenient than downshifting HOMO of donor. b) Chemical structure of $IC_{60}BA$ and $IC_{70}BA$ having upshifted LUMO levels of 0.17 eV and 0.19 eV respectively compared to $PC_{60}BM$. c) Energy level diagram of **P3HT**, $IC_{70}BA$ and $PC_{60}BM$ showing better electron transfer pathway in **P3HT**:ICBA leading to increased solar cell performance.

For example, Yang Yang *et al.* have developed a low band gap polymer poly[2,7-(5,5-bis-(3,7-dimethyloctyl)-5H-dithieno[3,2-b:2',3'-d]pyran)-alt-4,7-(5,6-difluoro-2,1,3-benzothiadiazole)](PDTP-DFBT) with a PCE of 8.1% in combination with $PC_{71}BM$ as an acceptor with inverted configurations and a highest PCE of 10.2% with tandem device architecture.[6] Yongfang Li *et al.* reported remarkable PCE of 7.4% using vertically aligned cross-linked fullerene derivative as electron transport layer in **P3HT**: fullerene based system.[7] Compared to the tedious synthetic process of polymer functionalization, rationally modifying the **PCBM** acceptor part for achieving improved charge transport properties became a strategy of interest in the scientific community.[8] Many research groups approached smart modification of **PCBM** by substituting visible absorbing moieties,[9-12] self-assembling units,[13,14] tuning the Lowest Unoccupied Molecular Orbitals (LUMO)[15,16] and increasing the electron mobility[17,18] in order to achieve higher PCE by increasing electron transport properties. Also, up-shifting the LUMO of acceptor is an alternative for solving the puzzle of increasing the Voc of active layer (Figure 3.1a). V_{oc} can be increased either by down-shifting the HOMO of donor or by up-shifting the LUMO of acceptor.[19] But, down-shifting the donor HOMO level will automatically increase the net energy gap and hence it is not a good strategy. As shown in the Figure 3.1b Indene-C_{60} bisadduct (ICBA) and Indene-C_{70} bisadduct ($IC_{70}BA$) having 0.17 eV and 0.19 eV higher LUMO energy levels respectively, than **PCBM** are excellent acceptors for the **P3HT**-based PSCs due to the electron-rich character of indene and the bisadduct effect (Figure 3.1c).[20,21]

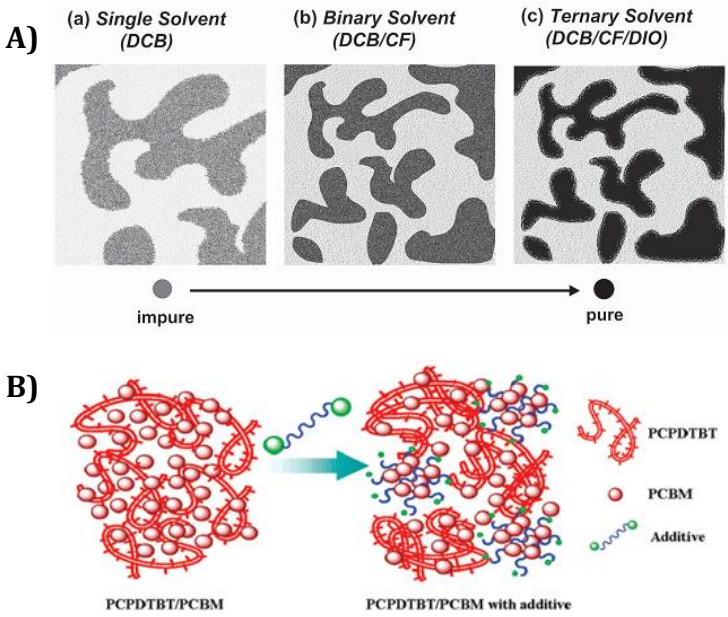

Figure 3.2. A) Morphological evolution of the PDPP3T/$PC_{71}BM$ blends prepared by different solvents, a) DCB: Dichlorobenzene, b) DCB/CF: Dichlorobenzene/Chloroform, c) DCB/CF//DIO: Dichlorobenzene/Chloroform/Diiodooctane (Adapted from reference 4). B) Schematic depiction of the role of the processing additive in the self-assembly of PCPDTBT, $PC_{71}BM$, and additives (Adapted from reference 24).

Out of many key parameters for the successful PSC device, active layer morphology plays crucial role and it is extremely necessary to obtain the bicontinuous interpenetrating architecture for better device performance.[22] Through systematic study many research groups adopted different strategies to optimize the morphology of polymer blend by varying the ratio and concentration of the donor-acceptor systems, choosing binary or ternary solvent, thermal annealing, solvent annealing and using appropriate solvent additives.[23,24] Jianhui Hou *et al*. observed the effect of ternary solvent composition 1,2-dichlorobenzene (ODCB), chloroform (CF) and 1,8-diiodooctane (DIO) on the bulk compositional morphology, and the crystallization behavior thereby tuning the net performance of the polymer solar cells.[4] The polymer

domain size and purity of the interface were better when moving from single solvent DCB to binary solvent, DCB/CF to ternary solvent, DCB/CF/DIO as shown in Figure 3.2A. They have scanned various solvent compositions and when the optimal composition of the ternary solvent is DCB/CF/DIO =76:19:5 (v/v/v) a PCE of 6.71% was recorded from the champion device, which is the highest one for DPP-based BHJ PSCs. In addition, Alan J. Heeger et *al.* showed the use of processing additives in creating phase separated active layer morphology.[24] During thermal annealing of polymer blend in presence of chorobenzene host solvent with added higher boiling point solvent alkanedithiol, the **PCBM** tends to remain in solution longer than the semiconducting polymer, thereby enabling controlled phase separated morphology as shown in Figure 3.2B.

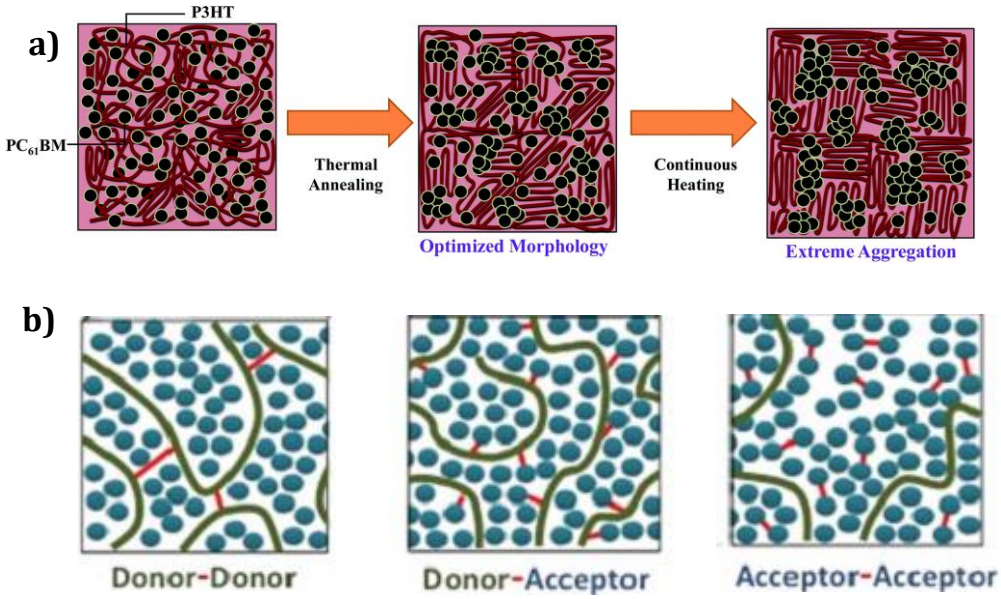

Figure 3.3. Schematic representation of a) changes in the active layer morphology due to aggregation tendency of fullerenes (Adapted from reference 26). b) Strategies used for freezing the nanostructure through cross-linking donor-donor, donor-acceptor or acceptor-acceptor units in the active layer (Adapted from reference 27).

Self-assembling nature of fullerenes also has been extensively used to organize them with polymer donor into one dimensional nanofibres or nanonetwork structures.[25] These soft techniques tend to give better nanoscale morphology and good phase separation. But, in actual solar cells these nanostructures undergo many heat-cool cycle over the time. As a result, the thermodynamically unstable nanostructures tend to aggregate into macroscopic phase separated structures and deteriorate device performance with time.[26] Since, fullerenes have higher tendency of aggregation compared to polymer donor, **PCBM** in the active layer is usually responsible for the formation of needle like structures upon ageing (Figure 3.3a). One way to overcome these problems is to arrest the morphology by cross-linking donor-donor, donor-acceptor or acceptor-acceptor units as shown in Figure 3.3b.[27,28] Following this strategy, many cross linkable units such as acetylene, styrene, oxetane, and epoxide have been attached to fullerene part in the design of new morphologically stable fullerene based acceptors.[29-32] But in many cases, post cross-linking methods fails to form monodisperse films and suffer from poor charge separation due to the presence of insulating cross-linkable groups.[33]

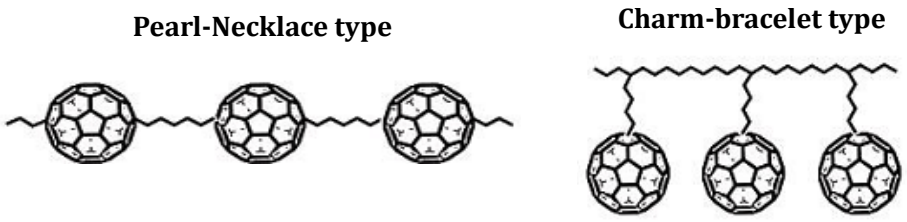

Figure 3.4. Representative structures of two types of polyfullerenes, Pearl-necklace type and Charm-bracelet type.

These limitations signifies the importance of new polymeric fullerene acceptor which in combination with the polymer donor can give resultant large interfacial area, efficient exciton dissociation and well separated pathways for free charge transport across the active layer. Most of the polymer based materials have the intrinsic one dimensional nanofibrous structure, easy polymerization conditions and excellent thermal stability. In this context, developing polyfullerene without affecting the core fullerene structure is of great scientific relevance for the optoelectronic applications.[28] Basically, there are two types of fullerene polymers known so far (Figure 3.4).[34] One is pearl necklace type, containing fullerene as the main chain polymer. Secondly, charm bracelet type polyfullerenes containing fullerenes in the pendent chain. Yuta Maeyoshi *et al.* used the single particle nanofabrication technique (SPNT) for the construction of organic nanowires by irradiating a polymer thin film with high-energy charged

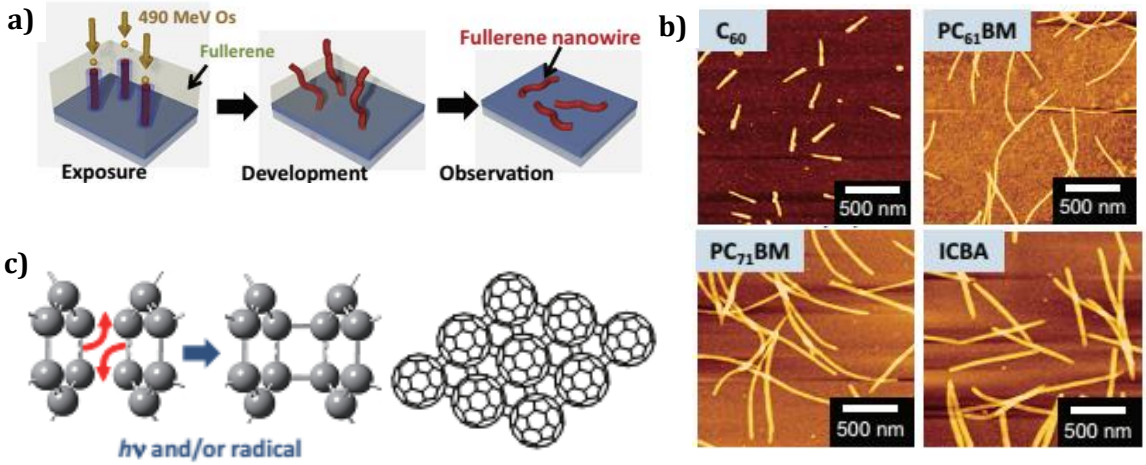

Figure 3.5. a) Schematic procedure for nanowire formation by SPNT; (left) irradiation of 490 MeV Os ions perpendicular to fullerene films, (center) development in CB or ODCB, where the non-irradiated area is dissolved, (right) nanowires formed are lying on the substrate. b) AFM images of nanowires formed from fullerene (C_{60}) and its derivatives ($PC_{61}BM$, $PC_{71}BM$ and ICBA). c) Proposed dimerization reaction via 2+2 cycloaddition (Adapted from reference 34).

particles.[35] The subsequent development process dissolves the unexposed area and isolated the nanowires from the film material as shown in Figure 3.5a. They have made nanowires of C_{60}, $PC_{61}BM$, $PC_{71}BM$, ICBA and extended the strategies to conjugated polymers such as poly(silane), poly(thiophene), and poly(fluorene) (Figure 3.5b). The proposed mechanism involves the cross-linking reaction of adjucent fullerenes via [2+2] cycloaddition reactions (Figure 3.5c). Although this technique leads to one dimensional polyfullerenes, they suffer from poor performance due to perturbation in the optoelectronic properties upon polymerisation. Many of such reported polyfullerenes have drawbacks such as tedious synthetic procedures, large insulating part in the substitution, solubility issues, and lack of one dimensional nanostructures.[36] Therefore, there exist need for the design of polyfullerene having facile monomer to polymer conversion, good miscibility with the donor counterpart, synthetic easiness and pocessing better optoelectronic properties than parental **PCBM**.

Out of numerous polymerizable groups available in the polymer chemistry arena, the polyaniline (**PANI**) is one of most extensively studied and cost effective polymer which is known for its high conductivity, synthetic easiness and good electrochemical properties.[37,38] Synthesis of **PANI** from its monomers by various methods such as oxidative polymerisation using APS or $FeCl_3$ both in aqueous and organic medium are known.[39] **PANI** can exist in three different oxidation states *viz.* the emeraldine (green form), leucoemaraldine (yellow form) and the pernigraniline oxidation state (black form) as shown in Figure 3.6.[40,41] These synthesized polymers often tend to give networked nano structure with improved electronic properties due

to which they can be better candidates for the design of polyfullerenes for the photovoltaic applications.[42] Fullerene-**PANI** composites and copolymerization of single fullerene unit with **PANI** tags have been previously studied.[38,43,44]

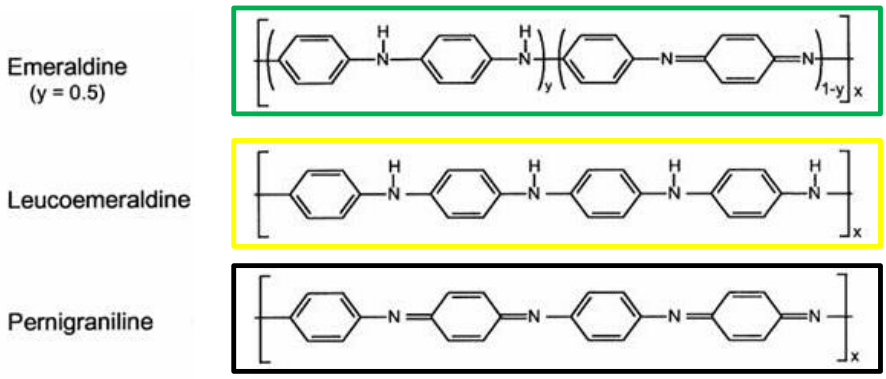

Figure 3.6. The three different oxidation states of **PANI** derivatives. The "green" form the emeraldine oxidation state, the "yellow" form represents the leucoemaraldine oxidation state and the "black" form the pernigraniline oxidation state of polyaniline (Adapted from reference 40).

Herein, we report the synthesis of a novel **PCBM** derivative with covalently modified aniline moiety, 3-aminobenzyl-[6, 6]-phenyl-C_{61}-butyrate ester (**PCBAn**) and its polymer, **P-PCBAn**. Detailed characterization of **PCBAn** and P- **PCBAn** along with photophysical and morphological analysis were undertaken with a view to understand their potential for applications in PSCs. The square wave voltammetry revealed the relatively upshifted LUMO levels of **P-PCBAn** compared to **PCBAn** and parental **PCBM**. Also, **P3HT**-fluorescence showed efficient quenching in the presence of **PCBAn** and **P-PCBAn** indicating efficient electron transport properties. The films of **P-PCBAn** exhibited networked nanostructure with enhanced absorption in the visible region compared to its monomer counterpart. The fabrication of BHJ-PSC device was

demonstrated using **P3HT**: **P-PCBAn** and **P3HT**: **PCBAn** polymer blends which revealed relatively higher device performance (1.1%) for **P-PCBAn** compared to **PCBAn** (0.9%).

3.3. RESULTS AND DISCUSSION

3.3.1. SYNTHESIS AND OXIDATIVE POLYMERISATION OF PCBAN

The synthesis of 3-aminobenzyl-[6,6]-phenyl-C_{61}-butyrate ester (**PCBAn**) was achieved by following Scheme 3.1. Acid hydrolysis of **PCBM** afforded [6,6]-Phenyl-C_{61}-butyric acid (**PCBA**) in quantitative yield which upon EDC mediated esterification reaction with tert-butyl-3-(hydroxymethyl)phenyl)carbamate gave the corresponding BOC protected **PCBAn** derivative in 57% yield. Further deprotection of Boc with trifluoroacetic acid, followed by neutralization with sodium bicarbonate resulted **PCBAn** in quantitative yield. Tert-butyl-(3-(hydroxymethyl)phenyl)carbamate was separately obtained in moderate yields by the BOC protection reaction of (3-aminophenyl)methanol and di-tert-butyl-dicarbonate. All the intermediates and final compounds were well characterized with various analytical and spectroscopic techniques. For example, ^{1}H NMR spectra of **PCBAn** showed characteristic proton signals corresponding to the methyl protons of the benzylamine group at 5.35 ppm and 4.94 ppm and the alkyl protons in the range of 2.19-2.9 ppm. In the ^{13}C NMR, we have observed chemically distinct carbon signals which can be assigned as per the structure of **PCBAn**. FT-IR spectrum of **PCBAn** showed peak at 1684 cm^{-1} corresponding to carbonyl stretching frequency. UV -Visible absorption spectrum revealed characteristic absorption of functionalized fullerene at 328 nm. The MALDI analysis showed the exact

mass of **PCBAn** at 1001.31. These spectral and analytical techniques confirm the successful coupling of the PCBA and benzoxazine moieties.

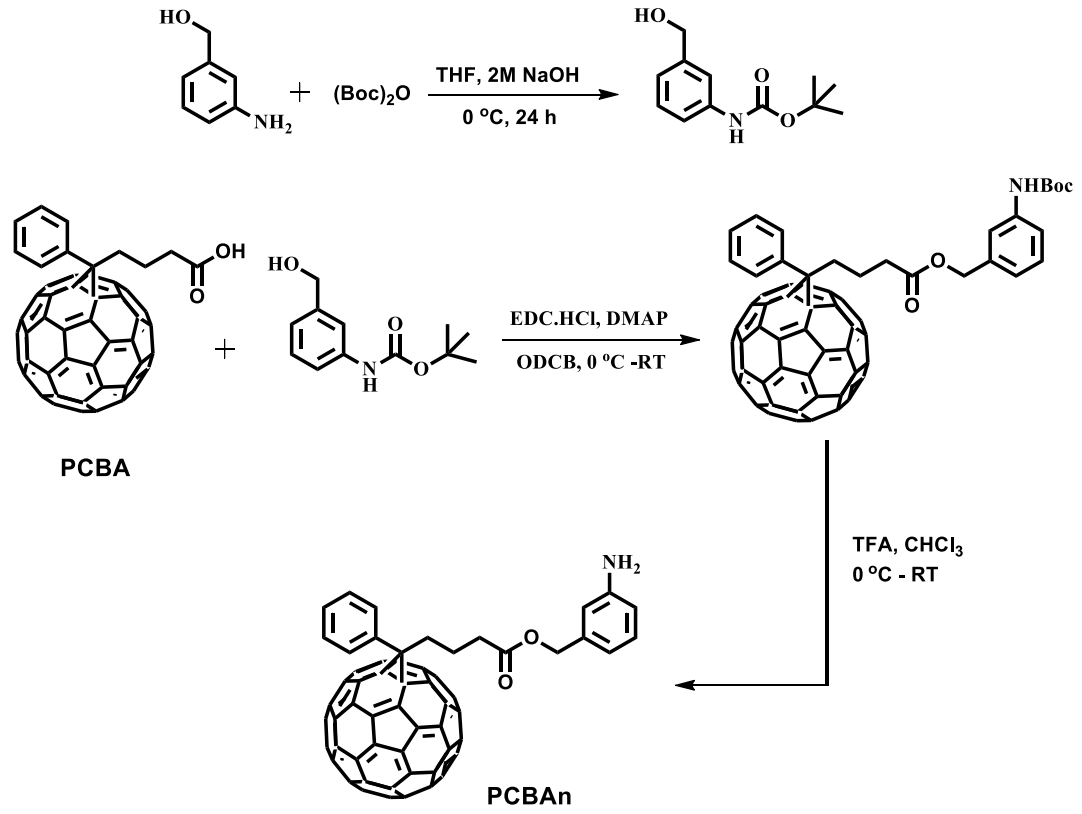

Scheme 3.1. Synthetic scheme for **PCBAn**. EDC: 1-ethyl-3-(3-(dimethylamino)propyl) carbodiimide, DMAP: 4-(dimethylamino)pyridine, ODCB: *ortho*-dichlorobenzene, TFA: Trifluoroaceticacid.

Oxidative polymerisation of aniline or anilinium salts can be easily carried out using APS or $FeCl_3$ reagents, yielding the corresponding conductive polymer with defined nanostructures.[45,46] Since the **PCBAn** have the aniline moiety, the oxidative polymerisation reaction may lead to the successful grafting of fullerene on polyaniline (**PANI**) backbone. The oxidative polymerization of **PCBAn** to obtain **P-PCBAn** was conducted in chloroform in the presence of $FeCl_3$ under reflux conditions, which yielded

the polymer as a brown solid residue in quantitative yields. The solid thus obtained was subsequently washed with chloroform and water to remove unreacted monomers and $FeCl_3$ to get **P-PCBAn** in 60% yield (Scheme 3.2). The formation of **P-PCBAn** polymer was further characterized through ^1H NMR, FT-IR and UV-Visible absorption spectroscopy.

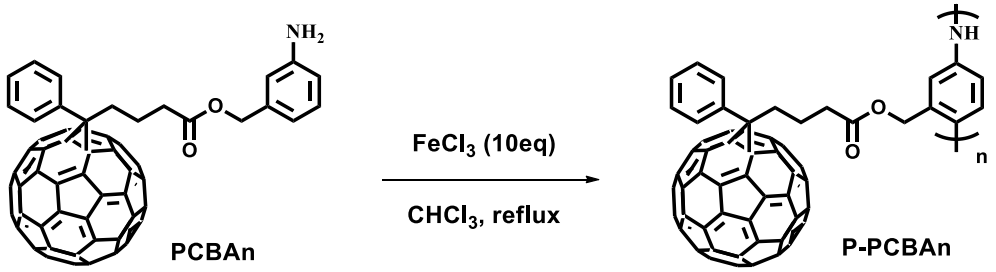

Scheme 3.2 Synthetic scheme for **P-PCBAn**, $FeCl_3$: Ferric chloride, $CHCl_3$: chloroform.

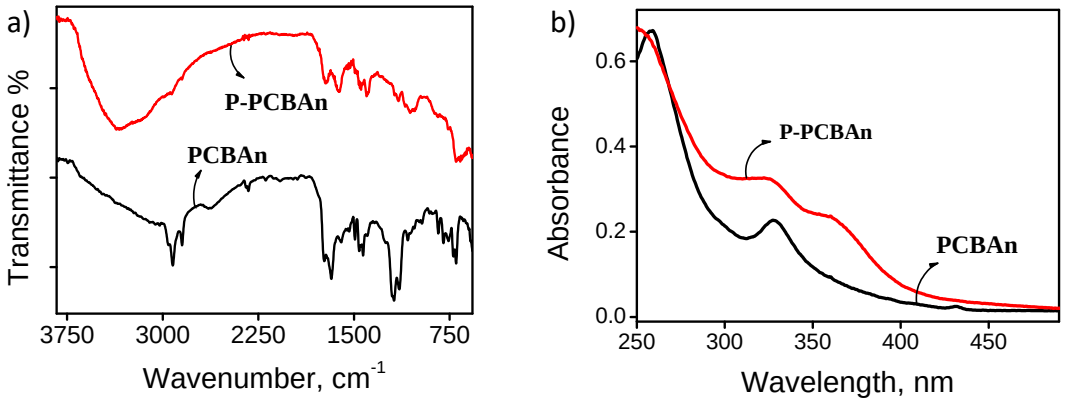

Figure 3.7. (a) Comparison of FT-IR spectra of **PCBAn** and **P-PCBAn** showing functional group transformation upon polymerisation. (b) Absorption spectra of **PCBAn** and **P-PCBAn** in THF (1 mg/mL).

A typical FT-IR spectrum of **PCBAn** and **P-PCBAn** were compared in Figure 3.7a. The **P-PCBAn** exhibited similar spectral characteristics as that of **PCBAn** monomer in the fingerprint region but showed a broad peak centered around 3345 cm^{-1},

characteristic of –NH stretching vibration, confirming successful polymerization. As discussed, the polyaniline can exist in three different oxidation states such as highly oxidized state penigraniline, conductive state emaraldine and non-conductive leucoemaraldine state. A comparison of the UV-Vis absorption spectra of **PCBAn** and **P-PCBAn** with reported **PANI** structures was made to understand the oxidation states of **PANI** formed during the oxidative polymerisation (Figure 3.7b). **PCBAn** in THF showed characteristic absorption peak at around 328 nm whereas **P-PCBAn** displayed an additional broad band, at 365 nm. Based on the absorption properties in comparison with reported **PANI** structures, the synthesized **P-PCBAn** is assigned to have non-conductive leucoemaraldine state of **PANI** as polymer backbone.[47]

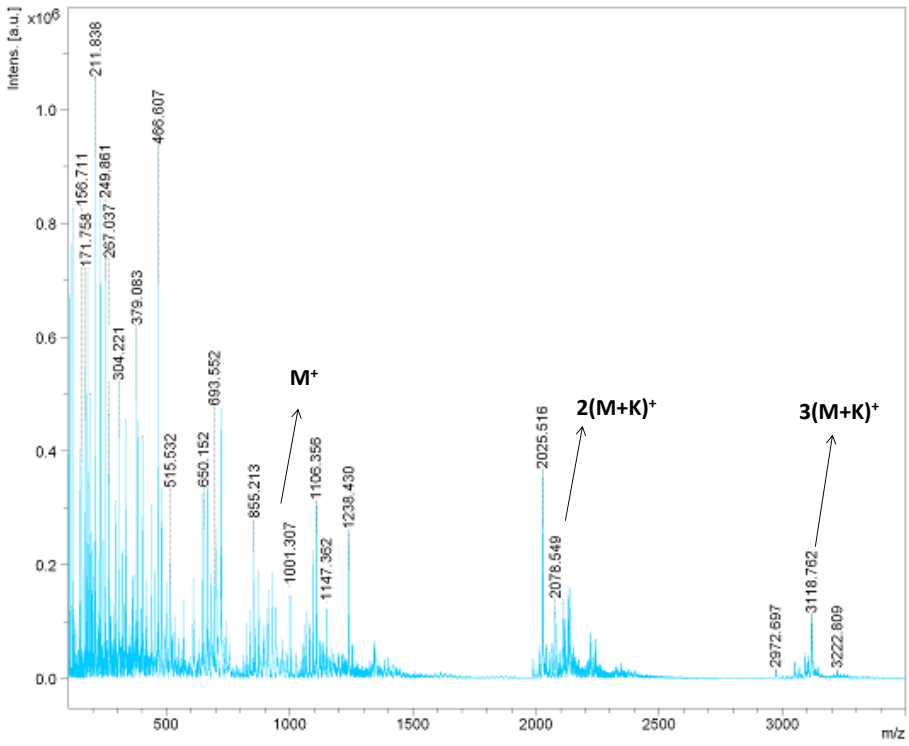

Figure 3.8. MALDI-TOF spectra of **P-PCBAn** showing m/z peak corresponding to M, 2M and 3M.

Matrix-assisted laser desorption ionization time-of flight (MALDI-TOF) studies of **PCBAn** and **P-PCBAn** were carried out using 2,5-dihydroxybenzoic acid as a matrix material (Figure 3.8). **PCBAn** showed typical m/z molecular ion peak at 1120 whereas **P-PCBAn** exhibited m/z ion peak corresponding to M^+, $2(M^+ + K)$ and $3(M^+ + K)$. The lack of higher mass peak might be due to the difficulty of polymers in being desorbed/ ionized without decomposing. Similar observations were earlier reported for the construction of polyfullerene from photochemical reactions of fullerene clusters.[48]

3.3.2. ELECTROCHEMICAL STUDIES

We compared the reduction potentials of **PCBAn** and **P-PCBAn** with **PCBM** using Square Wave Voltammetry (Figure 3.9) conducted on glassy carbon as working electrode in the presence of 0.1 M $TBAPF_6$ as supporting electrolyte, Ag/AgCl electrode as reference electrode and platinum wire as counter electrode in acetonitrile, calibrated

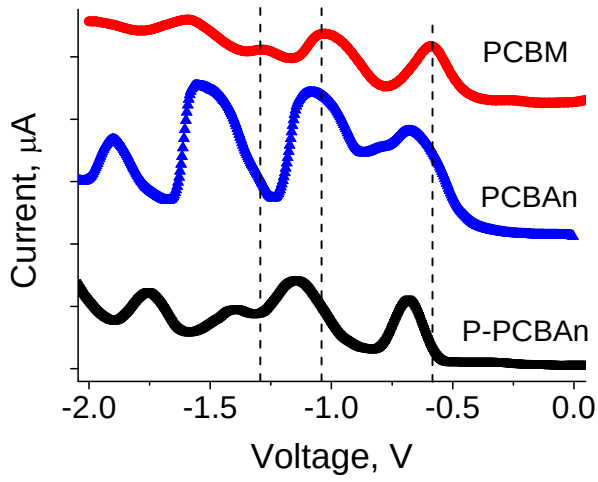

Figure 3.9. Square wave voltammetry of **PCBM**, **PCBAn** and **P-PCBAn** measured in acetonitrile at a scan rate of 0.1 V/s under N_2, 0.1 M Bu_4NPF_6 electrolyte with Pt (working electrode), Pt wire (counter electrode), $Ag/AgNO_3$ (reference electrode).

by ferrocene ($E_{1/2(ferrocene)}$ = 0.45 V vs. Ag/AgCl). The first reduction potentials of **PCBM**, **PCBAn** and **P-PCBAn** were observed at -0.57 V, -0.67 V and 0.69 V, respectively. The LUMO energy levels were calculated from reduction potentials using the formula,

$$E_{LUMO} = -e\,[4.8 + E_{red} - 0.45]\ eV \quad \ldots\ldots\ldots\ldots\ldots\ldots\ (1)$$

Where, E_{red} is the reduction potential vs Ag/AgCl electrode using ferrocene as the standard ($E_{1/2(ferrocene)}$ = 0.45 V vs. Ag/AgCl).[21] The LUMO energy levels of **PCBM**, **PCBAn** and **P-PCBAn** were found to be -3.78 eV, -3.68 eV and -3.66 eV, respectively. The HOMO energy levels were calculated using optical band gap (E_{gap}) using the formula E_{gap}= HOMO - LUMO and were found to be -5.5 eV, -5.38 and -5.34 eV, respectively. The reduction potentials, HOMO-LUMO energy levels and optical band gap of **PCBAn**, **P-PCBAn** and **PCBM** were listed in the table 3.1.

Table 3.1. HOMO and LUMO energy levels calculated from UV–vis absorption and square wave voltammetry.

C_{60} derivatives	E_1 [V]	E_2 [V]	E_3 [V]	LUMO [eV]	λ_{onset} [nm]	HOMO [eV]	E_{gap} [eV]
PCBM	-0.57	-1.02	-1.26	-3.78	723	-5.5	1.72
PCBAn	-0.67	-1.08	-1.52	-3.68	728	-5.38	1.70
P-PCBAn	-0.69	-1.15	-1.38	-3.66	737	-5.34	1.68

The observed changes in the reduction potentials indicate slight modification of the electronic energy levels in case of synthesized fullerene derivatives compared to **PCBM**. **PCBAn** and **P-PCBAn** exhibited upshift of LUMO energy levels by 0.10 eV and 0.12 eV, respectively compared to **PCBM**. This could be due to the cofacial pi-orbital

interaction between the C_{60} and the aniline moieties in **PCBAn** and **P-PCBAn**.[18] The pictorial representation of HOMO-LUMO levels of **PCBM**, **PCBAn**, **P-PCBAn** along with donor **P3HT** were depicted in the Figure 3.10. From this it is clear that, the rise in LUMO energy levels can help easy charge transport at the **P3HT** donor and fullerene acceptor interface. Hence, the relative upshift of **PCBAn** and **P-PCBAn** LUMO levels serves them as better electron acceptors rather than **PCBM**.

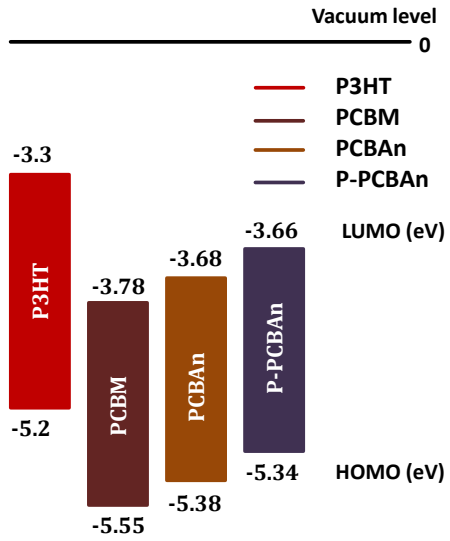

Figure 3.10. HOMO–LUMO energy level diagram of fullerene derivatives, **PCBM**, **PCBAn**, **P-PCBAn** and **P3HT**.[30] The energy levels were drawn relative to the vacuum level.

3.3.3. PHOTOPHYSICAL AND MORPHOLOGICAL STUDIES

A challenging task in fullerene chemistry is the construction of one dimensional nanostructures, which is advantageous for many optoelectronic applications.[49,50] In the present case, photophysical and morphological behaviour of **P-PCBAn** might differ from monomeric **PCBAn** due to the inherent polymeric nature of the former. Moreover, the fullerene derivatives are known to self-assemble into various shapes in binary

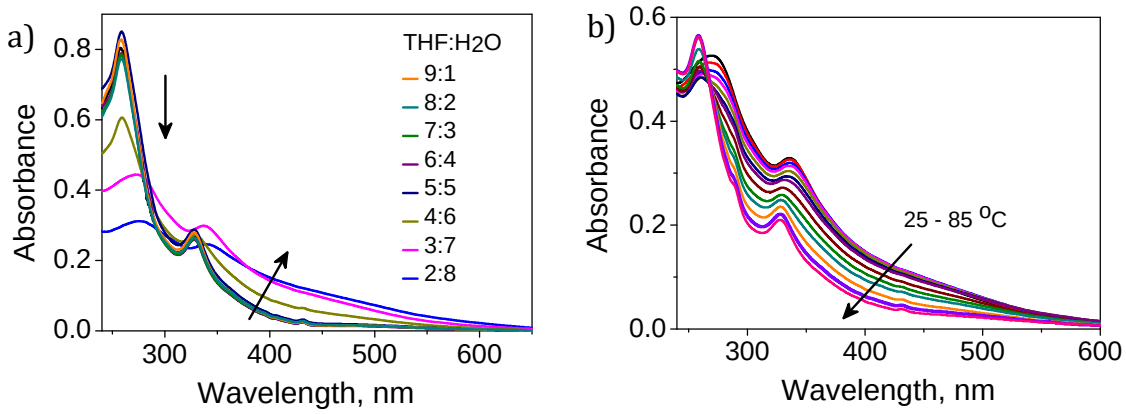

Figure 3.11. a) Changes in the UV-Visible absorption spectra of **PCBAn** (10 μM) in different THF/ H_2O solution. b) Temperature dependent studies of **PCBAn** (10 μM) in THF/H_2O (3:7) mixture.

solvents. Hence, we investigated the photophysical and morphological properties of self-assembled **PCBAn** in THF-H_2O mixtures and **P-PCBAn** in 1,2-dichlorobenzene.

Absorption spectra of **PCBAn** in THF (10 μM) showed characteristic fullerene absorption peaks at 258 nm and 328 nm (Figure 3.11a). The solvent polarity was changed by the fraction of water in the solvent mixture and we observe no significant changes upto a 1: 1 THF/H_2O mixture. At higher water fractions, a new band formation around 450 nm with concomitant hypochromism at 258 nm absorption band was observed. In THF/H_2O (3:7) mixture, a bathochromic shift of 16 nm and 10 nm for the 258 nm and 328 nm bands, respectively accompanied by pronounced 450 nm absorption band was observed. This might be attributed to the aggregation of **PCBAn** monomers due to the solvophobic effect in which fullerene core tend to come closer with more hydrophilic aniline group project outwards. To understand the reversibility of these aggregates, temperature dependent UV-visible absorption studies were carried

out (Figure 3.11b). Upon increasing the temperature from 25 °C to 85 °C, the absorption bands at 274 nm and 338 nm undergo hypsochromic shift to their initial value with concomitant disappearance of the 450 nm band. These results indicate the thermal reversibility of **PCBAn** aggregates in THF/H_2O (3:7) mixture.

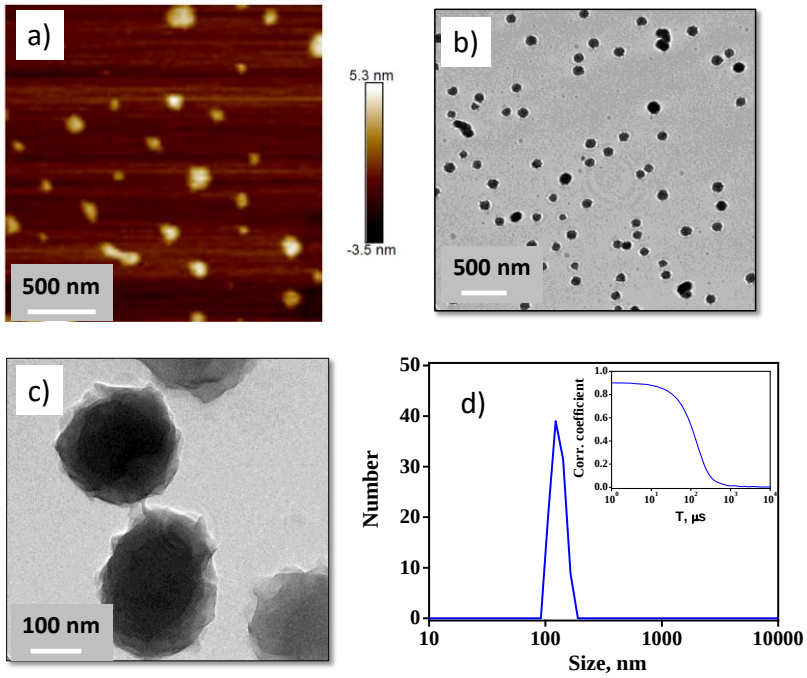

Figure 3.12. a) AFM height image; b) TEM image of **PCBAn** in THF/H_2O (3:7) mixture and c) zoomed portion showing wrinkled flake like nanostructure. d) DLS size distribution of **PCBAn** (inset: corresponding correlogram).

The self-assembly behaviour was further investigated through AFM and TEM analyses to understand the morphology of **PCBAn** aggregates. AFM analysis of a drop cast film of **PCBAn** (10 µM) from THF/H_2O (3:7) mixture on freshly cleaved mica (10 µL) exhibited particles of around 100-150 nm width (Figure 3.12a). TEM analysis of **PCBAn** drop-cast on a carbon coated copper grid, revealed particles with size ~150 nm similar to that observed in AFM (Figure 3.12b). Zoomed images of the particle clearly

showed wrinkled flake like nanostructures with multiple layers at the edges (Figure 3.12c). DLS experiments of the same solution which was used for the microscopic studies revealed an average hydrodynamic diameter of 125 nm with good correlogram (Figure 3.12d). These morphological studies reveal that **PCBAn** in the presence of binary solvent mixture (THF/H_2O) form particle like aggregates.

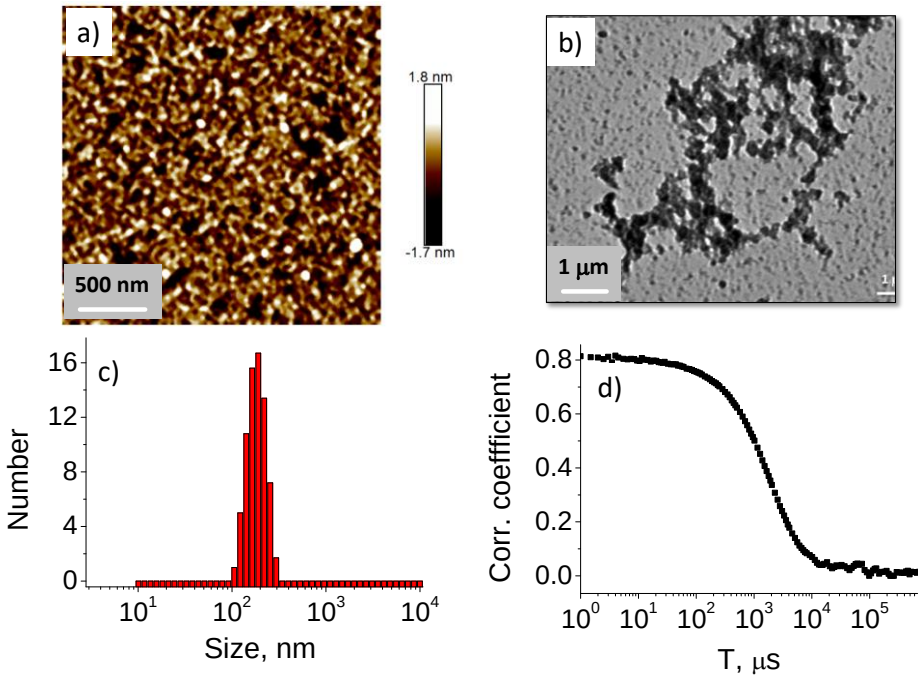

Figure 3.13. a) AFM height image; b) TEM image; c) DLS size distribution profile and d) corresponding correlogram of **P-PCBAn** in 1,2-dichlorobenzene.

AFM analysis of drop cast film of **P-PCBAn** (1 mg/mL, 1,2-dichlorobenzene) on mica and analyzed under AFM (Figure 3.13a) revealed interconnected nanonetwork structure with diameter of around 50-100 nm. HR-TEM analyses of same solution further confirmed the nanonetwork structure (Figure 3.13b). Since **PANI** polymers are known to give nanofibre network structure, the observed nanonetwork might consist of polyaniline main chain with pendent fullerene moieties. DLS experiment revealed

hydrodynamic particle size of 190 nm with good correlogram which was in line with AFM and TEM results. The **PCBAn** in 1,2-dichlorobenzene at similar concentrations did not show any nanostructures, as it is highly soluble and tend to exist as monomer.

3.3.4. WIDE ANGLE X-RAY SCATTERING (WAXS) STUDIES

The wide angle X-ray scattering (WAXS) studies of **PCBAn** cast film in THF/water (3:7) mixture and **P-PCBAn** in 1,2-dichlorobenzene was carried to understand the packing of molecules in the self-assembled nanostructures. **PCBAn** showed well defined peaks at two theta values of 2.55, 7.85, 10.3 degree corresponding to (001), (003), (004) plane reflections of lamellar mesophases (Figure 3.14a).[51,52] The broad peak from 15-25 degree corresponds to alkyl chain interactions with d-spacing of 3.4 nm which is consistent with the bilayer lamellar mesophases model shown in figure 3.14b where fullerene core point inwards and alkyl chain project outwards.[50] **P-PCBAn** in ODCB also showed similar but slightly shifted crystalline peaks at two theta value of 2.83, 5.81, 8.54, 10.48 degree corresponding to (001), (002), (003), (004) plane reflections of lamellar mesophases with d-spacing of 3 nm (Figure 3.14c). The decrease in the d-spacing is associated with the covalent linkage of **PCBAn** monomers in **P-PCBAn**, decreasing the distance between the adjucent C_{60} moieties without losing crystallinity as schematically represented in Figure 3.14d. This XRD study is in agreement with morphology obtained from AFM and TEM analyses and indicates a type of directed self-assembly through hydrophobic-hydrophilic balance in aqueous or solvophobic-solvophilic balance in non-aqueous media.

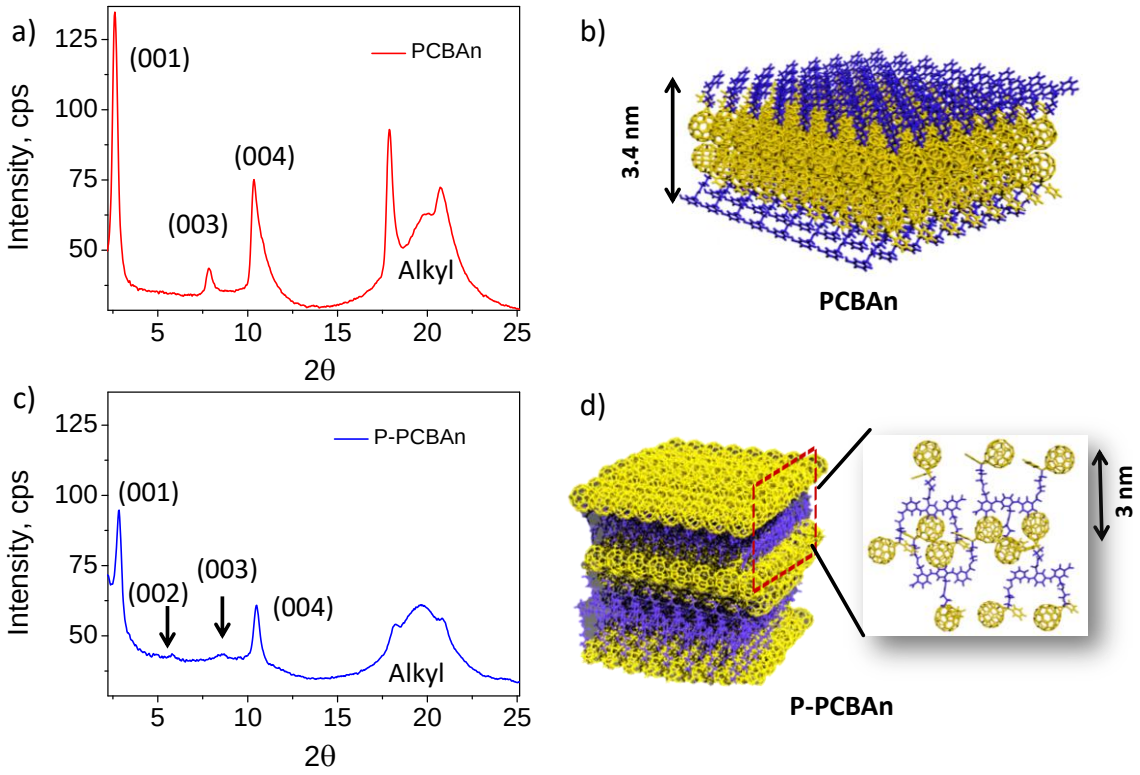

Figure 3.14. WAXS pattern of a) self-assembled **PCBAn** in THF/H_2O (3:7) and b) **P-PCBAn** in *ortho*-dichlorobenzene. Proposed schematic model for the nanostructure formed by the self-assembly of c) **PCBAn** and d) **P-PCBAn**.

3.3.5. SOLUTION STATE ABSORPTION AND EMISSION STUDIES

To further investigate the acceptor ability of the **PCBAn** monomer and **P-PCBAn** polymer, fluorescence quenching studies were carried out in the presence of **P3HT** polymer donor. The fluorescence emission spectra of **P3HT** solution in 1,2-dichlrobenzene were measured with different concentrations of **PCBAn** or **P-PCBAn** and the results are summarized in Figure 3.15. Pure **P3HT** donor in 1,2-dichlorbenzene solution displayed a fluorescence emission maximum at 583 nm. The fluorescent emission intensity decreased with increasing addition of fullerene derivatives. The fluorescence of **P3HT** underwent 22% quenching in the presence of 40 equivalents

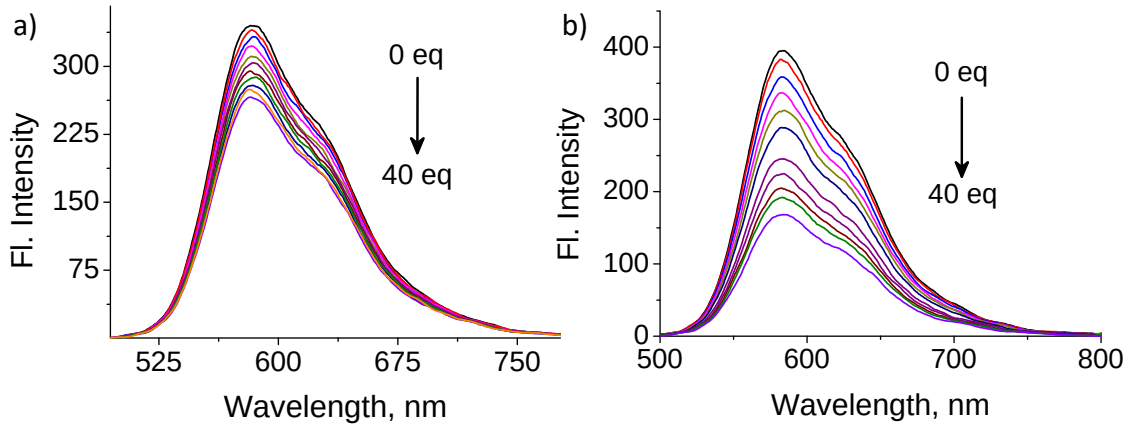

Figure 3.15. Changes in the fluorescence emission of **P3HT** (2.5 μg/mL) upon addition of a) **PCBAn** and b) **P-PCBAn** from 0 to 40 equivalents (100 μg/mL). λ_{exc}= 465 nm.

of **PCBAn** (Figure 3.15a). On the other hand, it exhibited two fold higher percentages of quenching (57%) with same equivalents of **P-PCBAn** (figure 3.15b). Inorder to understand the quenching efficiency of the fullerene acceptors, we used a Stern–Volmer quenching plot using the equation.

$$I_o/I = 1 + K_{sv}[Q] \quad \ldots\ldots\ldots\ldots\ldots\ldots (2)$$

where I_o and I are the measured fluorescence intensities in the absence and presence of the quencher, respectively, K_{sv} is the Stern-Volmer quenching constant, and [Q] is the concentration of the quencher. The Stern-Volmer equation provides useful information on intermolecular quenching process. Stern-Volmer quenching plots of **P3HT** donor in the presence of **PCBAn** and **P-PCBAn** as the quenchers are shown in Figure 3.16a. The **P3HT**-**PCBAn** displayed a straight line indicating dynamic quenching behaviour between the donor-acceptor molecules with a Stern-Volmer constant of K_{sv}= 4.3 x 10^3 M^{-1}, a value similar to that reported for **P3HT**-**PCBM** donor-acceptor pair. However, the plot corresponding to **P3HT**- **P-PCBAn** combination exhibited upward curvature

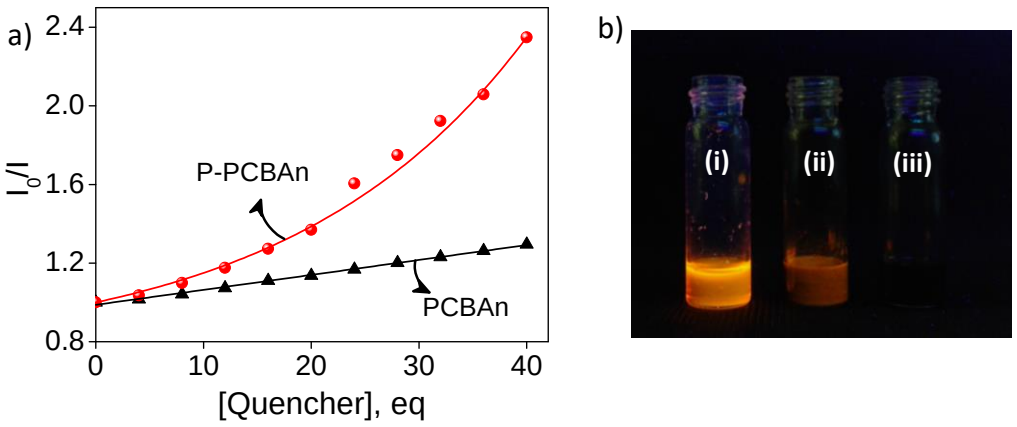

Figure 3.16. a) Stern-Volmer plot obtained from the fluorescence quenching between **P3HT** donor with **PCBAn** and **P-PCBAn** acceptor; b) Photograph of (i) **P3HT**, (ii) **P3HT**:**PCBAn** and (iii) **P3HT**:**P-PCBAn** (1 mg/mL each) under UV light (365 nm) showing difference in quenching behaviour of monomer and polymeric acceptors.

representing the existence of both static and dynamic quenching behaviour.[53] This can be correlated with a binding affinity between the fluorophore and the quencher. For instance, **P-PCBAn** exists as networked structure in the solution and hence it can undergo better pi-stacking with **P3HT**, accounting for the static quenching along with the usual collisional quenching. However, **PCBAn** exists in molecularly dissolved form in 1,2-dichlrobenzene and could cause quenching of **P3HT** fluorescence mainly through collision. The higher quenching behaviour of **P-PCBAn** can be visually identified by comparing the UV light illuminated solutions of **P3HT**, **P3HT**:**PCBAn** and **P3HT**:**P-PCBAn** as shown in Figure 3.16b.

Life time studies were carried out to get further insight into the quenching behaviour of **P3HT** donor in the presence of **PCBAn** and **P-PCBAn** acceptors (Figure3.17). The relative lifetime values upon excitation with 375 nm laser were summarized in Figure 3.17b. The **P3HT** showed the lifetime values of 0.53 ns

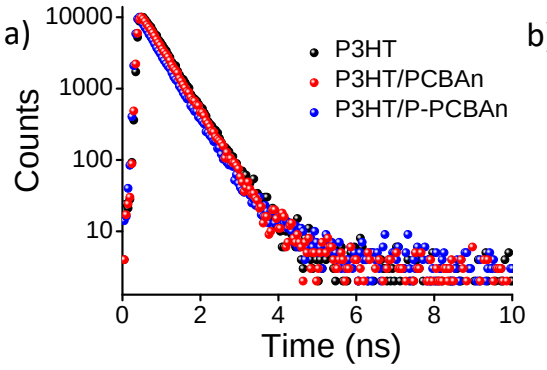

b)

Compound	Life time (ns)
P3HT	0.53
P3HT/PCBAn (1:40)	0.49
P3HT/P-PCBAn (1:40)	τ_1 = 0.21 (24.2%) τ_2 = 0.53 (75.8%) τ_{avg} = 0.45

Figure 3.17. a) Photoluminescence decay profiles of **P3HT** (2.5 μg/mL, 1:0), **P3HT**: **PCBAn** (1:40) and **P3HT**: **P-PCBAn** (1:40) and b) corresponding lifetime values, λ_{exc} = 375 nm and $\lambda_{collection}$ = 580 nm.

with single exponential decay. In the presence of **PCBAn** (1:40 equivalents), the life time reduced to 0.49 ns due to the dynamic quenching. While, **P3HT**: **P-PCBAn** (1:40 equivalents) experienced bi-exponential decay with life time of 0.21 ns (24.2%) and 0.53 ns (75.8%) with an average life time of 0.45 ns. The values correspond to different extent of fluorophore-quencher interactions in the P3HT-P-PCBAn blends with ideal static quenching lead to non-fluorescent complexes.

3.3.6. SOLID STATE ABSORPTION AND EMISSION STUDIES

Solid state UV-visible absorption and fluorescence quenching studies were also carried out for the donor-acceptor polymer blend active films. The pristine **P3HT** showed an intense visible absorption with maxima at 515 nm and 553 nm (Figure 3.18a). The shoulder band at 603 nm indicates the crystallinity of **P3HT** in the film state which was almost unchanged in the presence of **PCBAn**.[54] In the case of **P3HT**:**P-PCBAn** film the shoulder band underwent ~7 nm bathochromic shift which might be

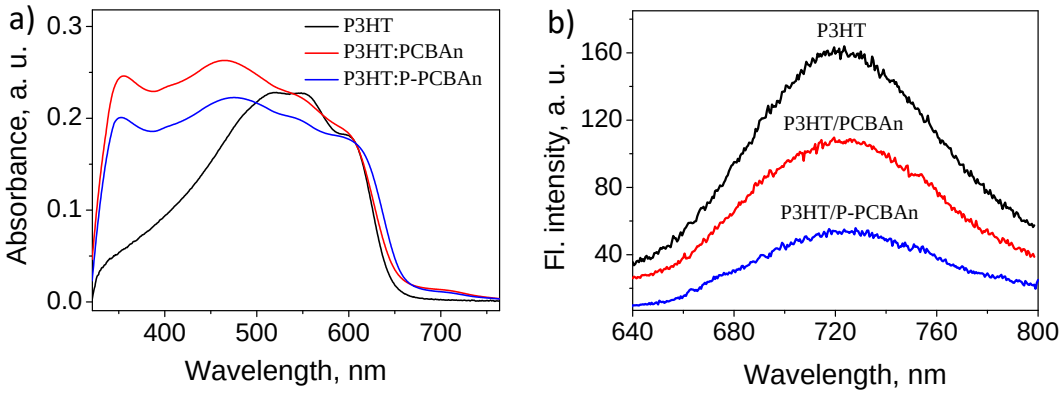

Figure 3.18. Solid state a) UV-visible absorption and b) emission spectral profile of **P3HT**, **P3HT**:**PCBAn** and **P3HT**:**P-PCBAn** polymer blend films, λ_{exc} = 600 nm.

attributed to the self-assembling behaviour of **P-PCBAn** polyfullerene with **P3HT** polymer.[23] Moreover, the pristine **P3HT** film showed an emission maximum at 720 nm upon excitation at 600 nm and the fluorescence intensity was decreased upon blending with acceptors (Figure 3.18b). Fluorescence emission intensity in **P3HT**: **PCBAn** blend film underwent 34% quenching at 720 nm relative to **P3HT**. Whereas in the case of **P3HT**: **P-PCBAn**, a 67% quenching was observed. This increased fluorescence quenching of **P3HT** in the presence of **P-PCBAn** is in line with the solution state quenching results and confirms that the charge transfer process is more efficient in the **P3HT**: **P-PCBAn** blend system compare to **P3HT**: **PCBAn**.

3.3.7. MORPHOLOGICAL ANALYSIS OF POLYMER BLENDS

The morphology of the resultant polymer blend plays important role in determining the performance of polymer solar cells. In this regard, AFM analysis was performed to understand the resultant morphology of the **P3HT**: **PCBAn** and **P3HT**: **P-PCBAn** polymer blends film after thermal annealing at 120 ^{o}C. AFM phase image

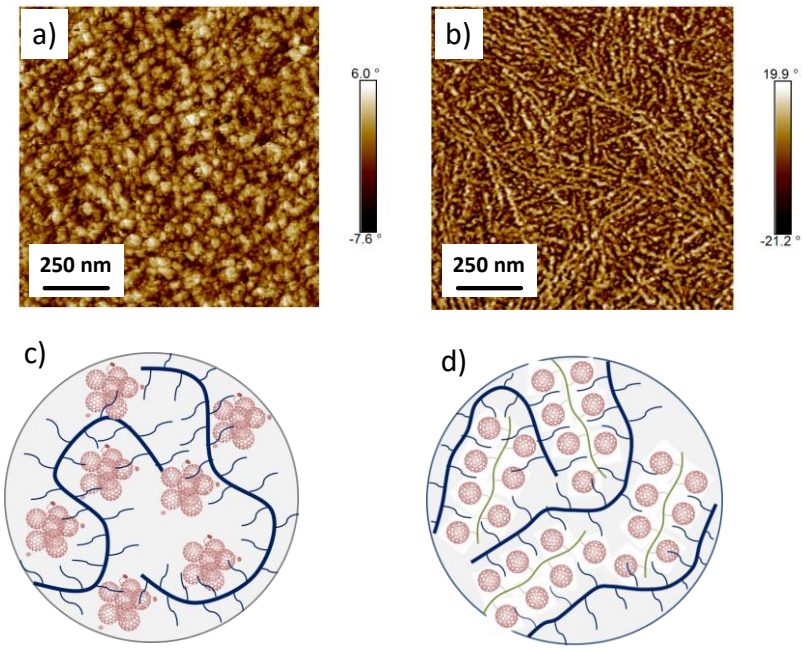

Figure 3.19. AFM phase image of a) **P3HT**: **PCBAn** and b) **P3HT**: **P-PCBAn** polymer blend films and (c-d) corresponding cartoonic representation of self-assembly process.

of the **P3HT**: **PCBAn** polymer blend film revealed the formation of spherical aggregates whereas **P3HT**: **P-PCBAn** blend showed interpenetrating network structures under similar conditions (Figure 3.18a and 3.18b). The particle like nanostructures of **P3HT**: **PCBAn** might be because of the aggregation of **PCBAn** monomer during thermal annealing process (figure 3.18c). The intrinsic networked nanostructure of **P3HT** and **P-PCBAn** rendered the formation of self-assembled interpenetrated nanonetwork architecture by means of various noncovalent interactions. Therefore, the morphological analysis of the polymeric blend films confirms the well-ordered interaction of **P3HT** with polymeric **P-PCBAn** than monomeric **PCBAn**.

3.3.8. PHOTOVOLTAIC PROPERTIES

BHJ-PSC devices were fabricated with inverted configuration ITO/ZnO/**P3HT**: **PCBAn**/V_2O_5/Ag (Device A) and ITO/ZnO/**P3HT**: **P-PCBAn**/V_2O_5/Ag (Device B) using **PCBAn** and **P-PCBAn** as active layer electron acceptors. Device A and B were prepared by spin-coating a mixture of **P3HT**/**PCBAn** (1:1, w/w) and **P3HT**/**P-PCBAn** (1:1, w/w) respectively, from 1,2-dichlorobenzene to form a 130 nm thin film on ZnO coated ITO substrates. Current-voltage characteristics were measured using a Keithley under the irradiation of AM 1.5G solar simulator. Under identical fabrication conditions, device A showed a PCE of 0.9% whereas in the **P3HT**: **P-PCBAn** device B, substantially improved

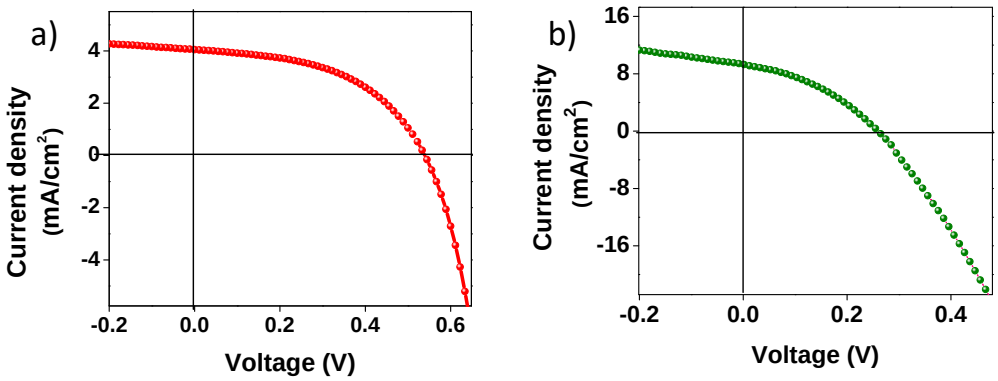

Figure 3.20. J-V curves of devices A and B under AM 1.5 G illumination.

Device	V_{oc} (V)	J_{sc} (mAcm^{-2})	FF (%)	PCE (%)
A	0.53	4.23	40.5	0.91
B	0.26	9.57	43.81	1.1

Table 3.2. Definitions: open-circuit voltage, Voc; short-circuit current, Jsc; fill factor, FF; PCE, η; Configurations: device A, ITO/ZnO/**P3HT**: **PCBAn**/V_2O_5/Ag and device B, ITO/ZnO/**P3HT**: **P-PCBAn**/V_2O_5/Ag.

PCE of 1.1% observed (Table 3.2). The increased PCE of Device B is mainly because of the simultaneous enhancement in the short-circuit current (J_{sc}) from 4.23 $mAcm^{-2}$ in device A to 9.57 $mAcm^{-2}$ device B and fill factor (FF) from 40.5 to 43.81. The overall PCE analysis of the inverted PSC devices using **P3HT**: **PCBAn** and **P3HT**: **P-PCBAn** active layer confirms that **P-PCBAn** is an efficient electron acceptor than **PCBAn**. The observed lower PCE of both devices in comparison to reported **P3HT**: **PCBM** device might be due to the presence of nitrogen groups of aniline moieties in both **PCBAn** and **P-PCBAn**. The aniline groups might involve in electron transfer to fullerene acceptor and hence induce charge imbalance in the BHJ active layer. Similarly, the non-conducting PANI form also may be reducing the charge mobilities across the heterojunctions.[55]

3.4. CONCLUSIONS

In summary, we have successfully synthesized a fullerene-aniline derivative, 3-aminobenzyl-[6,6]-phenyl-C_{61}-butyrate ester (**PCBAn**) and its polymer **P-PCBAn** and investigated their photophysical and morphological properties with a view to understand their potential as acceptor moieties in the PSCs. The optical and electrochemical studies revealed upshifted LUMO levels for **PCBAn** (-3.68 eV, ΔE = 0.1 eV) and **P-PCBAn** (-3.66 eV, ΔE = 0.12 eV) compared to the **PCBM** (-3.78 eV). Moreover, the morphology of **PCBAn** alone in binary solvent mixture (THF-H_2O) and **P-PCBAn** (in ODCB) were evaluated using AFM and TEM analysis which indicated nanoflake like aggregates for **PCBAn** and networked nanostructures for **P-PCBAn**. The solution/solid state fluorescence emission, quenching studies with **P3HT** electron donor indicated **P-**

PCBAn as an efficient electron acceptor than **PCBAn**. The morphological analysis of **P3HT**: **PCBAn** and **P3HT**: **P-PCBAn** polymer blend film revealed the formation of spherical aggregates and inter-connected networked nanostructures, respectively. The fabrication of BHJ-PSC device with **PCBAn** and **P-PCBAn** in combination with **P3HT** showed relative higher power conversion efficiency for **P-PCBAn** (PCE = 1.1%) compared to **PCBAn** (PCE = 0.9%). The increased PCE in case of **P-PCBAn** might be due to the combined effect of bicontinuous interpenetrating network structures and better charge transport properties of **P3HT**:**P-PCBAn** polymer blend compared to **P3HT**:**PCBAn**. The polymeric acceptor and rational design strategy used here could open up new opportunities in the PSC device fabrication.

3.5. EXPERIMENTAL SECTION

3.5.1. Materials and Methods

The materials and reagents for synthesis were purchased from Sigma-Aldrich, Merck, and Spectrochem chemical suppliers. Regioregular **P3HT** (55 kDa) was purchased from Rieke Metal Inc. and **PCBM** (>99.5%) was obtained from Nano-C. These chemicals were used as received without further purification. Vanadium Pentoxide (V_2O_5) (Baytron P VP AI 4083) was purchased from H. C. Stark and passed through a 0.45 μm syringe filter before spin-coating. Patterned ITO was obtained from Ossila Ltd. All other reagents were purchased from Sigma-Aldrich and used as received.

^{1}H (500 MHz) and ^{13}C NMR (125 MHz) spectra were measured on a Bruker Avance DPX spectrometer. Chemical shifts are reported in parts per million

(ppm) using tetramethylsilane (TMS) (δ_H = 0 ppm) or the solvent residual signal ($CDCl_3$: δ_C = 77.00 ppm) as an internal reference. The resonance multiplicity is described as s (singlet), d (doublet), t (triplet) and m (multiplet). High resolution mass spectral (HRMS) analysis was performed on a Thermo Scientific Q Exactive Hybrid Quadrupole-Orbitrap electrospray ionization mass spectrometer (ESI-MS) instrument. Infrared spectra were recorded in the diffused reflectance mode in the solid state (KBr) using Shimadzu IR Prestige-21 Fourier Transform Infrared Spectrophotometer. All experiments were carried out using spectroscopic grade solvents at room temperature (25± 1 ^oC) unless otherwise mentioned.

The UV/Vis absorption spectra were recorded on a Shimadzu UV-2600 Spectrophotometer. Fluorescence spectra were collected using a SPEX-Fluorolog F112X Spectrofluorimeter equipped with a 450 W Xenon arc lamp. Fluorescence Lifetime measurements were carried out using IBH (model 5000DPS) time-correlated single photon counting system (TCSPC). The lifetime values were obtained using DAS6 decay analysis software. The quality of fit has been judged by the fitting parameters such as χ^2 (<1.1) as well as the visual inspection of the residuals. The square wave voltammetry was done on CV, BASI CV-50W instrument using thin film coated glassy carbon as working electrode at room temperature in the presence of 0.1 M tetrabutylammonium hexafluorophosphate ($TBAPF_6$) as supporting electrolyte, Ag/AgCl electrode as reference electrode and platinum wire as counter electrode in acetonitrile under argon atmosphere with

a scan rate of 50 mV/s. A BRUKER MULTIMODE AFM operating with a tapping mode regime was used to record AFM images under ambient conditions. Micro-fabricated TiN cantilever tips (NSG10) with a resonance frequency of 299 kHz and a spring constant of 20–80 Nm^{-1} were used. AFM section analysis was done offline. Samples for the imaging and roughness measurements were prepared as explained in device fabrication section under ambient conditions. The thickness of various films was measured using Bruker profilometer. The current density-voltage (J–V) characteristics were measured with a Keithley 2400 source-meter under AM 1.5G (100 $mWcm^{-2}$) solar simulator.

3.5.2. AFM/TEM Sample Preparations

Samples for AFM analysis were prepared by drop-casting 10 μL solution of **PCBAn** (1 mg/mL, THF/H_2O, 3:7), **P-PCBAn** (1 mg/mL in ODCB) onto freshly cleaved mica sheet under ambient conditions and were dried under air. In case of polymer blend, the samples were prepared as discussed in device fabrication section. A BRUKER MULTIMODE AFM operating with a tapping mode regime was used to record AFM images under ambient conditions. Micro fabricated TiN cantilever tips (NT-MDT-NSG series) with a resonance frequency of 299 kHz and a spring constant of 20 to 80 Nm^{-1} were used. AFM section analysis was done offline. TEM samples were prepared by drop casting 10 μL solution of the sample on the top of the carbon-coated copper grid (400 mesh). The samples were allowed to adsorb on the grid overnight at ambient conditions. TEM analysis was performed with a JEOL 100 kV high-resolution transmission electron microscope.

The accelerating voltage of the TEM was 100 kV and the beam current was 65 A. Samples were imaged with a Hamamatsu ORCA CCD camera.

3.5.3. Synthesis of 2-(meta-(tert-butoxycarbonyl)aminobenzyl alcohol

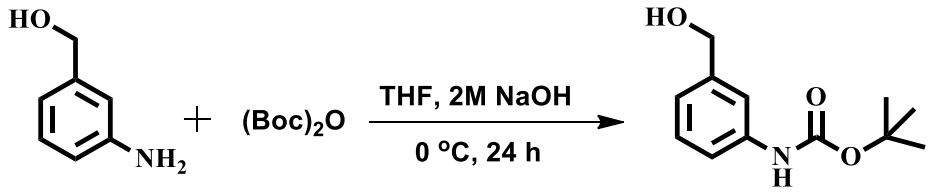

To a mixture of 3-aminobenzyl alcohol (1 g, 8.13 mmol) in 150 mL of THF was added 20 mL of 2 M aqueous sodium hydroxide and stirred for 15 minutes. A solution of di-tert-butyl bicarbonate (2.3 g, 9.75 mmol) in 75 mL THF was added slowly to the reaction and the mixture was stirred overnight at room temperature. The product was collected by filtration, extracted with ethylacetate (2 × 25 mL), dried over anhydrous sodium sulphate and concentrated. The crude product was purified through column chromatography using silica gel (100-200 mesh) with ethyl acetate/hexane as the eluent (R_f = 0.6, eluent: 30% ethyl acetate/hexane) to afford the product as creamy solid in 66% (1.2 g) yield.

^{1}H NMR (500 MHz, $CDCl_3$), δ (ppm): 7.42 (s, 1H), 7.26 (m, 1H), 7.22 (d, J = 8 Hz, 1H), 7.03 (d, J = 6 Hz, 1H), 6.5 (s, 1H), 4.65 (s, 2H), 1.51 (s, 9H).

^{13}C NMR (125 MHz, $CDCl_3$), δ (ppm): 152.81, 142.00, 138.59, 129.19, 121.53, 117.74, 117.02, 80.65, 65.20, 28.35.

Mass (HRMS): Calculated for $C_{12}H_{17}NO_3$: 223.12 (M); Found: 223.54 (M).

3.5.4. Synthesis of 2-(meta-(tert-butoxycarbonyl)aminobenzyl-[6, 6]-phenyl-C_{61}-butyrate (PCBAn-boc)

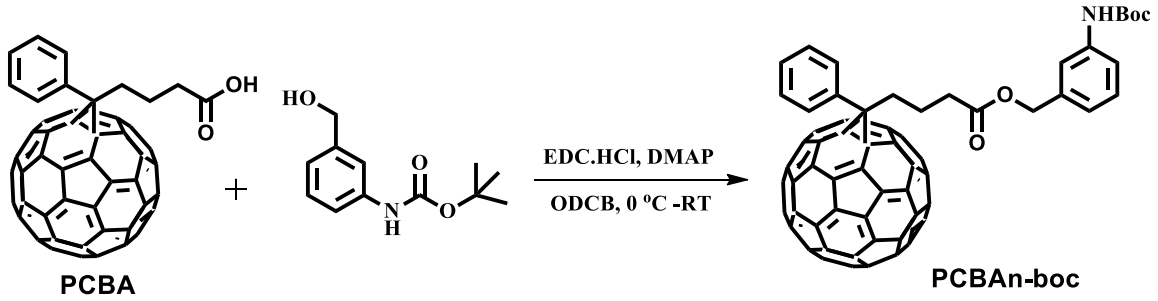

[6, 6]-Phenyl-C_{61}-butyric acid (50 mg, 0.057 mmol) was dispersed in HPLC grade 1,2-dichlorobenzene (8 mL). The mixture was kept in ice bath and added EDC.HCl (16 mg, 0.085 mmol), DMAP (7 mg, 0.057 mmol) and 2-(meta-(tert-butoxycarbonyl) aminobenzyl alcohol (12.7 mg, 0.057 mmol). The reaction mixture was stirred at room temperature for 24 h and the product was purified through column chromatography using 100-200 mesh silica gel with chloroform as the solvent (R_f = 0.7). The solvent was evaporated under vacuum and dried to obtain the brown solid in 57% (35 mg) yield.

^{1}H NMR (500 MHz, $CDCl_3$), δ (ppm): 7.94 (d, J = 7 Hz, 2H), 7.55 (d, J = 7.75 Hz, 2H), 7.48 (t, J = 7.5 Hz, 1H), 7.40 (s, 1H), 7.27 (d, 2H), 7.01 (d, J = 8 Hz, 1H), 6.49 (s,1H), 5.08 (s, 2H), 2.92 (t, J = 4.25 Hz, 2H), 2.58 (t, J = 4.25 Hz, 2H), 2.21 (t, J = 4.25 Hz, 2H), 1.52 (s, 9H).

^{13}C NMR (125 MHz, $CDCl_3$), δ (ppm): 174.92, 158.26, 157.54, 156.37, 154.21, 147.25, 145.69, 145.12, 145.03, 144.62, 144.58, 144.44, 143.94, 143.76, 142.53, 142.14, 141.61, 140.38, 138.15, 137.60, 134.06, 132.62, 130.47, 124.26, 119.25, 115.68, 112.21, 110.11, 100.92, 80.12, 64.10, 55.15, 3.90, 34.12, 27.85.

MALDI (m/z): M^+ Calculated for $C_{83}H_{27}NO_4$: 1102.48 (); Found: 1103.49 (M+H).

3.5.5. Synthesis of 3-aminobenzyl-[6, 6]-phenyl-C_{61}-butyrate (PCBAn)

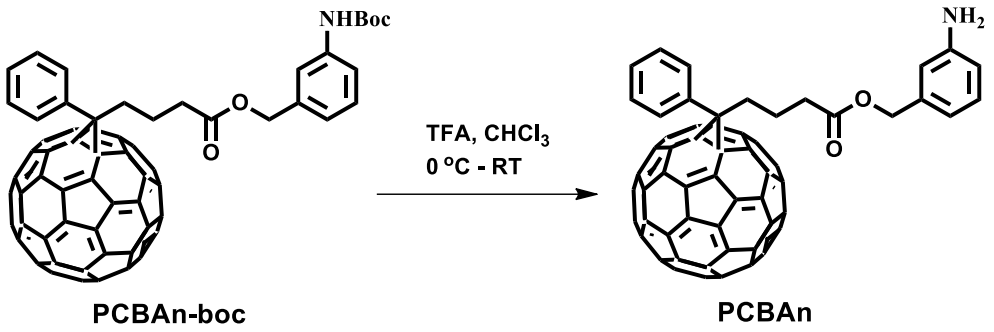

To a solution of **PCBAn-boc** (35 mg) in chloroform (10 mL) was added trifluoroacetic acid (2 mL) and stirred overnight at room temperature. The reaction was stopped and evaporated solvents, dried under vacuum to give the product as brown solid in quantitative yield (30 mg).

^{1}H NMR (500 MHz, $CDCl_3$), δ (ppm): 7.91 (d, J = 7 Hz, 2H), 7.54 (m, 6H), 7.39 (s, 1H), 5.19 (s, 2H), 2.90 (t, J = 4.25 Hz, 2H), 2.64 (m, 2H), 2.19 (t, J = 4.25 Hz, 2H); MALDI (m/z): Calculated for $C_{78}H_{20}NO_2$: 1102.37; Found: 1003.45.

^{13}C NMR (125 MHz, $CDCl_3$), δ (ppm): 172.96, 159.86, 159.54, 158.87, 148.65, 145.79, 145.22, 145.03, 144.82, 144.68, 144.54, 144.04, 143.76, 143.03, 142.14, 141.01, 140.78, 137.95, 137.60, 132.06, 130.82, 128.47, 122.66, 117.95, 115.68, 113.41, 111.14, 99.99, 79.72, 51.55, 33.90, 33.52.

MALDI (m/z): M^+ calculated for $C_{86}H_{25}NO_3^+$, 1001.36 (M); found, 1001.31 (M).

3.5.6. Synthesis of Poly-3-aminobenzyl-[6, 6]-phenyl-C_{61}-butyrate (P-PCBAn)

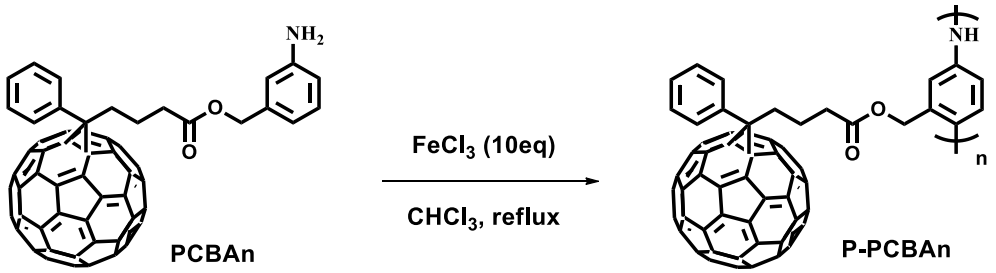

PCBAn (50 mg, 0.05 mmol) in Shlenck tube was dissolved in dry chloroform (10 mL) and was added anhydrous $FeCl_3$ (10 equivalents) at 0 °C. The reaction mixture was stirred for 15 minutes and refluxed overnight at 60 °C. The solvents were evaporated and the solid residue was washed with chloroform, water and methanol to obtain brown solid in 60% yield (30 mg).

^{1}H NMR (500 MHz, DMSO-d_6), δ (ppm): 8.2 (br), 7.2-7.7 (br), 5.35 (s).

MALDI (m/z): Calculated for M^+: 1001.36, $2M^+$: 2000.72, $3M^+$: 3000.08; Found: 1001.31 (M^+), 2078.55 [2(M+K) $^+$], 3118.76 [3(M+K) $^+$].

3.5.6. BHJ Device Fabrication

The ZnO sol was prepared using a sol-gel procedure by dissolving zinc acetate dihydrate ($C_4H_6O_4Zn.2H_2O$), 99.9%, 1.6 g) and monoethanolamine ($HOCH_2CH_2NH_2$, 99%, 0.045 g) in anhydrous 2-methoxyethanol (> 99.8%, 0.96 ml) under vigorous stirring for hydrolysis reaction and aging for 3 h. The solar cell devices were fabricated under optimized conditions according to the modified reported procedure. The patterned indium tin oxide (ITO)-coated glass substrate was first cleaned with detergent, ultrasonicated in DI-water, chloroform and isopropyl alcohol for 10 min, respectively and subsequently

dried in an oven overnight. After UV-ozone treatment for 15 min, nanosized ZnO thin films with a thickness of ca. 50 nm were spin-coated using the sol-gel precursor solution at 3000 rpm on top of the ITO substrate. The films were sintered at 200 ^{o}C for 30 min in air. During this process the precursor converts to ZnO gel and forms a transparent thin film of ZnO nanoparticle. For devices A and B, a *o*-DCB solution containing a mixture of **P3HT/PCBAn** (1:1, w/w) (Device A) and **P3HT/PCBAn** (1:1, w/w) (Device B) was then spin-cast to form a 130 nm thin film on top of the ZnO respectively. Both the devices were thermally annealed at 120 ^{o}C for 10 min in the glove box followed by spin-coating vanadium pentoxide with a thickness of ca. 40 nm and then heated at 120 ^{o}C in the glove box. Finally, the top electrode of Ag film (100 nm-thick), was evaporated thermally at a pressure below 10^{-6} torr. Devices without encapsulation were characterized in ambient condition. The active area used for the measurement was 0.1 cm^2 and were optimized by testing approximately 10-12 cells.

3.6. REFERENCES

1) Kippelen, B.; Brédas, J.-L., Organic photovoltaics. *Energ. Environ. Sci.* **2009**, *2*, 251-261.
2) Heremans, P.; Cheyns, D.; Rand, B. P., Strategies for increasing the efficiency of heterojunction organic solar cells: material selection and device architecture. *Acc. Chem. Res.* **2009**, *42*, 1740-1747.
3) Dang, M. T.; Hirsch, L.; Wantz, G.; Wuest, J. D., Controlling the morphology and performance of bulk heterojunctions in solar cells. Lessons learned from the benchmark poly(3-hexylthiophene):[6,6]-phenyl-C61-butyric acid methyl ester system. *Chem. Rev.* **2013**, *113*, 3734-3765.

4) Ye, L.; Zhang, S.; Ma, W.; Fan, B.; Guo, X.; Huang, Y.; Ade, H.; Hou, J., From Binary to Ternary Solvent: Morphology Fine-tuning of D/A Blends in PDPP3T-based Polymer Solar Cells. *Adv. Mater.* **2012**, *24*, 6335-6341.

5) Zhicai, H.; Chengmei, Z.; Shijian, S.; Miao, X.; Hongbin, W.; Yong, C., Enhanced power-conversion efficiency in polymer solar cells using an inverted device structure. *Nat. Photonics* **2012**, *6*, 591–595.

6) You, J.; Chen, C.-C.; Hong, Z.; Yoshimura, K.; Ohya, K.; Xu, R.; Ye, S.; Gao, J.; Li, G.; Yang, Y., 10.2% Power Conversion Efficiency Polymer Tandem Solar Cells Consisting of Two Identical Sub-Cells. *Adv. Mater.* **2013**, *25*, 3973-3978.

7) Chang, C. Y.; Wu, C. E.; Chen, S. Y.; Cui, C.; Cheng, Y. J.; Hsu, C. S.; Wang, Y. L.; Li, Y., Enhanced performance and stability of a polymer solar cell by incorporation of vertically aligned, cross-linked fullerene nanorods. *Angew. Chem. Int. Ed.* **2011**, *50*, 9386-90.

8) Li, C.-Z.; Yip, H.-L.; Jen, A. K. Y., Functional fullerenes for organic photovoltaics. *J. Mater. Chem.* **2012**, *22*, 4161-4177.

9) Kim, K.-H.; Kang, H.; Nam, S. Y.; Jung, J.; Kim, P. S.; Cho, C.-H.; Lee, C.; Yoon, S. C.; Kim, B. J., Facile Synthesis ofo-Xylenyl Fullerene Multiadducts for High Open Circuit Voltage and Efficient Polymer Solar Cells. *Chem. Mater.* **2011**, *23*, 5090-5095.

10) Backer, S. A.; Sivula, K.; Kavulak, D. F.; Frechet, J. M. J., High efficiency organic photovoltaics incorporating a new family of soluble fullerene derivatives. *Chem. Mater.* **2007**, *19*, 2927-2929.

11) Cheng, Y.-J.; Liao, M.-H.; Chang, C.-Y.; Kao, W.-S.; Wu, C.-E.; Hsu, C.-S., Di(4-methylphenyl)methano-C60Bis-Adduct for Efficient and Stable Organic Photovoltaics with Enhanced Open-Circuit Voltage. *Chem. Mater.* **2011**, *23*, 4056-4062.

12) Mikroyannidis, J. A.; Kabanakis, A. N.; Sharma, S. S.; Sharma, G. D., A Simple and Effective Modification of PCBM for Use as an Electron Acceptor in Efficient Bulk Heterojunction Solar Cells. *Adv. Funct. Mater.* **2011**, *21*, 746-755.

13) Kai, Y.; Lie, C.; Fan, L.; Peishan, W.; Yiwang, C., Cooperative Assembly Donor–Acceptor System Induced by Intermolecular Hydrogen Bonds Leading to Oriented Nanomorphology for Optimized Photovoltaic Performance. *J. Phys. Chem. C* **2012**, *116*, 714-721.

14) Ying, L.; Jung Ah, L.; Qingshuo, W.; Stefan, C. B. M.; Alejandro, L. B.; James, J. W., Cooperative Assembly of Hydrogen-Bonded Diblock Copolythiophene/Fullerene Blends

for Photovoltaic Devices with Well-Defined Morphologies and Enhanced Stability. *Chem. Mater.* **2012**, *24*, 622-632.

15) Li, C. Z.; Chien, S. C.; Yip, H. L.; Chueh, C. C.; Chen, F. C.; Matsuo, Y.; Nakamura, E.; Jen, A. K., Facile synthesis of a 56pi-electron 1,2-dihydromethano-[60]PCBM and its application for thermally stable polymer solar cells. *Chem. Commun.* **2011**, *47*, 10082-10084.

16) Lenes, M.; Wetzelaer, G.-J. A. H.; Kooistra, F. B.; Veenstra, S. C.; Hummelen, J. C.; Blom, P. W. M., Fullerene Bisadducts for Enhanced Open-Circuit Voltages and Efficiencies in Polymer Solar Cells. *Adv. Mater.* **2008**, *20*, 2116-2119.

17) Kim, H. U.; Kim, J. H.; Kang, H.; Grimsdale, A. C.; Kim, B. J.; Yoon, S. C.; Hwang, D. H., Naphthalene-, anthracene-, and pyrene-substituted fullerene derivatives as electron acceptors in polymer-based solar cells. *ACS Appl. Mater. Interfaces* **2014**, *6*, 20776-85.

18) Han, G. D.; Collins, W. R.; Andrew, T. L.; Bulović, V.; Swager, T. M., Cyclobutadiene–C60 Adducts: N-Type Materials for Organic Photovoltaic Cells with High VOC. *Adv. Funct. Mater.* **2013**, *23*, 3061-3069.

19) Li, Y., Molecular design of photovoltaic materials for polymer solar cells: toward suitable electronic energy levels and broad absorption. *Acc. Chem. Res.* **2012**, *45*, 723-33.

20) He, Y.; Chen, H.-Y. Y.; Hou, J.; Li, Y., Indene-C(60) bisadduct: a new acceptor for high-performance polymer solar cells. *J. Am. Chem. Soc.* **2010**, *132*, 1377-1382.

21) He, Y.; Zhao, G.; Peng, B.; Li, Y., High-Yield Synthesis and Electrochemical and Photovoltaic Properties of Indene-C70 Bisadduct. *Adv. Funct. Mater.* **2010**, *20*, 3383-3389.

22) Li, G., Zhu, R., and Yang, Y., Polymer solar cells. *Nat. Photonics* **2012**, *6*, 153-161.

23) Peet, J.; Heeger, A. J.; Bazan, G. C., "Plastic" solar cells: self-assembly of bulk heterojunction nanomaterials by spontaneous phase separation. *Acc. Chem. Res.* **2009**, *42*, 1700-1708.

24) Lee, J. K.; Ma, W. L.; Brabec, C. J.; Yuen, J.; Moon, J. S.; Kim, J. Y.; Lee, K.; Bazan, G. C.; Heeger, A. J., Processing Additives for Improved Efficiency from Bulk Heterojunction Solar Cells. *J. Am. Chem. Soc.* **2008**, *130*, 3619-3623.

25) Babu, S.; Möhwald, H.; Nakanishi, T., Recent progress in morphology control of supramolecular fullerene assemblies and its applications. *Chem. Soc. Rev.* **2010**, *39*, 4021-4035.

26) Lee, J. U.; Jung, J. W.; Jo, J. W.; Jo, W. H., Degradation and stability of polymer-based solar cells. *J. Mater. Chem.* **2012**, *22*, 24265-24283.

27) Wantz, G., Derue, L., Dautel, O., Rivaton, A., Hudhommed, P., and Dagron-Lartigau, C., Stabilizing polymer-based bulk heterojunction solar cells via crosslinking. *Polym. Int.* **2014**, *63*, 1346-1361.

28) Francesco, G.; Nazario, M., Fullerene Polymers: Synthesis and Properties. *Chem. Rev.* **2006**, *106*, 5136-5190.

29) Wang, J.; Shen, Y.; Kessel, S.; Fernandes, P.; Yoshida, K.; Yagai, S.; Kurth, D. G.; Möhwald, H.; Nakanishi, T., Self-assembly made durable: water-repellent materials formed by cross-linking fullerene derivatives. *Angew. Chem. Int. Ed.* **2009**, *48*, 2166-2170.

30) Hsieh, C.-H. H.; Cheng, Y.-J. J.; Li, P.-J. J.; Chen, C.-H. H.; Dubosc, M.; Liang, R.-M. M.; Hsu, C.-S. S., Highly efficient and stable inverted polymer solar cells integrated with a cross-linked fullerene material as an interlayer. *J. Am. Chem. Soc.* **2010**, *132*, 4887-4893.

31) Yen-Ju, C.; Fong-Yi, C.; Wei-Cheng, L.; Chiu-Hsiang, C.; Chao-Hsiang, H., Self-Assembled and Cross-Linked Fullerene Interlayer on Titanium Oxide for Highly Efficient Inverted Polymer Solar Cells. *Chem. Mater.* **2011**, *23*, 1512-1518.

32) Martin, D.; Harald, H.; Christoph, W.; Helmut, N.; Niyazi, S. S.; Wolfgang, S.; Friedrich, S.; Christoph, T.; Markus, C. S.; Zhengguo, Z.; Russell, G., Stabilization of the nanomorphology of polymer–fullerene "bulk heterojunction" blends using a novel polymerizable fullerene derivative. *J. Mater. Chem.* **2005**, *15*, 5158-5163.

33) Dan, H.; Xiaoyan, D.; Wei, Z.; Zuo, X.; Liming, D., Improving the stability of P3HT/PC61BM solar cells by a thermal crosslinker. *J. Mater. Chem. A* **2013**, *1*, 4589-4594

34) Lara, P.; Ali, N.; Emilie, P.; Christian, C.; Nicole, A.; Lionel, F., Fullerene-based processable polymers as plausible acceptors in photovoltaic applications. *J. Polym. Sci. Pol. Phys.* **2013**, *51*, 291-302.

35) Maeyoshi, Y.; Saeki, A.; Suwa, S.; Omichi, M.; Marui, H.; Asano, A.; Tsukuda, S.; Sugimoto, M.; Kishimura, A.; Kataoka, K.; Seki, S., Fullerene nanowires as a versatile platform for organic electronics. *Sci. Rep.* **2012**, *2*, 1-6.

36) Harry, W. G., Fullerene Polymers: Synthesis, Properties and Applications Fullerene Polymers: Synthesis, Properties and Applications. 2009, Edited by Nazario Martin (Universidad Complutense, Madrid, Spain) and Francesco Giacalone (Università Degli

Studi di Palermo, Italy). WILEY-VCH Verlag GmbH & Co. KGaA: Weinheim. *J. Am. Chem. Soc.* **2010**, *132*, 9929-9930.

37) Qiu, H. J.; Wan, M. X.; Matthews, B.; Dai, L. M., Conducting polyaniline nanotubes by template-free polymerization. *Macromolecules* **2001**, *34*, 675-677.

38) Dai, L. M.; Lu, J. P.; Matthews, B.; Mau, A. W. H., Doping of conducting polymers by sulfonated fullerene derivatives and dendrimers. *J. Phys. Chem. B* **1998**, *102*, 4049-4053.

39) Zhang, X.; Goux, W. J.; Manohar, S. K., Synthesis of polyaniline nanofibers by "nanofiber seeding". *J. Am. Chem. Soc.* **2004**, *126*, 4502-3.

40) Huang, J.; Virji, S.; Weiller, B. H.; Kaner, R. B., Polyaniline nanofibers: facile synthesis and chemical sensors. *J. Am. Chem. Soc.* **2003**, *125*, 314-5.

41) Datta, B.; Schuster, G. B., DNA-Directed Synthesis of Aniline and 4-Aminobiphenyl Oligomers: Programmed Transfer of Sequence Information to a Conjoined Polymer Nanowire. *J. Am. Chem. Soc.* **2008**, *130*, 2965-2973.

42) Surwade, S. P.; Agnihotra, S. R.; Dua, V.; Manohar, N.; Jain, S.; Ammu, S.; Manohar, S. K., Catalyst-free synthesis of oligoanilines and polyaniline nanofibers using H(2)O(2). *J. Am. Chem. Soc.* **2009**, *131*, 12528-9.

43) Lu, J.; Dai, L.; Mau, A. W. H., Multi-dimensional doping of polyaniline emeraldine base by hydrogensulfated fullerenol derivatives. *Acta Polym.* **1998**, *49*, 371-375.

44) Wang, Q. G.; Wang, S. M.; Li, J. P.; Moriyama, H., Synthesis and characterization of C60/polyaniline composites from interfacial polymerization. *J. Polym. Sci. Pol. Phys.* **2012**, *50*, 1426-1432.

45) Itoi, H.; Hayashi, S.; Matsufusa, H.; Ohzawa, Y., Electrochemical synthesis of polyaniline in the micropores of activated carbon for high-performance electrochemical capacitors. *Chem. Commun.* **2017**, *53*, 3201-3204.

46) Liao, Y.; Yu, D. G.; Wang, X.; Chain, W.; Li, X. G.; Hoek, E. M.; Kaner, R. B., Carbon nanotube-templated polyaniline nanofibers: synthesis, flash welding and ultrafiltration membranes. *Nanoscale* **2013**, *5*, 3856-62.

47) Anantharaj, V.; Wang, L. Y.; Canteenwala, T.; Chiang, L. Y., Synthesis of starburst hexa(oligoanilinated) C-60 using hexanitro[60]fullerene as a precursor. *J. Chem. Soc., Perkin Trans. 1* **1999**, 3357-3366.

48) McClenaghan, N. D.; Absalon, C.; Bassani, D. M., Facile Synthesis of a Fullerene-Barbituric Acid Derivative and Supramolecular Catalysis of Its Photoinduced Dimerization. *J. Am. Chem. Soc.* **2003**, *125*, 13004-13005.

49) Chang, C.-Y. Y.; Wu, C.-E. E.; Chen, S.-Y. Y.; Cui, C.; Cheng, Y.-J. J.; Hsu, C.-S. S.; Wang, Y.-L. L.; Li, Y., Enhanced performance and stability of a polymer solar cell by incorporation of vertically aligned, cross-linked fullerene nanorods. *Angew. Chem. Int. Ed.* **2011**, *50*, 9386-9390.

50) Edwardson, T. G. W.; Carneiro, K. M. M.; McLaughlin, C. K.; Serpell, C. J.; Sleiman, H. F., Site-specific positioning of dendritic alkyl chains on DNA cages enables their geometry-dependent self-assembly. *Nat. Chem.* **2013**, *5*, 868-875.

51) Nakanishi, T.; Michinobu, T.; Yoshida, K.; Shirahata, N.; Ariga, K.; Möhwald, H.; Kurth, D. G., Nanocarbon Superhydrophobic Surfaces created from Fullerene-Based Hierarchical Supramolecular Assemblies. *Adv. Mater.* **2008**, *20*, 443-446.

52) Nakanishi, T.; Ariga, K.; Michinobu, T.; Yoshida, K.; Takahashi, H.; Teranishi, T.; Mohwald, H.; D, G. K., Flower-shaped supramolecular assemblies: hierarchical organization of a fullerene bearing long aliphatic chains. *Small* **2007**, *3*, 2019-23.

53) Park, Y.; Liu, Z.; Routh, P. K.; Kuo, C.-Y.; Park, Y.-S.; Tsai, H.; Martinez, J. S.; Shreve, A. P.; Cotlet, M.; Wang, H.-L., DNA-assisted photoinduced charge transfer between a cationic poly(phenylene vinylene) and a cationic fullerene. *Phys. Chem. Chem. Phys.* **2015**, *17*, 15675-15678.

54) Jung, J. W.; Jo, J. W.; Jo, W. H., Enhanced performance and air stability of polymer solar cells by formation of a self-assembled buffer layer from fullerene-end-capped poly(ethylene glycol). *Adv Mater* **2011**, *23*, 1782-7.

55) Wang, T.; Pearson, A. J.; Lidzey, D. G., Correlating molecular morphology with optoelectronic function in solar cells based on low band-gap copolymer:fullerene blends. *J Mater Chem C* **2013**, *1*, 7266-7293.

SYNTHESIS OF FUNCTIONALISED FULLERENE DERIVATIVES: STUDY OF THEIR INTERACTION AND SELF-ASSEMBLY PROPERTIES WITH CT-DNA TEMPLATES

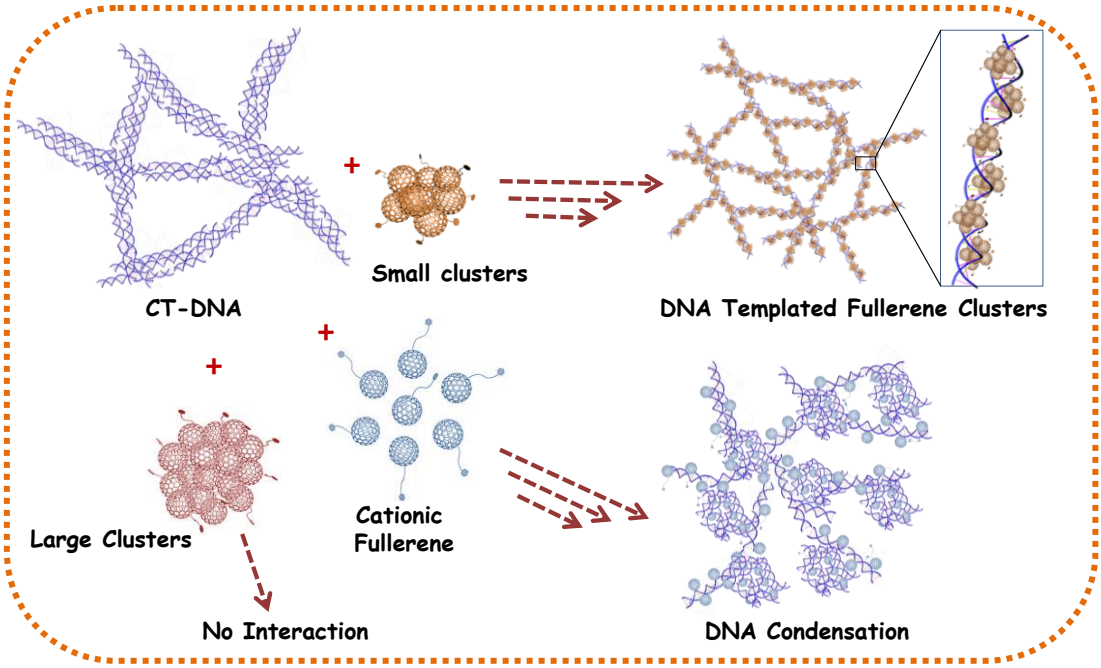

4A.1. ABSTRACT

*Herein we synthesized three monosubstituted fullerene derivatives having pyridinium, aniline or phenothiazine end groups (**F-Py**, **F-An** and **F-PTz**, respectively) and their differential interaction with calf thymus DNA (CT-DNA) was probed via spectroscopic and imaging techniques. The pyridinium derivative, **F-Py** gets molecularly dissolved in 10% DMSO-PBS and interact with CT-DNA via groove binding and electrostatic interactions leading to condensation of CT-DNA into micrometer sized aggregates. On the other hand, the aniline derivative **F-An,** which form nanoclusters of 3-5*

nm size, interact with DNA through ordered, chiral assemblies on CT-DNA template perturbing the highly networked structure of CT-DNA to form nanonetworks, which eventually transform to condensed aggregates. The binding interactions between CT-DNA and fullerene derivatives, ***F-An*** *and* ***F-Py*** *were established via UV-Vis, AFM and TEM analysis and the chiral nature of the* ***F-An*** *nanocluster assemblies on CT-DNA was confirmed through the induced circular dichroism exhibited around 250 nm - 370 nm region, corresponding to the* ***F-An*** *nanocluster absorption. In contrast, the phenothiazine derivative,* ***F-PTz****, which forms larger nanoclusters of ~70 nm in 10% DMSO-PBS showed only weak interactions with CT-DNA without affecting its network structure. These results demonstrate the role of the hydrophobic-hydrophilic balance in the design of DNA interacting fullerene derivatives in controlling their cluster size and interactions with CT-DNA and have significance in applications such as DNA condensation, gene delivery and dimension controlled nanomaterial fabrication.*

4A.2. INTRODUCTION

DNA condensation involves the compaction of long, highly charged genomic DNA into compact structures, usually with the aid of suitable compaction agents, to accommodate the genomic material inside the cell nuclei.[1-4] Several classes of compaction agents such as proteins, synthetic peptides, lipids, polyamines, linear/branched polycations, amphiphilic small molecules etc (Figure 4A.1) are known to aid DNA condensation process under *in vivo* and *in vitro* conditions and the mechanistic aspects of DNA compaction are fairly well understood.[5-9] Synthetic design of novel multivalent polycations and amphiphilic molecules,

which induce DNA condensation through multiple interactions with DNA *via* electrostatic, intercalative and/or groove binding, have attracted wide attention due to their potential applications in gene transfection and DNA nanotechnology.[10]

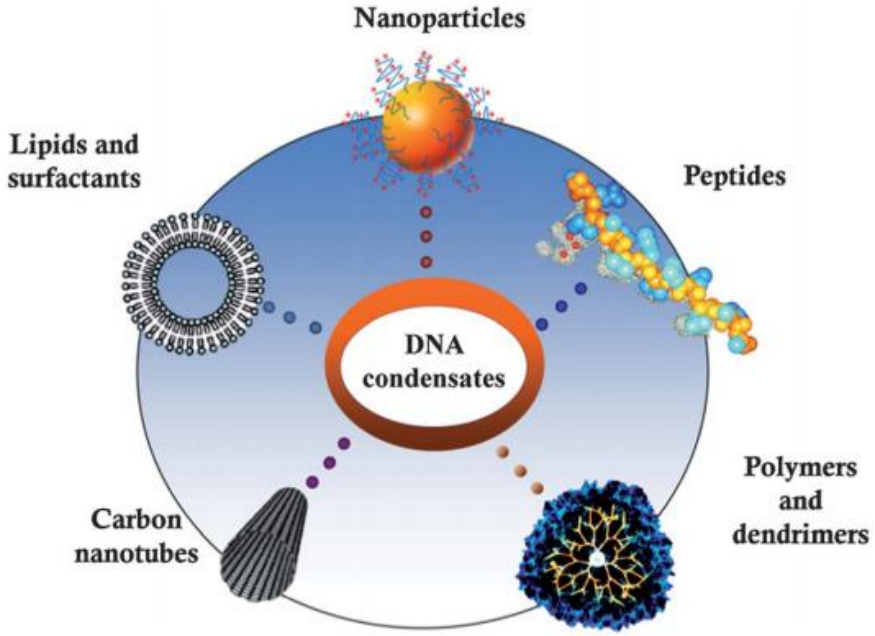

Figure 4A.1. Types of molecular nanostructures, polymeric nanostructures, and nanomaterials used as DNA condensing agents (Adapted from reference 3).

While, synthetic peptides and multivalent polycations which mimic the biological proteins and polyamines remain as the most studied classes of DNA compaction agents, carbon-based amphiphilic molecules such as fullerene derivatives also got considerable attention due to their unique structure and binding with DNA through groove and π-π interactions.[11-16] For example, Nakamura and co-workers have demonstrated a series of fullerene derivatives

for DNA condensation and subsequent applications including DNA photocleavage and fullerene-mediated *in vivo* gene delivery.[17]

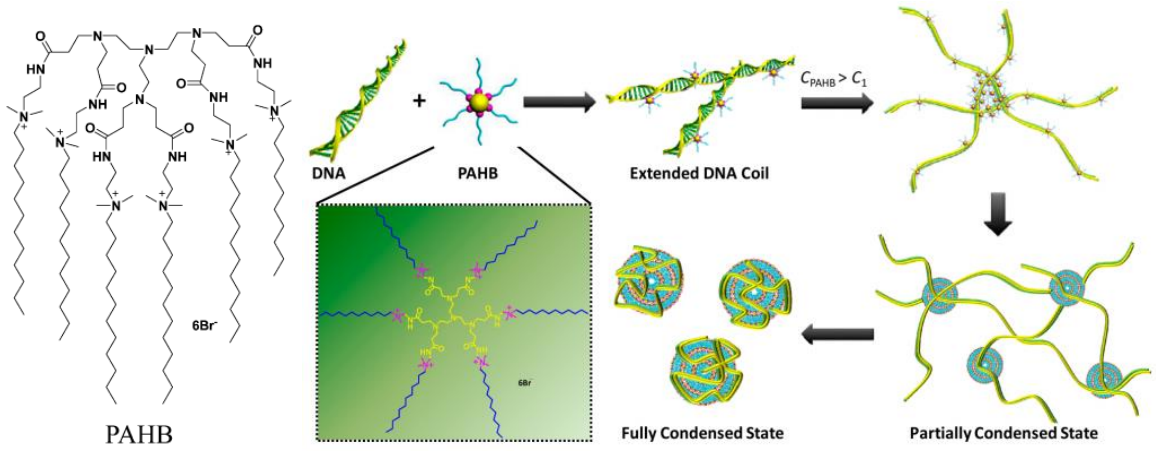

Figure 4A.2. Molecular structure of PAHB and schematic representation of PAHB-induced DNA condensation (Adapted from reference 24).

Various DNA structures such as duplex, three-way and higher order cross-over junctions, DNA origami based structures etc have been widely explored as templates and scaffolds for nanomaterial assembly via non-covalent and covalent strategies.[18-20] Similarly, well-defined nanostructures of compact DNA such as toroids, rods etc were also used as a template for the construction of nanomaterials with controlled shape and composition.[21-23] Recently, Yaxun Fan *et al.*, showed the condensation of CT-DNA using star-shaped hexameric cationic ammonium surfactant, PAHB bearing amide moieties through successive conformational transition as shown in Figure 4A.2.[24] DNA condensation with the aid of compaction agent proceeds via initial non-specific, non-covalent interactions of the multivalent molecules with DNA which may give rise to isolable intermediate morphologies (for eg. bead-on-a-string type of nanostructures)[22] which also are interesting templates for nanomaterial fabrication. In the case of water

soluble fullerene-based amphiphilic molecules, the DNA compaction properties and the obtained morphologies strongly depend on the initial fullerene nanostructures formed in aqueous/buffer conditions, which in turn offer a level of structural control via fullerene functionalization.[25-27] Moreover, the controlled self-assembly of DNA and fullerene derivatives into regular DNA based nanostructures incorporating fullerene molecules or clusters hold great promise in the context of DNA nanotechnology.

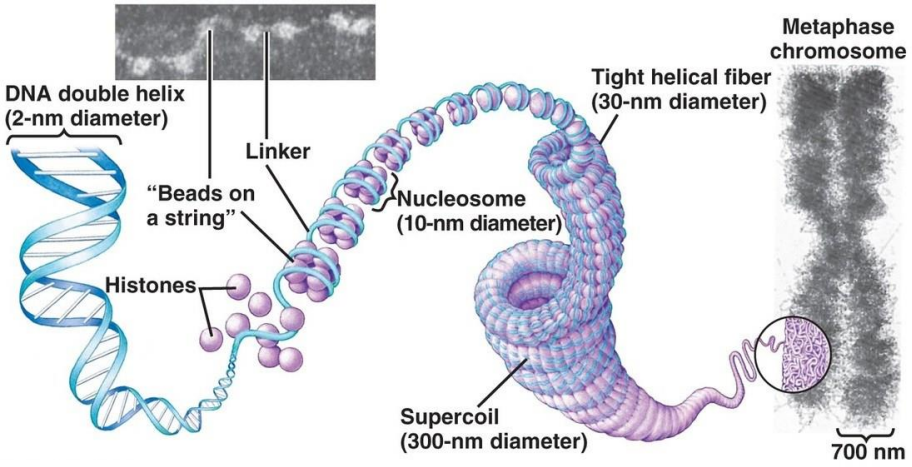

Figure 4A.3. Molecular structure of PAHB and schematic representation of PAHB-induced DNA condensation (Adapted from reference 29).

In a cellular context, nucleosomes are perfect examples of non-covalently assembled nanostructures of DNA, assisted by the octameric protein core template, which uses various types of histone-histone and histone-DNA interactions for making stable, rigid and compact structures.[28] Hence, chromatin which is DNA-histone protein complex can be packaged into a much smaller volume than DNA alone.[29] The schematic representation of various structural units involved in the chromosomal DNA compaction was shown in Figure 4A.3. Inspired by the natural design, we have attempted mimicking the octameric histone core using a fullerene derivative

functionalized with an aniline moiety which forms small fullerene clusters, roughly of the size of the histone core and are capable of interacting with duplex DNA through non-covalent interactions, results of which are discussed in chapter 4B of this thesis.[30] Herein, we report the cluster size dependent differential interactions of fullerene derivatives with CT-DNA probed via UV-Vis, fluorescence, circular dichroism (CD), atomic force microscopy (AFM), transmission electron microscopy (TEM) and dynamic light scattering (DLS) techniques.[31] The molecularly dissolved pyridinium derivative, **F-Py** interacts with CT-DNA via groove binding and electrostatic interactions leading to initial condensation of CT-DNA into micrometer sized aggregates and subsequent precipitation. In contrast, the phenothiazine derivative, **F-PTz** which forms larger nanoclusters of ~70 nm showed only weak interactions with CT-DNA without affecting its network structure. Interestingly, the nanoclusters of **F-An**, interact with DNA through ordered, chiral assemblies on CT-DNA template perturbing the highly networked structure of CT-DNA to form nanonetworks, which eventually transform to condensed aggregates.

4A.3. RESULTS AND DISCUSSION

4A.3.1. MOLECULAR DESIGN AND NANOCLUSTER FORMATION

For the construction of appropriate size nanoclusters, we rationally designed three fullerene molecular systems, **F-Py**, **F-An** and **F-PTz** substituted with the pyridinium, aniline and phenothiazine head groups respectively. In these molecules, the fullerene core was functionalized with triethylene glycol spacer imparting amphiphilic

nature to the derivatives rendering high solubility in polar solvents such as DMSO. These molecules were synthesized with multistep synthetic procedures using

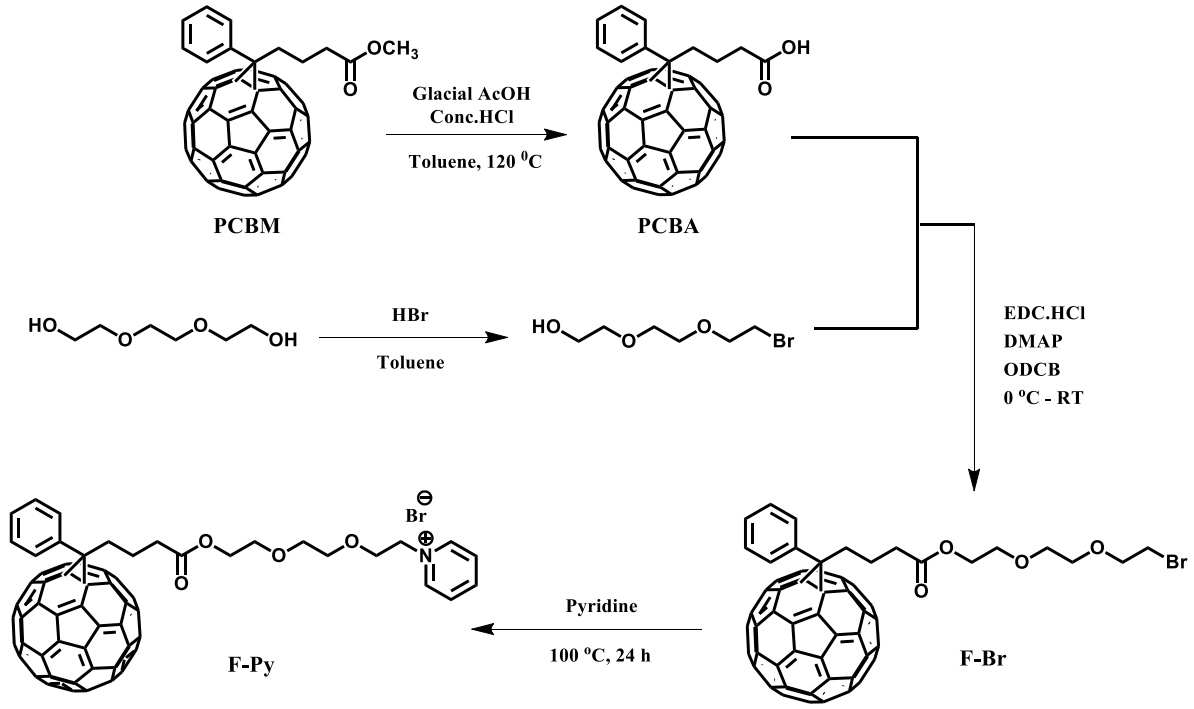

Scheme 4A.1. Synthesis of pyridinium modified fullerene derivative, **F-Py**.

EDC mediated coupling reactions (Scheme 4A.1, 4A.2 and 4A.3). The synthesis of pyridinium substituted fullerene derivative (**F-Py**) was achieved by following Scheme 4A.1. The methyl [6,6]-phenyl-C_{61}-butyrate (synonym: Phenyl-C_{61}-butyric acid methyl ester, **PCBM**) was synthesized using reported literature procedure. [32] Acid hydrolysis of PCBM afforded [6,6]-Phenyl-C_{61}-butyric acid (**PCBA**) in quantitative yield which upon EDC mediated esterification reaction with 2-(2-(2-bromoethoxy)ethoxy)ethanol gave bromo-substituted fullerene derivative (**F-Br**) in 64% yield. Quarternisation of **F-Br** with pyridine resulted **F-Py** in 49% yield.

Similarly, the synthesis of aniline substituted fullerene derivative (**F-An**) was achieved by following Scheme 4A.2. **PCBA** upon ester coupling with tert-butyl (2-(2-(2-(2-hydroxyethoxy)ethoxy)ethoxy)-phenyl)carbamate gave the corresponding Boc-protected **F-An** derivative in 71% yield. Further deprotection with trifluoroacetic acid, followed by neutralization with sodium bicarbonate resulted **F-An** in quantitative yield. tert-butyl(2-(2-(2-(2-hydroxyethoxy)ethoxy)ethoxy)phenyl)carbamate was separately

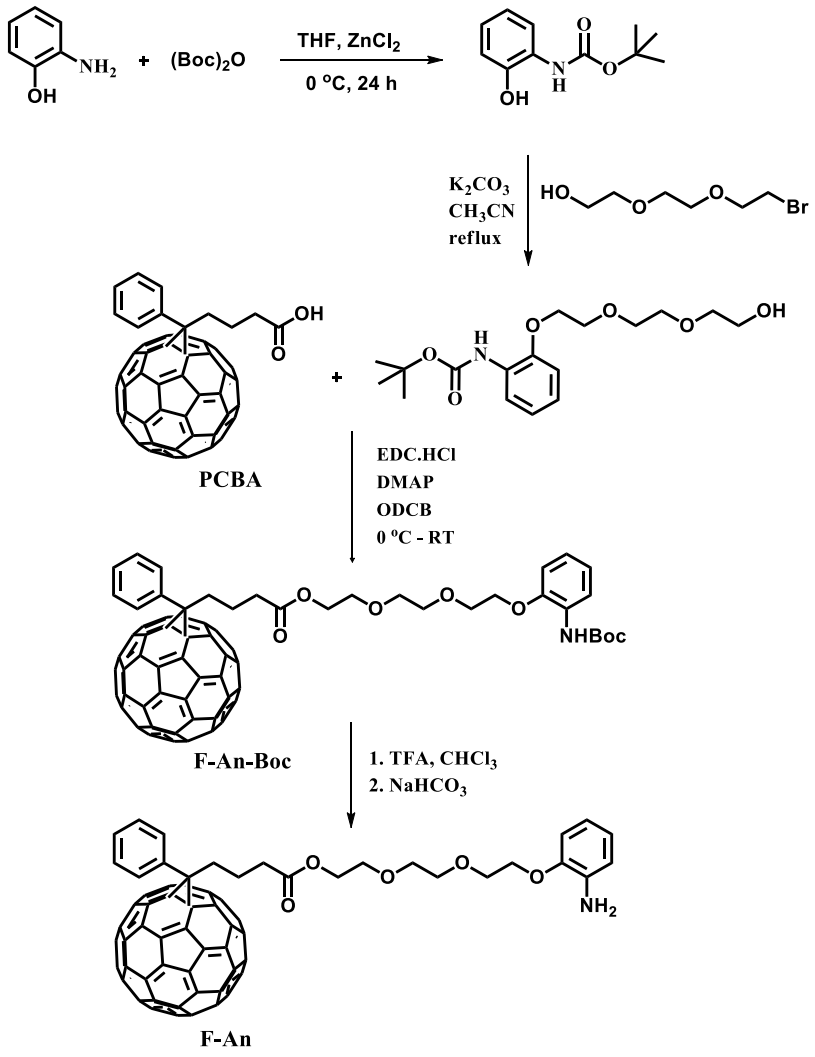

Scheme 4A.2. Synthesis of aniline modified fullerene derivative, **F-An**.

obtained in moderate yield by the alkylation reaction of tert-butyl (2-hydroxyphenyl)carbamate with 2-(2-(2-bromoethoxy)ethoxy)ethanol.

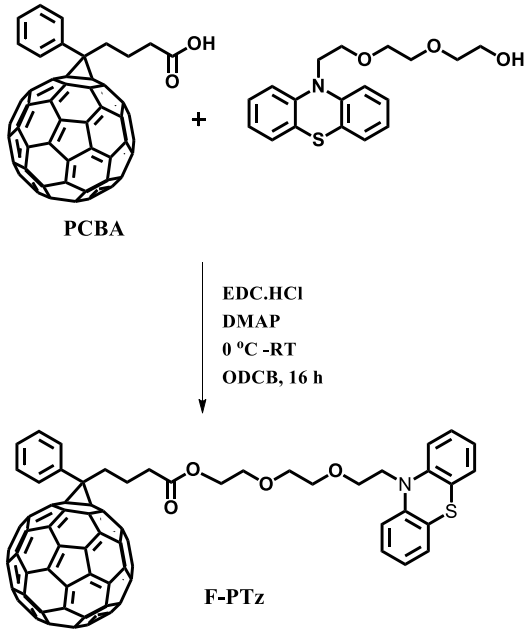

Scheme 4A.3. Synthesis of phenothiazine modified fullerene derivative, **F-PTz**.

The synthesis of phenothiazine substituted fullerene derivative (**F-PTz**) was achieved by following Scheme 4A.3. In this case, PCBA was coupled with 2-(2-(2-(10H-phenothiazin-10-yl)ethoxy)ethoxy)ethanol through EDC mediated reaction resulting **F-PTz** in 63% yield. Chemical structures of these molecules were characterized by, ^{1}H and ^{13}C NMR spectroscopy as well as by mass spectrometry, the details of which are discussed in the experimental section. Fullerene and the appended moieties are known to have non-covalent interactions with DNA through groove binding and partial intercalative interactions.[11,33-35] In order to understand the self-assembly properties, we have investigated the photophysical and morphological behaviour of **F-Py**, **F-An** and **F-PTz** in DMSO and in different DMSO-PBS (10 mM phosphate, 2 mM NaCl, pH = 7.4)

mixtures (Figure 4A.4a-c). DMSO solutions of all three molecule show characteristic monomeric absorptions corresponding to fullerene chromophore with a maximum around 330 nm as shown in Figure 4A.4 (red trace, d-f).

F-Py having polar pyridinium moiety showed almost unchanged absorption in 10% DMSO-PBS mixtures revealing the monomeric nature of **F-Py** even in higher buffer percentage (blue trace, Figure 4A.4d). In the case of **F-An** and **F-PTz**, negligible changes were observed in the absorption spectra upon increasing the buffer percentage up to

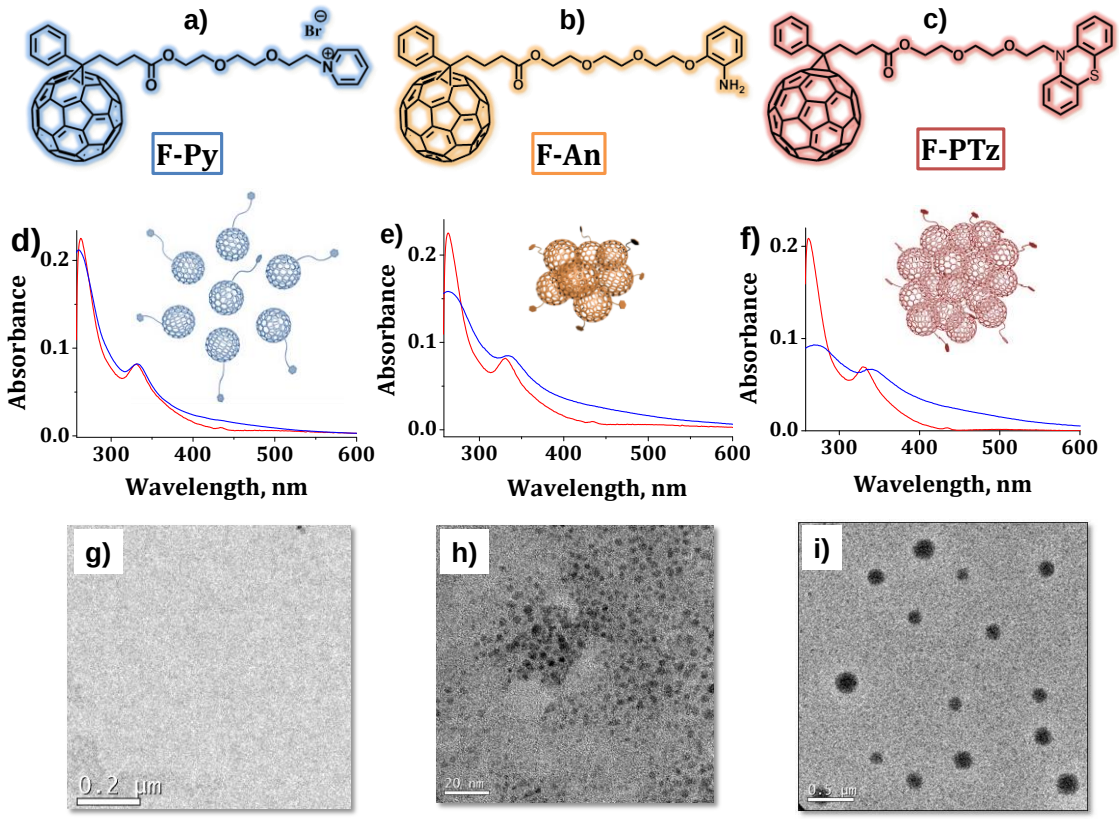

Figure 4A.4. Chemical structure of (a) **F-Py** (b) **F-An** (c) **F-PTz**. (d-f) represents the corresponding absorption spectrum (3 μM) in DMSO (red trace) and 10% DMSO-PBS (blue trace) and (g-i) show the corresponding TEM images respectively. Inset d-f shows pictorial illustration of monomeric **F-Py**, self-assembled aggregates of **F-An** and **F-PTz** into smaller and larger nanoclusters respectively.

50% (vol/vol). However, signature variations corresponding to aggregation of fullerene units were observed upon further increase in the buffer content. For example, in 10% DMSO-PBS mixture, both **F-An** and **F-PTz** showed a new broad band at longer wavelengths (400 nm - 500 nm) with a concomitant hypochromism at 262 nm and a 6 nm bathochromic shift of the 330 nm peak (Figure 4A.4e and 4f), leading to a visual colour change from pale brown to yellow (Figure 4A.5a). The morphological characterization of **F-Py**, **F-An** and **F-PTz** in 10% DMSO-PBS solution were carried out using Transmission Electron Microscopy to investigate their relative size (Figure 4A.4g-i). TEM analysis of a solution of **F-An** drop-cast on carbon coated copper grid revealed the formation of more or less uniform, spherical nanoclusters of size ranging from 3-5 nm (Figure 4A.4h). These results unambiguously demonstrate the formation of spherical nanoclusters of **F-An** with average size of <5 nm in 10% DMSO - PBS buffer mixture as schematically represented in Figure 4A.4e inset. Formation of the fullerene nanoclusters is controlled by the polarity of the molecule (the hydrophobic-hydrophilic

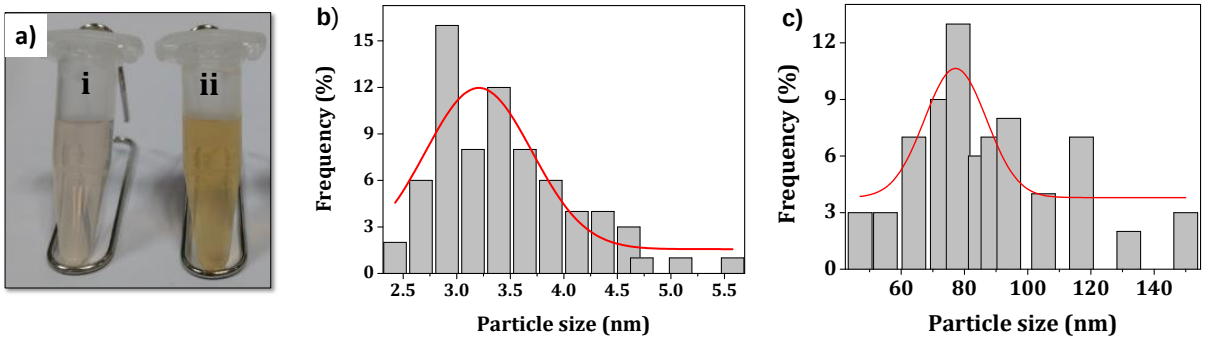

Figure 4A.5. (**a**) Photograph of **F-An** (100 μM) in (i) DMSO and (ii) 10% DMSO-PBS showing visual colour change from pale brown to yellow during the formation of nanoclusters. Fitted histograms (Gaussian fit) for the size (diameter) distribution of **b**) **F-An** nanoclusters, **c**) **F-PTz** nanoclusters, obtained from HR-TEM analyses.

balance) and hence the pendent hydrophilic group (aniline in the case of **F-An**) is crucial in regulating the size of the nanoclusters. TEM image of **F-Py** (Figure 4A.4g) under similar conditions did not result in any nanoclusters indicating the cationic pyridinium head group render the molecule soluble in 10% DMSO-PBS mixtures as schematically represented in Figure 4A.4d inset. Average diameter of seventy **F-An** clusters measured from TEM analysis is 3.2 nm (Figure 4A.5b), which is close to the size of smallest fullerene cluster composed of eight fullerene molecules. The backbone length of individual **F-An** molecule was found to be ~1.4 nm with core diameter of 0.7 nm. Whereas, substitution by a phenothiazine moiety (**F-PTz**) lead to larger nanoclusters as evidenced from TEM analysis (inset of Figure 4A.4f and Figure 4A.4i). The average size of seventy nanoclusters of **F-PTz** was calculated to be 77 nm from TEM size distribution (Figure 4A.5c). The observed higher nanocluster size in the case of **F-PTz** compared to **F-An** might be due to the increased tendency of aggregation in the presence of bulkier and less hydrophilic head group.

4A.3.2. CT-DNA INTERACTION STUDIES OF FULLERENE DERIVATIVES

With a view to understand the structure-property relationships governing the interaction of fullerene derivatives with long genomic DNA and their subsequent applications in DNA condensation and construction of ordered nanostructures, we have studied the interactions of **F-Py**, **F-An** and **F-PTz** with calf thymus DNA (CT-DNA). Initially, interactions of fullerene derivatives **F-Py**, **F-An** and **F-PTz**, with CT-DNA were studied through UV-Visible absorption

spectroscopy and the results are summarized in Figure 4A.6. Upon successive addition of CT-DNA to cationic **F-Py**, the absorption bands around 260 nm and

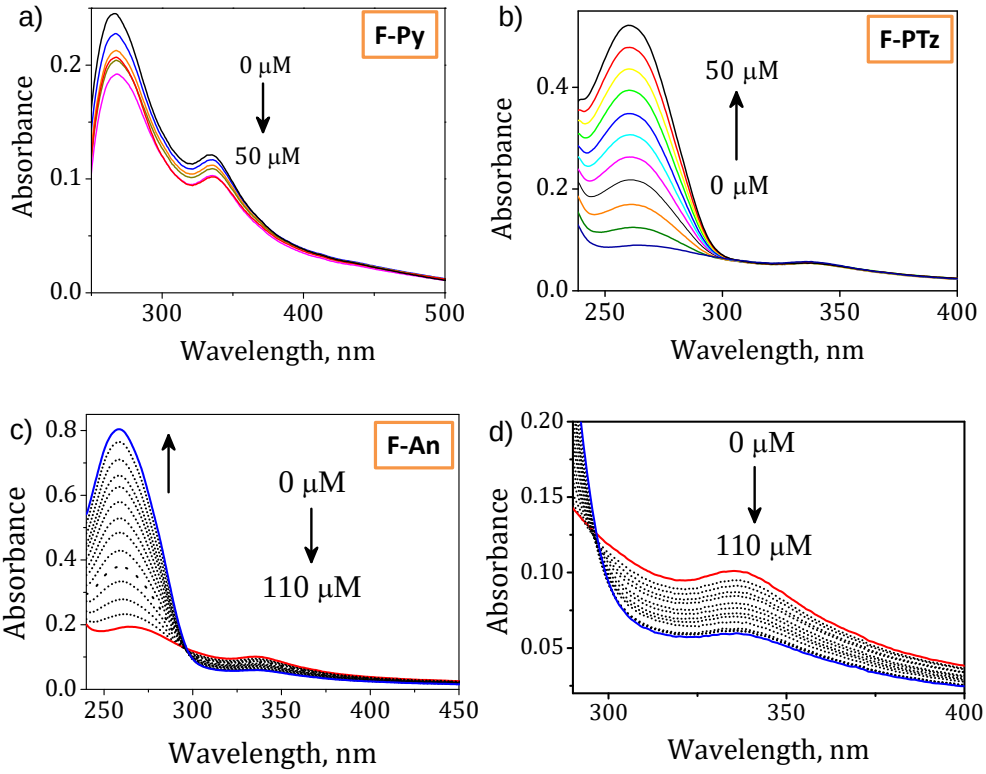

Figure 4A.6. Changes in the absorption spectra of (a) **F-Py**, (b) **F-An** and (c) **F-PTz** with sequential addition of CT-DNA in 10% DMSO-PBS; Inset in (d) shows zoomed portion between 290-400 nm.

334 nm decreased consistently (Figure 4A.6a), indicating subsequent aggregation of the DNA-**F-Py** complex. The decreases in absorbance around 260 nm where DNA bases have substantial absorption, even after successive addition of CT-DNA clearly indicate **F-Py** assisted aggregation of the added CT-DNA. The amphiphilic, **F-Py** derivative can interact with DNA through electrostatic interactions of the cationic, pyridinium group with anionic DNA backbone and

groove interactions of the fullerene moiety.[12] The observed aggregation behaviour of DNA-**F-Py** complex could be attributed to the synergistic effect of the charge neutralization by the cationic pyridinium group and to the increased hydrophobicity due to the groove binding of hydrophobic fullerene moieties.

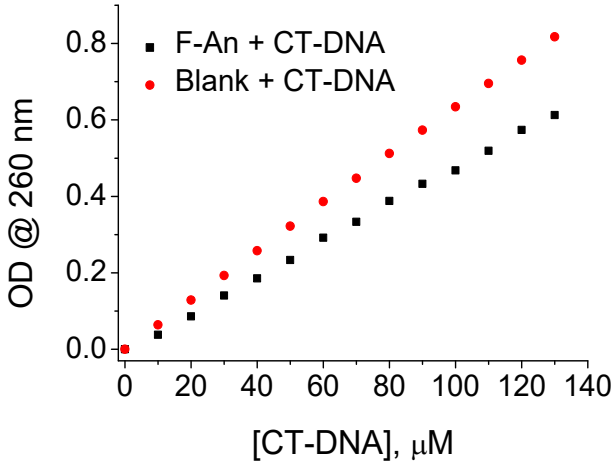

Figure 4A.7. Absorption changes at 260 nm in the presence and absence of **F-An** with increasing concentration of [CT-DNA]. CT-DNA was added in small aliquots to a 10% DMSO-PBS solution of **F-An** nanoclusters or to a 10% DMSO-PBS solution blank.

On the other hand, sequential addition of CT-DNA to **F-An** solution showed a regular increase in the absorption around 260 nm corresponding to the absorption of the DNA bases with a concomitant decrease in the **F-An** nanocluster absorption around 336 nm (Figure 4A.6c). The maximum hypochromicity observed around 336 nm was approximately 40% with an isosbestic point at 296 nm (Figure 4A.6d). The change in the absorption around 260 nm includes contribution from decreased absorption (hypochromicity) of **F-An** nanoclusters and nucleobases due to **F-An**-DNA interactions and enhancement due to the increase in DNA concentration. These opposing effects

result in an apparent, but diminished increase in the absorption around 260 nm, compared to a blank CT-DNA titration experiment without the **F-An** nanoclusters (Figure 4A.7). The observed changes could be due to the binding of **F-An** nanoclusters with CT-DNA through groove binding interactions of fullerene and aniline moieties.

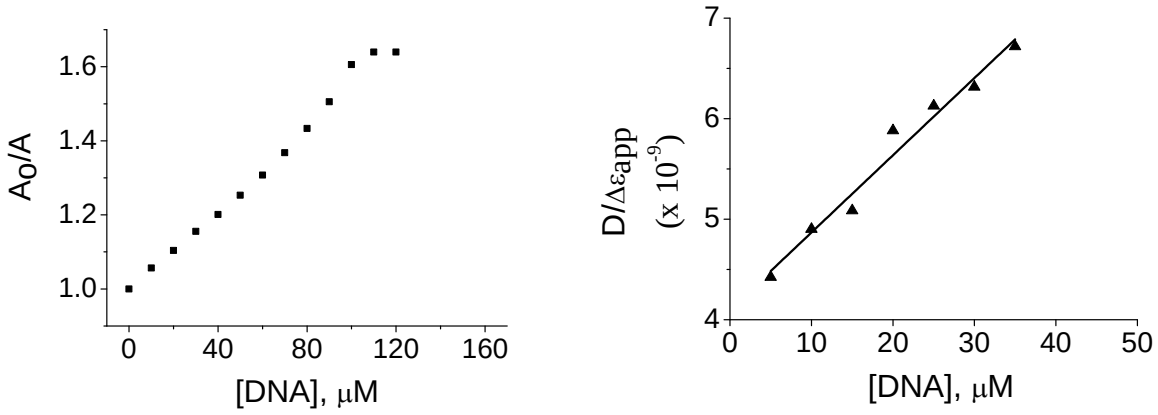

Figure 4A.8. a) Saturation plot of absorption changes at 336 nm upon addition of CT-DNA to **F-An** (3 μM) and b) corresponding half reciprocal plot with increase in [CT-DNA].

The intrinsic binding constant (K_{DNA}) for the binding of **F-An** nanoclusters was calculated through half reciprocal plots and was found to be 1.87 x 10^4 M^{-1} (Figure 4A.8). A similar titration experiment with CT-DNA and **F-PTz** showed negligible changes corresponding to the **F-PTz** cluster absorption around 340 nm (Figure 4A.6b), which clearly indicates that larger nanoclusters of **F-PTz** has negligible interactions with DNA. Both **F-An** and **F-PTz** remain as neutral clusters at physiological conditions used and hence any electrostatic interaction between these fullerene derivatives and DNA can be ruled out. Thus, the UV-Vis titration experiments indicate differential interactions of these fullerene derivatives with

CT-DNA due to the differences in their solubility and cluster formation behaviour in 10% DMSO-PBS. Individually solvated molecules of **F-Py** and 3-5 nm sized nanoclusters of **F-An** interact efficiently through electrostatic/groove interactions while larger nanoclusters of **F-PTz** fail to establish such interactions due to possible steric constraints.

4A.3.3. FLUORESCENCE DISPLACEMENT ASSAY

Ethidium bromide based fluorescence displacement assay is highly useful in understanding the mode of binding of small intercalator and groove binding molecules, where competitive displacement of the intercalated ethidium bromide lead to substantial quenching of the ethidium bromide fluorescence.[36,37] The aniline moieties in **F-An** nanoclusters, due to the small size and planar aromatic nature can interact with DNA through groove binding and intercalative interactions. To understand the role of aniline intercalation in the CT-DNA-**F-An** nanocluster interactions, we have conducted the ethidium bromide based fluorescence displacement assay. A highly fluorescent

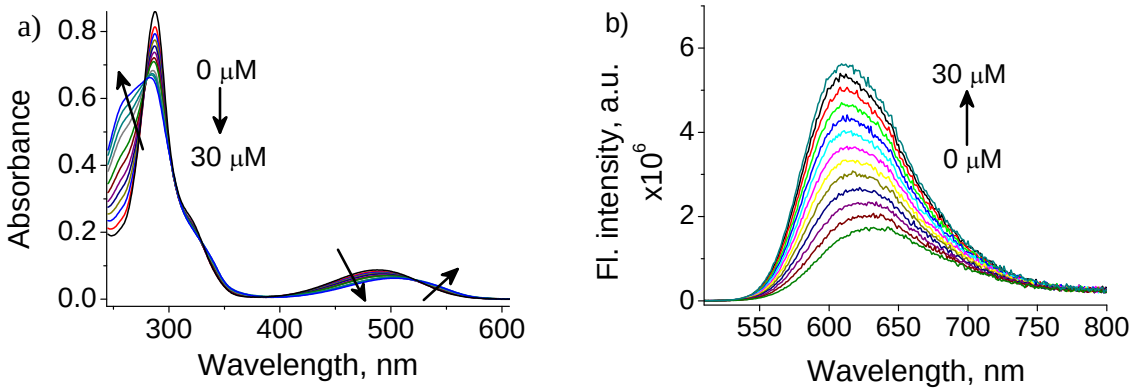

Figure 4A.9. Changes in the a) absorption spectra and b) emission spectra of ethidium bromide (30 μM) in the presence of increasing concentrations of CT-DNA.

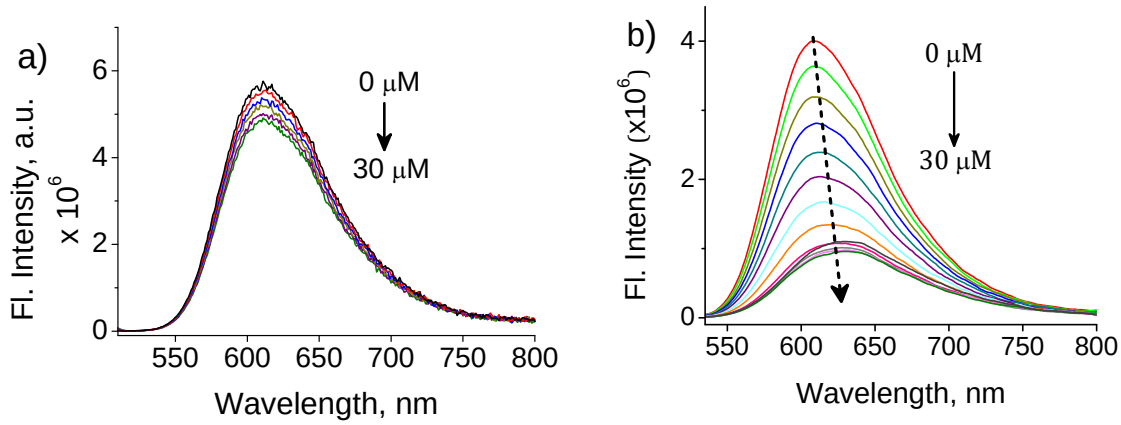

Figure 4A.10. Changes in the emission spectra of CT-DNA/ethidium bromide complex (30 μM/ 30 μM, 1:1) in the presence of increasing concentrations of a) **F-An** and b) **F-Py**.

ethidium bromide - CT-DNA complex was prepared via titration of ethidium bromide against CT-DNA as shown in Figure 4A.9. Further, **F-An** nanoclusters were titrated against this fluorescent ethidium bromide-CT-DNA complex, which showed only small changes in the fluorescence upon the addition of up to 30 μM of **F-An** (Figure 4A.10) indicating negligible displacement of the intercalated ethidium bromide. Therefore, the interaction of the **F-An** nanoclusters with CT-DNA could be attributed mostly to the groove interactions of the fullerene clusters and aniline moieties. On the other hand, titration of **F-Py** with EB/CT-DNA complex showed gradual decrease in fluorescence reflecting the displacement of intercalated EB from CT-DNA. Hence, cationic pyridinium moiety present in **F-Py** undergo intercalation mode of binding probably assisted by initial electrostatic interactions.

4A.3.4. CIRCULAR DICHROISM STUDIES

To understand the possible interactions between the CT-DNA/**F-An** nanoclusters and to verify the role of CT-DNA as a template in the self-assembly

of nanoclusters, we have carried out circular dichroism (CD) studies of CT-DNA (100 μM) in presence of varying amounts of **F-An** nanoclusters as shown in Figure 4A.11a. CT-DNA alone showed the characteristic CD spectra

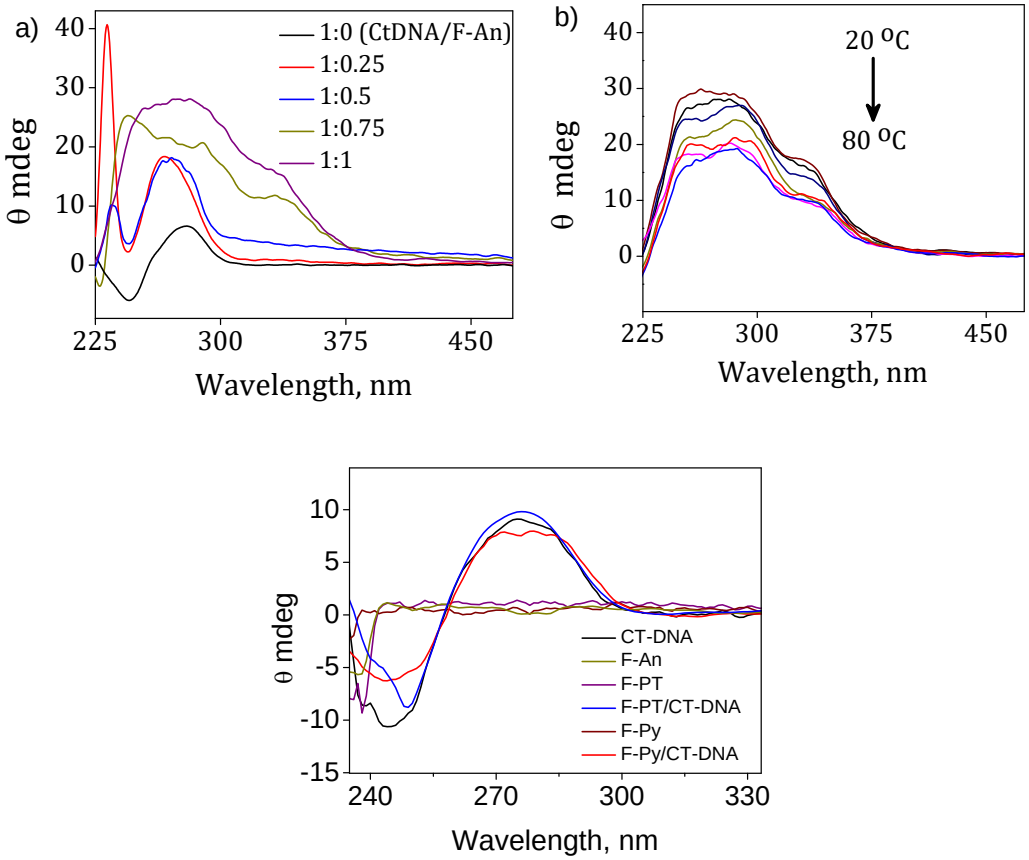

Figure 4A.11. (a) Changes in the CD spectra of CT-DNA with increasing addition of **F-An**; (b) Temperature dependent CD spectral profile of CT-DNA/**F-An** (1:1) from 20 °C to 80 °C; (c) CD spectra of **F-An**, **F-Py** and **F-PTz** with and without CT-DNA.

corresponding to the B-form DNA with a positive peak at 275 nm and a negative peak at 245 nm (Figure 4A.11a) as reported previously.[34,38] Upon increasing the concentration of **F-An** nanoclusters from 1:0 to 1:1, the CD spectra showed significant changes with the appearance of strong induced CD around 250 nm -

370 nm, the region corresponding to the **F-An** nanocluster absorption. Solutions of the **F-An** nanocluster alone at different concentrations didnot show any CD signal (Figure 4A.11c) and hence the observed positive induced CD signal could be attributed to the chiral organization of the **F-An** nanoclusters on the CT-DNA template facilitated by groove binding interactions and possible π-π interactions between adjacently bound **F-An** nanoclusters. The control experiments such as **F-Py**, **F-PTz** with and without CT-DNA showed no ICD confirming that only **F-An** with unique cluster size can undergo templated, chiral self-assembly with CT-DNA. Further, temperature dependent CD spectra were studied to understand the stability of CT-DNA/**F-An** self-assembled system in solution. The decrease in the CD intensity upon increasing the temperature from 20 ^{o}C to 80 ^{o}C demonstrate the disassembly of the nanoclusters from the CT-DNA template (Figure 4A.11b). The lack of complete disappearance of the CD signal could be attributed to the higher melting temperature of CT-DNA, preventing the complete disassembly of nanoclusters from its surface.

4A.3.5. MORPHOLOGICAL STUDIES

The morphology changes accompanying the interaction of the fullerene derivatives with CT-DNA were studied using AFM, TEM and DLS techniques. AFM experiments were carried out by drop casting 10 μL solution (10% DMSO-PBS) containing CT-DNA (100 μM) and CT-DNA/**F-An** (100 μM, 1:1) complex separately on freshly cleaved mica surface. The concentration of the samples were chosen based on CD studies. CT-DNA alone exhibited highly networked

structure with an average width of ~250 nm, due to the strong DNA-DNA interactions, which agree well with the previous reports (Figure 4A.12a).[39-41] On the other hand, the CT-DNA/**F-An** complex showed significantly different nanofibrous structure, where the highly networked structure of CT-DNA was broken down to smaller nanofibres of 50-100 nm size and subsequent

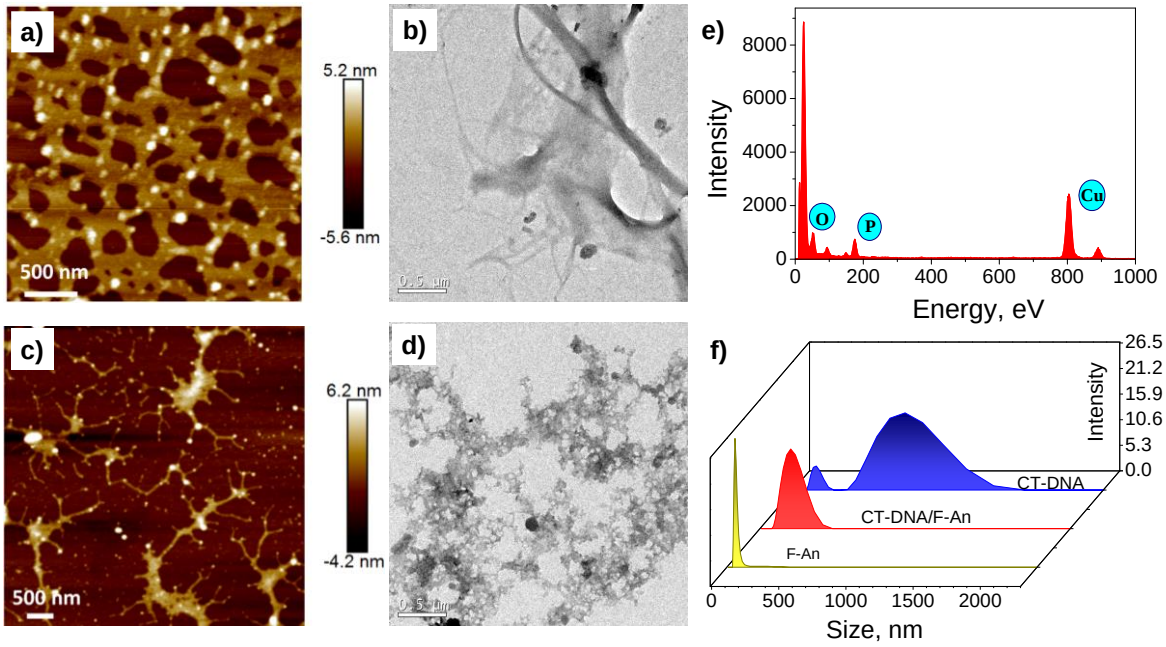

Figure 4A.12. (a-b) AFM and TEM image of CT-DNA. (b-d) AFM and TEM image of CT-DNA/**F-An** complex in 10% DMSO-PBS; e) EDAX analysis obtained from TEM; f) Size distribution of **F-An**, CT-DNA/**F-An** (1:1) and CT-DNA obtained from DLS measurements.

condensates (Figure 4A.12c). The change in morphology of CT-DNA upon **F-An** nanocluster binding could be attributed to the reduction in the DNA-DNA interactions subsequent to the groove binding of **F-An** nanoclusters. TEM analysis of CT-DNA alone and CT-DNA/**F-An** complex over carbon coated copper grid further confirmed the disruption of the CT-DNA network structure and DNA templated **F-An** nanocluster self-assembly (Figure 4A.12b and 12d). Moreover,

the EDAX analysis over the obtained nanostructures indicated the occurrence of phosphorous atoms which confirmed the presence of DNA throughout the obtained nanostructures (Figure 4A.12e). To ascertain that the formation of CT-DNA/**F-An** self-assembled nanostructures was not a surface dependent phenomenon, we have performed dynamic light scattering (DLS) studies under similar experimental conditions. The CT-DNA/**F-An** complex showed observable changes in the hydrodynamic radius compared to CT-DNA alone, indicating the breakdown of the highly networked structure of CT-DNA upon **F-An** nanocluster binding (Figure 4A.12f).These results coupled with the CD analysis further support the chiral self-assembly of **F-An** nanoclusters along the CT-DNA template facilitated by the groove binding and possible π-π interactions between the clusters, as shown schematically in Figure 4A.13.

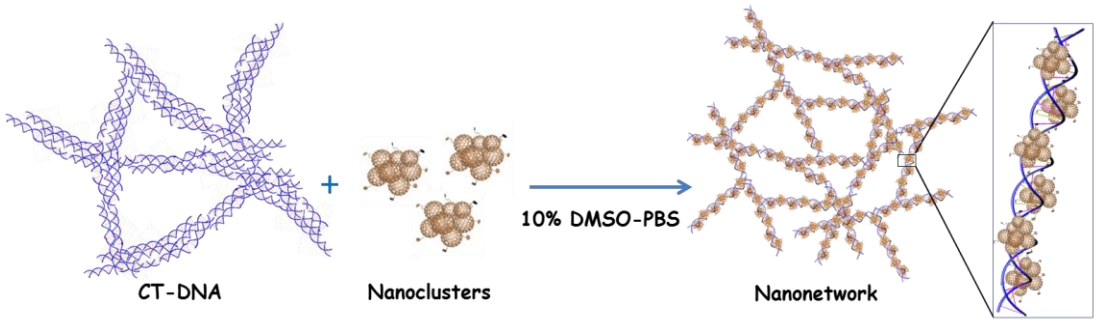

Figure 4A.13. Pictorial representation of CT-DNA templated nanonetwork formation of **F-An** nanoclusters in 10% DMSO-PBS mixture.

In order to understand the changes in the CT-DNA morphology in the process of the **F-Py** induced condensation, the morphologies of CT-DNA at different **F-Py** concentrations from 0 to 0.1 mM were analysed using AFM as

shown in Figure 4A.14. With the addition of 0.25 μM **F-Py**, slight perturbation of highly network structure of CT-DNA was observed. Upon further increasing the **F-Py** concentration to 0.5 μM the CT-DNA/**F-Py** aggregates present a beads-on-a-string structure, which is composed of about ~50 nm spherical aggregates interconnected by unfolded DNA chains. Further increase in the **F-Py** concentration led to the compaction of smaller aggregates into larger spherical aggregates with average sizes ranging from 100-250 nm. In contrast, AFM analysis of CT-DNA under similar conditions, in the presence of larger **F-PTz** nanoclusters (Figure 4A.15a), showed no visible disruption of the CT-DNA fibrous network structures (Figure 4A.15b).

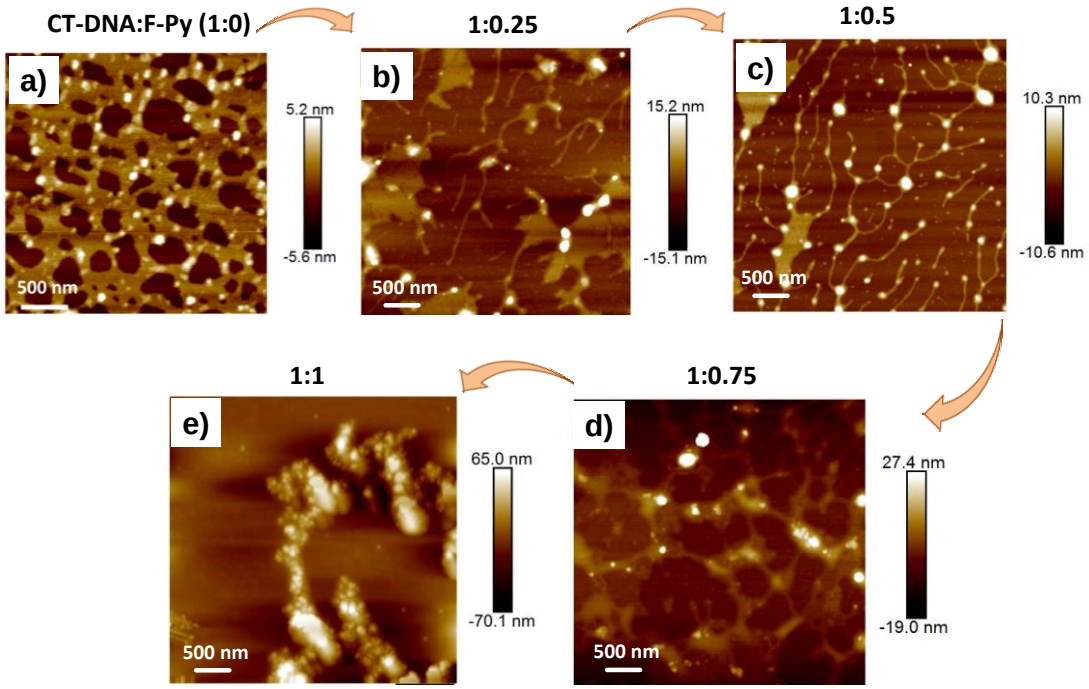

Figure 4A.14. AFM images representing the changes in the CT-DNA (100 μM) morphologies at a) 0, b) 0.25, c) 0.5, d) 0.75, d) 1 equivalents of **F-Py**.

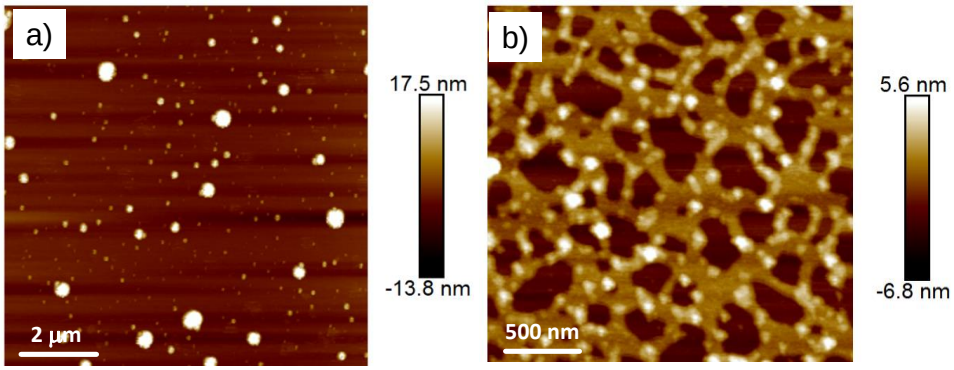

Figure 4A.15. AFM height image of a) **F-PTz** alone and b) CT-DNA/**F-PTz**.

To get further insight into the stepwise CT-DNA condensation, the changes in the zeta-potential and size of CT-DNA were measured upon successive increase in the **F-Py** concentration (Figure 4A.16). CT-DNA exhibited a zeta-potential of about -50 mV and a hydrodynamic diameter of 700 nm, which are consistent with the results reported previously.[24] With the initial additions of **F-Py** solution, the value started to decrease while the zeta-potential value became less negative, indicating that the binding of cationic F-Py with CT-DNA takes place even at extremely low **F-Py** concentration due to

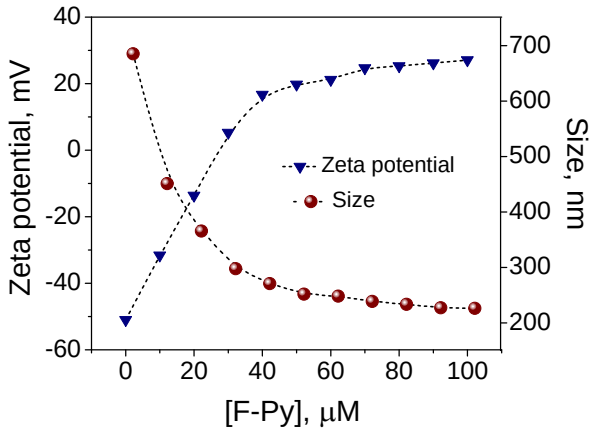

Figure 4A.16. Variation of the zeta-potential and the hydrodynamic diameter of CT-DNA (100 µM) measured by DLS as a function of **F-Py** concentration.

their strong electrostatic interaction. Onset of CT-DNA condensation was observed at **F-Py** concentration of 20 μM. At this point, the aggregate size becomes ~400 nm with a zeta potential of -20 mV. This indicates that the CT-DNA chains have been condensed into small aggregates with less negative charges in the presence of oppositely charged **F-Py** molecules. Upon further increasing **F-Py** concentration, the values of both the size and zeta-potential significantly reaches constant values, which are about 200 nm and 30 mV, respectively indicating the completion of CT-DNA condensation where additional **F-Py** molecules will not get incorporated into the CT-DNA/**F-Py** aggregates.

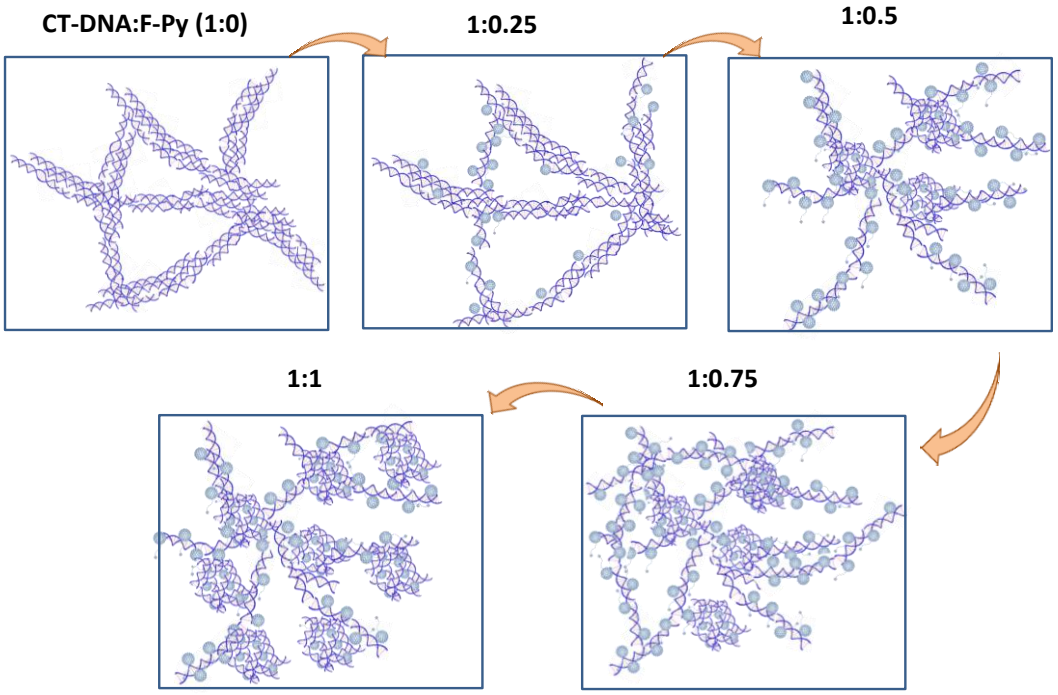

Figure 4A.17. Pictorial representation of **F-Py** induced concentration dependent CT-DNA condensation.

From these experimental observations, the mechanism of **F-Py** induced DNA condensation can be proposed as shown in Figure 4A.17. Initially, the double stranded

CT-DNA exist in a highly network structure due to the interstrand interaction. Upon increase in the concentration, **F-Py** bind to the DNA through strong electrostatic and intercalative binding modes, leading to the disruption of CT-DNA network. Further increase in the concentration of **F-Py** induces the conformational transition of the DNA chains, forming partially condensed cluster-like aggregates, then beads-on-a-string structure, and finally fully condensed CT-DNA/**F-Py** aggregates.

4A.4. CONCLUSIONS

In summary, we have reported the differential interaction of three monosubstituted fullerene derivatives, **F-Py**, **F-An** and **F-PTz** having pyridinium, aniline or phenothiazine end groups with CT-DNA. The nature of the end group and subsequent changes in the hydrophobic-hydrophilic balance in these derivatives resulted in significant differences in their solvation and cluster formation behaviour in 10% DMSO-PBS and in their interactions with CT-DNA. For example, the cationic fullerene derivative, **F-Py** gets molecularly dissolved in 10% DMSO-PBS and strongly interact with CT DNA via electrostatic and intercalative binding interactions leading to the formation of micrometer sized condensed aggregates. On the other hand, the phenothiazine derivative, **F-PTZ**, forms larger nanoclusters and fails to interact with CT-DNA. In contrast, the aniline derivative, **F-An** which forms 3-5 nm sized nanoclusters efficiently interact with CT-DNA and induce perturbations in the highly network structure of the CT-DNA. CD and morphological studies of CT-DNA/**F-An** complex confirmed the chiral self-assembly of **F-An** nanoclusters along the CT-DNA

template and the disruption in the CT-DNA network structure to form smaller, nanofibrous structure with subsequent condensation.

4A.5. EXPERIMENTAL SECTION

4A.5.1. Materials and Methods

The double stranded calf-thymus DNA (CT-DNA) and Ethidium bromide (EB) were purchased from Sigma Aldrich. Spectroscopic grade (99.9%) DMSO solvent was purchased from Merck. All the chemicals and reagents were used as received without further purification. Milli Q deionized water (18.2 MΩ.cm) was used throughout the studies.

All the experiments were performed in 10% DMSO-PBS solvent mixture. The fullerene derivatives were initially dissolved in DMSO and then diluted with deionized water to obtain appropriate concentrations in 10% DMSO-PBS solvent mixture. The UV-Visible absorption spectra were recorded on a Shimadzu UV-2600 Spectrophotometer. For these studies, the concentration of fullerene derivative was kept constant (3 μM) and DNA solution (2.5 mM) in small aliquots was added. All optical measurements were carried out using 1 cm cuvettes at room temperature (25± 1 ^{o}C) unless otherwise mentioned. The fluorescence emission spectra were recorded on a SPEX FLUOROLOG-3 (FL3-221) spectrofluorimeter. The wavelength of excitation was 515 nm. The fluorescence of CT-DNA/**EB** complex (30 μM/30 μM) was measured by subsequent addition of **F-An** in small portions. Circular dichroism measurements were performed on a Jasco J-810 spectropolarimeter having Peltier controlled thermostatic cell holder

where the sensitivity, integration time and scan rate were chosen appropriately. The DLS experiments were performed in quartz cuvettes using the same solutions which are used for microscopic studies. The hydrodynamic diameters of the nanoclusters were determined using a Malvern Zeta Nano-ZS system.

4A.5.2. CT-DNA Binding Studies

A solution of calf thymus DNA was dissolved in Millipore water to minimize complexities arising from DNA flexibility and filtered through 0.45 μm syringe filter. The concentrations of DNA solutions were determined by using the average value of 6600 $M^{-1}cm^{-1}$ for the extinction coefficient of a single nucleotide at 260 nm.[42] A stock solution of 2.5 mM CT-DNA in 10 mM phosphate buffer containing 2 mM NaCl was used for all further studies. The intrinsic binding constant of the **F-An** with CT-DNA was determined using absorbance at the respective maxima (336 nm) recorded after each addition of CT-DNA. The intrinsic binding constant K_{DNA} was determined from the half reciprocal plot of $D/\Delta\varepsilon_{app}$, vs D, using

$$D/\Delta\varepsilon_{app} = D/\Delta\varepsilon + 1/ (\Delta\varepsilon K_{DNA}) \quad (1)$$

where D is the base pair concentration of CTDNA, $\Delta\varepsilon_{ap} = [\varepsilon_a - \varepsilon_F]$ and $\Delta\varepsilon = [\varepsilon_b - \varepsilon_F]$.[43,44] The apparent extinction coefficient, ε_a is obtained by calculating $A_{[obsd]}$ / [**F-An**], ε_b and ε_F correspond to the extinction coefficient of the bound form of the **F-An** and the extinction coefficient of the free **F-An** derivatives, respectively. The data were fitted to the equation (1), with a slope equal to $1/\Delta\varepsilon_{app}$ and a y-intercept equal to $(1/K_{DNA})$. ε_b was determined from $\Delta\varepsilon$ and K_{DNA} was obtained from the ratio of the slope to the y-intercept.

4A.5.3. AFM/TEM Sample Preparations

Samples for AFM analysis were prepared by drop-casting 10 μL solution (10% DMSO-PBS) of CT-DNA (100 μM), CT-DNA/fullerene derivative complex (100 μM, 1:1) onto freshly cleaved mica sheet under ambient conditions and were dried under air. A BRUKER MULTIMODE AFM operating with a tapping mode regime was used to record AFM images under ambient conditions. Micro fabricated TiN cantilever tips (NT-MDT-NSG series) with a resonance frequency of 299 kHz and a spring constant of 20 to 80 Nm^{-1} were used. AFM section analysis was done offline. TEM samples were prepared by drop casting 10 μL solution (concentration were chosen based on AFM experiments) of the sample on the top of the carbon-coated copper grid (400 mesh). The samples were allowed to adsorb on the grid overnight at ambient conditions and were added Millipore water (2 x 10 μL) to remove buffer salts. TEM analysis was performed with a JEOL 100 kV high-resolution transmission electron microscope. The accelerating voltage of the TEM was 100 kV and the beam current was 65 A. Samples were imaged with a Hamamatsu ORCA CCD camera.

4A.5.4. SYNTHETIC PROCEDURES

4A.5.4.1. Synthesis of 2-(2-(2-bromoethoxy)ethoxy)ethanol,[45]

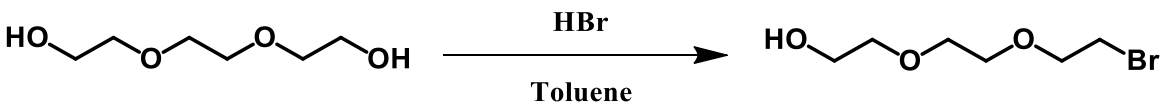

To a solution of 2,2'-(ethane-1,2-diylbis(oxy))diethanol (10 g, 0.066 mmol) and toluene (150 mL) was added hydrobromic acid (15 mL of 48% aqueous solution). The heterogeneous mixture was stirred and refluxed at 110 ^{o}C. After 36 h, the organic layer was separated using ethyl acetate (2 x 100 mL). The solvent was rotary evaporated and the crude product was separated by column chromatography using 30% ethylacetate-hexane mixture (R_f : 0.5) to obtain yellow liquid in 21% yield (3 g).

^{1}H NMR (500 MHz, $CDCl_3$), δ (ppm): 3.84 (t, J = 6 Hz, 2H), 3.76 (t, J = 4.75 Hz, 2H), 3.69 (s, 4H), 3.64 (t, J = 4.25 Hz, 2H), 3.51 (t, J = 6.25 Hz, 2H).

^{13}C NMR (125 MHz, $CDCl_3$), δ (ppm): 72.56, 71.15, 70.50, 61.70, 30.56.

HRMS (m/z): $[M]^+$ calcd. for $C_6H_{13}BrO_3$, 212.00; found, 213.01 (M+H).

4A.5.4.2. Synthesis of 2-(2-(2-bromoethoxy)ethoxy)ethyl [6,6]-phenyl-C_{61}-butyrate, F-Br

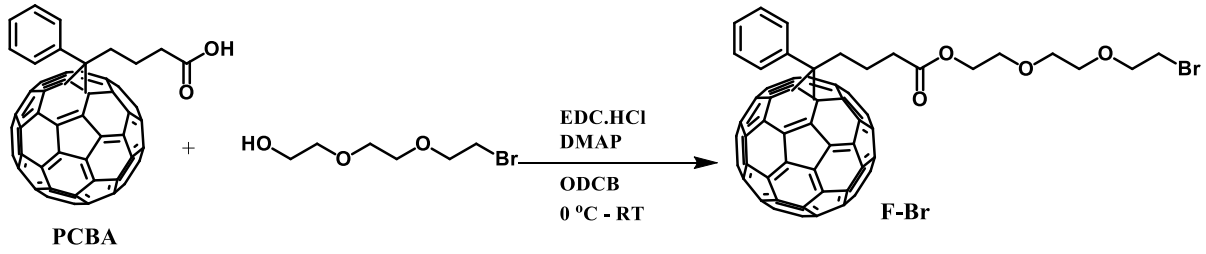

To a solution of **PCBA** (100 mg, 0.0558 mmol) in 1,2-dichlorobenzene (6 mL) was added 4-dimethylaminopyridine (12 mg, 0.0558 mmol), EDC-HCl (64 mg, 0.1674 mmol) and stirred for 10 min at 0 ^{0}C. 2-(2-(2-bromoethoxy)ethoxy)ethanol (32 μL, 0.1116 mmol) was added directly to the reaction mixture and stirred overnight at room temperature. The crude mixture was purified by column chromatography using chloroform (R_f : 0.7) which afforded brown colour solid in 64% yield (77.80 mg).

^{1}H NMR (500 MHz, $CDCl_3$), δ (ppm): 7.95 (d, J = 7.5 Hz, 2H), 7.58 (t, J = 7.5 Hz, 2H), 7.51 (t, J = 7.25 Hz, 1H), 4.27 (t, J = 4.75 Hz, 2H), 3.83 (t, J = 6.25 Hz, 2H), 3.73 (t, J = 6.5 Hz, 2H), 2.97 (t, J = 9.125 Hz, 2H), 2.59 (t, J = 7.5 Hz, 2H), 2.24 (m, J = 7.87 Hz, 2H).

^{13}C NMR (125 MHz, $CDCl_3$), δ (ppm): 174.23, 148.29, 147.80, 145.85, 145.70, 145.26, 145.01, 144.88, 144.69, 144.58, 144.43, 144.32, 144.17, 144.03, 143.61, 143.05, 142.73, 142.08, 142.12, 141.19, 141.06, 139.04, 138.57, 135.79, 133.61, 128.04, 127.26, 121.72, 78.97, 70.06, 69.43, 68.20, 67.93, 62.9, 32.91, 27.42, 22.3.

MALDI (m/z): M^+ calcd. for $C_{77}H_{23}BrO_4^+$, 1090.07; found, 1113.06 (M+Na).

4A.5.4.3. Synthesis of 1-(2-(2-(2-(([6,6]-phenyl-C_{61}-butyroyl)oxy)ethoxy)ethoxy) -ethyl) pyridine-1-ium bromide, F-Py

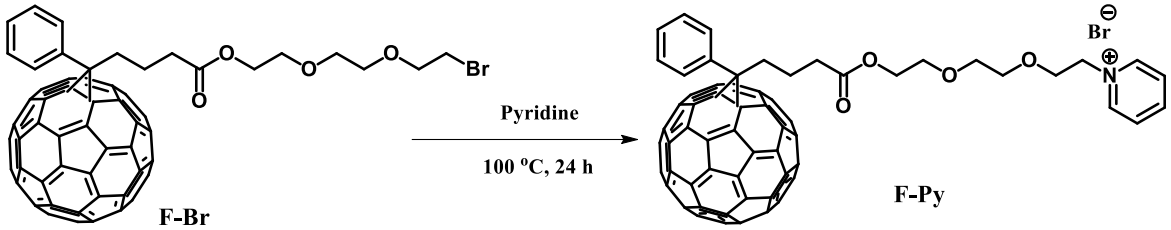

2-(2-(2-bromoethoxy)ethoxy)ethyl [6,6]-phenyl-C_{61}-butyrate (20 mg, 0.018 mmol) was added 2 mL of pyridine and the resultant solution was refluxed at 100 ^{o}C for 24 h. The solvent was evaporated and the residue was washed with methanol to afford the product **F-Py** as black colour solid (10 mg, 49% yield).

^{1}H NMR (500 MHz, DMSO-d_6), δ (ppm): 9.03 (d, J = 5.5 Hz, 2H), 8.18 (t, J = 7 Hz, 2H), 8.06 (d, J = 7.5 Hz, 2H), 7.60 (t, J = 7.5 Hz, 2H), 7.49 (s, 1H), 4.8 (t, J = 4.5 Hz, 2H), 4.08 (t, J = 4.5 Hz, 2H), 3.91 (t, J = 4.75 Hz, 2H), 3.47 (t, J = 4.25 Hz, 4H), 2.93 (t, J = 8 Hz, 2H), 2.56 (t, J = 7 Hz, 2H), 2.07 (m, J = 7.66 Hz, 2H).

^{13}C NMR (125 MHz, $CDCl_3$), δ (ppm): 173.09, 146.06, 145.21, 145.12, 145.07, 144.71, 144.57, 144.52, 144.42, 144.22, 143.37, 143.13, 143.05, 142.98, 142.95, 142.91, 142.69, 142.15, 142.10, 141.98, 141.76, 139.02, 138.47, 136.71, 133.10, 128.34, 125.27, 122.55, 100.81, 79.46, 71.31, 70.20, 69.18, 68.10, 64.29, 50.15, 32.66, 22.19.

MALDI (m/z): M^+ calcd. for $C_{82}H_{28}NO_4^+$, 1090.20; found, 1090.20 (M).

4A.5.4.4. Synthesis of tert-butyl(2-hydroxyphenyl)carbamate[46]

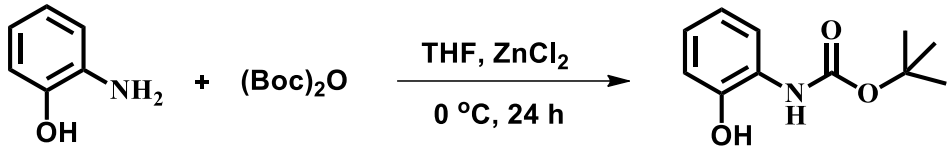

Di-tert-butyl dicarbonate (19.79 g, 0.0916 mol) and zinc chloride (12.48 g, 0.0916 mol) were added to a solution of 2-aminophenol (10 g, 0.0916 mol) in THF (200 mL), and the reaction mixture was stirred for 24 h. The solvent was removed under reduced pressure and the reaction mixture was extracted with ethyl acetate (100 mL). The organic layer was washed (2 x 50 mL) with water. It was then separated, dried over Na_2SO_4 and evaporated under reduced pressure. The residue obtained was purified by column chromatography on silica gel by using 5% EtOAc-hexane as eluent to give the pure product as white crystals in 26 % yield. (R_f : 0.5, 30% EtOAc-hexane).

^{1}H NMR (500 MHz, $CDCl_3$), δ (ppm): 8.13 (s, 1H), 7.08 (m, 2H), 6.97 (d, J = 8 Hz, 1H), 6.86 (d, J = 6.5 Hz, 1H), 6.65 (s, 1H), 1.53 (s, 9H).

^{13}C NMR (125 MHz, $CDCl_3$), δ (ppm): 155.01, 147.38, 125.62, 125.54, 121.34, 120.76, 82.06, 28.26.

HRMS (m/z): $[M]^+$ calcd. for $C_{11}H_{15}NO_3$, 209.11; found, 232.09 (M+Na).

4A.5.4.5. Synthesis of tert-butyl-(2-(2-(2-(2-hydroxyethoxy)ethoxy)ethoxy)-phenyl)carbamate

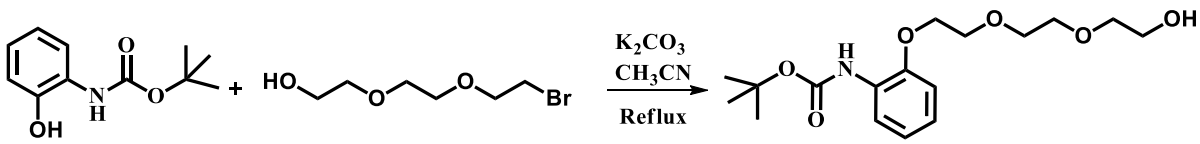

To a solution of tert-butyl (2-hydroxyphenyl) carbamate (500 mg, 2.39 mmol) and potassium carbonate (660 mg, 4.78 mmol) in acetonitrile (15 mL) was added 2-(2-(2-bromoethoxy)ethoxy)ethanol, 1 (509 mg, 2.39 mmol). The reaction mixture was stirred and refluxed for 24 h. The solvent was evaporated and reaction mixture was extracted with ethyl acetate (2 x 50 mL) and water (10 mL). Organic layer was separated and dried. The crude product was purified through column chromatography using 30% ethylacetate-hexane mixture (R_f : 0.2). The product was obtained as pale yellow viscous liquid in 36 % yield (300 mg).

^{1}H NMR (500 MHz, $CDCl_3$), δ (ppm): 0.97 (s, 1H), 7.51 (d, J = 8 Hz, 1H), 6.94 (m, 2H), 6.86 (d, J = 7.5 Hz, 1H), 4.17 (t, J = 4.5 Hz, 2H), 3.86 (t, J = 4.5 Hz, 2H), 3.72 (m, 6H), 3.63 (t, J = 5 Hz, 2H), 1.53 (s, 9H).

^{13}C NMR (125 MHz, $CDCl_3$), δ (ppm):153.06, 146.84, 128.95, 123.68, 122.39, 121.78, 112.39, 72.61, 70.71, 70.35, 68.47, 61.80, 28.40.

HRMS (m/z): M^+ calcd. for $C_{17}H_{27}NO_6$, 341.18; found, 364.17 (M+Na).

4A.5.4.6. Synthesis of 2-(2-(2-(2-((tert-butoxycarbonyl)amino)phenoxy)ethoxy) ethoxy)ethyl-[6,6]-phenyl-C_{61}-butyrate, F-An-Boc

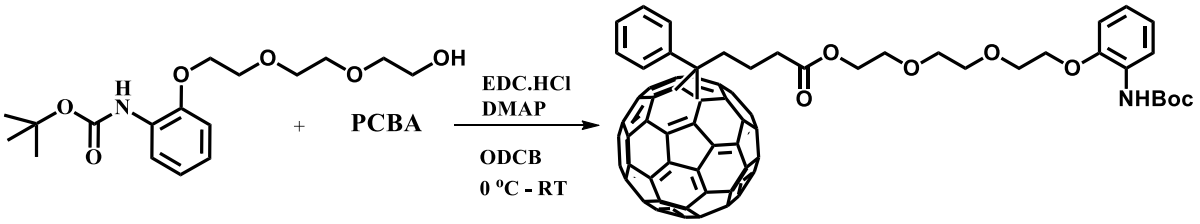

To a solution of **PCBA** (50 mg, 0.056 mmol) in 1,2-dichlorobenzene (6 mL) was added 4-dimethylaminopyridine (6.8 mg, 0.056 mmol), EDC.HCl (16 mg, 0.083 mmol) and stirred for 10 min at 0 °C. Compound **3** (19 mg, 0.056 mmol) was added directly to the reaction mixture and stirred overnight at room temperature. The crude mixture was purified by column chromatography using chloroform (R_f : 0.4) which afforded **F-An-Boc** as a brown colour powder in 71% yield (45 mg).

^{1}H NMR (500 MHz, $CDCl_3$), δ (ppm): 8.06 (s, 1H), 7.92 (d, *J* = 7 Hz, 2H), 7.53 (t, *J* = 7.5 Hz, 2H), 7.46 (t, *J* = 7.5 Hz, 1H), 6.95 (m, 2H), 6.88 (d, *J* = 7.5 Hz, 1H), 4.24 (t, *J* = 5 Hz, 2H), 4.17 (t, *J* = 4.5 Hz, 2H), 3.84 (t, *J* = 5 Hz, 2H), 3.7 (m, 6H), 2.89 (t, *J* = 8 Hz, 2H), 2.53 (t, *J* = 7.5 Hz, 2H), 2.19 (m, 2H), 1.55 (s, 9H).

^{13}C NMR (125 MHz, $CDCl_3$), δ (ppm): 173.05, 148.80, 147.80, 145.85, 145.20, 145.16, 145.05, 144.80, 144.67, 144.52, 144.43, 144.02, 143.77, 143.13, 143.01, 142.95, 142.23, 142.18, 142.14, 140.99, 140.76, 138.04, 137.57, 136.74, 132.11, 128.44, 128.26, 122.32, 121.94, 112.73, 100, 79.87, 70.66, 69.62, 69.20, 68.83, 63.59, 33.93, 28.43, 21.8.

MALDI (m/z): M^+ calcd. for $C_{88}H_{37}NO_7$, 1219.25; found, 1242.25 (M+Na).

4A.5.4.7. Synthesis of 2-(2-(2-(2-aminophenoxy)ethoxy)ethoxy)ethyl-[6,6]-phenyl-C_{61}-butyrate, F-An

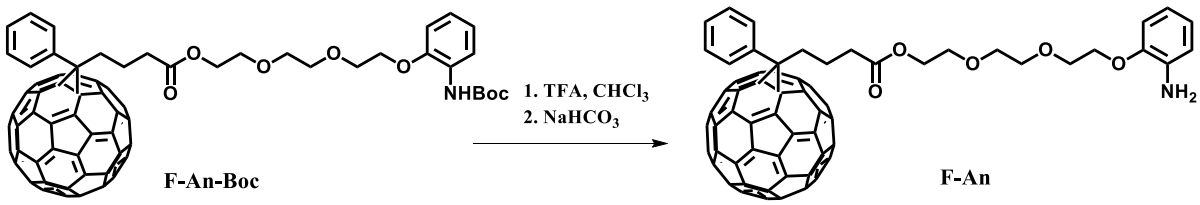

F-An-Boc (45 mg, 0.037 mmol) in chloroform (10 ml) was added trifluoroacetic acid (2 mL) and stirred overnight at room temperature. The solvent was removed under reduced pressure and the reaction mixture was extracted with chloroform (10 mL). The organic layer was washed (2 x 10 mL) with water and neutralised with sodium bicarbonate (1 M). It was then separated, dried over Na_2SO_4 and evaporated under reduced pressure to give the product as brown solid in quantitative yield.

^{1}H NMR (500 MHz, $CDCl_3$), δ (ppm): 7.91 (d, *J* = 7.5 Hz, 2H), 7.53 (t, *J* = 7 Hz, 2H), 7.46 (t, *J* = 7.5 Hz, 1H), 7.16 (d, *J* = 8 Hz, 1H), 7.08 (t, *J* = 8.5 Hz, 1H), 6.95 (m, 2H), 4.27 (t, *J* = 4.5 Hz, 2H), 4.19 (t, *J* = 4.5 Hz, 2H), 3.81 (t, *J* = 4.5 Hz, 2H), 3.66 (m, 6H), 2.88 (t, *J* = 8 Hz, 2H), 2.52 (t, *J* = 8 Hz, 2H), 2.17 (m, 2H).

^{13}C NMR (125 MHz, $CDCl_3$), δ (ppm): 173.05, 145.86, 145.21, 145.16, 145.07, 144.81, 144.67, 144.52, 144.42, 144.02, 143.77, 143.13, 143.05, 143.01, 142.95, 142.91, 142.19, 142.15, 142.10, 140.98, 140.76, 138.02, 137.57, 136.71, 132.10, 128.44, 128.27, 123.17, 122.55, 100, 79.86, 70.31, 70.20, 69.28, 69.10, 63.39, 51.85, 33.86, 22.21.

HRMS (m/z): M^+ calcd. for $C_{83}H_{29}NO_5$, 1119.20; found, 1120.20 (M+H).

4A.5.4.8. Synthesis of 2-(2-(2-(10H-phenothiazin-10-yl)ethoxy)ethoxy)ethanol[47]

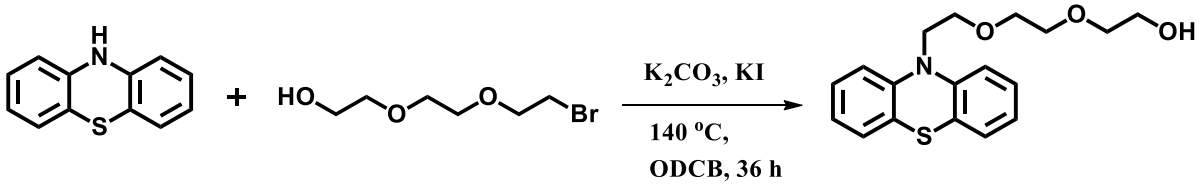

A mixture of Phenothiazine (0.5 g, 2.5 mmol), potassium carbonate (1.03 g, 7.5 mmol), potassium iodide (0.2 g, 6 mmol), and 2-(2-(2-bromoethoxy)ethoxy)ethanol (0.6 g) was refluxed in 1,2-dichlorobenzene for 36 h. On cooling, solvent was removed under reduced pressure and the crude product was purified by column chromatography using 15% ethyl acetate-hexane mixture followed by ethyl acetate as eluting solvent to obtained 0.3 g yellow liquid in 36% yield. R_f = 0.1 (10% ethyl acetate-hexane).

^{1}H NMR (500 MHz, acetone-d_6), δ (ppm): 6.9 (m, 2H), 7.13 (m, 6H), 3.86 (t, J = 5 Hz, 2H), 3.53 (t, J = 4.5 Hz, 2H), 3.34 (t, J = 4.25 Hz, 2H), 3.61 (m, 4H), 3.34 (t, J = 4.5 Hz, 2H).

^{13}C NMR (125 MHz, acetone-d_6), δ (ppm): 159.90, 127.11, 126.09, 121.40, 115.58, 114.63, 79.96, 72.16, 71.09, 60.02, 32.42.

HRMS (m/z): M^+ calcd. for $C_{18}H_{21}NO_3S^+$, 331.12; found, 354.11 (M+Na).

4A.5.4.9. Synthesis of (10H-phenothiazin-10-yl)-propyl-[6,6]-phenyl-C_{61}-butyrate, F-PTz

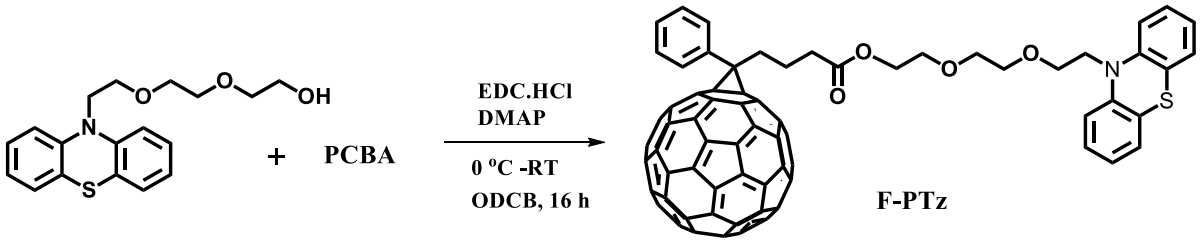

To a solution of **PCBA** (50 mg, 0.055 mmol) in 1,2-dichlorobenzene (10 mL) was added DMAP (6.7 mg, 0.055 mmol), EDC-HCl (31 mg, 0.165 mmol) and stirred for 10 min at 0 ^{o}C. 2-(2-(2-(10H-phenothiazin-10-yl)ethoxy)ethoxy)ethanol (14 mg, 0.055 mmol) was added directly to the reaction mixture and stirred overnight at room temperature. The solvent was rotary evaporated and the crude product was separated by column chromatography using toluene to obtain 40 mg black solid in 63% yield.

^{1}H NMR (500 MHz, $CDCl_3$), δ (ppm): 7.93 (d, J = 8 Hz, 2H), 7.56 (q, J = 7.5 Hz, 2H), 7.53 (m, 1H), 7.24 (m, 4H), 7.18 (m, 4H), 4.23 (t, J = 4.5 Hz, 2H), 3.76 (t, J = 5 Hz, 2H), 3.69 (t, J = 4.25 Hz, 2H), 3.61 (m, 4H), 3.26 (t, J = 4.5 Hz, 2H), 2.93 (t, J = 8 Hz, 2H), 2.53 (m, 2H), 2.2 (t, J = 7.65 Hz, 2H).

^{13}C NMR (125 MHz, acetone-d_6), δ (ppm): 177.23, 161.09, 147.89, 146.78, 145.75, 145.60, 145.16, 144.91, 144.78, 144.59, 144.32, 144.29, 144.17, 144.07, 144.02, 143.21, 142.95, 142.63, 142.18, 142.02, 141.59, 141.01, 139.34, 138.35, 135.34, 133.78, 128.14, 127.06, 127.21, 126.19, 121.82, 121.80, 115.78, 114.73, 77.67, 71.06, 68.43, 67.20, 66.53, 62.42, 34.81, 26.64, 24.03.

HRMS (m/z): M^+ calcd. for $C_{83}H_{29}NO_5S$, 1209.19; found, 1210.29 (M+H).

4A.6. REFERENCES

1) Estevez-Torres, A.; Baigl, D., DNA compaction: fundamentals and applications. *Soft Matter* **2011**, *7*, 6746-6756.
2) Carrivain, P.; Cournac, A.; Lavelle, C.; Lesne, A.; Mozziconacci, J.; Paillusson, F.; Signon, L.; Victor, J.-M.; Barbi, M., Electrostatics of DNA compaction in viruses, bacteria and eukaryotes: functional insights and evolutionary perspective. *Soft Matter* **2012**, *8*, 9285-9301.

3) Zhou, T.; Llizo, A.; Wang, C.; Xu, G.; Yang, Y., Nanostructure-induced DNA condensation. *Nanoscale* **2013**, *5*, 8288-8306.

4) Barbara, D.; Zahra, H.; Jean-Paul, B., Towards Multifunctional Synthetic Vectors. *Curr. Gene Ther.* **2004**, *4*, 445-455.

5) Dias, A. G.-P. a. R. S., Different strategies for controlling DNA conformation: compaction and decompaction. *Front. Biosci.* **2009**, *1*, 228–241.

6) Bloomfield, V. A., DNA condensation. *Curr. Opin. Struct. Biol.* **1996**, *6*, 334-341.

7) Midoux, P.; Pichon, C.; Yaouanc, J.-J.; Jaffrès, P.-A., Chemical vectors for gene delivery: a current review on polymers, peptides and lipids containing histidine or imidazole as nucleic acids carriers. *Br. J. Pharmacol.* **2009**, *157*, 166-178.

8) Liu, K.; Zheng, L.; Ma, C.; Gostl, R.; Herrmann, A., DNA-surfactant complexes: self-assembly properties and applications. *Chem. Soc. Rev.* **2017**, *46*, 5147-5172.

9) Hariharan, M.; Kuruvilla, E.; Ramaiah, D., Direct Evidence on the External Stimuli Induced Dissembly of DNA through Microscopic Techniques. *J. Phys. Chem. Lett.* **2010**, *1*, 834-838.

10) Bloomfield, V. A., DNA condensation by multivalent cations. *Biopolymers* **1997**, *44*, 269-282.

11) Cassell, A. M.; Scrivens, W. A.; Tour, J. M., Assembly of DNA/Fullerene Hybrid Materials. *Angew. Chem. Int. Ed. Engl.* **1998**, *37*, 1528-1531.

12) Patel, M. B.; Harikrishnan, U.; Valand, N. N.; Mehta, D. S.; Joshi, K. V.; Kumar, S. P.; Chikhalia, K. H.; George, L. B.; Jasrai, Y. T.; Menon, S. K., Novel cationic fullerene derivatized s-triazine scaffolds as photoinduced DNA cleavage agents: design, synthesis, biological evaluation and computational investigation. *Rsc Adv* **2013**, *3*, 8734-8746.

13) Nitta, H.; Minami, K.; Harano, K.; Nakamura, E., DNA Binding of Pentaamino[60]fullerene Synthesized Using Click Chemistry. *Chem. Lett.* **2014**, *44*, 378-380.

14) Minami, K.; Okamoto, K.; Doi, K.; Harano, K.; Noiri, E.; Nakamura, E., siRNA delivery targeting to the lung via agglutination-induced accumulation and clearance of cationic tetraamino fullerene. *Sci. Rep.* **2014**, *4*, 4916.

15) Klumpp, C.; Lacerda, L.; Chaloin, O.; Ros, T. D.; Kostarelos, K.; Prato, M.; Bianco, A., Multifunctionalised cationic fullerene adducts for gene transfer: design, synthesis and DNA complexation. *Chem. Commun.* **2007**, 3762-3764.

16) Isobe, H.; Sugiyama, S.; Fukui, K.-i.; Iwasawa, Y.; Nakamura, E., Atomic Force Microscope Studies on Condensation of Plasmid DNA with Functionalized Fullerenes. *Angew. Chem. Int. Ed. Engl.* **2001**, *40*, 3364-3367.

17) Nakamura, E.; Isobe, H., In vitro and in vivo gene delivery with tailor-designed aminofullerenes. *Chem. Rec.* **2010**, *10*, 260-270.

18) Malinovskii, V. L.; Wenger, D.; Häner, R., Nucleic acid-guided assembly of aromatic chromophores. *Chem. Soc. Rev.* **2010**, *39*, 410-422.

19) Aldaye, F. A.; Palmer, A. L.; Sleiman, H. F., Assembling Materials with DNA as the Guide. *Science* **2008**, *321*, 1795-1799.

20) Benvin, A. L.; Creeger, Y.; Fisher, G. W.; Ballou, B.; Waggoner, A. S.; Armitage, B. A., Fluorescent DNA Nanotags: Supramolecular Fluorescent Labels Based on Intercalating Dye Arrays Assembled on Nanostructured DNA Templates. *J. Am. Chem. Soc.* **2007**, *129*, 2025-2034.

21) Hud, N. V.; Downing, K. H., Cryoelectron microscopy of λ phage DNA condensates in vitreous ice: the fine structure of DNA toroids. *Proc. Natl. Acad. Sci. USA* **2001**, *98*, 14925-14930.

22) Shen, M. R.; Downing, K. H.; Balhorn, R.; Hud, N. V., Nucleation of DNA Condensation by Static Loops: Formation of DNA Toroids with Reduced Dimensions. *J. Am. Chem. Soc.* **2000**, *122*, 4833-4834.

23) Osada, K.; Oshima, H.; Kobayashi, D.; Doi, M.; Enoki, M.; Yamasaki, Y.; Kataoka, K., Quantized Folding of Plasmid DNA Condensed with Block Catiomer into Characteristic Rod Structures Promoting Transgene Efficacy. *J. Am. Chem. Soc.* **2010**, *132*, 12343-12348.

24) Fan, Y.; Wang, H.; He, C.; Qiao, F.; Wang, S.; Wang, Y., DNA Condensation Induced by a Star-Shaped Hexameric Cationic Surfactant. *ACS Appl. Mater. Interfaces* **2017**, *9*, 23333-23341.

25) Donskyi, I.; Achazi, K.; Wycisk, V.; Bottcher, C.; Adeli, M., Synthesis, self-assembly, and photocrosslinking of fullerene-polyglycerol amphiphiles as nanocarriers with controlled transport properties. *Chem. Commun.* **2016**, *52*, 4373-4376.

26) Homma, T.; Harano, K.; Isobe, H.; Nakamura, E., Nanometer-Sized Fluorous Fullerene Vesicles in Water and on Solid Surfaces. *Angew. Chem. Int. Ed. Engl.* **2010**, *49*, 1665-1668.

27) Homma, T.; Harano, K.; Isobe, H.; Nakamura, E., Preparation and Properties of Vesicles Made of Nonpolar/Polar/Nonpolar Fullerene Amphiphiles. *J. Am. Chem. Soc.* **2011**, *133*, 6364-6370.

28) Richmond, T. J.; Davey, C. A., The structure of DNA in the nucleosome core. *Nature* **2003**, *423*, 145-150.

29) Bednar, J.; Horowitz, R. A.; Grigoryev, S. A.; Carruthers, L. M.; Hansen, J. C.; Koster, A. J.; Woodcock, C. L., Nucleosomes, linker DNA, and linker histone form a unique structural motif that directs the higher-order folding and compaction of chromatin. *Proc. Natl. Acad. Sci. USA* **1998**, *95*, 14173-14178.

30) Vittala, S. K.; Saraswathi, S. K.; Joseph, J., Fullerene cluster assisted self-assembly of short DNA strands into semiconducting nanowires. *Chem. Eur. J.*, *23*, 15759-15765.

31) Vittala, S. K.; Joseph, J., Chiral self-assembly of fullerene clusters on CT-DNA templates. *Faraday Discuss.* **2018**, *207*, 459 - 469.

32) Hummelen, J. C.; Knight, B. W.; LePeq, F.; Wudl, F.; Yao, J.; Wilkins, C. L., Preparation and Characterization of Fulleroid and Methanofullerene Derivatives. *J. Org. Chem.* **1995**, *60*, 532-538.

33) Nagarajan, R.; Liu, W.; Kumar, J.; Tripathy, S. K.; Bruno, F. F.; Samuelson, L. A., Manipulating DNA Conformation Using Intertwined Conducting Polymer Chains. *Macromolecules* **2001**, *34*, 3921-3927.

34) Shankar, B. H.; Jayaram, D. T.; Ramaiah , D., Naphthalene Imide Conjugates: Formation of Supramolecular Assemblies, and the Encapsulation and Release of Dyes through DNA-Mediated Disassembly. *Chem. Eur. J.* **2015**, *21*, 17657-17663.

35) Takada, T.; Kawai, K.; Fujitsuka, M.; Majima, T., Rapid Long-Distance Hole Transfer through Consecutive Adenine Sequence. *J. Am. Chem. Soc.* **2006**, *128*, 11012-11013.

36) Boger, D. L.; Fink, B. E.; Brunette, S. R.; Tse, W. C.; Hedrick, M. P., A Simple, High-Resolution Method for Establishing DNA Binding Affinity and Sequence Selectivity. *J. Am. Chem. Soc.* **2001**, *123*, 5878-5891.

37) Garbett, N. C.; Hammond, N. B.; Graves, D. E., Influence of the Amino Substituents in the Interaction of Ethidium Bromide with DNA. *Biophys. J.* **2004**, *87*, 3974-3981.

38) Yang, H.; Tang, P.; Tang, B.; Huang, Y.; Xiong, X.; Li, H., Novel poly(ADP-ribose) polymerase inhibitor veliparib: biophysical studies on its binding to calf thymus DNA. *Rsc. Adv.* **2017**, *7*, 10242-10251.

39) Mahesh, H.; Elizabeth, K.; Danaboyina, R., Direct Evidence on the External Stimuli Induced Dissembly of DNA through Microscopic Techniques. *The Journal of Physical Chemistry Letters* **2010**, *1*.

40) Oliveira Brett, A. M.; Chiorcea, A.-M., Atomic Force Microscopy of DNA Immobilized onto a Highly Oriented Pyrolytic Graphite Electrode Surface. *Langmuir* **2003**, *19*, 3830-3839.

41) Terawaki, A.; Otsuka, Y.; Lee, H.; Matsumoto, T.; Tanaka, H.; Kawai, T., Conductance measurement of a DNA network in nanoscale by point contact current imaging atomic force microscopy. *Appl. Phys. Lett.* **2005**, *86*, 113901.

42) Baguley, B. C.; Falkenhaug, E. M., The interaction of ethidium with synthetic double-stranded polynucleotides at low ionic strength. *Nucleic Acids Res.* **1978**, *5*, 161-171.

43) Joseph, J.; Kuruvilla, E.; Achuthan, A. T.; Ramaiah, D.; Schuster, G. B., Tuning of intercalation and electron-transfer processes between DNA and acridinium derivatives through steric effects. *Bioconjugate Chem.* **2004**, *15*, 1230-1235.

44) Kuruvilla, E.; Joseph, J.; Ramaiah, D., Novel Bifunctional Acridine–Acridinium Conjugates: Synthesis and Study of Their Chromophore-Selective Electron-Transfer and DNA-Binding Properties. *J. Phys. Chem. B* **2005**, *109*, 21997-22002.

45) Chong, J. M.; Heuft, M. A.; Rabbat, P., Solvent Effects on the Monobromination of α,ω-Diols: A Convenient Preparation of ω-Bromoalkanols. *J. Org. Chem.* **2000**, *65*, 5837-5838.

46) Chacun-Lefevre, L.; Buon, C.; Bouyssou, P.; Coudert, G., Synthesis of 3-substituted-4H-1,4-benzoxazines. *Tetrahedron Lett.* **1998**, *39*, 5763-5764.

47) Thomas, K. G.; Biju, V.; Kamat, P. V.; George, M. V.; Guldi, D. M., Dynamics of Photoinduced Electron-Transfer Processes in Fullerene-Based Dyads: Effects of Varying the Donor Strength. *ChemPhysChem* **2003**, *4*, 1299-1307.

MUTUALLY ASSISTED SELF-ASSEMBLY OF FULLERENE NANOCLUSTERS AND SHORT DNA STRANDS INTO NANOWIRES, NANOSHEETS AND NANONETWORKS

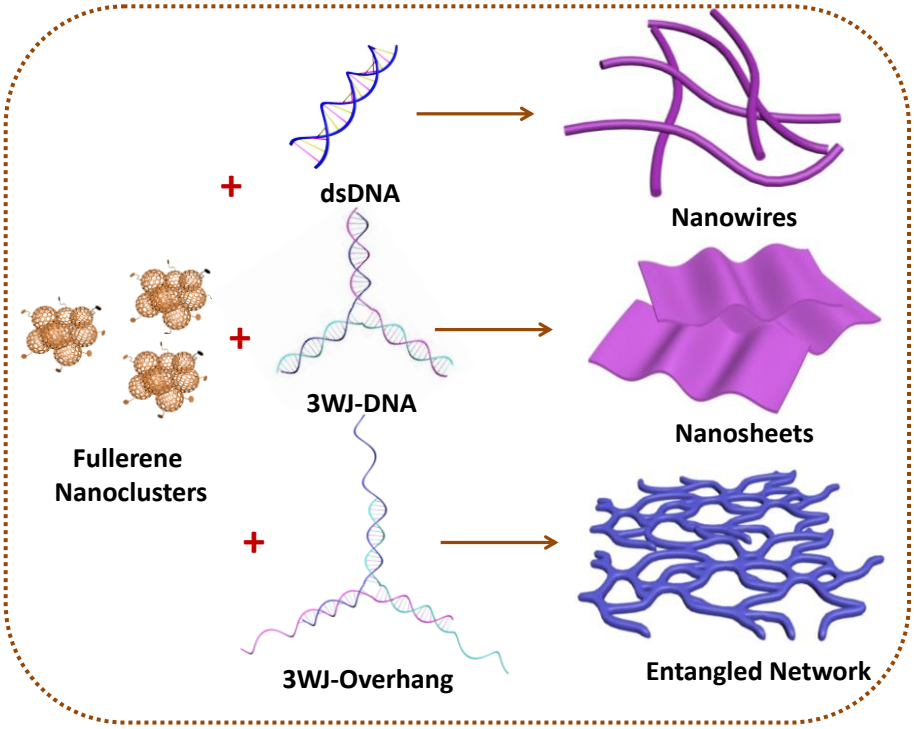

4B.1. ABSTRACT

Programmable, hierarchical assembly of DNA nanostructures with the precise organization of functional components have been demonstrated previously with tiled assembly and DNA Origami. However, building organized nanostructures with random oligonucleotide strands remains as an elusive problem. Herein, we describe a simple and general strategy in which nanoclusters of a fullerene derivative act as stapler motifs in bringing ordered nanoscale assembly of short oligonucleotide duplexes (dsDNA), three-way junction DNA (3WJ-DNA) and 3WJ-Overhang (3WJ-OH) into micrometer-sized

nanowires, nanosheets and nanonetwork respectively. In this approach, the fullerene derivative by virtue of its amphiphilic structure and unique hydrophobic-hydrophilic balance pre-assemble to form 3-5 nm sized clusters in DMSO - phosphate buffer mixture, which further assist the assembly of DNA strands. We demonstrate that the optimum cluster size, availability of DNA anchoring motifs and the nature of the DNA strands control the structure of these nanomaterials. Further, the horizontal conductivity measurements using c-AFM confirmed the charge transport properties of these nanowires. Further, the programmability and templated decoration with fluorescent silver nanocluster (AgNCs) was exploited using (3WJ-OH) which formed nanonetwork structure due to the differential interaction of fullerene nanocluster with single and duplex strands of 3WJ-OH. The nanonetwork structures obtained from 3WJ-OH/fullerene clusters self-assembly showed 40% enhancement in fluorescence of AgNCs compared to bare 3WJ-OH. The current strategy could be employed to organize random DNA duplexes and tiles into functional nanostructures and hence open up new avenues in DNA nanotechnology.

4B.2. INTRODUCTION

DNA nanotechnology got expanded over the last two decades incorporating strategies to harness the sequence programmability of DNA in building hierarchical nanostructures[1-4] and subsequently using it for organizing functional motifs in an ordered fashion.[5-9] While initial efforts were relying on the complementarity of simple oligonucleotide strands in making nanostructures with topologically defined architectures, their conformational flexibility diminished further applications.[10-15] Two seminal concepts brought a paradigm shift in DNA nanotechnology by introducing rigid

nanoscale building blocks and advancing it to the design of programmable 2D and 3D nanostructures: (i) the use of rigid nanoparticle cores for building long-range ordered, DNA based lattices[16-19] and (ii) the introduction of hybridization based intricately woven multiple cross-over tiles as used in DNA tiles & DNA origami.[20,21]

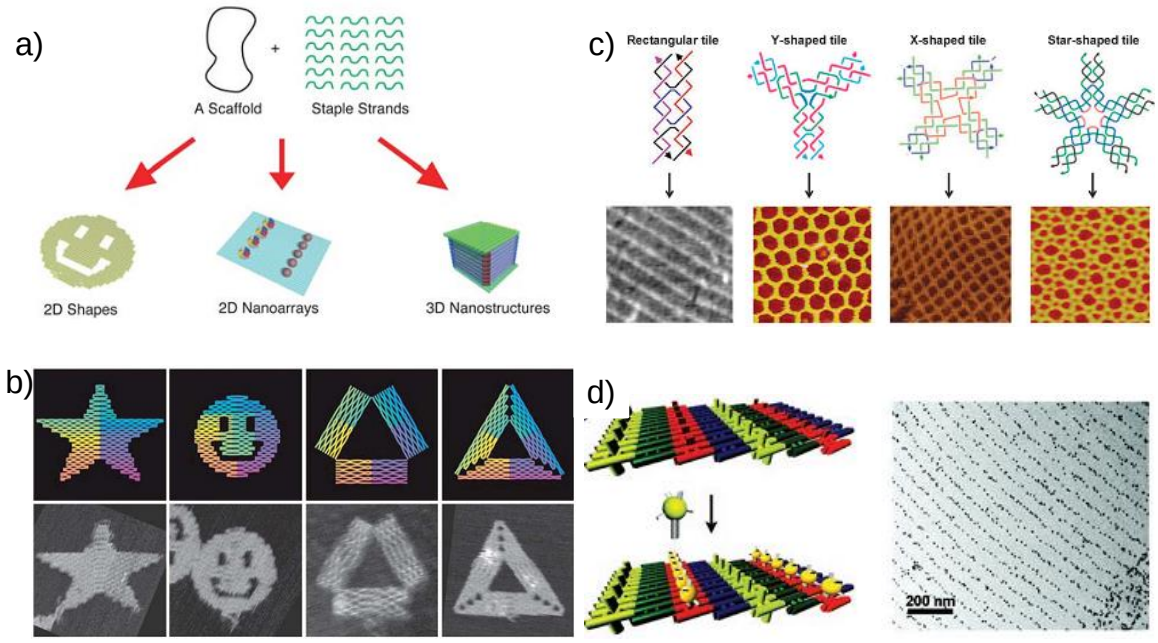

Figure 4B.1. Schematic representation of a) DNA scaffold and staple stands used in the construction of DNA origami based 2D and 3D nanostructures (Adapted from reference 22); b) 2D nanostructures prepared from DNA origami (Adapted from reference 24); c) DNA tiles rectangular, Y-shaped, X-shaped, and star-shaped 2D structures with corresponding AFM images (Adapted from reference 25); d) DNA tile templated organization of 5 nm gold nanoparticle with corresponding TEM image (Adapted from reference 26).

DNA origami, a hybridization based DNA folding technique use a large (>1000 bp), circular single-stranded DNA in constructing predefined nano-architectures with the help of short 'staple' strands (Figure 4B.1a).[22] These approaches also have the flexibility of incorporating addressable, sticky-end sequences at precise locations in the nanoscale architectures, making it useful in organizing functional materials.[23] DNA

origami was used in the construction of several predefined nanostructures such as star, smiley, triangle as shown in the Figure 4B.1b.[24] Similarly, DNA tiles have also been used in the construction of variety of 2D nanostructures using various rectangular, Y-shaped, X-shaped, and star-shaped DNA tiles (Figure 4B.1c).[25] In a representative example Nadrian C. Seeman and coworkers demonstrated the templated organization of 5 nm sized thiol modified gold nanoparticle arrays on the DNA tile (Figure 4B.1d).[26]

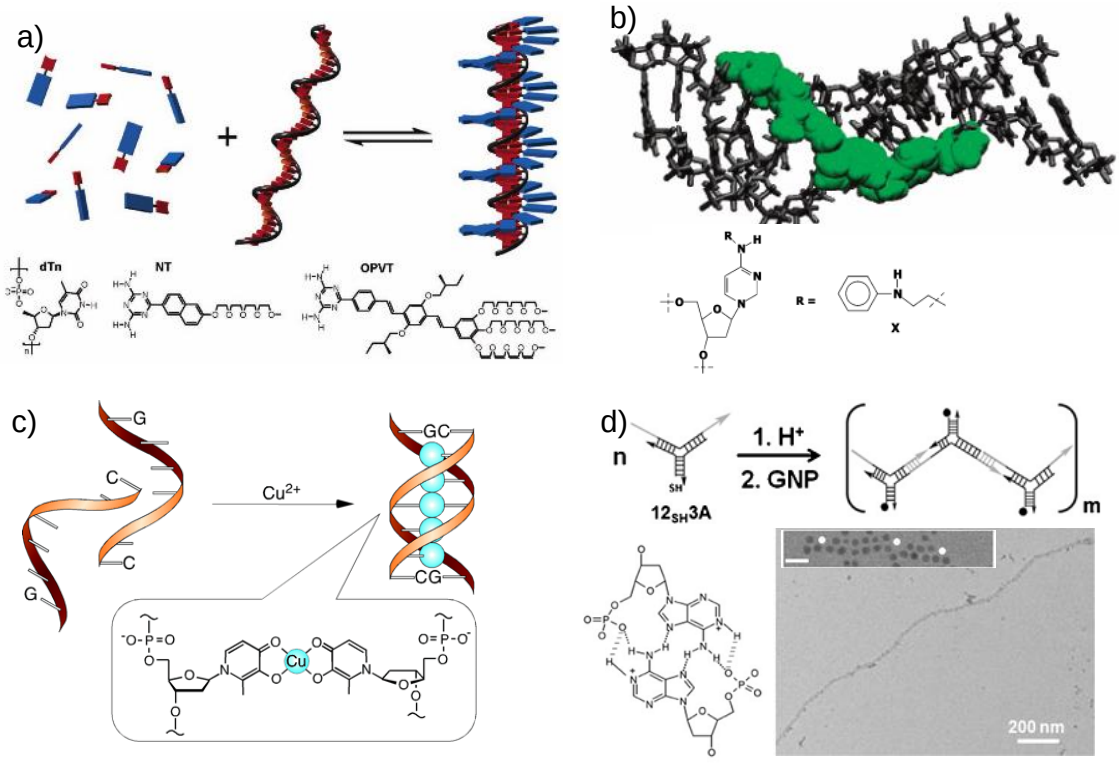

Figure 4B.2. Pictorial representation of a) ssdna templated self-assembly of organic chromphores (Adapted from reference 37); b) DNA based synthesis of conjoined polyaniline nanowire with consecutively six aniline modified nucleobases (Adapted from reference 38); c) Cu^{2+}-mediated duplex formation between two modified DNA strands in which nucleobases were replaced by hydroxypyridone moiety (Adapted from reference 39); d) DNA templated assembly of gold nanoparticle using thiol modified three way junction ($12_{SH}3A$) with corresponding TEM image (Adapted from reference 40).

Nanoparticle templated DNA building blocks and DNA tiles are focused on the development of small number of building blocks which self-assemble into large periodic structures.[27] However, a closer review reveals that these strategies are inadequate in building nanostructures with random, unmodified oligonucleotides, partly because of compromise with the programmability of the self-assembly and the precise control offered by these techniques on the size and shape of subsequent nanostructures. Previously, DNA has been successfully utilized as a template for organizing various small molecules,[28] metal ions,[29,30] clusters,[31,32] nanoparticles[23,26,33] and polymers[34-36] for the construction of supramolecular architectures of various size and shape with remarkable control. Some representative examples were depicted in Figure 4B.2. Mejier and coworkers showed ssdna (dT_{40}) templated self-assembly of naphthalene chromophore (NT) using complementary hydrogen bonding upto 40 units (Figure 4B.2a).[37] Moreover, this strategy has been extended to oligophenylenevinylene conjugated thymine (OPVT) system also. Gary Schuster et al. showed the controlled synthesis of conjoined polymer in a unique way by using aniline modified oligonucleotides using HRP/H_2O_2 as catalyst (Figure 4B.2b).[38] In another example, two modified DNA strands with nucleobases replaced by hydroxypyridone moiety were used for templated assembly of Cu^{2+} metal ions upon duplex formation (Figure 4B.2c).[39] Further, Yamuna krishnan and coworkers showed the templated assembly of gold nanoparticle using thiol modified three way junction DNA ($12_{SH}3A$)[40] by utilizing pH induced polymerisation of three way junction through overhang A-motif formation. The

templated assembly was further confirmed by means of TEM analysis using the thiol modified DNA at one end to specifically bind to gold nanoparticles (Figure 4B.2d).

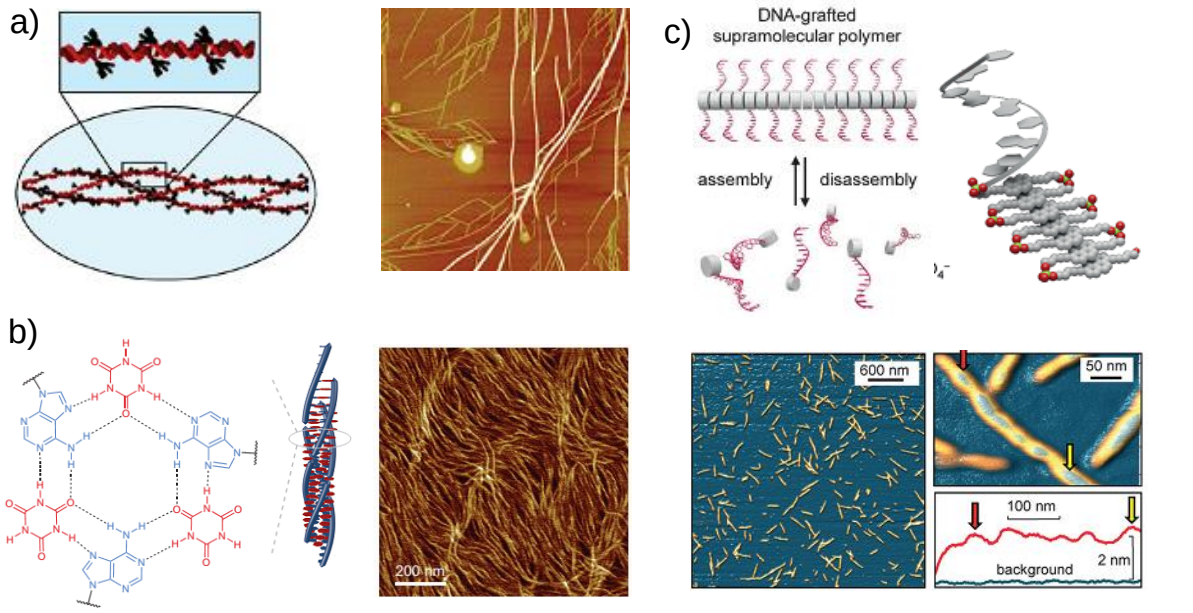

Figure 4B.3. a) Long range ordered assembly of oligoethyleneglycol dendron appended short DNA duplex into nanofibre (Adapted from reference 41). b) Cyanuric acid induced hexameric rosette type assembly of Poly(adenine) DNA into bundled nanofibres (Adapted from reference 44). c) Assembly and disassembly of DNA-grafted supramolecular polymer using DNA-hybrid sequences containing phosphodiester-linked pyrene units (Adapted from reference 43).

On the other hand, DNA assisted or templated self-assembly by small molecules,[41] nanoparticles,[42] oligomers[43] etc or mutually assisted self-assembly into nanostructures are rarely reported. Sleiman and co-workers reported formation of long range bundled nanofibres using oligoethyleneglycol dendron appended short DNA duplex in 75% acetonitrile-water mixture (Figure 4B.3a).[41] Recently, same group described a small molecule assisted assembly of unmodified DNA into nanofibres, where hydrogen bonding interactions with adenines and cyanuric acid play a crucial role in realizing hexameric rossette structure-assisted cooperative polymerization

(Figure 4B.3b).[44] In the same line, Robert Häner and coworkers described the construction of DNA-grafted supramolecular polymer using covalently modified phosphodiester-linked pyrene units (Figure 4B.3c).[43] Thermally assisted assembly and disassembly of these supramolecular polymers was studied using AFM analysis. Also, chiral templated assembly of pyrene units was confirmed by AFM height analysis.

The DNA based conducting one-dimensional nanowires are anticipated to be pertinent materials for smart connections between metal electrodes in nanodevices.[45,46] Erez Braun *et al.* demonstrated a general method for the construction of one dimensional conducting nanowire between the gold electrodes by using the DNA guided silver metallization where DNA serves as template for the growth of electrostatically bound metal ions (Figure 4B.4a).[47] Templated assembly was confirmed by AFM analysis (Figure 4B.4b) and the I-V measurement represents the conductivity of these silver metal nanowires (Figure 4B.4c). Previously reported DNA based conducting metal nanowires, conjoined conducting polymers, metal nanoparticle arrays etc. also show the exclusive assembly potential of DNA.[48] Danny Porath and co-workers showed horizontal charge transport through single G-quadruplex DNA molecules over the distances more than 100 nm by cleverly coating the gold electrode on one side of DNA nanofibres as shown in Figure 4d.[49] The height of these nanofibres was 20 nm while the electrode thickness was 35 nm (Figure 4B.4e). *I-V* profile obtained from c-AFM measurement at different positions across the nanofibre confirms the distance dependent conductivity of DNA nanofibres. The control experiment such as

conductivity above mica and above gold electrode showed zero and maximum conductivity, respectively (Figure 4B.4f).

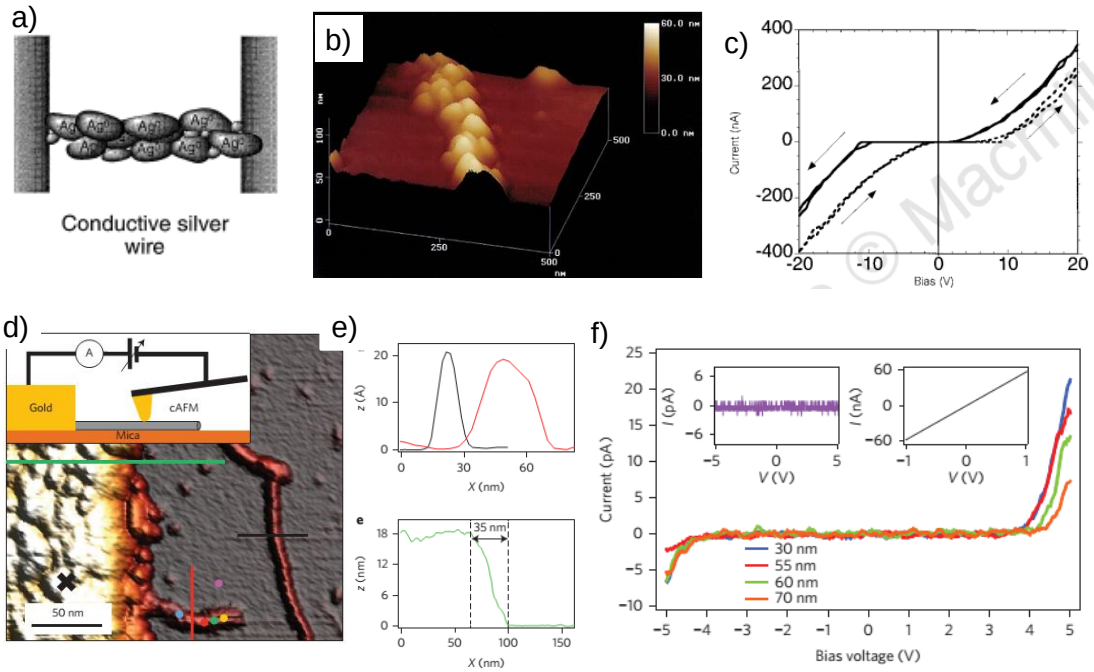

Figure 4B.4. Schematic representation of a) DNA templated silver nanowire construction between the gold electrode with corresponding b) AFM image and c) I-V profile (Adapted from reference 47); d) Horizontal conductivity measurement of G4-DNA protruding from gold electrode with corresponding AFM image; e) Height profile of nanofibre and electrode; f) I-V profile at various distances, inset: Conductivity measured above mica and electrode (Adapted from reference 49).

Herein, we show that the initial nanoclusters formed by the amphiphilic fullerene derivative (**F-An**, Figure 4B.9a) in 10% DMSO-phosphate buffer, act like stapler motifs in bringing small duplexes together, leading to micrometer long nanofibres.[50] The detailed synthesis of fullerene derivative, **F-An** and its nanocluster characterization in 10% DMSO-PBS was reported in the chapter 4, part A. The charge transport properties of these nanofibres were confirmed by using c-AFM analysis.

Further, the tunability of these nanostructures were demonstrated by replacing the duplex by a three way junction DNA (3WJ-DNA) which extend these assemblies into two dimension leading to few layer nanosheets. Finally, the three way junction DNA with an overhang (3WJ-Overhang) was shown to form nanonetwork structures. To our knowledge, this represents the first example where a non-covalently assembled template assists short oligonucleotide duplexes to form nanostructures with long-range order.

4B.3. RESULTS AND DISCUSSION

4B.3.1. F-AN NANOCLUSTER-dsDNA INTERACTIONS

Interactions between **F-An** nanoclusters (Figure 4B.5a and 5b) and dsDNA (Figure 4B.5c) were investigated initially through UV-Visible absorption spectroscopy

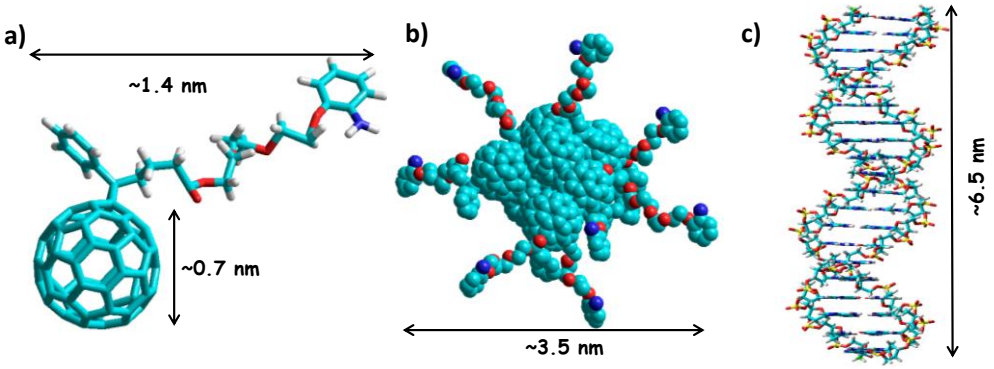

Figure 4B.5. (a) The size of the molecule **F-An** was calculated using Hyperchem model structure (drawn using tubes) gave the backbone length of ~1.4 nm and core diameter of fullerene ~0.7 nm. (b) Model drawn for the smallest nanocluster formed by self-assembly of eight **F-An** molecules (using overlapping spheres, hydrogen atoms were omitted for clarity) gave the maximum distance of ~3.5 nm. (c) The length of dsDNA (drawn using tubes) was calculated to be ~6.5 nm. Colour codes: cyan for carbon, white for hydrogen, red for oxygen, blue for nitrogen and yellow for phosphorous atom.

and Circular Dichroism spectroscopy. Small aliquots (3 μL) of dsDNA were titrated against 3 μM solution of **F-An** in 10% DMSO-PBS. Upon successive addition of dsDNA to **F-An**, DNA absorption at 260 nm increased as expected, with a concomitant decrease in the absorption at 336 nm (Figure 4B.6a). The maximum hypochromicity observed at 336 nm was approximately 27% with an isosbestic point at 300 nm (inset Figure 4B.6a). The observed perturbation in the fullerene absorption is indicative of the

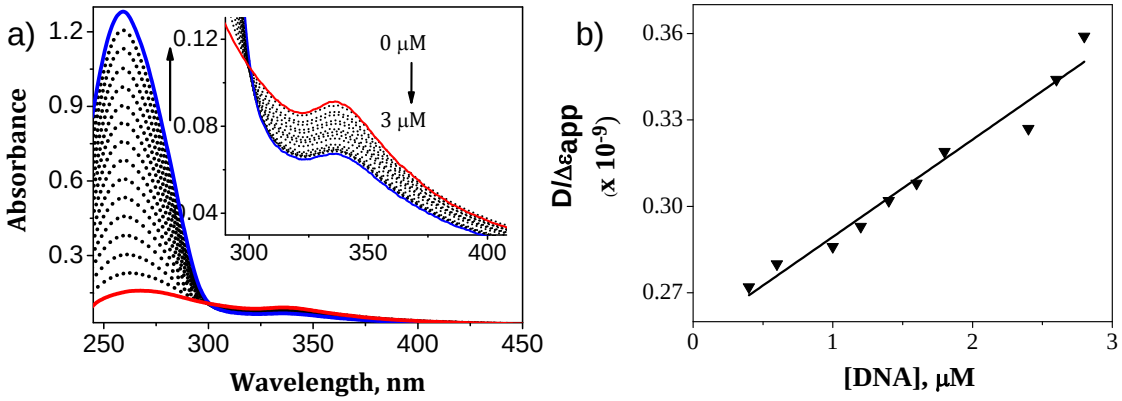

Figure 4B.6. (a) Changes in the absorption spectra of **F-An** (3 μM) in the presence of dsDNA (inset: zoomed portion from 290-400 nm). (b) Saturation plot obtained by monitoring the absorption at 336 nm.

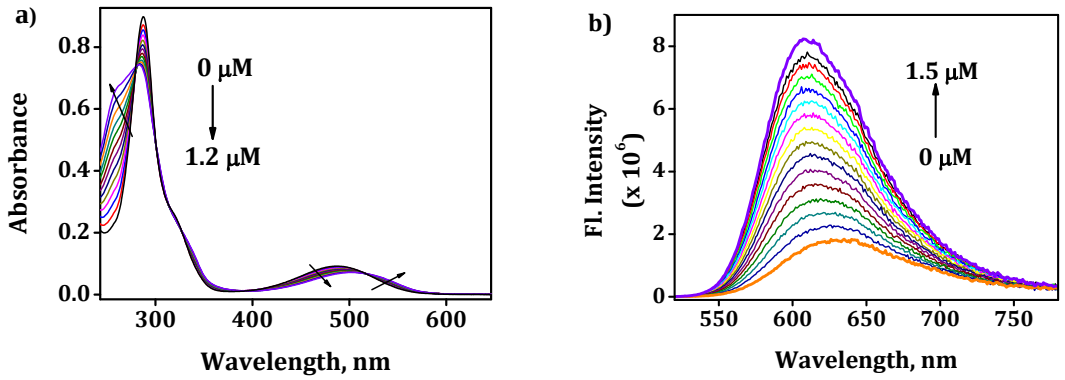

Figure 4B.7. Changes in the (a) absorption spectra and (b) corresponding fluorescence emission spectrum of EB (30 μM) in the presence of increasing [dsDNA]. λ_{ex}, 515 nm.

interaction between fullerene nanoclusters and dsDNA through non-covalent interactions such as groove binding and/or partial intercalation.[31,32] The binding constant was measured using half-reciprocal plots and found to be 1.32 x 10^5 M^{-1} (Figure 4B.6b).

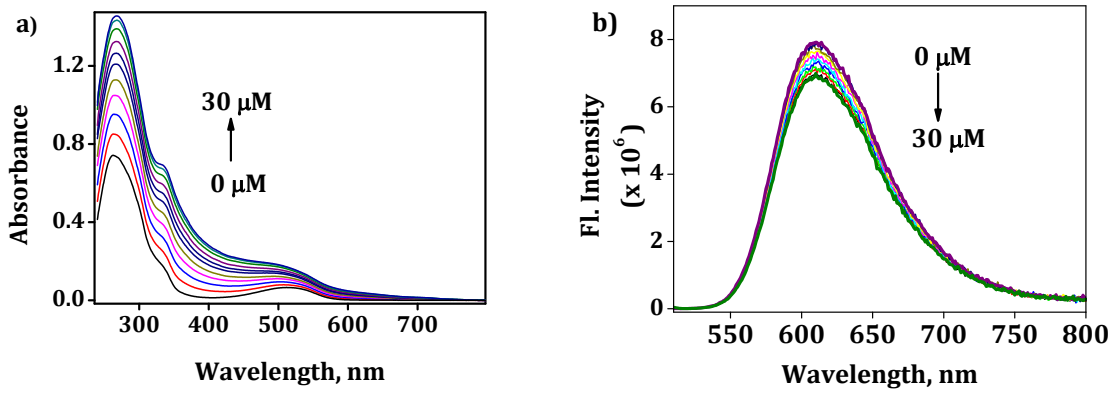

Figure 4B.8. Changes in the (**a**) absorption spectra of EB/dsDNA (30 μM/1.5 μM) in the presence of increasing [**F-An**]. (**b**) Corresponding fluorescence emission spectrum. λ_{ex}, 515 nm.

The possible interactions of the pendent aniline moiety via complete intercalation was ruled out based on DNA melting studies and ethidium bromide displacement assay. Initially, the fluorescence of EB was found to increase with increase in dsDNA due to intercalation of EB (Figure 4B.7a and 7b). Further, the changes in the fluorescence of 1:1 complex of dsDNA and ethidium bromide was measured by subsequent addition of **F-An** in small portions. The fluorescence emission of dsDNA/EB (3 μM/3 μM) complex addition of **F-An** upto 30 μM does not changed the fluorescence significantly (Figure 4B.8a and 8b).

Furthermore, the thermal denaturation studies (Figure 4B.9a) showed the melting temperature (T_m) of 49 ^oC for dsDNA (3 μM) and 47 ^oC for dsDNA/**F-An** (1:1).

Typically, the molecule which undergoes intercalative mode of binding increases the T_m by stabilizing the duplex DNA. Hence, the observed marginal destabilization of the dsDNA in the presence of nanocluster confirms the absence of intercalative mode of interaction. At 1:1 and 1:2 dsDNA/**F-An** there was no change in the CD signal validating the intact B-form structure of the dsDNA (Figure 4B.9b). Moreover, no significant induced circular dichroism (ICD) corresponding to the nanocluster absorption was observed which rules out the possibility of any chiral organization of the nanocluster in the presence of dsDNA. Further, the length of the dsDNA (~ 6.8 nm) and size of the nanocluster (~3.2 nm) allow interactions of: (i) multiple dsDNA with a single nanocluster and (ii) a single dsDNA with multiple nanoclusters, adding to the complexity of the solution state assemblies. Hence, the preferred self-assembly is mutual assisted interactions between **F-An** nanocluster with dsDNA and therefore, ICD for nanocluster in the presence of dsDNA were not observed.

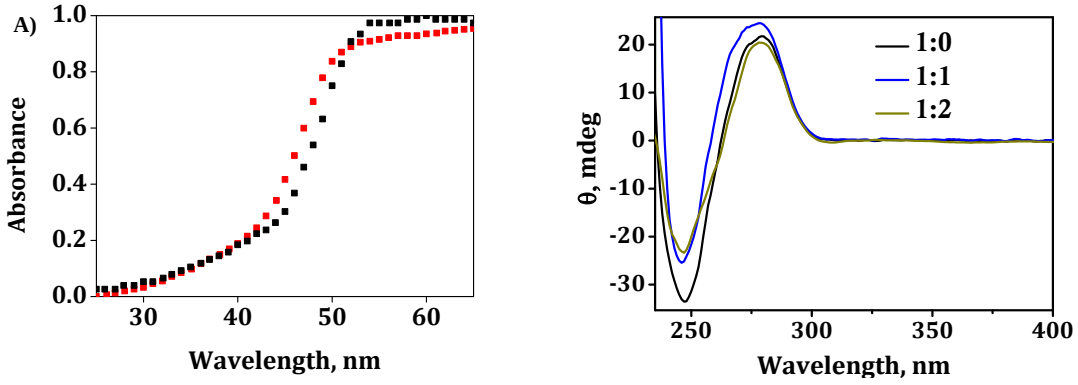

Figure 4B.9. a) Thermal denaturation curves for dsDNA (3 μM, T_m = 49 °C) and dsDNA/**F-An** (1:1, 3 μM each, T_m = 47 °C), absorbance monitored at 260 nm. b) Changes in the CD spectra of dsDNA (5 μM) in the presence of **F-An** nanoclusters (1 and 2 equivalents), suggesting the negligible changes in the DNA B-form structure.

4B.3.2. MORPHOLOGICAL STUDIES OF F-AN NANOCLUSTER/dS-DNA

The stabilized morphologies of the nanocluster-dsDNA assemblies were analyzed using AFM after drop casting a solution containing 1:1 dsDNA/**F-An** on a freshly cleaved mica surface. AFM images as shown in Figure 4B.10a, reveal the formation of nanofibres extending over several micrometers in length with a uniform thickness of ~ 80 nm or ~120 nm (joined bundles) and average height of 2 nm. The size estimations from AFM could be erroneous as in the previous case due to the possible interactions with the mica surface.[51,52] Further analysis of the nanocluster-dsDNA assemblies using TEM confirmed the formation of long, uniform nanofibres with average thickness of ~12 nm (Figure 4B.10b). High resolution TEM images of these

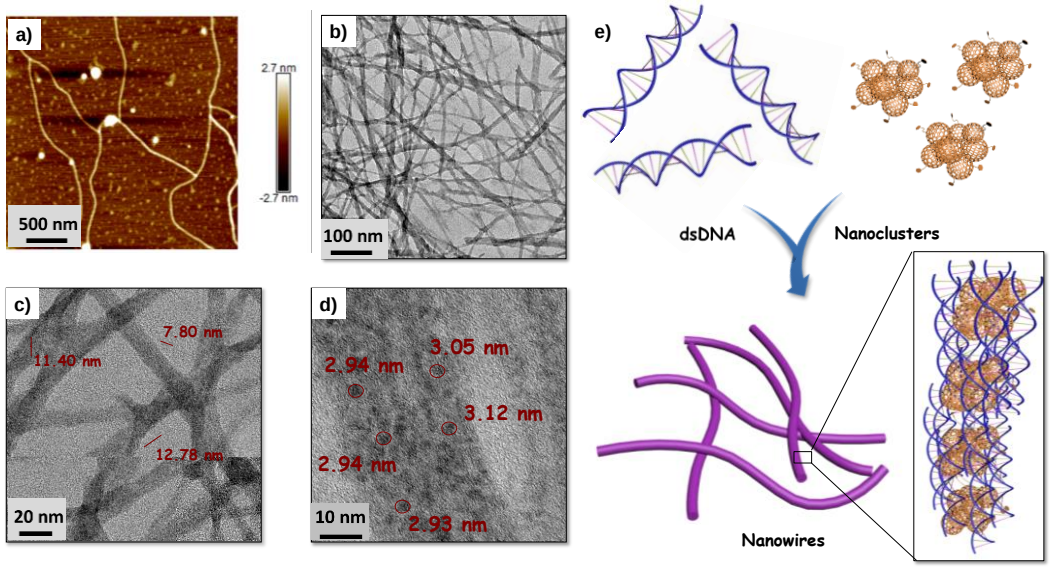

Figure 4B.10. (a) AFM height image of the dsDNA/**F-An** (1:1, 3 μM each) sample showing uniform nanowires with an average height of ~2 nm. (b) TEM image showing the formation of micrometer long nanowires. (c) Zoomed portion of b indicating the average thickness of ~12 nm. (d) Further zooming of TEM image revealing the embedded **F-An** nanoclusters of ~3 nm size. (e) Schematic illustration of overall self-assembly process of dsDNA and **F-An** nanoclusters into micrometer size nanowires.

nanofibres showed dark spherical regions corresponding to the fullerene nanoclusters with an average diameter of ~3 nm which further confirmed the incorporation of the **F-An** nanoclusters in the assemblies (Figure 4B.10c and 10d).

The presence of DNA in the observed nanofibres was corroborated through a TEM supported EDAX analysis which revealed signatures of phosphorous atoms from the phosphate backbone of dsDNA, throughout the nanofibres (Figure 4B.11). Size and correlogram studies (Figure 4B.12a and 12b) obtained from DLS measurement of a solution containing 1:1 dsDNA/**F-An** also indicated the formation of larger aggregates when compared to **F-An** nanoclusters confirming the occurrence of the self-assembly of nanoclusters with DNA template in the solution. A schematic summary of the concept adopted is shown in Figure 4B.10e.

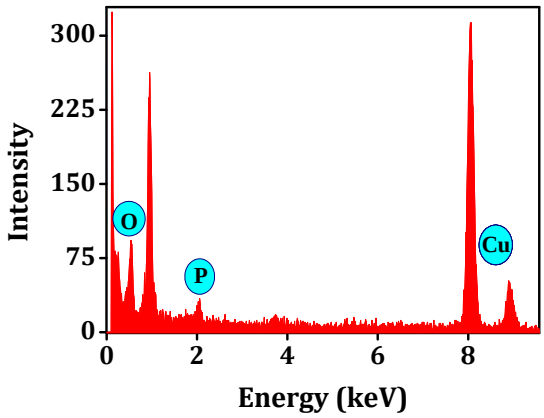

Figure 4B.11. EDAX measured over single fibre from dsDNA/**F-An** (1:1) showing corresponding peaks arising from the phosphorous and oxygen atoms of DNA backbone. This proves the fact that nanofibres mainly comprise of DNA wrapped around **F-An** nanoclusters.

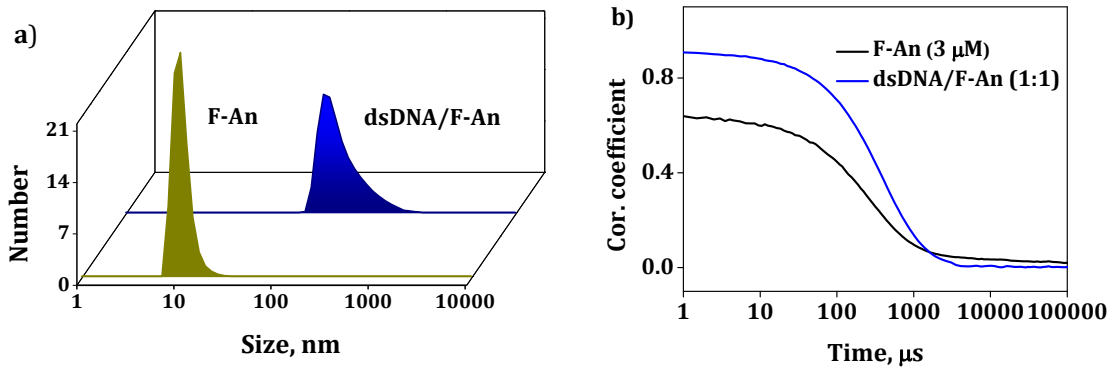

Figure 4B.12. Comparison of (**a**) size distribution profile of **F-An** (3 μM) and dsDNA/ **F-An** (1:1, 3 μM each). (**b**) Corresponding correlogram.

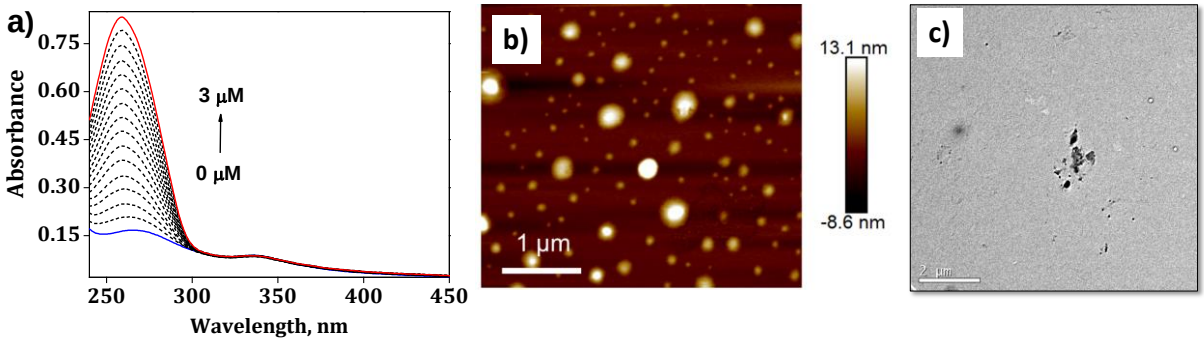

Figure 4B.13. The control experiments were carried out for the deeper understanding of **F-An**-DNA interaction. (**a**) Changes in the absorption of **F-An** with the sequential addition of DNA 1. (**b**) AFM image of **F-An**-DNA 1 (1:1, 3 μM each) complex. The unchanged absorption at 330 nm and the presence of nanoclusters instead of nanofibres in AFM rules out the possible interaction of **F-An** with single strand oligonucleotides. (**c**) TEM image of dsDNA (3 μM) showing featureless structure indicating the nanofibres formed were not from the individual dsDNA components.

The interaction of **F-An** nanoclusters with single strand were studied to get further insight into the self-assembly behaviour. The absorption of **F-An** at 330 nm was unchanged with the sequential addition of DNA 1 (Figure 4B.13a). Also, AFM image of DNA 1/**F-An** (1:1, 3 μM each) complex rendered nanoclusters instead of nanowires

(Figure 4B.13b). Control TEM experiments of dsDNA (3 μM) alone under similar experimental conditions failed to show any significant nanostructures (Figure 4B.13c). These results ruled out possible interactions of ssdna with **F-An** nanoclusters and indicate the crucial role of duplex nature of DNA in the mutual assisted self-assembly with **F-An** nanoclusters.

4B.3.3. THERMAL STABILITY OF dsDNA/F-An NANOWIRES

The thermal stability of the nanofibres formed by the self-assembly of **F-An** nanoclusters and dsDNA were probed by UV-Visible absorption spectroscopy, AFM and TEM techniques by varying the temperature of the solution between 25 ^{o}C and 70 ^{o}C and subsequent analysis at different temperatures. For example, upon increasing the temperature, the absorption corresponding to dsDNA at 260 nm showed characteristic enhancement at around 50 ^{o}C corresponding to the melting of the duplex (Figure 4B.14) an event which will break the nanowires apart leading to the release of **F-An** nanoclusters to the solution. A concomitant enhancement in the tail end absorption

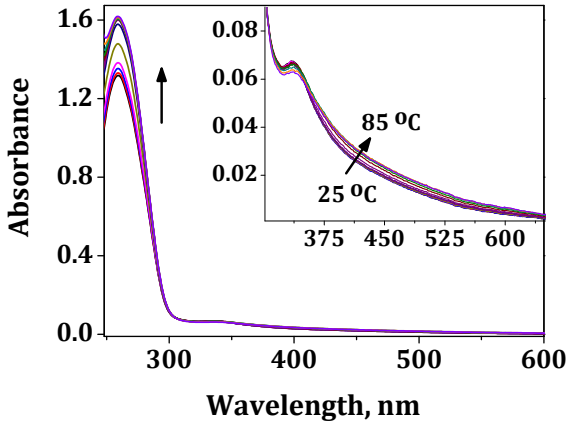

Figure 4B.14. Temperature dependent absorption spectra of dsDNA/**F-An** (1:1, 3 μM each), inset shows zoomed portion from 300-650 nm.

(400 nm - 600 nm) was also observed indicating possible interactions between the **F-An** nanoclusters leading to further aggregation of **F-An** nanoclusters (inset Figure 4B.14). Morphology analysis of an aliquot withdrawn at 70 °C and drop casted for TEM and AFM analysis showed the presence of 100-150 nm sized **F-An** nanoclusters, indicating complete dissolution of the nanofibre network (Figure 4B.15a and 15b). On the other hand, analysis of a sample withdrawn at 25 °C, following heating and slow cooling of the solution, showed the presence of bundled nanofibres having width of the individual fibers comparable to initially formed nanofibres (Figure 4B.15c and 15d). These results demonstrate the potential disassembly and reassembly of dsDNA/**F-An** nanofibres upon thermal cycling as schematically represented in Figure 4B.15e.

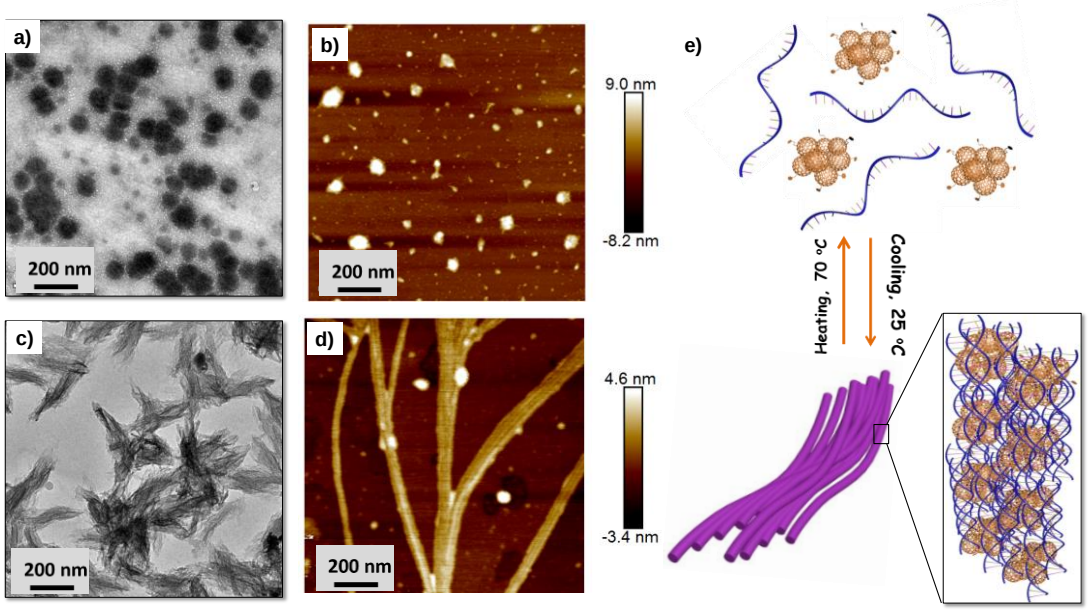

Figure 4B.15. (a) TEM and (b) AFM images of dsDNA/**F-An** sample upon heating to 70 °C indicating disassembly of nanowires. (c) TEM and (d) AFM images of the same sample after cooling back to 25 °C showing reassembly of nanowires. (e) Schematic representation of the disassembly and reassembly of dsDNA/**F-An** nanostructures upon heat-cool cycle.

4B.3.4. CONDUCTIVITY STUDIES

The self-organized nanostructures derived from fullerenes were reported to have improved optoelectronic properties.[53-56] So, we performed electrical measurements on dsDNA/**F-An** nanowire using c-AFM as represented schematically in Figure 4B.16a. A gold electrode was evaporated using chemical vapor deposition technique on top of the nanowires that has been pre-adsorbed on mica surface. In a typical experiment, the micrometer long nanowires protruding outwards from gold electrode were located by tapping mode using AFM conductive tip (Figure 4B.16b).

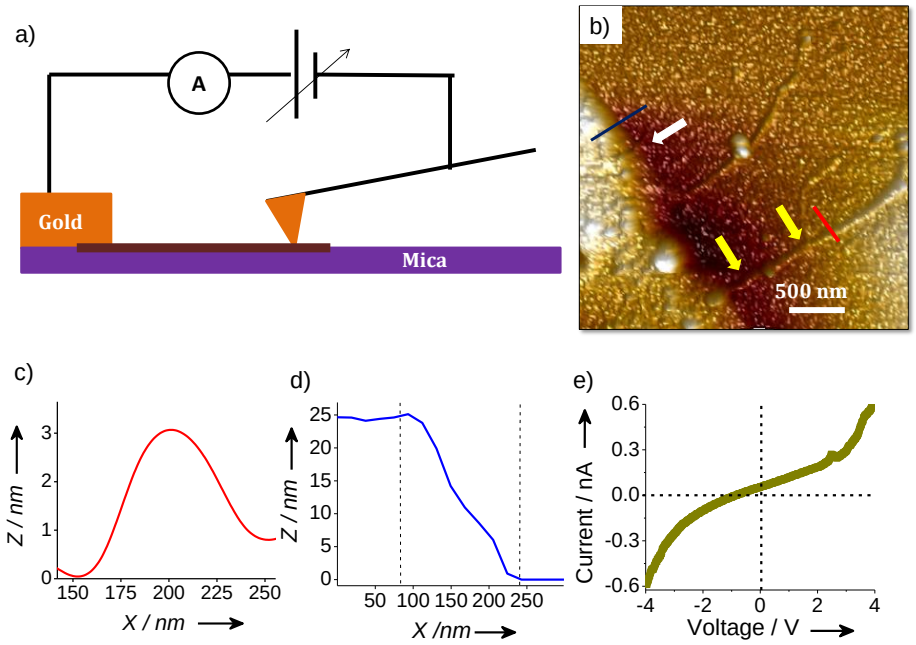

Figure 4B.16. (a) Schematic representation of the c-AFM measurement set-up. (b) AFM image showing dsDNA/**F-An** nanowire protruding from the edge of the metal electrode (c) AFM height profile of the nanowire at the location indicated by red line in b. (d) AFM height profile across the electrode and mica indicated by blue line in b. (e) I-V measurements taken at the position indicated by yellow arrow on the nanowire shown in b.

Height and width of the nanowires were quite similar to that obtained earlier (Figure 4B.16c). The thickness of the gold electrode was found to be ~25 nm (Figure 4B.16d). Subsequently, the tip was brought into contact with the sample, and the current along the nanowire was measured. The current-voltage (*I-V*) characteristics of the nanowire measured between +4 V to -4 V with applied bias voltage of 400 mV were presented in Figure 4B.16e. The nonlinear diode like characteristics clearly indicates the semiconducting property of the nanowires.

Under similar experimental conditions, measurements on the gold surface rendered ohmic behaviour due to the direct contact while mica surface showed insulator like behaviour due to the incomplete electrical contact between the tip and mica (Figure 4B.17). The conductivity behaviour of molecular C_{60} was reported previously[57] and in the present case, **F-An** nanoclusters were found to be semiconducting on HOPG surface (Figure 4B.18). Hence the observed semiconducting behaviour of the dsDNA/**F-An** nanowires could be attributed to the incorporated **F-An**

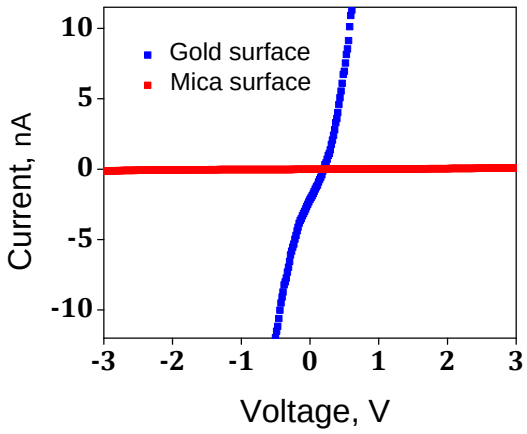

Figure 4B.17. Conductivity measurements. c-AFM measurements on gold (blue trace) and mica surface (red trace) indicates the ohmic and insulator behaviour respectively.

nanoclusters. The horizontal conductivity of the sample was calculated to be 8.12 x 10^{-5} S/m for a nanowire height of 3 nm and tip contact radius of 35 nm.[58,59]

The experiments were repeated multiple times and consistent current values were obtained each time confirming the negligible role of solvent/moisture in the conductivity measurements. Further, in order to exclude possible influence of metal deposits on nanowires beyond the electrode edge assisting the conduction path, we have conducted additional experimental analysis at longer distances from the electrode edge which were found to show similar conducting behaviour. These results confirm the semiconducting behaviour of the supramolecular nanowires obtained from mutual noncovalent interaction between the fullerene nanoclusters and dsDNA.

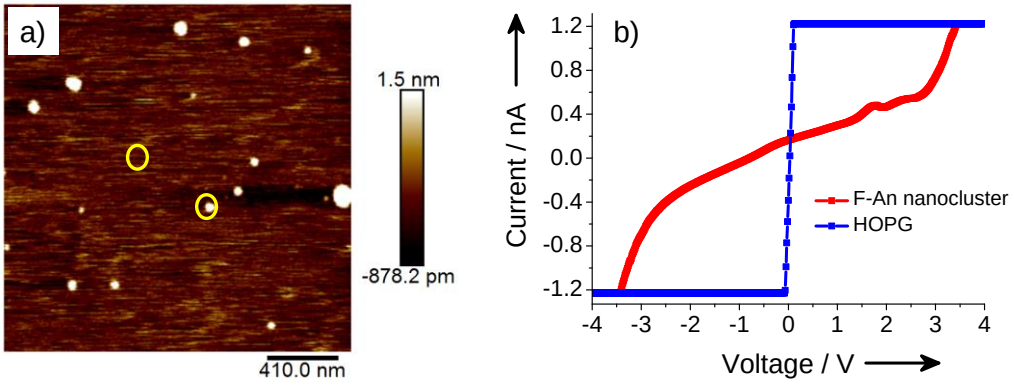

Figure 4B.18. Conductivity of **F-An** nanocluster. a) AFM image showing **F-An** nanocluster on HOPG surface b) corresponding I-V profile measured above nanocluster (red trace) and above HOPG surface (blue trace) at the region marked with yellow circle. The ohmic behaviour of HOPG surface is due to the high conducting behaviour whereas **F-An** nanocluster exhibits nonlinear diode like response.

4B.3.5. F-An NANOCLUSTER/3WJ-DNA INTERACTIONS

The prospect of fullerene nanoclusters in bringing small oligonucleotide duplexes into nanowires open up wide range of opportunities in DNA nanotechnology.

The possibilities of extending these assemblies to go beyond 1D nanostructure incorporating other DNA constructs are immediate challenges which will expand the scope and generality of the scheme. Herein, we report the construction of 2D nanosheets using fullerene derivative, **F-An** and 'Y' shaped three way junction-DNA (3WJ-DNA). Two different 3WJ-DNA namely, 3WJ-20 and 3WJ-30 containing 20 and 30 nucleobases respectively, were used which were synthesized through hybridization of three individual oligonucleotides. The interaction of **F-An** nanoclusters with 3WJ-DNA was investigated using UV-Visible absorption, fluorescence, circular dichroism (CD) studies and correspondingly, the morphological behaviour was probed through atomic force microscopy (AFM), transmission electron microscopy (TEM) and dynamic light scattering (DLS) techniques. The 3WJ-DNA was further modified with the cytosine rich overhang sequence which gives characteristic fluorescence emission upon binding with silver nanoclusters to obtain 3WJ-Overhang (3WJ-OH) structure. The 3WJ- OH/**F-An**

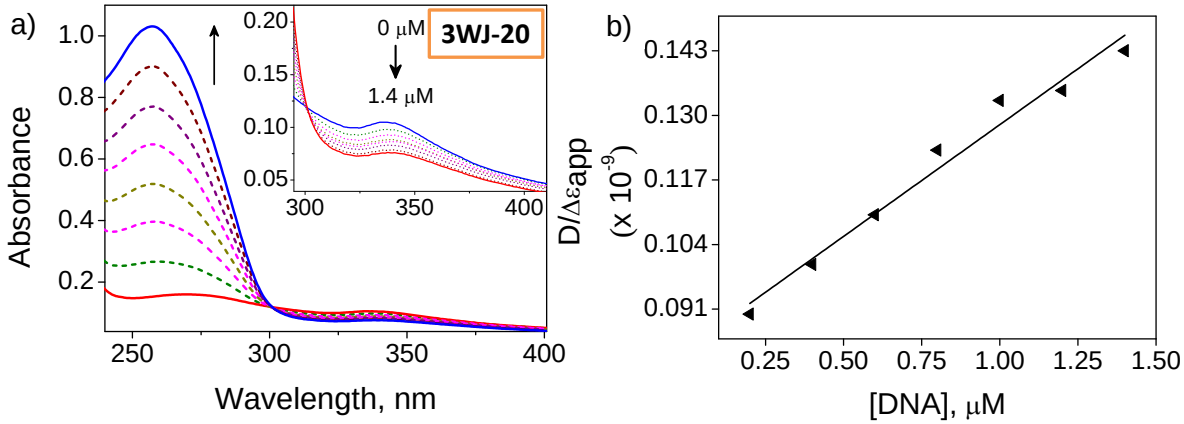

Figure 4B.19. a) Changes in the UV-Visible absorption of **F-An** nanoclusters (3 μM) upon addition of 3WJ-20 b) corresponding half reciprocal plot with increase in [3WJ-20].

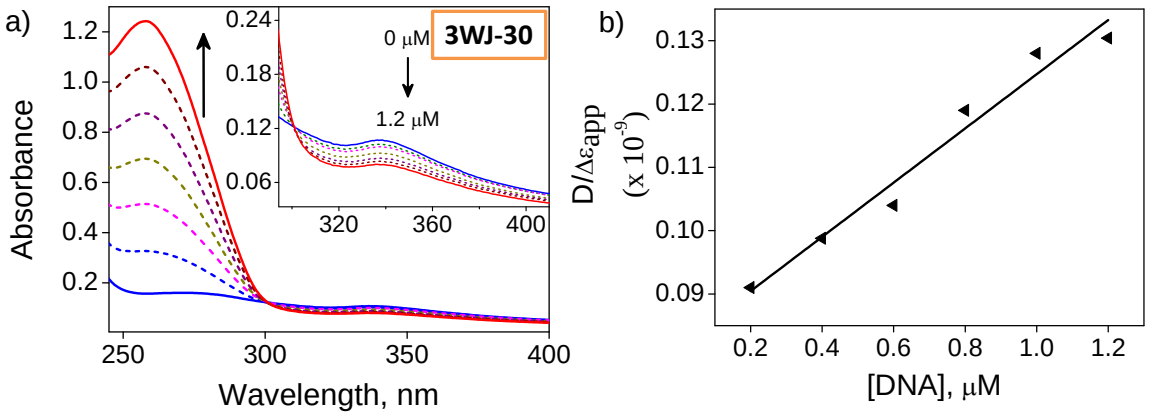

Figure 4B.20. a) Changes in the UV-Visible absorption of **F-An** nanoclusters (3 μM) upon addition of 3WJ-30 b) corresponding half reciprocal plot with increase in [3WJ-30].

complex resulted in two dimensional entangled nanonetwork structures due to the differential interaction of **F-An** nanocluster with duplex and single strand DNA. To the best of our knowledge, this represents the first example where two dimensional nanostructures constructed by the mutual self-assembly of DNA-fullerene nanoclusters were used in templated assembly of fluorescent AgNCs.

Initially, the interaction of **F-An** nanocluster with 3WJ-20 and 3WJ-30 was studied using UV-Visible absorption spectroscopy. Upon sequential addition of 3WJ-20 and 3WJ-30 to 10% DMSO-PBS containing **F-An** nanoclusters showed gradual increase at 260 nm with concomitant decrease in corresponding **F-An** absorption at 336 nm (Figure 4B.19a and 20a). Both 3WJ-20 and 3WJ-30 exhibited 26% and 28% hypochromicity respectively with an isosbestic point at 300 nm (inset of Figure 4B.19a and 20a) which is a clear indication of **F-An** nanocluster interacting with grooves of 3WJ-DNA. The intrinsic binding constant was calculated through half reciprocal plot

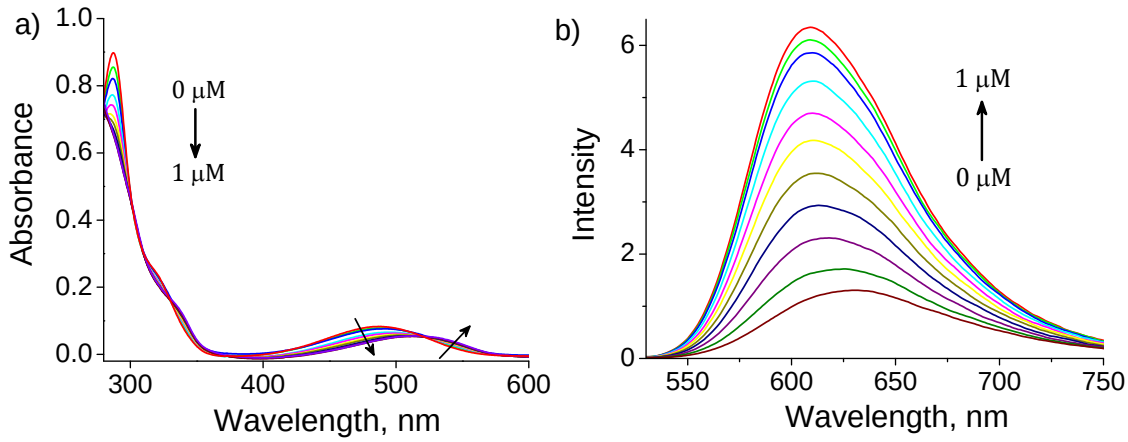

Figure 4B.21. Changes in the (a) absorption spectra and (b) emission spectra of ethidium bromide (30 μM) in the presence of increasing concentrations of 3WJ-30. λ_{ex}, 515 nm.

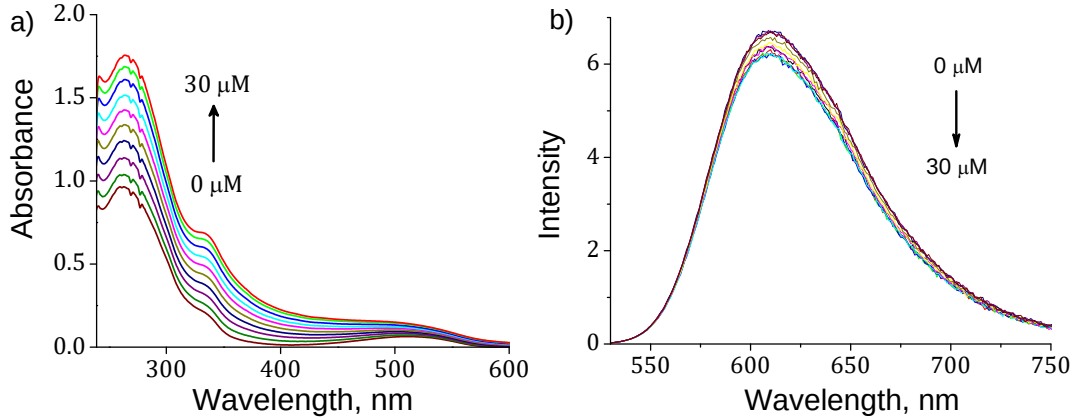

Figure 4B.22. Changes in the (a) absorption spectra and (b) emission spectra of ethidium bromide/3WJ-30 complex (30 μM/1 μM) in the presence of increasing concentrations of **F-An**. λ_{ex}, 515 nm.

and was found to be 5.46 x 10^5 M^{-1} for both 3WJ-DNA (Figure 4B.19b and 20b). Moreover, ethidium bromide (**EB**) based fluorescent displacement assay was used to get more insight into the mode of binding. Under similar conditions, the titration of 3WJ-20 and 3WJ-30 with **EB** rendered highly fluorescent complex (Figure 4B.21). The

titration of **F-An** nanocluster with 3WJ-30/**EB** complex rendered almost negligible changes in the fluorescence intensity even upto 30 μM of **F-An** revealing negligible displacement of bound **EB** (Figure 4B.22). Further, thermal denaturation studies of 3WJ-30 in the presence of **F-An** nanoclusters (1:1, 3 μM each; T_m = 48 °C) showed a destabilization of ~7 °C compared to 3WJ-30 alone (3 μM; T_m = 55 °C) following a similar trend as in the case of nanocluster duplex DNA interactions (Figure 4B.23a). Also, negligible CD changes for 3WJ-DNA in the presence of 1:1 **F-An** nanoclusters ruled out the possible intercalation mode of binding (Figure 4B.23b). These results unambiguously confirmed the interaction of **F-An** nanoclusters with 3WJ-DNA through groove interaction of fullerene and aniline moieties.

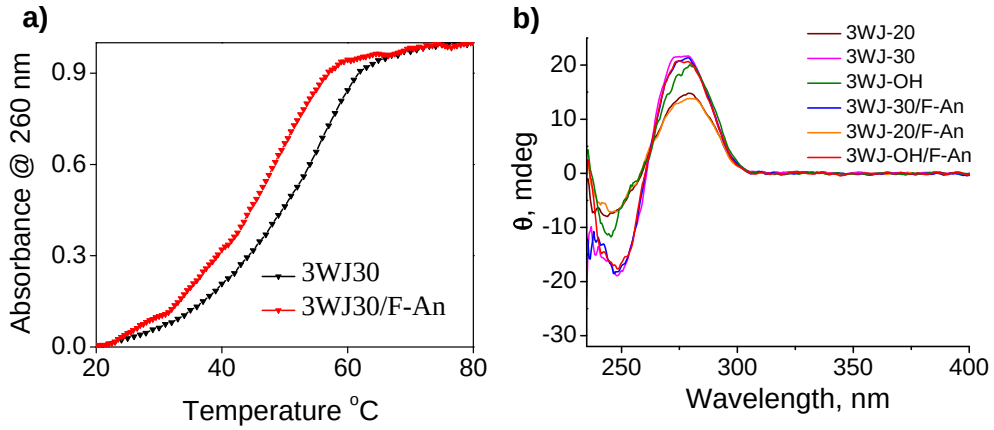

Figure 4B.23. a) Thermal denaturation curves for 3WJ-30 (1 μM, T_m = 55 °C) and 3WJ-30/**F-An** (1:1, 1 μM each, T_m = 48 °C), absorbance monitored at 260 nm (10 mM phosphate buffer, 100 mM NaCl, pH=7.4). b) The circular dichroism spectra of 3WJ-20, 3WJ-30, 3WJ-OH, **F-An**, 3WJ-20/**F-An** 3WJ-30/**F-An** and, 3WJ-OH/**F-An** (*c* = 3 μM each).

4B.3.6. MORPHOLOGICAL STUDIES OF F-An NANOCLUSTER/3WJ-DNA

The morphological studies accompanied by the interaction of **F-An** nanoclusters with 3WJ-DNA was investigated using AFM, TEM and DLS techniques. AFM studies of both 3WJ-30/**F-An** (1:1) and 3WJ-20/**F-An** (1:1) solutions drop cast on mica revealed the formation of micrometer sized, few layer nanosheets with a height ranging from 2-3 nm indicating a 2D nanoassembly as envisaged (Figure 4B.24a and 24b). The sheet-like morphology is a consequence of the three-way branched DNA geometry with a propensity of nanostructure growth in three different directions. High resolution TEM analysis of drop cast solutions of 1:1 3WJ-30/**F-An** also exhibited micrometer sized nanosheets, confirming the observations made during the AFM analyses (Figure

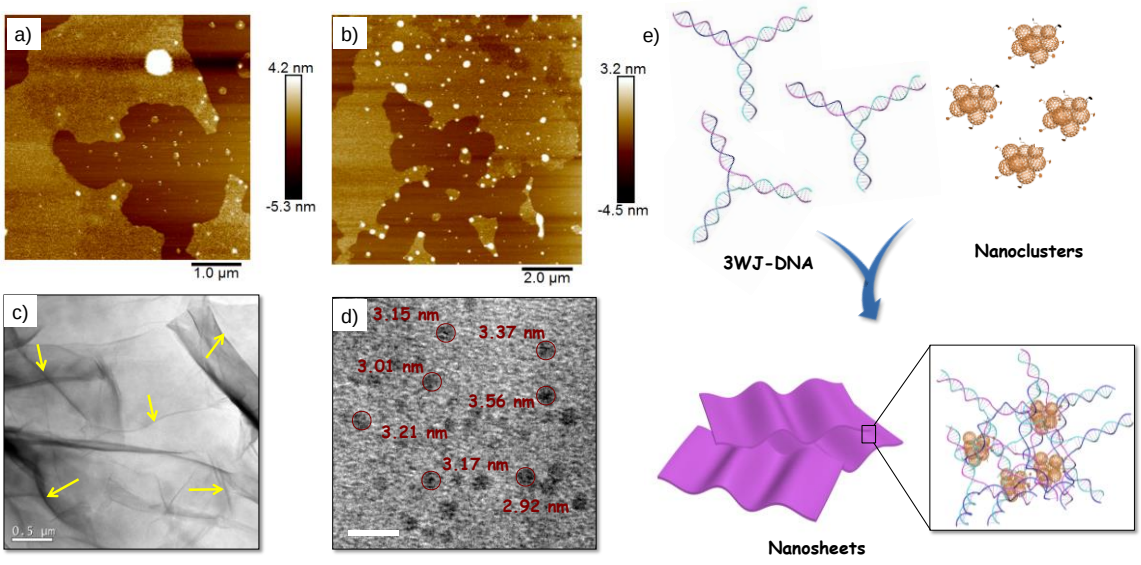

Figure 4B.24. AFM height image of the a) 3WJ-30/**F-An** and b) 3WJ-20/**F-An** (1:1, 3 µM each) sample showing micrometer sized nanosheets with an average height of ~2 nm. c) Corresponding TEM image of 3WJ-30/**F-An** showing few layered nanosheets (indicated with yellow arrow mark). d) Zoomed portion of the TEM image in c revealing the ~3 nm sized **F-An** nanoclusters embedded in the nanosheets. e) Schematic illustration of mutually assisted self-assembly between 3WJ-DNA and **F-An** nanoclusters into nanosheets.

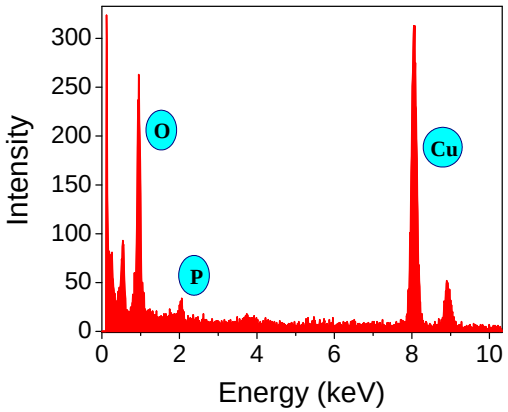

Figure 4B.25. EDAX analysis measurement of 3WJ-30/**F-An** (1:1) nanosheets showing corresponding peaks arising from the phosphorous and oxygen atoms of DNA backbone.

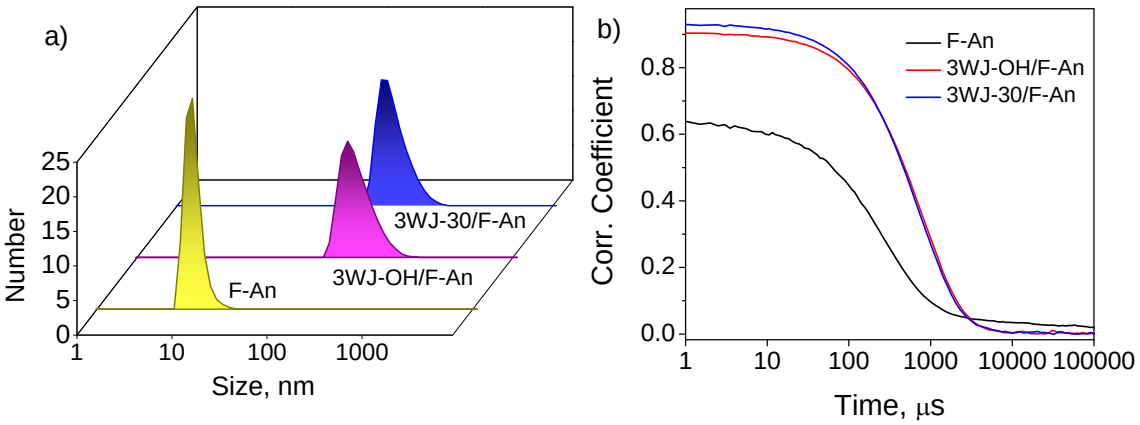

Figure 4B.26. a) The size distribution of **F-An**, 3WJ-30/**F-An** and 3WJ-OH/**F-An** obtained from DLS measurements. b) Corresponding correlogram plots.

4B.24c). Further, the embedded **F-An** nanoclusters of average size of ~3.2 nm were clearly visible in the high resolution TEM image (Figure 4B.24d), indicating the role of these nanoclusters in the observed nanosheet morphology. EDAX measurements validated the signatures of phosphorous and nitrogen atoms all through the nanosheets confirming the presence of 3WJ-DNA (Figure 4B.25). The 3WJ-DNA/**F-An** complex

showed observable changes in the hydrodynamic radius compared to **F-An** alone with smooth correlogram (Figure 4B.26). A cartoonic representation of the proposed self-assembly of 3WJ-DNA and **F-An** nanoclusters is given in Figure 4B.24e.

4B.3.7. MORPHOLOGICAL STUDIES OF F-An NANOCLUSTER/3WJ-OVERHANG

To further explore the application of these 2D nanosheets, we replaced the 3WJ-DNA by 3WJ-overhang DNA (3WJ-OH) with two clear objectives. i) To get more insight into the resultant nanostructures due to the differential interaction of **F-An** nanocluster with single strand and double strand DNA. ii) Application of these nanostructures in construction of DNA overhangs templated fluorescent AgNCs. Initially, the morphological behaviour of 3WJ-OH/**F-An** (1:1) complex was probed using AFM and

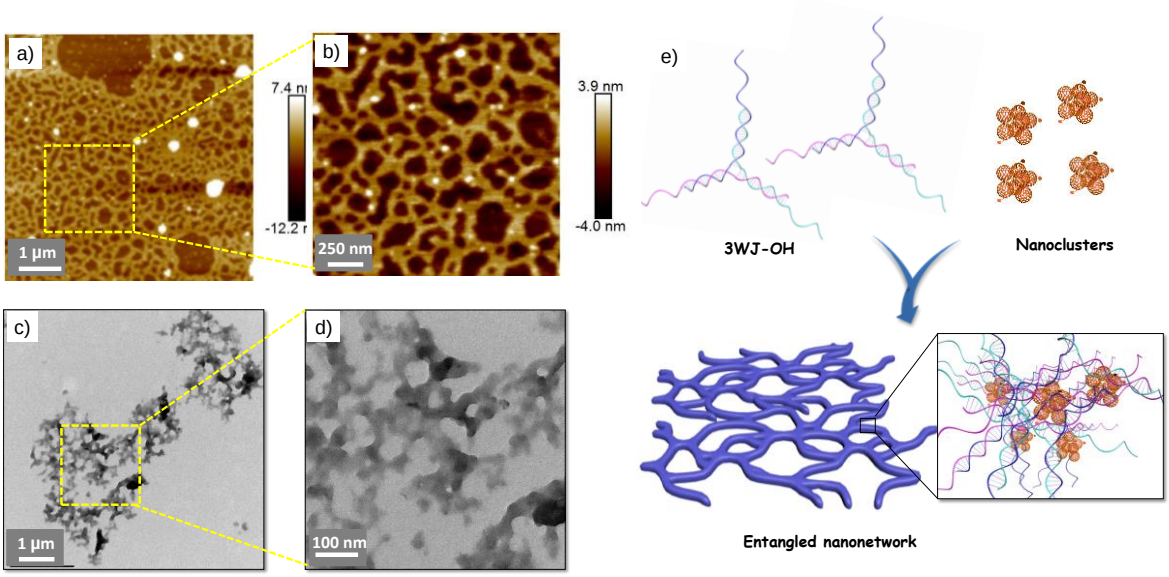

Figure 4B.27. AFM height image of the a) 3WJ-OH/**F-An** and b) Zoomed AFM image of selected portion showing micrometer sized entangled nanonetwork. c) Corresponding TEM image of 3WJ-OH/**F-An** and d) Zoomed TEM image of selected portion. e) Schematic illustration of mutually assisted self-assembly of 3WJ-OH and **F-An** nanoclusters into entangled nanonetwork structure.

TEM analyses. AFM studies exhibited micrometer sized entangled nanonetwork structure with height of about 2-3 nm representing distinct interaction of **F-An** nanocluster with 3WJ-OH compared to 3WJ-DNA (Figure 4B.27a and 27b). This could be attributed to the existence of single strand DNA overhang in 3WJ-OH which perturbs the continuous two dimensional growth of nanostructure unlike in 3WJ-DNA. TEM analysis of same solution also revealed the nanonetwork structure, in agreement with the result obtained from AFM studies (Figure 4B.27c and 27d). EDAX analysis further confirmed the presence of 3WJ-OH DNA as observed in the case of nanosheets (Figure 4B.28). The self-assembly process between 3WJ-OH and **F-An** nanoclusters was pictorially illustrated in Figure 4B.27e.

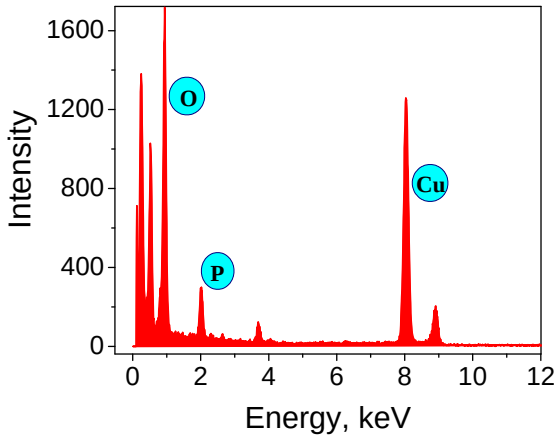

Figure 4B.28. EDAX analysis of 3WJ-OH/**F-An** (1:1) entangled nanonetwork showing corresponding peaks arising from the phosphorous and oxygen atoms of DNA backbone.

4B.3.8. 3WJ-OVERHANG DNA TEMPLATED SILVER NANOCLUSTER

The cytosine rich sequence (5'-CCC CTC CTT CCT CC-3') present as an overhang in 3WJ-OH was chosen specifically to assemble fluorescent silver nanoclusters (AgNCs)

on the self-assembled nanostructures.[60] As reported in the previous section, 3WJ-OH forms nanonetwork type structures in which the single strands of overhang regions could nucleate and stabilize AgNCs. This design will place the formed AgNCs causes the nanonetwork structures making the entire construct fluorescent active. We have initially assembled the nanonetwork structure by mixing 3WJ-OH/**F-An** (1:1, 15 μM, 50 μL). To this mixture we have added silver nitrate (135 μM) and sodium borohydride (67.5 μM) to provide DNA: $AgNO_3$: $NaBH_4$ molar ratio of 1: 9: 4.5. The AgNCs on the

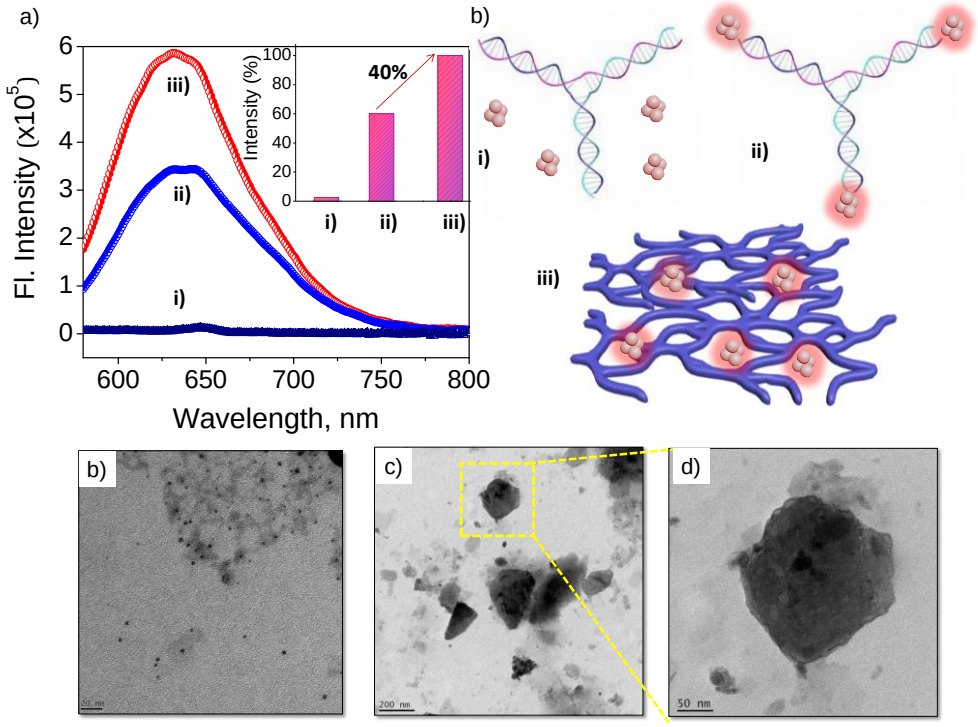

Figure 4B.29. a) The fluorescence emission spectra of silver nanoclusters in the presence of different DNA templates, i) 3WJ-30, ii) 3WJ-OH and iii) 3WJ-OH/**F-An**. b) The corresponding pictorial representation is depicted in right side, i) 3WJ-30/AgNCs, ii) 3WJ-OH/AgNCs and iii) 3WJ-OH/**F-An** nanonetwork embedded AgNCs. TEM image of c) 3WJ-OH/AgNCs d) 3WJ-OH/**F-An** appended AgNCs and e) Zoomed TEM image of selected portion showing realigned nanosheet structure after the formation of overhang templated AgNCs.

network was purified by centrifugation and washing to remove unbound starting materials before investigation of the photophysical properties. Control experiments with 3WJ-30/AgNCs did not show any fluorescence due to the absence of cytosine rich overhang (Figure 4B.29a, i). The emission of AgNCs stabilized with 3WJ-OH and 3WJ-OH/**F-An** nanonetwork was monitored under the similar conditions. The 3WJ-OH/AgNCs complex showed characteristic fluorescence emission maximum at 632 nm (λ_{exc} = 560 nm, Figure 4B.29a, ii) which corresponds to the AgNCs bound cytosine rich overhang as reported earlier.[61] 3WJ-OH/**F-An** nanonetwork stabilized AgNCs showed enhanced emission intensity compared to bare 3WJ-OH/AgNCs (Figure 4B.29a, iii). This shows 40% enhancement in the fluorescence of AgNCs in the 3WJ-OH/**F-An** nanonetwork compared to bare 3WJ-OH (inset, Figure 4B.29a). The AgNCs fluorescence enhancement and stabilization was schematically explained as shown in Figure 4B.29b. The AgNCs in the presence of 3WJ-20 or 3WJ-30 is non-emissive due to the absence of

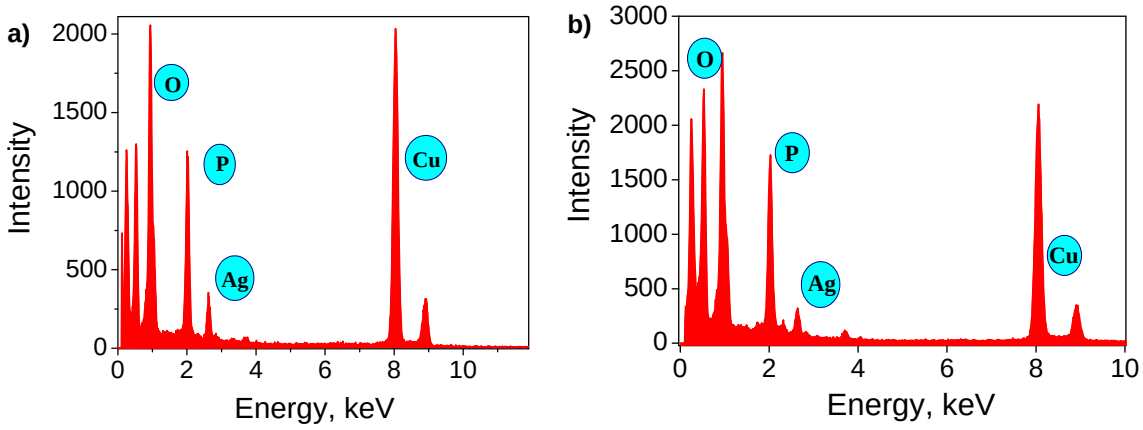

Figure 4B.30. EDAX analysis of a) 3WJ-OH/AgNCs and b) 3WJ-OH/**F-An** nanonetwork embedded AgNCs showing corresponding peaks arising from the phosphorous, oxygen of DNA backbone and silver atoms from AgNCs.

cytosine rich stabilizing overhang (Figure 4B.29b, i) whereas, AgNCs in the presence of 3WJ-OH will show characteristic fluorescence emission due to the stabilization of AgNCs in the cytosine rich overhang (Figure 4B.29b, ii). On the other hand, 3WJ-OH/**F-An** nanonetwork structure provides extra stability for the AgNCs (Figure 4B.29b, iii) which might be responsible for the enhanced emission relative to bare 3WJ-OH as reported earlier.[62]

Further analysis of 3WJ-OH/AgNCs using TEM showed presence of ~5 nm size silver nanoclusters (Figure 4B.29c). The signature of silver atoms from the obtained nanocluster was evidenced from EDAX analysis (Figure 4B.30a). TEM analyses of 3WJ-OH/**F-An** stabilized AgNCs clearly indicate the formation of two dimensional nanosheet structures (Figure 4B.29d and 29e), unlike previously observed 3WJ-OH/**F-An** nanonetworks. This structural realignment of nanonetwork into nanosheets might be due to the continuous growth of DNA and **F-An** nanoclusters in the AgNCs stabilized 3WJ-OH. The occurrence of silver atom was further proved from EDAX measurement (Figure 4B.30b). These results unambiguously demonstrate the structural programmability of two dimensional nanoarchitectures constructed from 3WJ-DNA/**F-An** and their application as a platform for immobilization of organic/inorganic functional motifs.

4B.4. CONCLUSIONS

In summary, we have presented a new strategy for hierarchical assembly of random, unmodified duplex DNA into functional nanomaterials where self-assembled fullerene nanoclusters act as stapler motifs. This assembly, in the true sense, is mutually

assisted where both fullerene clusters and dsDNA get included in the nanostructures, and both are essential for the continuous growth. Initially, the fullerene derivative, **F-An** forms nanoclusters with an average size of 3.2 nm in 10% DMSO-PBS, which further interact with DNA through multiple non-covalent interactions. The interactions between **F-An** nanoclusters and short oligonucleotide duplexes such as dsDNA, 3WJ-DNA and 3WJ-OH used in this study lead to the formation of micrometer sized nanowires, nanosheets and entangled nanonetwork structure. The double helical B-form structure of dsDNA are unperturbed during the nanostructure formation, which further demonstrates the potential of this strategy in building higher order nanostructures without compromising secondary structures of the component duplex DNA strands. Moreover, the semiconducting nature of these nanowires as revealed by c-AFM measurements offers the prospect of DNA based molecular electronics. We also have presented the application of extended 2D nanostructures in stabilizing the AgNCs more efficiently, enhancing the emission by 40% compared to bare 3WJ-OH. Thus the strategies presented here could be used for hierarchical assembly of unmodified short DNA strands into 1D/2D nanomaterials with possible post functional properties and hence open up new avenues in the field of DNA nanotechnology.

4B.5. EXPERIMENTAL SECTION

4B.5.1. Materials and Methods

All chemicals and reagents used for the organic synthesis were purchased from Sigma Aldrich and were used as received. Solvents were dried using the standard procedures. TLC analysis were done on aluminium plates coated with silica gel 60 F_{254},

column chromatography were performed on 200-400 mesh silica gel. ^{1}H NMR (500 MHz) and ^{13}C NMR (125 MHz) spectra were measured on a Bruker Avance DPX spectrometer. Chemical shifts are reported in parts per million (ppm) using tetramethylsilane (TMS) (δ_H = 0 ppm) or the solvent residual signal ($CDCl_3$: δ_C = 77.00 ppm) as an internal reference. The resonance multiplicity is described as s (singlet), d (doublet), t (triplet) and m (multiplet). High resolution mass spectral (HRMS) analysis was performed on a Thermo Scientific Q Exactive Hybrid Quadrupole-Orbitrap electrospray ionization mass spectrometer (ESI-MS) instrument. Measurements were done in ESI mode. Matrix-assisted laser desorption ionization time-off-flight (MALDI-TOF) mass spectra were obtained on an AXIMA-CFR PLUS (KRATOS SHIMADZU) MALDI-TOF mass spectrometer.

The spectroscopic grade (99.8%) solvents were used as received for the measurements. Water used for all studies was Milli Q deionised water (18.2 MΩ.cm). The UV/Vis absorption spectra were recorded on a Shimadzu UV-2600 Spectrophotometer. The fluorescence emission spectra were recorded on a SPEX FFLUOROLOG-3 (FL3-221) spectrofluorimeter. Circular dichroism measurements were performed on a Jasco J-810 spectropolarimeter having peltier controlled thermostatic cell holder where the sensitivity, time constant and scan rate were chosen appropriately. All optical measurements were carried out using 1 cm cuvettes at room temperature (25± 1 ^{o}C), unless otherwise mentioned. The DLS experiments were performed in quartz cuvettes using the same solutions which are used for microscopic

studies. The hydrodynamic diameters of the nanoclusters were determined using a Malvern Zeta Nano-ZS system.

4B.5.2. Oligonucleotide Sequences

Oligonucleotide sequences used in the present work were as follows,

dsDNA

DNA1: 5'-CGT CAC GTA AAT CGG TTA AC-3'

DNA2: 5'-GTT AAC CGA TTT ACG TGA CG-3'

3WJ-20

DNA 3: 5'-GGT GGC GAG AGC GAC GAT CC-3'

DNA 4: 5'-GGA TCG TCG CAG AGT TGA CC-3'

DNA 5: 5'-GGT CAA CTC TTC TCG CCA CC-3'

3WJ-30

DNA 6: 5'-ATT ACG GTG GCG AGA GCG ACG ATC CTG TAT-3'

DNA 7: 5'-ATA CAG GAT CGT CGC AGA GTT GAC CAT GCT-3'

DNA 8: 5'-AGC ATG GTC AAC TCT TCT CGC CAC CGT AAT-3'

3WJ-OH

DNA 9: 5'-GGT GGC GAG AGC GAC GAT CCC CTC CTT CCT CC-3'

DNA 10: 5'-GGA TCG TCG CAG AGT TGA CCC CTC CTT CCT CC-3'

DNA 11: 5'-GGT CAA CTC TTC TCG CCA CCC CTC CTT CCT CC-3'

Phosphoramidites for automated solid phase DNA synthesis were purchased from Glen Research (http://www.glenresearch.com/index.php). Other reagents needed for DNA syntheses were purchased from Sigma Aldrich. Oligonucleotides were

synthesized on H-8 K&A DNA synthesizers by following standard protocols.[50] The synthesized oligonucleotides were purified by LC-6AD Shimadzu Reverse Phase High Performance Liquid Chromatography (RP-HPLC) with an Inertsil® ODS-3, 5 µm, 10 x 250 mm reversed phase column. The oligonucleotide samples were then desalted using Sep-Pak C18 cartridge. The concentrations of corresponding strands were determined by monitoring UV absorbance at 260 nm. Hybridisation of dsDNA was carried out by annealing complementary single strands (DNA 1 & DNA 2) in 10 mM phosphate buffer containing 2 mM NaCl (pH = 7.4). Melting curves were measured by monitoring the absorbance at 260 nm while the temperature was increased at a rate of 1 °C/min. A stock solution of 100 µM of dsDNA solutions was used for all further studies.

4B.5.3. Preparation of DNA-Templated Silver Nanoclusters (DNA-AgNCs)

DNA stabilized AgNCs were synthesized according to the modified literature procedure.[63] In a typical experiment, 7.5 µL of 3WJ-OH (100 µM) was mixed with 5 µL of $AgNO_3$ (1.35 mM) in 10 mM phosphate buffer and 100 mM NaCl. The mixture was incubated for 10 minutes with a gentle stirring and reduced using freshly prepared solution of $NaBH_4$ (2.5 µL, 1.35 mM). The standardized concentrations were chosen to provide DNA: $AgNO_3$: $NaBH_4$ molar ratio of 1: 9: 4.5 which was found to give better fluorescent AgNCs. The sample was further vortexed for 2 minutes and allowed to react in the dark at room temperature for 12 hours before spectral measurements. The final concentrations of 3WJ-OH, $AgNO_3$ and $NaBH_4$ were 15 µM, 135 µM and 67.5 µM respectively (final volume of 50 µL).

The concentration of DNA-AgNCs was referred to the concentration of DNA unless otherwise mentioned. In case of 3WJ-OH/**F-An** templated AgNCs preparations, a similar procedure was followed in which 3WJ-OH was replaced with 3WJ-OH/**F-An** complex (1:1, 15 μM each). Similarly, the control experiments were also carried out in the absence of DNA template and in the absence of overhang (using 3WJ-20). A solution of 20 μL DNA-AgNCs (15 μM) diluted to 1 mL using 10 mM phosphate buffer and 100 mM NaCl was used for all further photophysical and morphological studies.

4B.5.4. AFM/TEM Sample Preparations

Samples for the AFM imaging were prepared by drop-casting 10 μL solution of **F-An** (3 μM), dsDNA/**F-An** (1:1, 3 μM) onto freshly cleaved mica sheet under ambient conditions and were dried under air. A BRUKER MULTIMODE AFM operating with a tapping mode regime was used to record AFM images under ambient conditions. Micro fabricated TiN cantilever tips (NT-MDT-NSG series) with a resonance frequency of 299 kHz and a spring constant of 20 to 80 Nm^{-1} were used. AFM section analysis was done offline. For c-AFM measurements, the gold electrode deposition were carried out in ultra-high vacuum chamber and the platinum coated conductive probes (NT-MDT-CSG series) were used in humidity controlled atmosphere (<40% relative humidity). The corresponding conductivity was calculated as reported in the literature.[58,59] The conductivity measurement of **F-An** nanoclusters was performed similar to that of nanowires by drop casting the **F-An** solution (10 μL) on HOPG surface. AFM image of disassembled and reassembled samples were prepared by drop

casting the solution of dsDNA/**F-An** complex at 70 ^{o}C and 25 ^{o}C, respectively. TEM samples were prepared by drop casting 10 μL solution of the sample on the top of the carbon-coated Cu grid. The samples were allowed to adsorb on the grid overnight at ambient conditions and was added Millipore water (2 x 10 μL) to remove buffer salts. TEM analysis was performed with a JEOL 100 kV high-resolution transmission electron microscope. The accelerating voltage of the TEM was 100 kV and the beam current was 65 A. Samples were imaged with a Hamamatsu ORCA CCD camera.

4B.6. REFERENCES

1) Yin, P.; Choi, H. M. T.; Calvert, C. R.; Pierce, N. A., Programming biomolecular self-assembly pathways. *Nature* **2008**, *451*, 318-322.
2) James, J. S.; Chad, A. M., Programmed Materials Synthesis with DNA. *Chem. Rev.* **1999**, *99*.
3) Pinheiro, A. V.; Han, D.; Shih, W. M.; Yan, H., Challenges and opportunities for structural DNA nanotechnology. *Nat. Nanotechnol.* **2011**, *6*, 763-772.
4) Yang, D. Y.; Campolongo, M. J.; Tran, T. N. N.; Ruiz, R. C. H.; Kahn, J. S.; Luo, D., Novel DNA materials and their applications. *WIREs Nanomed. Nanobiotechnol.* **2010**, *2*, 648-669.
5) Mangalum, A.; Rahman, M.; Norton, M. L., Site-Specific Immobilization of Single-Walled Carbon Nanotubes onto Single and One-Dimensional DNA Origami. *J. Am. Chem. Soc.* **2013**, *135*, 2451-2454.
6) Maune, H. T.; Han, S. P.; Barish, R. D.; Bockrath, M.; Iii, W. A.; Rothemund, P. W.; Winfree, E., Self-assembly of carbon nanotubes into two-dimensional geometries using DNA origami templates. *Nat. Nanotechnol.* **2010**, *5*, 61-6.
7) Bhatia, D.; Arumugam, S.; Nasilowski, M.; Joshi, H.; Wunder, C.; Chambon, V.; Prakash, V.; Grazon, C.; Nadal, B.; Maiti, P. K.; Johannes, L.; Dubertret, B.; Krishnan,

Y., Quantum dot-loaded monofunctionalized DNA icosahedra for single-particle tracking of endocytic pathways. *Nat. Nanotechnol.* **2016**, *11*, 1112-1119.

8) Wilner, O. I.; Orbach, R.; Henning, A.; Teller, C.; Yehezkeli, O.; Mertig, M.; Harries, D.; Willner, I., Self-assembly of DNA nanotubes with controllable diameters. *Nat. Commun.* **2011**, *2*, 540.

9) Park, S. Y.; Lytton-Jean, A. K. R.; Lee, B.; Weigand, S.; Schatz, G. C.; Mirkin, C. A., DNA-programmable nanoparticle crystallization. *Nature* **2008**, *451*, 553-556.

10) Li, X.; Yang, X.; Qi, J.; Seeman, N. C., Antiparallel DNA Double Crossover Molecules As Components for Nanoconstruction. *J. Am. Chem. Soc.* **1996**, *118*, 6131-6140.

11) Rothemund, P. W. K., Folding DNA to create nanoscale shapes and patterns. *Nature* **2006**, *440*, 297-302.

12) Bujold, K. E.; Hsu, J. C. C.; Sleiman, H. F., Optimized DNA "Nanosuitcases" for Encapsulation and Conditional Release of siRNA. *J. Am. Chem. Soc.* **2016**, *138*, 14030-14038.

13) Ko, S. H.; Su, M.; Zhang, C.; Ribbe, A. E.; Jiang, W.; Mao, C., Synergistic self-assembly of RNA and DNA molecules. *Nat. Chem.* **2010**, *2*, 1050-1055.

14) Rahbani, J. F.; Hariri, A. A.; Cosa, G.; Sleiman, H. F., Dynamic DNA Nanotubes: Reversible Switching between Single and Double-Stranded Forms, and Effect of Base Deletions. *ACS Nano* **2015**, *9*, 11898-11908.

15) Liu, D.; Wang, M.; Deng, Z.; Walulu, R.; Mao, C., Tensegrity: Construction of Rigid DNA Triangles with Flexible Four-Arm DNA Junctions. *J. Am. Chem. Soc.* **2004**, *126*, 2324-2325.

16) Tian, Y.; Zhang, Y.; Wang, T.; Xin, H. L.; Li, H.; Gang, O., Lattice engineering through nanoparticle-DNA frameworks. *Nat. Mater.* **2016**, *15*, 654-661.

17) Auyeung, E.; Li, T. I. N. G.; Senesi, A. J.; Schmucker, A. L.; Pals, B. C.; de la Cruz, M. O.; Mirkin, C. A., DNA-mediated nanoparticle crystallization into Wulff polyhedra. *Nature* **2014**, *505*, 73-77.

18) Jones, M. R.; Macfarlane, R. J.; Lee, B.; Zhang, J.; Young, K. L.; Senesi, A. J.; Mirkin, C. A., DNA-nanoparticle superlattices formed from anisotropic building blocks. *Nat. Mater.* **2010**, *9*, 913-917.

19) Cheng, W.; Campolongo, M. J.; Cha, J. J.; Tan, S. J.; Umbach, C. C.; Muller, D. A.; Luo, D., Free-standing nanoparticle superlattice sheets controlled by DNA. *Nat. Mater.* **2009**, *8*, 519-525.

20) Ke, Y.; Ong, L. L.; Shih, W. M.; Yin, P., Three-Dimensional Structures Self-Assembled from DNA Bricks. *Science* **2012**, *338*, 1177-1183.

21) Liu, W.; Halverson, J.; Tian, Y.; Tkachenko, A. V.; Gang, O., Self-organized architectures from assorted DNA-framed nanoparticles. *Nat. Chem.* **2016**, *8*, 867-873.

22) Aldaye, F. A.; Palmer, A. L.; Sleiman, H. F., Assembling Materials with DNA as the Guide. *Science* **2008**, *321*, 1795-1799.

23) Mirkin, C. A.; Letsinger, R. L.; Mucic, R. C.; Storhoff, J. J., A DNA-based method for rationally assembling nanoparticles into macroscopic materials. *Nature* **1996**, *382*, 607-9.

24) Jones, M. R.; Seeman, N. C.; Mirkin, C. A., Programmable materials and the nature of the DNA bond. *Science* **2015**, *347*, 1260901.

25) Zhang, D. Y.; Hariadi, R. F.; Choi, H. M. T.; Winfree, E., Integrating DNA strand-displacement circuitry with DNA tile self-assembly. *Nat. Commun.* **2013**, *4*, 1965.

26) Zheng, J.; Constantinou, P. E.; Micheel, C.; Alivisatos, A. P.; Kiehl, R. A.; Seeman, N. C., Two-Dimensional Nanoparticle Arrays Show the Organizational Power of Robust DNA Motifs. *Nano Lett.* **2006**, *6*, 1502-1504.

27) Edwardson, T. G. W.; Lau, K. L.; Bousmail, D.; Serpell, C. J.; Sleiman, H. F., Transfer of molecular recognition information from DNA nanostructures to gold nanoparticles. *Nat. Chem.* **2016**, *8*, 162-170.

28) Malinovskii, V. L.; Wenger, D.; Häner, R., Nucleic acid-guided assembly of aromatic chromophores. *Chem. Soc. Rev.* **2010**, *39*, 410-422.

29) Kankia, B. I.; Buckin, V.; Bloomfield, V. A., Hexamminecobalt(III)-induced condensation of calf thymus DNA: circular dichroism and hydration measurements. *Nucleic Acids Res.* **2001**, *29*, 2795-2801.

30) Kankia, B. I., Hydration effects of Ni2+ binding to synthetic polynucleotides with regularly alternating purine–pyrimidine sequences. *Nucleic Acids Res.* **2000**, *28*, 911-916.

31) Petty, J. T.; Zheng, J.; Hud, N. V.; Dickson, R. M., DNA-Templated Ag Nanocluster Formation. *J. Am. Chem. Soc.* **2004**, *126*, 5207-5212.

32) Buceta, D.; Busto, N.; Barone, G.; Leal, J. M.; Domínguez, F.; Giovanetti, L. J.; Requejo, F. G.; García, B.; López-Quintela, A. M., Ag2 and Ag3 Clusters: Synthesis, Characterization, and Interaction with DNA. *Angew. Chem. Int. Ed. Engl.* **2015**, *54*, 7612-7616.

33) Warner, M. G.; Hutchison, J. E., Linear assemblies of nanoparticles electrostatically organized on DNA scaffolds. *Nat. Mater.* **2003**, *2*, 272-277.

34) Ma, Y.; Zhang, J.; Zhang, G.; He, H., Polyaniline Nanowires on Si Surfaces Fabricated with DNA Templates. *J. Am. Chem. Soc.* **2004**, *126*, 7097-7101.

35) Watson, S. M. D.; Galindo, M. A.; Horrocks, B. R.; Houlton, A., Mechanism of Formation of Supramolecular DNA-Templated Polymer Nanowires. *J. Am. Chem. Soc.* **2014**, *136*, 6649-6655.

36) Pruneanu, S.; Al-Said, S. A. F.; Dong, L.; Hollis, T. A.; Galindo, M. A.; Wright, N. G.; Houlton, A.; Horrocks, B. R., Self-Assembly of DNA-Templated Polypyrrole Nanowires: Spontaneous Formation of Conductive Nanoropes. *Adv. Funct. Mater.* **2008**, *18*, 2444-2454.

37) Janssen, P.; Vandenbergh, J.; van Dongen, J.; Meijer, E.; Schenning, A., ssDNA templated self-assembly of chromophores. *J. Am. Chem. Soc.* **2007**, *129*, 6078-6079.

38) Datta, B.; Schuster, G. B.; McCook, A.; Harvey, S. C.; Zakrzewska, K., DNA-directed assembly of polyanilines: modified cytosine nucleotides transfer sequence

programmability to a conjoined polymer. *J. Am. Chem. Soc.* **2006**, *128*, 14428-14429.

39) Tanaka, K.; Tengeiji, A.; Kato, T.; Toyama, N.; Shionoya, M., A discrete self-assembled metal array in artificial DNA. *Science* **2003**, *299*, 1212-3.

40) Saha, S.; Bhatia, D.; Krishnan, Y., pH-Toggled DNA Architectures: Reversible Assembly of Three-Way Junctions into Extended 1D Architectures Through A-Motif Formation. *Small* **2010**, *6*, 1288-1292.

41) Carneiro, K. M. M.; Aldaye, F. A.; Sleiman, H. F., Long-Range Assembly of DNA into Nanofibers and Highly Ordered Networks Using a Block Copolymer Approach. *J. Am. Chem. Soc.* **2010**, *132*, 679-685.

42) Li, Z.; Chung, S.-W.; Nam, J.-M.; Ginger, D. S.; Mirkin, C. A., Living Templates for the Hierarchical Assembly of Gold Nanoparticles. *Angew. Chem. Int. Ed. Engl.* **2003**, *42*, 2306-2309.

43) Vyborna, Y.; Vybornyi, M.; Rudnev, A. V.; Häner, R., DNA-Grafted Supramolecular Polymers: Helical Ribbon Structures Formed by Self-Assembly of Pyrene–DNA Chimeric Oligomers. *Angew. Chem. Int. Ed. Engl.* **2015**, *54*, 7934-7938.

44) Avakyan, N.; Greschner, A. A.; Aldaye, F.; Serpell, C. J.; Toader, V.; Petitjean, A.; Sleiman, H. F., Reprogramming the assembly of unmodified DNA with a small molecule. *Nat. Chem.* **2016**, *8*, 368-376.

45) Park, S.; Kang, Y. J.; Majd, S., A Review of Patterned Organic Bioelectronic Materials and their Biomedical Applications. *Adv. Mater.* **2015**, *27*, 7583-7619.

46) Krishnan, Y.; Simmel, F. C., Nucleic Acid Based Molecular Devices. *Angew. Chem. Int. Ed. Engl.* **2011**, *50*, 3124-3156.

47) Braun, E.; Eichen, Y.; Sivan, U.; Ben-Yoseph, G., DNA-templated assembly and electrode attachment of a conducting silver wire. *Nature* **1998**, *391*, 775-778.

48) Zhang, G.; Surwade, S. P.; Zhou, F.; Liu, H., DNA nanostructure meets nanofabrication. *Chem. Soc. Rev.* **2013**, *42*, 2488-2496.

49) Livshits, G. I.; Stern, A.; Rotem, D.; Borovok, N.; Eidelshtein, G.; Migliore, A.; Penzo, E.; Wind, S. J.; Di Felice, R.; Skourtis, S. S.; Cuevas, J. C.; Gurevich, L.;

Kotlyar, A. B.; Porath, D., Long-range charge transport in single G-quadruplex DNA molecules. *Nat. Nanotechnol.* **2014**, *9*, 1040-1046.

50) Vittala, S. K.; Saraswathi, S. K.; Joseph, J., Fullerene cluster assisted self-assembly of short DNA strands into semiconducting nanowires. *Chem. Eur. J.*, *23*, 15759-15765.

51) Butt, H. J.; Guckenberger, R.; Rabe, J. P., Quantitative scanning tunneling microscopy and scanning force microscopy of organic materials. *Ultramicroscopy* **1992**, *46*, 375-393.

52) Samorí, P.; Francke, V.; Mangel, T.; Müllen, K.; Rabe, J. P., Poly-para-phenylene-ethynylene assemblies for a potential molecular nanowire: an SFM study. *Optical Materials* **1998**, *9*, 390-393.

53) Nair, V. S.; Mukhopadhyay, R. D.; Saeki, A.; Seki, S.; Ajayaghosh, A., A π-gel scaffold for assembling fullerene to photoconducting supramolecular rods. *Sci. Adv.* **2016**, *2*, e1600142.

54) Insuasty, A.; Atienza, C.; Luis López, J.; Marco-Martínez, J.; Casado, S.; Saha, A.; Guldi, D. M.; Martín, N., Supramolecular One-Dimensional n/p-Nanofibers. *Sci. Rep.* **2015**, *5*, 14154.

55) Babu, S. S.; Mohwald, H.; Nakanishi, T., Recent progress in morphology control of supramolecular fullerene assemblies and its applications. *Chem. Soc. Rev.* **2010**, *39*, 4021-4035.

56) Shen, Y.; Reparaz, J. S.; Wagner, M. R.; Hoffmann, A.; Thomsen, C.; Lee, J.-O.; Heeg, S.; Hatting, B.; Reich, S.; Saeki, A.; Seki, S.; Yoshida, K.; Babu, S. S.; Mohwald, H.; Nakanishi, T., Assembly of carbon nanotubes and alkylated fullerenes: nanocarbon hybrid towards photovoltaic applications. *Chem. Sci.* **2011**, *2*, 2243-2250.

57) Randel, J. C.; Niestemski, F. C.; Botello-Mendez, A. R.; Mar, W.; Ndabashimiye, G.; Melinte, S.; Dahl, J. E. P.; Carlson, R. M. K.; Butova, E. D.; Fokin, A. A.; Schreiner, P. R.; Charlier, J.-C.; Manoharan, H. C., Unconventional molecule-resolved current rectification in diamondoid–fullerene hybrids. *Nat. Commun.* **2014**, *5*, 4877.

58) Prasanthkumar, S.; Gopal, A.; Ajayaghosh, A., Self-Assembly of Thienylenevinylene Molecular Wires to Semiconducting Gels with Doped Metallic Conductivity. *J. Am. Chem. Soc.* **2010**, *132*, 13206-13207.

59) Vedhanarayanan, B.; Babu, B.; Shaijumon, M. M.; Ajayaghosh, A., Exfoliation of Reduced Graphene Oxide with Self-Assembled pi-Gelators for Improved Electrochemical Performance. *ACS Appl. Mater. Interfaces* **2017** *9*, 19417–19426.

60) New, S. Y.; Lee, S. T.; Su, X. D., DNA-templated silver nanoclusters: structural correlation and fluorescence modulation. *Nanoscale* **2016**, *8*, 17729-17746.

61) Teng, Y.; Yang, X.; Han, L.; Wang, E., The relationship between DNA sequences and oligonucleotide-templated silver nanoclusters and their fluorescence properties. *Chem. Eur. J.* **2014**, *20*, 1111-5.

62) Zhu, J., Zhang, L., Teng, Y., Lou, B., Jia, X., Gua, X., and Wang, E., G-quadruplex enhanced fluorescence of DNA-silver nanoclusters and its application in bioimaging. *Nanoscale* **2012**, *7*, 13224-13229.

63) Richards, C. I. C., S.; Hsiang, J.-C.; Antoku, Y.; Vosch, T.; Bongiorno, A.; Tzeng, Y.-L.; Dickson, R. M., Oligonucleotide-Stabilized Ag Nanocluster Fluorophores. *J. Am. Chem. Soc.* **2008**, *130*, 5038-5039.

Papers Presented at Conferences (Posters/Oral)

1. **Sandeepa K. V.**, Sajena K. S. and Joshy Joseph*, *Fullerene Cluster Assisted Self-Assembly of DNA Strands into Semiconducting Nanowires*", A **Poster** presentation at the International Conference on Nanoscience and Technology held at Centre for Nano and Soft matter Sciences (CeNS), Jalahalli on March 21-23, 2018, Bengaluru, India (***Best Poster Award***).

2. **Sandeepa K. V.**, Remya R., Biswapriya Deb and Joshy Joseph*, "*Stimuli Responsive Cross-Linkable Fullerene: Investigation of their Photophysical, Morphological and Photovoltaic Properties*", **Oral** presentation at the International Conference on Advances in Analytical Sciences held at CSIR-Indian Institute of Petroleum, Dehradun on March 15-17, 2018.

3. **Sandeepa K. V.**, Remya R., Biswapriya Deb and Joshy Joseph*, "*Rational Synthesis of Polymerizable Fullerene: Study of their Photophysical, Morphological and Photovoltaic Properties*", A **Poster** presentation at the National Conference on Luminescence and its Applications held at CSIR- National Institute for Interdisciplinary Science and Technology on February 14-16, 2018, Trivandrum, India.

4. **Sandeepa K. V.**, Sajena K. S. and Joshy Joseph*, "*Construction of Semiconducting Nanowires via Self-Assembly of Fullerene Clusters and DNA Strands*", **Oral** presentation at the 30th Kerala Science Congress held at Govt. Brennen College, Thalassery during 28-30th January 2018.

5. **Sandeepa K. V.**, Sajena K. S. and Joshy Joseph*, *Mutual Self-Assembly of Fullerene Nanoclusters and Short DNA strands*, A **Poster** Presentation at the Photoinduced Processes in Nucleic Acids and Proteins: Faraday Discussion, to be held at Residency Towers on 11-13, January, 2018, Trivandrum.

6. **Sandeepa K. V.**, Sajena K. S. and Joshy Joseph*, *Mutually Assisted Self-Assembly of DNA Strands and Fullerene Clusters into Semiconducting Nanowires*, A **Poster** Presented at the 8th East Asia Symposium on Functional dyes and Advanced Materials, held at CSIR-National Institute for Interdisciplinary Science and Technology, Trivandrum during 20-22 September, 2017, Trivandrum, India.

7. **Sandeepa K. V.** and Joshy Joseph*, R*ational Design of Polymerizable Fullerenes: Optoelectronics and Self-Assembly Aspects*, **Oral and Poster** Presentation at the Short Course on Polymer Science and Indo-Japan Joint Symposium, held at Residency Tower, Trivandrum, India from 31st February to 1st March 2017.

8. **Sandeepa K. V.** and Joshy Joseph*, *Functionalized C_{60}-Fullerene Derivatives: Photophysical and Morphological Investigation of Self-Assembled Polyfullerenes*, A **Poster** Presented at the 18th CRSI National Symposium in Chemistry at Punjab University, Chandigarh, India from February 05-07, 2016.

9. **Sandeepa K. V.** and Joshy Joseph*, *Dual-stimuli Responsive Cross Linkable Fullerene: Tuning of Band gap and Morphological Evolution through Polyfullerene Formation,* A **Poster** Presented at the 8th Asian Photochemistry Conference (APC-2014), Trivandrum, Kerala, India, 2014, November 10-13.

List of Publications and Book Chapter

1. **Sandeepa K. Vittala**, Sajena K. Saraswathi and Joshy Joseph*, Fullerene Cluster Assisted Self-Assembly of Short DNA Strands into Semiconducting Nanowires, *Chem. Eur. J.,* **2017***,* 23, 15759-15765.

2. **Sandeepa K. Vittala**, and Joshy Joseph*, Chiral Self-Assembly of Fullerene Clusters on CT-DNA Template, *Faraday Discuss.,* **2017**, 207, 459 - 469.

3. **Sandeepa K. Vittala**, Sajena K. Saraswathi. and Joshy Joseph*, (2018), *Self-assembled Functional Fullerenes and DNA Hybrid Nanomaterials for Various Applications*, editor T. Govindaraju, Chapter 8, 'Templated DNA Nanotechnology: Functional Nucleic Acid Nanoarchitectures', Pan Stanford Publishing (Submitted).

4. **Sandeepa K. Vittala**, Sajena K. Saraswathi. and Joshy Joseph*, Self-assembled Nanosheets of DNA-Fullerene Clusters and their Templated Silver Nanocluster Formation, , *Chem. Commun*., (To be submitted).

5. **Sandeepa K. Vittala**, Remya R., Biswapriya Deb and Joshy Joseph*, A Novel Electron Transporting Cross-Linkable Fullerene Derivative for Inverted Polymer Solar Cells, *J. Mater. Chem. C* (To be submitted).

6. **Sandeepa K. Vittala**, Remya R, Biswapriya Deb and Joshy Joseph*, Side Chain Functionalized Fullerene: Synthesis, Oxidative Polymerisation, Morphological Studies and Utilization in Inverted Polymer Solar Cells (To be submitted).